UNIVERSITÄT DUISBURG ESSEN

Open-Minded

Dissertation on

Development of a Modular Multi-field Mechanical Setup for the Investigation of Magnetoelectric Materials

approved by

The Faculty of Engineering,
Department of Civil Engineering
Institute for Materials Science
for the fulfillment of the requirements for the degree of
Doctor in Natural Sciences (Dr. rer. nat.)

by

Ahmadshah Shahob Nazrabi

First referee : Prof. Dr. rer. nat. Doru C. Lupascu
Second referee : Prof. Dr.-Ing. Marc Kamlah
Date of Defense : 11th May 2023, Essen

DOI: 10.17185/duepublico/81935
URN: urn:nbn:de:hbz:465-20240515-073419-3

Abstract

The central theme of this thesis revolves around the development of setups dedicated to the mechanical characterization of functional materials. Here, two phase compound magnetoelectric multiferroics, composed of a ferromagnetic and ferroelectric phase are the functional composite material, and have the potential to transform many technological applications. They would enable the development of newer and more efficient architectures for electronic modules, like devices based on sensors. The functionality of the magnetoelectric multiferroics is based on the ferroelastic sensitivity of two phases in the compound, with ferroelasticity as their common property. As a result, the associated strain of each phase the field response mediates stress elastically into the other phase. The important composite *x*$CoFe_2O_4$-*(1-x)*-$BaTiO_3$ belongs to the magnetoelectric multiferroics family.

In order to design the composite materials in advance, material simulation tools are necessary. However, the existing data set of the magneto-electro-mechanical properties, which are used for modelling, are so far incomplete. The mechanical characterization of the composite material, given the mechanical nature of these properties, is key to understanding them. In light of this, a magneto-electro-mechanical characterization setup was designed and constructed to deliver a reliable data basis for the constitutive laws of the magnetoelectric coupling.

Given the diverse properties of the functional materials, several modular measurement options have been designed to measure them. They can be used in separate or complex multi-field arrangements, providing magnetic and electric fields as well as axial loading conditions. In addition, the setup has the option to apply an AC-stimulus of all three fields in addition to their DC offset fields. Moreover, the setup is equipped with detection capabilities which can be used to monitor strain, polarization, and magnetoelectric coupling. In particular, the integration of the Fabry-Pèrot interferometer in the setup is a novel approach which allows for the mechanical investigation of nanometer strain effects. By using the apparatus in a multiple fields arrangement would enable to quantify the effects of cross-coupling on the functional properties of the magnetoelectric composite. The data from experiments demonstrate the overall quality of the setup for a given property of the composite magnetoelectric materials and they set the benchmarks for the setup. They also prove that the modularity concept of the setup is successful.

With regard to the constitutive data on the magnetoelectric composite, the measurements with different modules of the setup deliver the piezoelectric coefficient d_{33} and the piezomagnetic coefficient q_{33}, which are proportional to the magnetoelectric coupling coefficient α_{ME}. For the d_{33} measurement, the module option for electrostriction is used. Its design allows the measurement of the strain, $\epsilon|_{\sigma,H}$, together with the polarization under constant magnetic fields and axial stress. Furthermore, the magnetoelectric coupling curve was measured under axial loads ($\alpha_{ME}|_{\sigma}$).

By using the developed magnetostriction measurement module, the magnetostriction of polycrystalline $CoFe_2O_4$ is measured with a Fabry-Pèrot interferometer for the first time. This measurement facilitate the derivation of the piezomagnetic coefficient q_{33}, which correlates with the ME coupling coefficient and establishing a functional relationship to the magnetoelectric coupling curve.

For the investigation of the influence of mechanical effects on magnetization, a pressure cell was constructed in order to apply axial loads. In this process, the concept for the calibration of the applied loads was crucial. This was solved by using an ex-situ method to measure the load. In general, for all the mechanical characterization measurements, the preparation of samples with high mechanical strength and large magnetoelectric effects was difficult and time-intensive. For this purpose, the synthesis route was modified in order to meet the requirements.

Kurzfassung

Die vorliegende Arbeit konzentriert sich auf die Entwicklung von Messaufbauten, die sich der mechanischen Charakterisierung der Funktionswerkstoffe widmen. Hierzu gehören die magnetoelektrischen Funktionswerkstoffe, die sich aus einer ferromagnetischen und ferroelektrischen Phase zusammensetzen. Zu der Familie gehört der Verbundwerkstoff $x\mathrm{CoFe_2O_4}$- *(1- x)*$\mathrm{BaTiO_3}$ und dient in Rahmen der Arbeit als Referenz-Werkstoff. Die Funktionsweise der magnetoelektrischen Multiferroika beruht auf der ferroelastischen Empfindlichkeit beider Phasen. Dabei ist die Feldantwort jeder Phase in dem Verbundwerkstoff mit einer Dehn- ung gekoppelt, die sich elastisch in die andere Phase übermitteln lässt. Die Multiferroika besitzen das Potenzial, die bestehenden technologischen Anwendungen in effizientere Versionen zu überführen und erlauben die Entwicklung neuer Architekturen für die elektronischen Module, wie z.B. für neuartige Konzepte in der Sensorik.

Um die Verbundwerkstoffe im Voraus zu konzipieren, sind Werkstoffsimulationen nötig. Hier, bedingt durch das mechanische Funktionsprinzip, ist die mechanische Charakterisierung des Verbundwerkstoffs der Schlüsselaspekt. Da jedoch die bisher vorhandenen Datensätzen für die mechanischen Simulationsmodelle lückenhaft sind, hat sich hierzu die vorliegende Arbeit zur Aufgabe gemacht, die Messinfrastruktur für eine zuverlässige experimentelle Charakterisierung der konstitutiven Datensätze zu entwickeln. Die dabei entstandenen Aufbauten ermöglichen das simultane Aufbringen der magnetischen und elektrischen Felder sowie der axialen mechanischen Spannungen. Darüber hinaus bedingt durch die vielfaltigen Eigenschaften der Funktionswerkstoffe, sind mehrere Messoptionen als modularisierte Einheiten konzipiert worden, so dass sie in separater oder komplexer Mehrfeldanordnung verwendet werden können. Zudem verfügt der Messaufbau zusätzlich die Optionen, alle drei konstanten Offset-Feldern mit ihren zughörigen Wechselfeldern zu überlagern. Die Detektierungsmöglichkeiten des Messaufbaus erlauben das Ermitteln der Dehnung, Polarisation und der magnetoelektrischen Kopplung bei konstanten Offset-Felder. Insbesondere die Integration des Interferometers in den Aufbauten zeichnet den neuartigen Ansatz aus, wodurch Dehnungseffekte ($\epsilon|_{\sigma,H}$) in Abhängigkeit konstanten Magnetfelder und axialer Lasten in nm-Bereich auflöst werden können. Die vielseitigen Messungen in dieser Arbeit beweisen die Modularität sowie Leistungsfähigkeit der Aufbauten. Damit lassen sich die funktionellen Eigenschaften sowie die Kreuzkopplungseffekte durch die zusätzlichen Felder für den magnetoelektrischen Werkstoff quantifizieren.

Hier liefert der Aufbau im Hinblick auf die konstitutiven Datensätze die piezomagnetischen Koeffizienten $\mathrm{q_{33}}$ und die piezoelektrischen Koeffizienten $\mathrm{d_{33}}$, die die Proportionalitätsparameter für die magnetoelektrischen Kopplungskoeffizienten α_{ME} darstellen. Dabei ist die $\mathrm{d_{33}}$ aus der Elektrostriktion hergeleitet.

Mit einem weiteren Modul des Aufbaus wurde die Magnetostriktion von polykristallinem $\mathrm{CoFe_2O_4}$ mit dem Fabry-Pèrot-Interferometer gemessen. Aus dieser Messung wird der piezomagnetische Koeffizient $\mathrm{q_{33}}$ hergeleitet. Hier korreliert die Dehnungsempfindlichkeitskurve mit der magnetoelektrischen Kopplungskoeffizienten-Kurve α_{ME}, die auch unter axialen Lasten gemessen ist. Das Ergebnis liefert die Produkteigenschaft der einzelnen Phasen unter axiale Belastung.

Hinblick auf die Auswirkung von Axiallasten auf die Magnetisierung wurde eine Druckzelle konstruiert. Dabei wurde ein Konzept zur Kalibrierung der aufgebrachten Lasten entwickelt, welches durch eine Ex-situ-Methode gelöst wurde. Insgesamt waren für alle mechanischen Charakterisierungsmessungen, die Herstellung von Proben mit hohen Festigkeitsgrad bei gleichzeitigem hohem, magnetoelektrischen Effekt maßgebend. Hierzu wurde die Syntheseroute modifiziert, um die Anforderungen zu erreichen.

Declaration of Authorship

I, Ahmadshah Shahob NAZRABI, declare that this thesis titled, "Development of a Modular Multi-field Mechanical Setup for the Investigation of Functional Materials" and the work presented in it are my own. I confirm that I worked without prohibited assistance of third parties other than those specified; notions taken over directly or indirectly from other sources have been identified as such. This work has not previously been presented in identical or similar form to any other German or foreign examination board.

Signed:

Date:

کنون ای خردمند وصف خرد
بدین جایگه گفتن اندرخورد

Speak, sage! How the saying goes
On the portray of wisdom

کنون تا چه داری بیار از خرد
که گوش نیوشنده زو برخورد

Now bring it to the wisdom as much as you can
The hearts of those that hearken to thy voice,

خرد بهتر از هر چه ایزد بداد
ستایش خرد را به از راه داد

As the creator's best gift
He extolled the worth of wisdom,

•
•
•

به گفتار دانندگان راه جوی
به گیتی بپوی و به هر کس بگوی

Learn by the words of sages how to wend
Thy way, roam earth, converse with every one;

ز هر دانشی چون سخن بشنوی
از آموختن یک زمان نغنوی

Hearest ever knowledge as you face
At no moment deprive from wisdom's store

چو دیدار یابی به شاخ سخن
بدانی که دانش نیاید به بن

While investigating at the boughs of knowledge
Mark, how much its roots are beyond the reach

Firdawsī. From Shahnameh (1000 AC) [1].

For my family and supporters. . .

Contents

Abstract ii

Declaration of Authorship vii

1 Introduction 1

2 Theory 5
2.1 Electric and magnetic fields . . . 5
2.1.1 Field interaction with matter . . . 7
2.1.2 Constitutive laws and basic formulation . . . 9
2.2 Thermodynamics and ordering phenomena . . . 11
2.2.1 Phase transitions . . . 12
2.3 Ferroic orders in magnetoelectrics . . . 13
2.3.1 First-order ferroic phase transition and related topics . . . 14
2.3.2 Ferroelectricity . . . 14
2.3.3 Magnetism . . . 16
2.3.4 Effects of ordering in magnetism . . . 19
2.3.5 Ferroic hysteresis: Characteristic and comparison . . . 20
2.3.6 Domains . . . 24
2.4 Mechanical effects in ferroic materials . . . 26
2.4.1 Electrostriction . . . 26
2.4.2 Magnetoelastic properties: Magnetostriction . . . 28
2.5 Secondary ferroic effects . . . 32
2.5.1 Electric and magnetic susceptibility . . . 32
2.5.2 Linear magnetoelectric effect . . . 33
2.6 Multiferroics . . . 33
2.6.1 A brief historical review . . . 34
2.6.2 Composite Multiferroics: . . . 34
2.6.3 Strain-mediated composite multiferroics . . . 35
2.6.4 Choice of materials . . . 39

3 Materials and Characterization Methods 43
3.1 Requirement specification for composite ceramic . . . 43
3.1.1 Synthesis . . . 44
3.1.2 Sample preparation . . . 48
3.2 Characterization devices . . . 49
3.2.1 Structural Characterization . . . 50
3.2.2 Topographical imaging . . . 51
3.3 Electrical characterization . . . 52
3.3.1 Ferroelectric hysteresis . . . 52
3.3.2 Dielectric measurements . . . 55
3.4 Mechanical characterization . . . 55
3.4.1 Ferroelastic hysteresis . . . 56

3.5 Magnetic characterization . . . 57
3.5.1 VSM . . . 58
3.5.2 SQUIDS . . . 60
3.6 Magnetoelectric measurement devices . . . 61
3.6.1 Measurement principle and materials . . . 61
3.7 ME-coefficient measurement with Lock-In amplifier . . . 63
3.7.1 Converse-ME technique with SQUID . . . 65

4 Development of a multi-purpose modular setup 67
4.0.1 Probing functional materials . . . 67
4.1 Requirement analysis for the setup . . . 68
4.2 Automation of data acquisition . . . 78
4.2.1 LabVIEW© . . . 78
4.3 Strain measurement . . . 80
4.3.1 Analysis of a suitable method . . . 80
4.3.2 Strain method for multiferroics . . . 82
4.3.3 The use of interferometry . . . 82
4.4 Strain sensor integration . . . 86
4.4.1 P-E_H& S-E_H-loops measurement with interferometry . . . 88
4.4.2 Setup option for P-$E_{\sigma H}$ & S-$E_{\sigma H}$-loops . . . 91
4.4.3 Magnetostriction measurement of composites . . . 92
4.5 Magnetization under Stress . . . 97
4.5.1 Pressure cell for VSM . . . 98

5 Results and Conclusions 105
5.1 Studying 0-3 connectivity composites . . . 105
5.2 Composite Characterization . . . 106
5.3 Magnetoelectric properties with new setups . . . 111
5.3.1 Magnetostriction of the composites with interferometry . . . 111
5.3.2 Mechanical characterization . . . 113
5.4 Composite effects under uniaxial stress . . . 114
5.4.1 Effect of pores under uniaxial stress . . . 115
5.4.2 Influence of uniaxial stress on the magnetization . . . 115
5.5 Polarization and strain under constant external fields . . . 119
5.5.1 Polarization and strain under magnetic field . . . 119
5.5.2 Uniaxial pressure device . . . 121
5.6 Magnetoeletric coupling values . . . 126
5.6.1 ME value under uniaxial stress . . . 128
5.6.2 Comparison of different composite systems regarding $\alpha_D(H)\,|_\sigma$ . . . 134

6 Summary and outlook 135
6.1 Ideas for further investigations . . . 136

A Complementary topics 141
A.1 Symmetry and phase . . . 141
A.2 Sol-gel Synthesis Route . . . 142

B Device characterization 145
B.1 FEA and FEM . . . 145
Parameters used for FEA stress analysis simulation . . . 146
B.2 Alternative aspects . . . 146
B.2.1 Alternative strain measurement approach. . . . 146

B.3 Sensor head verification 147
B.3.1 Compatible measurement geometry for the initial setup design . . . 151
Signal alignment and calibration for Fabry-P'erot Interferometer . . 151
B.4 Supplementary figures related to setups 155
B.4.1 PSELoop-Device 155

Bibliography **159**

1

Introduction

The upcoming decade will be strongly driven by industry 4.0, with the **I**nternet **o**f **T**hings (IoT) as one of the major driving forces spurring smart manufacturing along. Smart objects with autonomous sensor networks embedded in systems – along with artificial intelligence and data analytics- are expected to be the basic building blocks of this technological revolution [2, 3].

Here, the development of robust and intelligent sensors is of great importance. In general, sensors consist of sensing (MEMS[1] [4, 5]), and processing elements (ASIC[2]).

In this context, ferroic functional materials are already used as MEMS elements in various applications such as piezoresistive and piezoelectric pressure sensors [6]. They exhibit a broad range of phenomena, such as magnetoresistance [7], magnetic shape memory [8, 9], and magnetocaloric effects. The magnetoelectric effect is particularly suited to an application as a MEMS element for magnetic field sensing [10]. Generally, the nature of the functional response to a field in the MEMS elements is crucial, as it determines the sensitivity, accuracy, and robustness of the effect. Furthermore, its exact behaviour defines the complexity of the associated processing unit. In this regard, a voltage response to a stimulus is easier to process than if the response is a current or magnetization change. In functional materials, such a response is delivered by the magnetoelectric effect.

The field of multiferroics is set to transform other applications besides magnetic field sensors and transducers, as it enables entirely new device architectures [11–15]. For instance, its use in data storage devices would allow data to be written electrically and read magnetically, which increases the efficiency of the process in terms of speed, and current consumption, and it would also contribute to miniaturization. The characteristic feature of a magnetoelectric composite is the artificial coupling between the electric and magnetic phases. In these, an applied electric field induces magnetization, while an applied magnetic field induces polarization [16, 17].

For the optimum performance of the functional material, the understanding and engineering of the active materials is essential. Therefore, before any material engineering is done, advanced simulation tools should be used to help tailor the desired effect. For more advanced engineering concepts, the formation of particular functional properties needs diverse preconditions. This requires also increasingly complex instruments for the characterization of the underlying material properties [18, 19].

The goal of this work was to characterize magnetoelectric multiferroic composite ceramics. However, most of the conventional characterization test benches cannot provide a complex measurement possibilities to cover the broad range of properties. Given this,

[1] Microelectromechanical systems combine electrical and mechanical components into a single chip -MEMS sensors represent a continuum bridging electronic sensors at one end of the spectrum, and mechanical sensors at the other.

[2] Application-specific integrated circuit

the thesis intends to overcome this deficiency. For this purpose, some new experimental methods and setups have been designed and constructed to meet the need for multi-characterization requirements. The setups are devised in a modular fashion. Therefore, they can also be used to characterize functional materials with different cross-functional effects as the modular setups enable multi-field arrangements to be used [20].

The switchability of a conjugate field by another is an interfacial effect, which is mediated between the two phases of the material. This makes the mechanics of both materials, in terms of their coupling parameters, an important aspect of its functionality. In this regard, finding material combinations with an optimum coupling is a central engineering task involving a broad range of material parameters. Therefore, A central aspect of the developed setups is related to the mechanics of the samples.

The development of modelling tools is essential in order to iterate through multiple material combinations and reduce the experimental effort. In the framework of the research group (DFG FOR 1509[3]), a team of experimentalists and experts on modelling joined up to develop tools which were able to describe the non-linearities and the complex interplay of ferroic materials. Models of magneto-electro-mechanical interactions in composites need to take effects into account which are distributed over different length scales. For this purpose, findings from atomic (magnetization) and crystal unit cell level (electrical polarization) first-principle models can be used as approximate values for the macroscopic model in the framework of continuum thermodynamics and computational mechanics (homogenization methods [21]). This enables multiscale simulations to be made. The work of the research group limits itself to the coupling of electrical polarization, magnetization, and strain. The developed multi-field setup will be used to understand the coupled material behaviour and derive the material parameters in order to calibrate the constitutive models used in the simulations. The experiments in this work will be used to investigate the magnetic, electric, and magnetoelectric properties while *uniaxial stress* is applied.

Outline The first chapter is dedicated to the theoretical principles and it introduces the basic understanding of physical fields and the concept of field interaction with matter in the framework of a constitutive formulation. Furthermore, ferromagnetism and ferroelectricity are presented from the perspective of thermodynamical ordering phenomena. In particular, due to the similarity of both materials, the effect of mechanical stress on the ferroic properties are presented. The last section of this chapter deals with multiferroics which exhibit more than one primary ferroic order. The relevant materials and conditions needed to merge them as composite materials are elaborated on in detail.

Chapter 2 describes the synthesis of magnetoelectric $x\mathrm{CoFe_2O_4}$-$(1\text{-}x)\mathrm{BaTiO_3}$ composites, in the form of an optimized electrically resistive and highly dense ceramic, which are prerequisites for any mechanical testing. Furthermore, the standard methods used to verify the properties that qualify the samples as magnetoelectric composites are presented. For this, the typical set of experimental techniques used for the structural, microscopical, dielectric/piezoelectric, and magnetic characterization are introduced. In addition, the methods used to characterize the magnetoelectric coupling coefficient are reviewed.

Chapter 3 forms the main part of the thesis. It focuses on the development of custom built setups for coupled mechanical characterization. Given the wide-ranging properties of magnetoelectric composite phases, a detailed overview of the requirements needed to build a modular setup is given. In this case, the engineering challenge is to incorporate the three relevant fields to the magnetoelectric composites in the setup. Besides the static fields,

[3]The German research community (DFG) has dedicated to the topic of multiferroics 3 Collaborative Research groups, SFB, 608,762,1261

options for an AC-field in the sample space are also integrated. In addition, an analysis of the integration of a suitable strain detection technique in the sample space is made.

With this setup, in addition to the mechanics, the ferroelectric, magnetic, and magnetoelectric coupling properties under uniaxial mechanical stress can be investigated. In another setup, a pressure cell for magnetization measurements under uniaxial stress was also developed. The crucial task in the development of the pressure cell was the stress calibration concept, for which an ex-situ method was developed.

In Chapter 4 the results of the characterization measurements made on composites are presented. They elucidate the structure, morphology, and other fundamental parameters of the magnetoelectric composites. These are needed as guides in order to ensure their applicability for the stress measurements. The feasibility measurements show that characterizations with the various options integrated into the setup are possible. In this work, the main focus is on the effect of a constant stress level, as an external parameter, on the functional properties. A discussion of the results related to the functional mechanical properties of the material enables improvements to be made in the set of parameters that are relevant to the mechanisms of magnetoelectric coupling. Their systematic study, allows an evaluation to be made of how external physical influences would affect the product properties. The most novel findings of this work concern the effect of uniaxial compressive stress conditions on the evaluation of magnetoelectric coupling in different composite ceramics.

2

Theory

" My direct path to the special theory of relativity was mainly determined by the conviction that the electromotive force induced in a conductor moving in a magnetic field is nothing more than an electric field."

– Albert Einstein, *to the centennial of Albert Michelson's,1952*

Generally, the design of any framework devoted to the characterization of functional properties of a particular class of materials assumes that there is already an understanding of its physical nature and a theoretical description. The material response to a systematic stimulus allows the nature of its underlying interrelations to be understood. With this data, it is possible to fathom the underlying physics, which constitutes the behaviour of the respective properties.

The setups built in this work are based on concepts that address magnetoelectric (ME) multiferroics (MF) composite materials. Their functional properties combine ferroelectric and ferromagnetic properties in a single compound material, where the new functionality as cross-coupled product property arises. In light of the new property, it is essential to classify all the effects related to each constituent. As a consequence, before these compound materials are considered, a brief introduction to fields and their interaction with each constituent of the composite material is essential. In this regard, to indicate their similarities and differences, both classes of materials are treated simultaneously.

A detailed understanding of ME materials requires the knowledge about the atomic origin of the properties related to each constituent and their coupling mechanism. Furthermore, the mechanism of the phase transitions, which give rise to the emergence of each phase effect is reviewed. In particular, the nature of spontaneous polarization and magnetization as a consequence of the reordering of the associated crystal structure is reviewed. A further section is dedicated to treating the nonlinear effects driven by electric and magnetic fields.

2.1 Electric and magnetic fields

The link between magnetism and electricity was first uncovered by Oersted, and further investigated in Faraday's seminal experiments, which demonstrated that electric currents generate magnetic fields. Maxwell went on to describe this relationship of electromagnetism in more detail. Later, it was shown with relativistic theory of electrodynamics that fundamentally electricity and magnetism origin from phenomena related to the behaviour of charged particles (q). However, in order to describe a wide range of phenomena, it is convenient to divide them into two components: electrostatic and magnetostatic fields ($\mathbf{E}^{St}, \mathbf{H}^{St}$) and their corresponding forces ($\mathbf{F}^{St}_{E/M}$). According to electrostatics, a test charge(q_0) is experiencing (proportional to its charge) an electrostatic force, which is described by Coulomb's Law [22].

$$\mathbf{F}^{St}_{E}(\mathbf{r}) = \frac{q_0 q_A}{4\pi\varepsilon_0} \frac{\mathbf{r}_0 - \mathbf{r}_A}{\|\mathbf{r}_0 - \mathbf{r}_A\|^3} \tag{2.1}$$

where $\mathbf{r}_0$, and $\mathbf{r}_A$ are respectively the distance vectors to the position of q_0 and q_A, and ε_0 is the vacuum permittivity. The interaction described in terms of a "force action at a distance", is not suitable for most purposes. Therefore, the concept of a generalized electric vector field for the charge distribution $\rho(r)$ was introduced by M. Faraday

$$\mathbf{E}^{St}(\mathbf{r}) \overset{def}{\equiv} \lim_{q_0 \to 0} \frac{\mathbf{F}(\mathbf{r})}{q_0} \approx \int_V \frac{\rho(\mathbf{r})}{4\pi\varepsilon_0} \cdot \frac{\mathbf{r} - \mathbf{r}_A}{\|\mathbf{r} - \mathbf{r}_A\|^3} d^3\mathbf{r} \tag{2.2}$$

where there is an integral over the total volume V of the charge distribution, as illustrated schematically in Fig. 2.1A. In the static case, the electric field possesses the properties of a conservative vector field. Therefore, the concept of an electrostatic scalar potential $\phi(\mathbf{r})$ is used for its description [23].

$$\nabla \cdot \mathbf{E}(\mathbf{r}) = \frac{\rho(\mathbf{r})}{\varepsilon_0} \tag{2.3}$$

$$\mathbf{E}(\mathbf{r}) = -\nabla\phi(\mathbf{r}) \tag{2.4}$$

The Eq. 2.4 represents a conservative potential, and it indicates that the work $W_{A \mapsto B}$ along A to B is independent of the work path. Therefore, $\phi(\mathbf{r}_A) - \phi(\mathbf{r}_B) = \frac{\rho(\mathbf{r})}{\mathbf{r}_A - \mathbf{r}_B}$ is related to the potential difference.

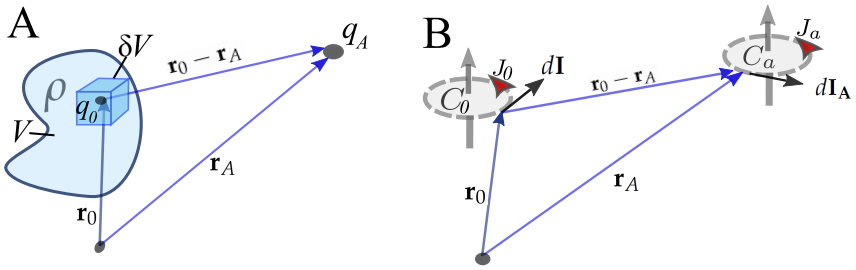

FIGURE 2.1: A) Electrical force exerted on a charged particle by a charge distribution. B) Illustrates Ampeŕe's law with a static electric current, I circulating a loop C_a through its tangential element dI located at r_A and current density j_A. It experiences a magnetostatic force from loop C_0 located at the point r_0. The shape of the loop is not relevant as long it is a closed-loop

In free space, the direction and magnitude of the field acting on an individual charge point depends on the density of the charge distribution, and its polarity Fig. 2.1A. Consequently, the interaction force results either in repulsion or attraction Eq. 2.1. This induces a related *motion of the charged particle* in their shared coordinate system, thereby yielding Faraday's law on the origin of magnetic flux. It also establishes the link to the "electromotive force".

As a result of this, in the case of two stationary electric currents, a force of constant magnitude acts on the current element d$\mathbf{I}$, which manifests itself in a mechanical force, either repulsive or attractive in nature depending on the relative polarity of the current. For the case of two closed wires, Ampère's law of magnetostatics is given by (see Fig. 2.1B).

$$\mathbf{F}_M^{St}(\mathbf{r}) = -\frac{\mu_0 I \cdot I_A}{4\pi} \oint_{C_0} \oint_{C_A} \cdot \frac{\mathbf{r_0} - \mathbf{r_A}}{\|\mathbf{r_0} - \mathbf{r_A}\|^3} d\mathbf{I} \cdot d\mathbf{I_A} \tag{2.5}$$

where $\mu_0 = 4\pi 10^{-7} Hm^{-1}$ is the permeability of free space. Similarly, as for the case of electrostatics, the interaction is attributed to a vector magnetic field, however; this field possesses an axial symmetry unlike the electric field vector, which is a polar vector.

$$d\mathbf{B}^{St}(\mathbf{r}) \overset{def}{\equiv} \frac{\mu_0 I_A}{4\pi} d\mathbf{I_A} \times \frac{\mathbf{r_0} - \mathbf{r_A}}{\|\mathbf{r_0} - \mathbf{r_A}\|^3} \tag{2.6}$$

Where d**B** is the magnetic flux density at the field point **r** caused by a small line element $d\mathbf{I_A}$. The magnetic field can be described by the linearly related vector fields **B** and **H**, where the SI unit of magnetic flux density B is the Tesla (T), which describes the density and direction of the field lines that run through an area A in free space.

$$\mathbf{B} = \mu_0 \mathbf{H} \tag{2.7}$$

In free space, **H** is just the scaled version of **B** and is measured in $Am^{-}1$. A generalized expression of Eq. (2.5), and Eq. (2.6) can be written in the format of the Biot-Savart law

$$\mathbf{F}_{M_\mathbf{r}} = Id\mathbf{I_A} \times \mathbf{B}^{St}(\mathbf{r}), \tag{2.8}$$

This gives the electromagnetic force acting on a particle as it moves through a thin wire.

2.1.1 Field interaction with matter

In contrast to unbound charges in free space, the effect of electrostatics in condensed matter is related to the specific electronic band structure of the observed material class. In metals, as a result of orbital overlap, a conduction band is formed. In this case, the electrons of the Fermi sea[1] flow in the direction of the external field. In contrast to metals, in insulators (= *dielectric materials*) there is an energy bandgap between the conduction and valence band. As a consequence, the charge carriers are located below the Fermi level[2], and they are confined to a specific band. Therefore, an applied electric field cannot remove the electrons from their atomic orbits given their high electronic binding energy originating from the ionic bounding. However, the centre of positive and negative charges can be *displaced* by the external field, whereas in the absence of the field the dielectric stays in a neutral state. In these materials an external electric field is super-posed for the internal fields due to the locally distributed bound charges ρ. As a consequence, the negatively charged electrons and positively charged atom core will be attracted by the field. Thus, they migrate in opposing directions, away from the neutral ground state, and thereby cause the *polarization* of the dielectric.

Its macroscopic behaviour in the presence of an external electric field $\mathbf{E}^{St}$ can be described sufficiently accurately by using a simplified term for the distribution of bound charges $\rho(\mathbf{r})$. Starting with a multipole Taylor expansion of $\frac{\rho(\mathbf{r})}{\mathbf{r}_A - \mathbf{r}_B}$ charge distribution would lead to an approximated expression for a dipole moment of,

$$\mathbf{p} \overset{def}{\equiv} q\mathbf{d} \tag{2.9}$$

which is formed as a result of an interaction with the external field. If no field were applied it would be in its charge-neutral state [3].

[1] Electronic band structure of metals above the fermi -level have an overlap between the conduction- and valence-band. As a result, this leads to the formation of free electrons in the conduction band.

[2] A bandgap higher than 4eV is not anymore considered as a semiconductor.

[3] Charge distribution: Which is used to deduce the dependency between $\rho(\mathbf{r})$ and its dielectric potential coming from the dielectric region of interest.

The presence of the electric field imposes a force and a torque on the dipoles which align them in the same direction. Experimentally, however, the measured value is the polarization on the surface of the macroscopic body, representing the quantity for the density of the dipole moments [$\mu C/cm^2$];

$$\mathbf{P} \overset{def}{\equiv} \lim_{V \to 0} \frac{\mathbf{\Delta p}}{\Delta V} \approx \frac{d\mathbf{p}}{dV}. \tag{2.10}$$

It is defined as the dipole moment per volume unit, yielding a polar vector. With the concept of polarization one can introduce the electric displacement field D, as

$$\mathbf{D} \overset{def}{\equiv} \varepsilon_0 \mathbf{E} + \mathbf{P}. \tag{2.11}$$

where ε_0 is denoted as the dielectric permittivity, which describes the ability of a substance to hold an electrical charge. ε_0 stands for the permittivity of free space, and **P**, is related to a linear dependency of polarization which is applicable up to moderate electric field strengths pretty well for most dielectric materials. Furthermore, χ as the dielectric susceptibility of the material,

$$\mathbf{P} = \varepsilon_0 \chi \mathbf{E}, \tag{2.12}$$

determines the linear dependency of polarization and electric field. It should be noted that χ is a temperature and frequency-dependent parameter, which will be discussed in detail in section 2.5.1.

Most of the formalism for the interaction of an **E**-field with electric dipoles in dielectric materials can be carried over to the magnetic dipole interaction with an external **H**-field.

The magnetic dipole can be induced either by another magnetic pole or electric current loops. The above understanding of the magnetic field (Eq. 2.5) has been historically driven by observations made on currents flowing in two wires.

A more fundamental formulation of magnetism is based on the current loop around an area, where the magnetic moment is given as:

$$\mathcal{M}_{dm} = I \int \mathbf{dA} \tag{2.13}$$

The length of the vector dA is equal to the area of the loop. Accordingly, its unit is Am^2.

In contrast to the polarization, the nature of the magnetic "dipole" is different by being a magnetic monopole. As a monopole, it is the source and the sink of the field at the same time. However, it is considered to be equivalent to an electric dipole in order to keep the analogy. As a consequence, the spin of an electron, which is the elementary unit, is regarded to be the magnetic dipole moment. Furthermore, as its vector direction is normal to the loop plane the magnetic field has axial symmetry.

This property causes the break of time-reversal symmetry when the sign of the vector of the moment changes direction, which in turn is dependent on the direction of current flow in the loop. Moreover, the spin of the electron is the origin of magnetism [24], where the interaction of multiple spins combine according to the Pauli exclusion principle Sec. 2.3.3.

Similarly, as in the case of electric dipole-dipole interaction, the magnetic dipole interaction leads to mutual alignment of the dipoles in the material. This gives rise to the appearance of macroscopic dipole moments per unit volume, yielding the magnetization M, Sec. 2.3.1. The majority of materials are magnetized when they are exposed to a magnetic field.

$$\mathbf{M} = \mu_0(1 + \chi_m)\mathbf{H} = \mu_0\mu_r\mathbf{H}, \tag{2.14}$$

where χ_m is a dimensionless quantity, the magnetic susceptibility, and $\mu_r = 1 + \chi$ is the relative permeability of the material. The magnetic flux density can be introduced in a similar way to its dielectric counterpart electric displacement field **D**. It is depending on the sum of the external field **H**, and the magnetization **M** of the material;

$$\mathbf{B} = \mu_0(\mathbf{H} + \mathbf{M}) \tag{2.15}$$

Not unexpectedly, materials respond differently to the magnetic field. The value of relative permeability $\mu_r = \frac{\mu}{\mu_0}$ helps to distinguish between the different kinds of material responses.

Most materials have a diamagnetic ($\mu_r < 1$) or paramagnetic ($\mu_r > 1$) response to an applied field. In addition, 3-d transition metals have an atomic structure in which the electron spins are permanently aligned, thereby they obtain a permanent magnetic moment. These are the materials of interest for this work and will be the topic of section 2.3.3, with focus placed on non-linear and hysteric behaviour as they are exposed to an **H**-field.

It should be noted that the *magnetoelectric effect* is especially interesting as it involves the unexpected coupling of the alignment parameters and the formation of a product property effect between the orders of polarization and magnetization in a single material. This effect does not appear in Maxwell's equations [25].

2.1.2 Constitutive laws and basic formulation

Material models describe the microscopical behaviour properties of a material based on an energy criterion, from which the macroscopic behaviour is obtained by averaging over a large number of unit cells. This section starts with a brief introduction to the necessary terminology linked to *Constitutive laws*, which are linearly approximated behaviour models of materials that describe macroscopic properties. Constitutive laws relate the measurable physical quantity of materials to field dependencies. This description is needed since the fundamental balance laws[4] are not fully sufficient to specify or model the response of a material in terms of experimental values. This can be due to imperfections in materials and experimental conditions. The constitutive laws link experimental observation with fundamental physics by considering a macroscopic response as the collaborative effect of the intermolecular or inter-atomic forces in matter. For the mechanics, the description of the constitutive equations requires the nomenclature of continuous media in order to describe the internal stresses and macroscopic deformation.

From strain and stress tensors towards constitutive equations for piezoelectric and piezomagnetic materials

Spontaneous polarization and magnetization as well as an applied mechanical stress can cause a deformation, and its related strain can be measured experimentally.

In all these three cases, a point x_i moves to a new position $x_i^\star$. A displacement vector $u_i = x_i^\star - x_i$ can be used to represent the evolution of the deformation.

$$dx_i^\star = dx_i + du_i = dx_i + u_{i,j}dx_i \quad \text{with displacement gradient tensor} \quad u_{i,j} = \frac{du_i}{dx_j}. \tag{2.16}$$

[4] conversation of energy and momentum regarding laws of thermodynamic.

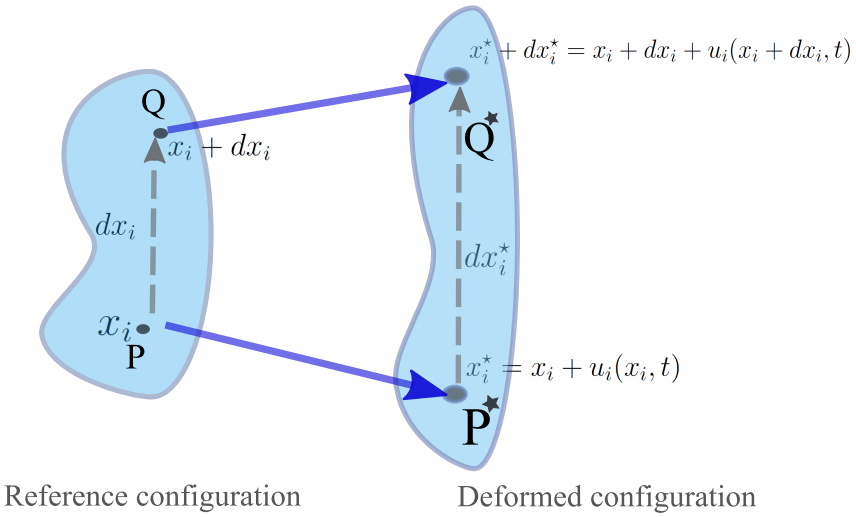

FIGURE 2.2: The displacement as a result of a force acting between the neighbouring points P and Q [26]

For a small displacement gradient, the small strain tensor $\mathbb{S}$ is introduced:

$$\mathbb{S} = \epsilon_{ij} \equiv \frac{1}{2}(u_{i,j} + u_{j,i}) \tag{2.17}$$

In order to link the stress and strain of a linear-elastic body, the related constitutive equation is needed:

$$\sigma_{ij} = \mathbb{C}_{ijkl} \cdot \epsilon_{kl} \tag{2.18}$$

This is known as Hooke's law, and its origin depends on the intermolecular forces and bonds. The proportionality factor $\mathbb{C}_{ijkl}$ is a stiffness tensor of rank four[5]. This indicates that four directions are involved in the measurement of *elastic constants*, with two directions needed for each stress and strain tensor. $\mathbb{C}_{ijkl}$ contains 81 components, although the symmetry of σ_{ij} and ϵ_{kl} reduces the number of independent stiffness coefficients to 36, and a further simplification is derived from an energy argument[6]. The existence of a strain energy reduces it further to 21 independent coefficients for an anisotropic material [25].

Most of the properties discussed are tensorial, however, for the simpler treatment, the scalar notation is used, where the tensor indices are often omitted.

Piezoelectric constitutive equations: Piezoelectricity describes the appearance of an electric field in response to mechanical loading. In addition, it couples the dielectric and elastic properties of the solids in a linear first-order fashion. The inverse effect creates a strain as a response to an applied electric field on a piezoelectric crystal. By considering both the *electrostatic and mechanical constitutive equations*, Eq. 2.11 and Eq. 2.18 for a given crystal, an extended version of both can be given:

$$\epsilon_{ij} = (\mathbb{C}_{ijkl})^{-1} \cdot \sigma_{kl} + \mathbb{d}_{kij} \cdot E_k \tag{2.19}$$

$$D_i = \mathbb{d}_{ijk} \cdot \sigma_{jk} + \varepsilon_{ij} \cdot E_j \tag{2.20}$$

[5]This assumes Einstein'summation rule.

[6]The product of stress and strain is the stored mechanical energy density, and its 2^{nd} partial differentiation is not affected by its order: $\frac{\partial^2 W}{\partial \epsilon_2 \partial \epsilon_1} = \frac{\partial^2 W}{\partial \epsilon_1 \partial \epsilon_2}$.

with being isothermal and stress-free as precondition [27]. Where

$\mathbb{C}^{-1}_{ijkl}$	being the inverse mechanical stiffness
$\mathfrak{d}_{kij}$	piezoelectric coupling tensor, quantifies the magnitude of the effect
ε_{ij}	the dielectric constant of the stress-free material

The constitutive equations can be introduced for various electrical and mechanical boundary conditions by using thermodynamic arguments [25].

Piezomagnetic constitutive equations: By subjecting magnetostrictive materials to a magnetic field H_0, the magnetic material experiences a strain. Its magnetostriction is quadratically dependent on the H-field. However, in this work, the magnetic induction tensors will be treated the same way as for a piezomagnet, which is defined as a linear response[7]. In contrast to magnetostriction and electrostriction, it is a second-order effect (for more details on magnetostriction of ferrites, Sec.2.4.2). Nevertheless, for the theoretical models describing the ME effect, this approach (Eq. 2.21) is sufficiently accurate [29, 30].

$$\epsilon_{ij} = (\mathbb{C}_{ijkl})^{-1} \cdot \sigma_{kl} + \mathfrak{q}_{kij} \cdot H_k, \tag{2.21}$$

$$B_i = \mathfrak{q}_{ijk} \cdot \sigma_{jk} + \mu_{ij} \cdot H_j \tag{2.22}$$

The magnetostrictive component are:

$\mathfrak{q}_{kij}$	the piezomagnetic coefficient and
μ_{ij}	the permeability matrix.

So far, the equations deliver an understanding of how the fields and materials are coupling at the macroscopic level to strain in terms of tensorial properties. However, other important properties are coupling to the fields as well. These are the physical quantities of *magnetization* and *polarization*, which are involved in Eq. 2.21 and Eq. 2.19. Treatment of these is essential to an improved constitutive model, which accounts for nonlinear behaviour and hysteresis effects. The improved models of these quantities are based on a phenomenological description within the framework of thermodynamics. The thermodynamic approach for the approximation reduces the number of internal variables [31]. The relationships of these responses are influenced by the degree of symmetries, which will be discussed in the following sections.

2.2 Thermodynamics and ordering phenomena

Some classes of materials undergo a "spontaneous" change in their physical properties upon the onset of a "driving force". In many materials, it is the temperature, where a change causes crystal structure variation, accompanied by a new *order*. For instance, the transition from liquid to solid. The underlying mechanism is the re-ordering of the crystal structure, which induces a new property, which can also be excited by external forces aside from temperature. The emergence of the new order is considered to be a collective phenomenon, which occurs when a large number of strongly correlated particles are involved. Hence, an exact ab-initio computational-based prediction would be out of reach. Therefore, the development of models is essential, where the considered physical quantity converges to a

[7] Ferrites used in magnetoelectric compounds are not piezomagnet, but they are used as a replacement for it, as they have linear behavior at a certain biased field, they are pseudo-piezomagnetic. See the nomenclature on the topic in [28].

macroscopic value. Thus, the development of approximating models is necessary to capture the collective phenomena of the macroscopic property emergence. In this respect, the phenomenological thermodynamic approach is one of them.

In the context of constitutive models based on the principles of thermodynamics, the behaviour models of material are determined by a specific free energy function [32]. These models can be applied to the ferroic crystal systems, such as ferromagnets and ferroelectrics, which are constituents of magneto-electric materials.

The next section will explain the properties of a phase and its transition.

2.2.1 Phase transitions

The term phase transition describes the phenomena related to the transition of a physically measurable quantity, an "'observable"', into an ordered or disordered phase. In the case of the transition into an ordered phase, it is connected with the breaking of symmetry, as the order lowers the degree of degeneracy of the states. It also explains how the appearance of different phases is connected with the crystal structure of the material class and its symmetry elements, Sec. A.1. An understanding of the phase and its symmetries concerning various properties are reviewed in Appendix A.1.

The ferromagnetic and ferroelectric constituents of magnetoelectric materials have order parameters of magnetization (**M**) and polarization (**P**), respectively. Both physical properties are zero for $T > T_c$ and non-zero for $T < T_c$. Below the transition (Curie-temperature) the rise of a new structure changes the property. For these two cases, it is accompanied by a new order as it can be measured in the absence of an external field. It is, therefore, known as a *spontaneous "order"*, with T_c the transition temperature that indicates the transition between two ordered states. However, each ferromagnetic and ferroelectric phase has its own curie temperature and mostly they do not coincide with each other. The mathematical model describing it is covered in Landau-Ginsburg theory, which describes the transition from one phase into another by a series of potentially metastable states existing around the transition point, accompanied by different symmetries of the order parameter.

In order to capture the phase transition of interest, the free energy density has to be considered in terms of the relevant thermodynamic field[8]. Temperature is one such field, it gives rise to drastic property changes or causes their emergence, upon its variation in the phase transition region. Therefore, near the phase transition point, it is expedient to expand the Gibbs free energy G in terms of a polynomial Taylor expansion of the order parameter Q, which is zero before its emergence. Given symmetry of the system [9] all odd expansion coefficients have to be zero, which yields:

$$G = G_0 + \alpha Q^2 + \beta Q^4 \tag{2.23}$$

where α, and β are the expansion (Landau) coefficients of the even orders[10].

In the vicinity of a phase transition point, a small change in the external control parameter can result in a huge change of the physical properties of the observed system, e.g., specific heat or the dielectric constant. The phenomenological approach is applied to the emergence of magnetization M as the order parameter.

It should be noted, that the thermodynamical approach doesn't deliver the precise underlying physical reason for the appearance of ordering properties for the ferroics. The

[8] Control parameters of the specific property.

[9] As the energy cannot be created and deleted by the sign change of a thermodynamic field.

[10] They specify the height and the shape of the free energy landscape.

underlying physical nature of magnetism is a quantum mechanical effect which has its origin in electron configuration in the shell of the atoms. For polarization, it is the dipole formation in the crystal unit cell.

2.3 Ferroic orders in magnetoelectrics

A single material with more than one ferroic order is called a multiferroic [33]. For its phenomenological description, an expansion of the free energy F as a power series in the presence of the fields **E**, **H**, or mechanical stress σ can be used, Eq. 2.23. It is convenient to formulate F in such a way that it doesn't add to any existing electric and magnetic energies in the absence of the fields. Further, F is constructed for a single-phase multiferroic[11] [34]. However, the coefficients are also applicable to composite magnetoelectric multiferroics, given that they are partial derivatives for the corresponding fields. In these equations, the magnetic and electric parts of the free energy correspond to the magnetic and ferroelectric phases. At the same time, the magnetoelectric coupling term (which is not necessarily linear) describes the effective interaction between the order parameters of each phase [35, 36]. By expanding the free thermodynamic potential F

$$F(\mathbf{E},\mathbf{H},\sigma,\mathcal{T}) = TS + E_i D_i + H_i B_i + \sigma_{ij}\epsilon_{ij} + \mathcal{T}_i\tau_i \tag{2.24}$$

with consideration the Eq. 2.10 and 2.14, in terms of **E**, **H**, σ would lead to[12]:

$$\begin{aligned}
(i)\quad & F(\mathbf{E},\mathbf{H},\sigma) = F_0 + \mathbf{P^s}\mathbf{E} + \mu_0\mathbf{M^s}\mathbf{H} + \epsilon^s_{ij}\sigma_{ij} \\
(ii)\quad & \qquad + \frac{1}{2}\varepsilon_0\chi^e_{ij}E_iE_j + \frac{1}{2}\mu_0\chi^m_{ij}H_iH_j + \mathbb{C}^{-1}_{ijkl}\sigma_{ij}\sigma_{kl} \\
(iii)\quad & \qquad + \alpha_{ij}E_iH_j + d_{ijk}E_i\sigma_{jk} + q_{ijk}H_i\sigma_{jk}
\end{aligned} \tag{2.25}$$

In Eq. 2.24, S is the entropy density, and $\mathcal{T}$ is the toroidal moment[13]. Both are introduced in this equation for the first time. The Landau theory model considers a non-ferroic material around its phase transitions temperature T^e_C and T^m_C, where both electrical polarization P and the magnetization M are the temperature-dependent order parameters. Dependencies of the ME effect are obtained from the expansion of the free energy.

The first line of Eq. 2.25 is related to first-order ferroic effects such as spontaneous polarization $\mathbf{P^s}$,Sec. 2.3.2, spontaneous magnetization $\mathbf{M^s}$, Sec. 2.3.3, and spontaneous deformation ϵ^s_{ij}. $\mathbf{P^s}$, $\mathbf{M^s}$ were introduced in the previous section, however, a more detailed review will cover both in the following section. Furthermore, ϵ^s_{ij}, magnetostriction, and electrostriction will be reviewed in detail, given their relevance to the topic, in Sec. 2.4.2.

The second line of Eq. 2.25(ii) comprises of the linear coupling coefficients -secondary ferroic effects-, such as the electrical and magnetic susceptibility χ^e_{ij},χ^m_{ij}, which were introduced in Sec.2.1.1 as well as of the elastic compliance tensor $\mathbb{C}^{-1}_{ijkl}$, which is covered in 2.6.3. The third line deals with the cross-coupling effects, in particular, it contains the linear magnetoelectric effect tensor α_{ij}. The effects in the third line are also referred to as the secondary coupling effects. In addition, the piezoelectric effect d_{ijk} and the piezomagnetic effect q_{ijk} are the decisive parameters in Eq. 2.52.

[11] Detailed Sec. 2.6

[12] The Einstein Summation Convention is used. Indices occurring twice in a term are summed from 1 to 3.

[13] It has no real relevance to this work, but for the sake of completeness it is mentioned here; however, in further treatment of F will be neglected.

In the following of this chapter, each term in Eq. 2.25 will be reviewed. The underlying property in each term covers the essential physics of these materials and gives rise to effects that are part of the study in this thesis.

2.3.1 First-order ferroic phase transition and related topics

In a thermodynamic system, a *physical quantity* possesses a corresponding *order parameter*. Its *sudden* appearance or its *abrupt* change indicates the occurrence of a phase transformation of *first order*. In this context, the *spontaneous* macroscopic emergence of polarization, magnetization, or deformation in the absence of any respective external fields is related to first-order ferroic effects. Furthermore, with order as a state parameter, the degree of symmetry or degeneracy of the thermodynamic system decreases as the system enters the ferroic phase ($\equiv$ an ordered phase). As a result, at least two domain states emerge (Fig. 2.3), which can be switched by a corresponding external field, Sec. 2.6. The hysteric behaviour of a ferroic material depicts the nature of the switching process between the ordered states, Sec. 2.8.

2.3.2 Ferroelectricity

The spontaneous polarization P_s evolves from the phase transition of a non-ferroic state into ferrioc state. This leads to a polar state of the material. If the polarization further switches by electric, it is termed a ferroelectric[14] The mechanism driving it takes place in the unit cell as its crystal structure reorganizes. Whether a crystal structure can show spontaneous polarization or not, is related to the point group symmetry specification. 32-point groups are needed to describe all crystalline systems, and 11 of them are centrosymmetric point groups with an inversion centre, and these don't display spontaneous polarization. From the remaining 21 non-centrosymmetric point groups, 10 are part of the polar group with a preferential polar axis which allows spontaneous polarization and ferroelectricity. A further criterion that needs to be fulfilled if crystals are being designated as ferroelectric is related to the switching of the polarization by an electric field, and its transition between two stable states of opposite polarization, Sec. 2.6.

In order to avoid a too general discussion, the case of phase transitions for the $BaTiO_3$ (BTO) crystal, from the perovskite family[15], Sec. 2.3 is considered. By considering the symmetry point groups argument from above, the cubic structure possesses a higher structural symmetry than the tetragonal one. The structural phase transition yields the ferroelectric state, when the transition from cubic to tetragonal takes place and centrosymmetric point group system with its inversion centre transfers to a polar group with a polar axis. This is since tetragonality is not a sufficient condition for being polar.

The underlying *physical* picture of its genesis with associated phenomenological argument can be understood as follows: In the cubic phase of BTO, the Ti-atom possesses higher thermal energy, as it is above the Curie temperature. As a consequence, it is able to explore a broader energy landscape. In terms of statistical mechanics, the higher the thermal energy the more access it has to micro-states. In the cubic phase, the Ti-atom has eight energetically equally possible positions inside the cubic unit cell. With respect to times shorter than the fluctuation time, each position appears in a rhombohedral position. When averaged over longer times than the fluctuation frequency, it appears to be cubic.

[14] For this section, the following literature has been consulted [37–41].

[15] For which Devonshire [42] used the principles of the Landau-Ginsburg theory to formulate a model for its *structural* phase transition from the para-electric cubic phase to ferroelectric tetragonal phase of $BaTiO_3$.

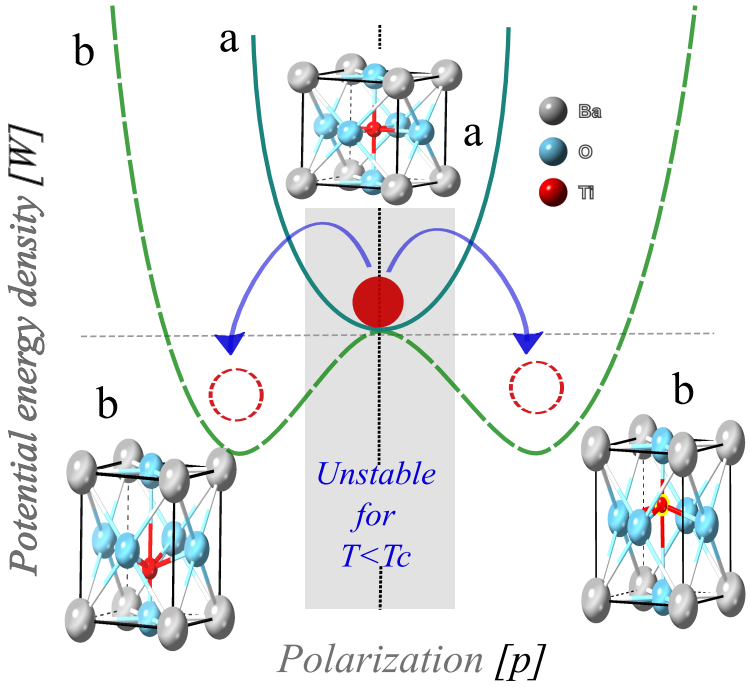

FIGURE 2.3: The potential energy landscape of ferroelectric perovskites, here BTO[16], above and below the Curie temperature, showing unpolarized (a) and polarized (b) atomic configurations, respectively. The non-linearity arises from a crystal being cooled down below its Curie temperature T_C, which causes a new state order and property formation (double well potential is formed Sec. 2.6).

At lower temperatures than T_c, the number of accessible micro-states decreases. The Ti-atom cannot fluctuate anymore between all states as it appears to be "frozen" to a certain subset of four out of eight states. These on average yield a polar tetragonal structure.

Consequently, the cubic unit cell will be distorted to a tetragonal structure. Due to the asymmetry of this displacement, the titanium atom gets closer to one of six oxygen neighbours, resulting in a relative shift of the positive charge centre within the unit cell. It becomes polar due to the associated charge of the Ti-atom, which leads to the permanent tetragonal deformation of the unit cell. In this state, there are a lower number of accessible micro-states available for the Ti-atom, each as a thermal average over four rhombohedral Ti-positions.

The thermodynamic picture delivers an explanation of the spontaneous polarization in a broader scope, while a more fundamental understanding requires an understanding of the electronic bonding structure inside the crystal unit cell [44]. The ferroelectric state is favoured by the long-range Coulomb interaction, determined from a balance with short-range repulsions, which is supporting the cubic structure [45]. The ionic off-centring, which changes the chemical bonding, acts as an additional bonding influence which can stabilize the distortions that enable the formation of the ferroelectric phase. The changes in chemical bonding that lead to stabilization are the second-order Jahn–Teller effects [22].

[16]BTO crystal structure is illustrated with CrystalMaker. Cif file no: 1525437 [43] has been used in its display

2.3.3 Magnetism

[17]As introduced in Sec. 2.1.1, a current loop has a particular magnetic moment, and it is regarded as a dipole moment vector with axial symmetry. The Bohr magneton [μ_B] with its axial-vector property is viewed as the basic unit of magnetism.

Consequently, the interaction of a magnetic material with an external field results in the collective alignment of the spins inside the material, thus *magnetization* arises. However, ferromagnets possess a *spontaneous* magnetization M_s even in the absence of an external field. Its macroscopic emergence is analogous to the case of ferroelectricity. The *macroscopic model* for the understanding of both phenomena is based on the phase transition formulation, as it delivers the description of non-linear behaviour related to the respective fields in both. However, the major difference between them is their microscopic origin. Indeed, ferromagnetism arises fundamentally as the spins in certain 3d transition metals align. Further, its macroscopic appearance is due to the collective spin-orbit coupling inside the crystal lattice. In the following the underlying natural phenomenon causing the alignment will be addressed.

Pierre Weiss proposed the first modern theory of ferromagnetism, based on the formulation of an effective field H_{eff}. His approach based this on the existence of an internal 'molecular field' which is proportional to the magnetization of the ferromagnet. He argued further that at high temperatures, the thermal energy k_BT, and its related entropic effects would overcome the alignment energy of the molecular field. Consequently, the magnetic moments would have random orientation and it would lead to paramagnetic behaviour.

$$H_{eff} = n_w M + H \tag{2.26}$$

However, at low temperatures, this model would lead to higher fields, which is not the case in real ferromagnets. Nevertheless, his approach indicated the right direction. Later, the Heisenberg model corrected this with the idea of a *limited interaction range* for the spins.

Landau explained the emergence of ferromagnetism from a thermodynamic perspective in a phase transition model, sec 2.2.1. In this model, the free energy F of a ferromagnetic system is expanded in a Taylor series with magnetization M as its order parameter. The magnetization M_0 is zero above the phase transition temperature T_c and $M > 0$ below T_c. With regard to the symmetry argument for "up" or "down" states of the magnetization M, they are energetically equal as the time-reversal symmetry[18] ($\widehat{=}$ reversing of magnetization) implies that the *energy* is conserved. Hence, the series cannot possess any odd power of M and it leads to an expression for the free energy $F(M)$ in agreement with Eq. 2.23 [24]:

$$F(M) = F_0 + a(T)M^2 + bM^4 \tag{2.27}$$

F_0 and $b > 0$ are constants of the model, and a(T) is a temperature-dependent variable. At the transition Temperature T_C, $a(T)$ changes its sign. By taking the arguments of Sec. 2.2.1 into account, it is valid to write $a(T) = a_0(T - T_C)$ near the transition point, with $a_0 = const > 0$. Minimizing free energy yields the ground state of the system.

$$2M[a_0(T - T_C) + 2bM^2] = 0 \tag{2.28}$$

The solution of the quadratic equation delivers two terms:

[17]This section is based on [24, 40, 46, 47].

[18]This symmetry operation states that an associated physical property doesn't change, if time runs backwards, by that the related *motion* is reversed.

$$M = 0 \quad or \quad M = \pm \left[\frac{a_0(T - T_C)}{2b}\right]^{1/2} \tag{2.29}$$

The second solution is fulfilled for the condition $T < T_C$. Landau's approach to the phase transition is in accordance with the mean-field theory, which assumes that all the spins 'feel' an identical average exchange field, produced by all their neighbours. This field is proportional to magnetization.

Exchange interactions: The alignment of the spins is a quantum mechanical effect that gives rise to magnetism. On the question of how two electrons interact and align, an answer can be obtained from the exchange interactions, which deliver an explanation on the atomic scale. If two electrons are exchanged, their energy will remain either unchanged (symmetric), or changes sign (antisymmetric). As the wave function of two electrons is identical, they have an *exchange symmetry* under the condition of indistinguishability.

In a similar manner that two magnetic moments with the same orientations repel each other in order to lower their overall energy, it is also the case with spins ($\varsigma(a)$, $\varsigma(a)$). Each spin represents one orientation, and it occupies one state. For fermions, one state cannot be occupied by more than one electron. Consequently, they repel a further electron in the same state.

The spin states are effectively an extended correction to the Coulomb energy of electrons in their degenerate state. As electrons are indistinguishable, their total wave function $\Psi(a,b) = \phi(r_a, r_b) \cdot \varsigma(a,b)$ is a product function of a spatial state and spin state. Therefore, the exchange of two electrons must deliver the same electron density:

$$|\Psi(a,b)|^2 = |\Psi(b,a)|^2 \quad \Rightarrow \quad \Psi(a,b) = -\Psi(b,a) \tag{2.30}$$

This necessary condition is only fulfilled under an antisymmetric ***total*** wave function, indicating that there is no probability of finding two electrons with the same spin at the same point in space. The spin-spin interaction splits the fourfold degeneracy into singlet-triplet energies, where either the spin part of the total wave function is in an antisymmetric singlet state ς_s, $(s = 0)$ with a symmetric spatial state ϕ_t or the spin is in a symmetric triplet state ς_t, $(s = 1)$ with an antisymmetric spatial state ϕ_s.

The total wave functions Ψ for the singlet and the triplet cases are:

$$(i) \quad \Psi_s = \phi_t \cdot \varsigma_s \quad \text{and} \quad (ii) \quad \Psi_t = \phi_s \cdot \varsigma_t \tag{2.31}$$

$$\text{The energy difference:} \quad E_s - E_t = \int (\Psi_s^* \hat{\mathcal{H}} \Psi_s - \Psi_t^* \hat{\mathcal{H}} \Psi_t) d\mathbf{r}_1 d\mathbf{r}_2 \tag{2.32}$$

between the $\uparrow_i\downarrow_j$ and $\uparrow_i\uparrow_j$ configuration of the spins of neighbouring atoms i, j delivers the effective Hamiltonian $\hat{\mathcal{H}}$, with a spin-dependent exchange integral, J:

$$\hat{\mathcal{H}} = \underbrace{\frac{1}{4}(E_s + 3E_t)}_{\text{const. term}} - \underbrace{(E_s - E_T)}_{\text{exchange integral } \mathbf{J}} \mathbf{S_a} \cdot \mathbf{S_b} \tag{2.33}$$

In the Heisenberg model, J is generalized for a many-body system spin vector[19]. By applying Eq. 2.34 to the crystal, a macroscopic magnetization will be derived. It applies to all

[19]The dimensionality (D_s) of spins is regarded as its *order parameter*, in Ising model spins have only one dimension, pointing up and down, while sitting on the lattice with the dimension of $d_l = 1, 2, 3$.

nearest neighbouring atoms of the system, which is sufficient to explain the magnetic long range order. However, the origin of spontaneous magnetization, as an order phenomenon with its unbalanced orbital motion, is related to spin-orbit coupling.

$$\hat{\mathcal{H}}^{spin} = -\mathbf{J}\sum_{ij}\mathbf{S_i}\cdot\mathbf{S_j} \quad (2.34)$$

- $\mathbf{S_i}$ & $\mathbf{S_j}$ are the quantum mechanical spin operators for a given spin quantum number $S \in \{1/2, 1, 3/2, 2\}$
- The indices i & j refer to the neighboring lattice positions

Furthermore, J is associated to the overlap of the charge distributions of the atoms i and j. If J is positive, the spins i and j are preferentially aligned parallel in order to minimize their interaction energy, Sec. 2.4B. If J is negative, an *antiferromagnetic* spin alignment with vanishing macroscopic magnetization will be formed.

Another idea that can be extracted from Eq. 2.30 is the Pauli principle (Pauli repulsion) that forbids two electrons ($\phi(a)$, $\phi(b)$) in the same from entering the same quantum state. This is reflected in Hund's first rule, which explains the origins of uncompensated spin distributions in 3d bands of the transition metals. It states that the electrons fill the lowest energy orbitals first. This leads to the rise of a net magnetic moment in these materials, Sec. 2.4A. The figure shows the dependence of J_{ex} with r_a/r_{3d} ratio with r_a the atomic radius and r_{3d} the radius of the 3d electron shell. A decrease in the inter-atomic distance brings the 3d electrons close together so that their spins must become anti-parallel (negative J_{ex}). Therefore this curve predicts the transition from antiferromagnetism (3) to ferromagnetism (1).

A comprehensive treatment of order formation in the magnetic system can be found in [24, 47].

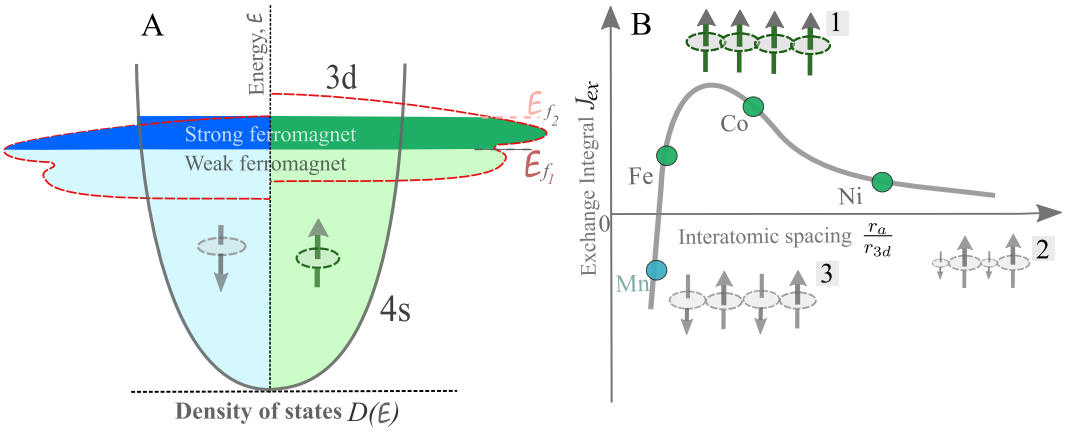

FIGURE 2.4: A) Displays the density of states in 3d transition metals [47]. The electron spins with orientation in one direction remain uncompensated and give rise to an unequal spin distribution. Thus, a net magnetic moment appears. B) Schematic of the Bethe–Slater curve as a result of the exchange interaction between neighbouring atoms, Eq. 2.34. [48, 49].

Ferrimagnets; For some crystal systems the parallel alignment of the magnetic moments between the atoms below the phase transition is not always energetically favourable. Other types of alignments, can take place at the phase transition. The antiferromagnetic alignment at the Neel temperature T_N is the opposite of the ferromagnetic alignment. Depending on the topology of the crystal lattice, ferrimagnets with spontaneous magnetization also arise.

These crystal systems are characterized by two unequal oppositely directed magnetic sublattices, with their magnetization, M_A and M_B where $\mathrm{M}_A \neq \mathrm{M}_B$. Most oxides that possess a net ordered magnetic moment are ferrimagnets, Sec. 2.4B, case 2.

The ferrite $CoFe_2o_4$, an important constituent in composite magnetoelectrics, belongs to the family of ferrimagnets, Sec. 2.6.4. At the atomic level, ferrimagnets are obeying the exchange integral formulation, its occurrence can be explained as a consequence of the exact inter-atomic spacing of the 3d transition metals.

2.3.4 Effects of ordering in magnetism

As a consequence of magnetic ordering in some crystal lattices, a preferential enhancement of certain properties like magnetization direction or magnetostriction will be established.

Anisotropy

The ***isotropic*** nature of any property in materials indicates the existence of symmetries in the internal structure of the material. For instance, the structure symmetry in materials with associated stiffness tensor results in the invariance of the stiffness tensor to the specific transformations related to the symmetry elements. The mathematical formulation of a symmetrical property of a structure can be defined in terms of a simple property tensor with only principle diagonal elements[20].

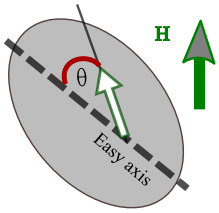

FIGURE 2.5: Easy axis and magnetization are not aligned as H-field is applied.

Anisotropy, however, refers to the directional dependency of certain properties, in this case, the magnetization direction. Consequently, the transformation of the tensor property is not invariant, which means the value of the related parameters, that indicate the nature of the dependency needs to be specified in the property tensor. To determine the element of the corresponding tensor, as it is required for the constitutive formulation, a directionally dependent measurement would be needed to be served. In the case of ferromagnets for instance, at first glance, the isotropic nature of exchange interaction suggests that there is no preferential direction in the crystal that would change the internal energy. However, the additional interaction energy comes from spin-orbit interaction $H_{spin-orb.} \propto \mathbf{L} * \mathbf{S}$ causing the preferential direction of the magnetization. The reason for this is the position of the atoms in the crystal structure. Consequently, this would cause a natural tendency of the spins, which are fixed in the lattice points, to have a preferred alignment direction. With this, an anisotropy can lay along the lattice axis and would inherit the same symmetry as the crystal structure of the material. Here, the preferential direction of magnetization arises due to the coupling of the valence electrons with the spontaneous magnetization of ferro- or ferrimagnetic materials [49]. Therefore, the magnetization (as measured property) is varying in magnetic material with the direction.

As the crystal structure defines the direction of the property, the term has been coined the magnetocrystalline anisotropy. This term gives, e.g., the easy axis[21] for magnetization, as depicted in Fig. 2.5. It illustrates that the magnetization does not need to be parallel to $\mathbf{H}$, except when the directions of the applied field and the easy axis are matching. A rotation away from the easy axis caused by the external field is connected with the existence of additional field energy [47], or external forces like uniaxial stress. Magnetocrystalline

[20] see Sec. on constitutive laws,2.1.2 on page 9 and implication of symmetry in appendixA.1 on page 141.

[21] Soft magnetic property of the materials referred to the fact, that the magnetic hysteresis is slim regarding the switching field (see Sec. 2.8).

anisotropy is the only intrinsic anisotropy since it is related directly to the crystal symmetry of the material. All the other magnetic anisotropies are induced.

The related anisotropy energy is given by

$$E_{ani} = K_{ani} sin^2\theta \tag{2.35}$$

where θ is the angle between the direction of M and the easy axis. Accordingly, a strong easy-axis anisotropy is a precondition for hard magnetism. A near-zero anisotropy describes the behaviour of soft magnets, Sec. 2.8. Furthermore, it should be noted that a rotation of the magnetization away from the easy axis is possible by applying a higher external magnetic field.

The largest values of uniaxial anisotropy are found in hexagonal and other uniaxial crystals. The smallest values are found in certain cubic alloys and amorphous ferromagnets.

Polycrystalline materials have grains with random orientations. Accordingly, the anisotropy of the individual grains is averaged out, resulting in the absence of crystal anisotropy on the macroscopic scale [49, p. 229]. On the other hand, in the case of a polycrystalline material a *crystallographic texture* is possible; where the polycrystalline material aggregates itself to have an anisotropy by control of the easy-axis orientation during manufacturing. This control can be achieved by the application of an external magnetic field or pressure [50]. However, this alignment will not happen, if the individual particles are themselves random poly-crystals with a random multi-domain structure.

2.3.5 Ferroic hysteresis: Characteristic and comparison

Ferroic ordering[22] is a consequence of a phase transition[23], accompanied by the structural change in a crystal. It gives rise to spontaneous polarization ($\mathbf{P}$), magnetization ($\mathbf{M}$) and strain ($\mathbf{S}$) order.In the absence of external stimuli fields (magnetic or electric) the *spontaneous* polarization or magnetization will be oriented along one of the family of crystallographic directions with the lowest free energy.

Upon onset of the respective fields (H, E, σ) in ferromagnetic, ferroelectric, and ferroelastic materials a *nonlinear response behaviour* occurs. It is manifested in the form of a hysteretic measurable physical quantity of the respective "order quantity", such as polarization ($\mathbf{P}$-E), magnetization ($\mathbf{M}$-H), and/ or strain ($\mathbf{S}$-σ) order [24], see the curve in Sec. 2.7 (Fig. 2.10) [25]. The reversibility of order is a necessary condition of both classes. It is expressed in the shape of their behaviour curve, as the energy argument in both cases obeys the same principles and dependencies [51].

The associated switching behaviour of ferroelectrics and ferromagnets with its hysteresis behaviour is characterized in the following, also see Sec. 2.7.

Once a ferroic crystal is exposed for the first time to an external field (H or E), the dependent property follows the virgin curve until it reaches a plateau, position 1-2. At this point, the saturation of ferroic ordering $P_{sat}|M_{sat}$ is indicating that the internal "'dipoles"' inside material are fully aligned or ordered with the field, indicated in Sec. 2.7 with the

[22] From now on, the more general term of "'ferroic ordering"' is used to cover both polarization/magnetization.

[23] As a crystal is cooled down below its Curie temperature T_C, a new state of order (with that property) is formed (double-well potential is formed Sec. 2.6).

[24] Ancient Greek word meaning "deficiency" or "lagging behind". It was coined by Sir James Alfred Ewing to describe the anomaly behavior of magnetic materials (Wikipedia).

[25] Ferroelastic hysteresis will be treated separately (Sec. 3.4) as they are intrinsic to both ferromagnetism and ferroelectricity.

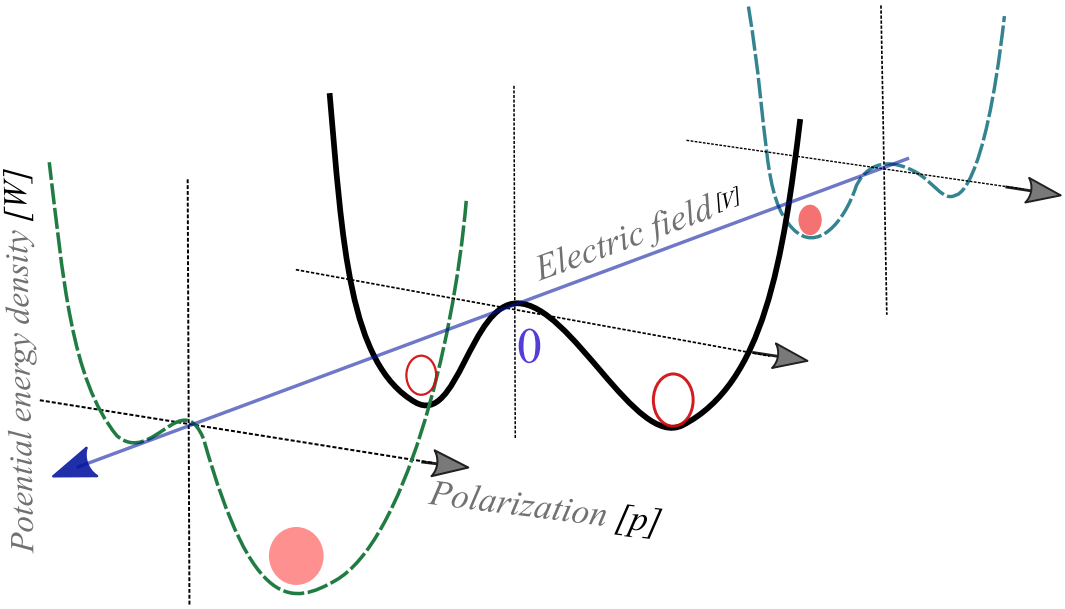

FIGURE 2.6: Illustration of the potential energy landscape of the two states accessible by applying fields. The energy levels in Sec. 2.3 shift during the application of an electric field, causing the polarization to switch.

arrows, position 6. If the driving field is withdrawn, a "'remnant"' polarization | magnetization order will "remain", position 3. A reversal of the ordering requires the application of a field with the opposite polarity and with a magnitude greater than zero. The critical field needed to cause reversal of the polarisation/magnetisation is referred to as the coercive field $\mathbf{F}^{ield}_{(E_c/B_c)}$, the threshold where switching is happening, Sec. 2.7, position 4.

The values for the remnant, saturation, and spontaneous magnetization | polarization are not the same. The latter is deduced from the slope of the saturation plateau above the coercive field, and it is extrapolated to cross the zero-field y- xis, position 5. The remnant polarization is usually lower, and it is the point at which the hysteresis curve cuts the y-axis, position 3 [52, 53].

In spite of the hysteretic similarities for both prominent ferroics, there are differences in their origin and meaning. As both properties are found in multiferroic materials, it is reasonable to compare them. Their study delivers valuable information on the different physical processes that take place in ferroic domain switching due to domain wall motion, Sec. 2.3.6.

In addition to obtaining an understanding of the switching field and remnant constant, a close look at hysteresis also provides insight into the magnitude of the energy stored. From the materials science point of view, it delivers details on defects and impurities as they can lead to a nonsymmetric hysteresis curve. This and other processes such as domain-wall pinning, defect ordering, and the nature of defects are expressed in the hysteresis shape.

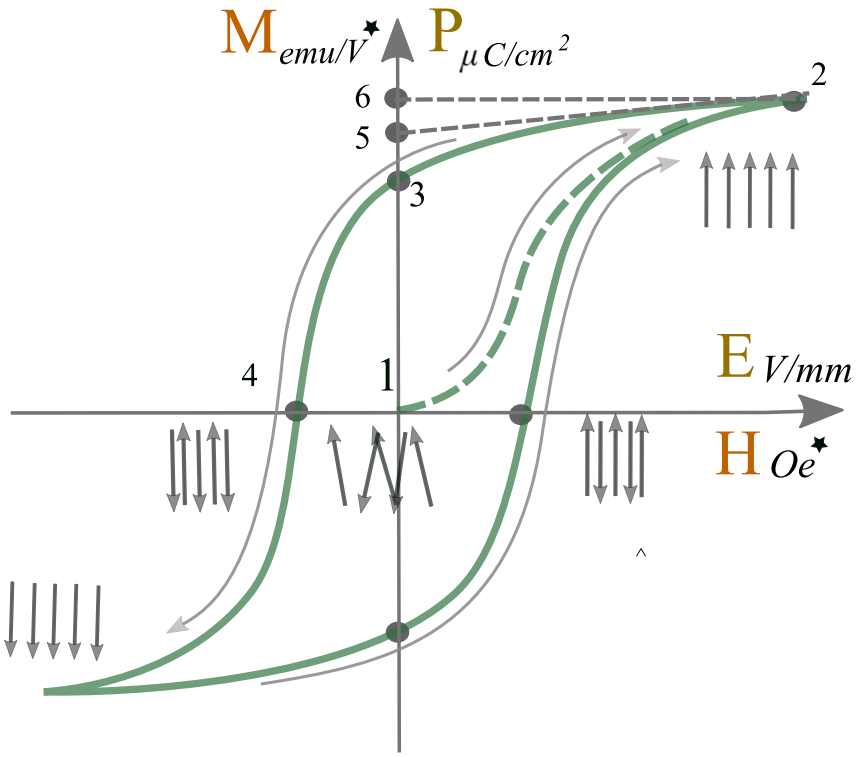

FIGURE 2.7: For comparison reasons, the hysteresis curve as a nonlinear response of a field interaction with matter between both forroic materials schematically illustrated for both forroic materials. The arrows represent domain switching, which gives rise to hysteresis in the macroscopic order. This curve is typical for the *ferroic* materials; $M - H$ curves, where M is spontaneous magnetization reversal upon application of H. $P - E$ curves, with P spontaneous polarization reversal due to application of an E-field. For both, it starts with an unmagnetized or unpolarized state at the origin "zero" order, with the application of a field ferroic ordering is aligned. The important hysteresis parameters are; E_c: coercive field; P_s: spontaneous polarization; and P_r: remnant polarization. the equivalent points in a $B - H$ curve would be B_s: saturation induction and B_r: magnetic remanence. Measured curves show at first glance similarities between both material classes. The difference is the order parameters, as magnetization is a volume quantity while polarization is a surface quantity.

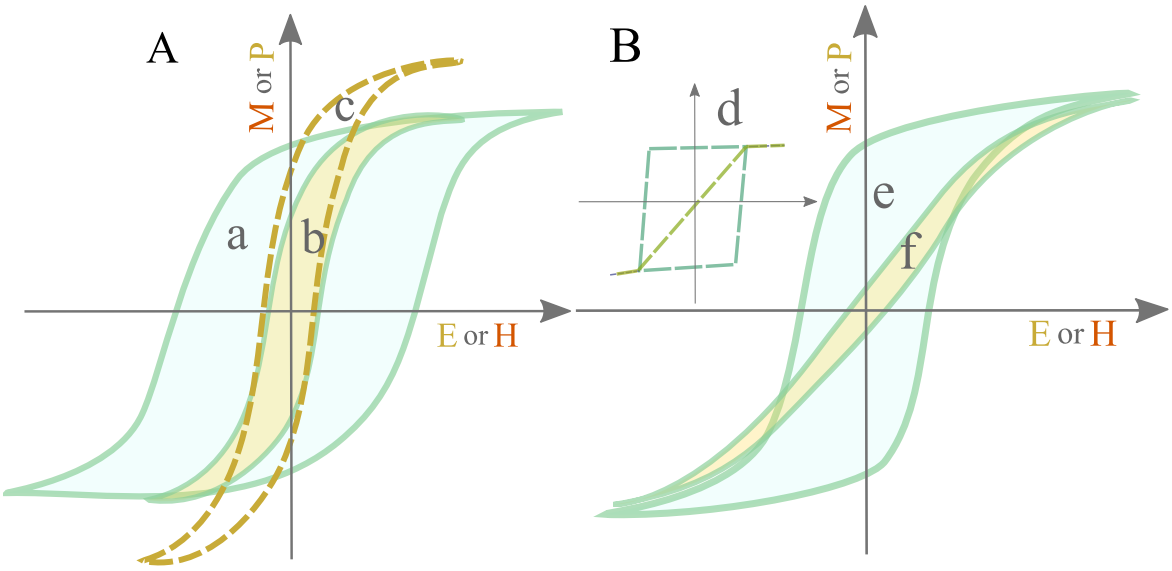

FIGURE 2.8: Illustration of the hysteresis for both hard and soft ferroelectric and magnetic materials. A) Soft and hard hystereses are due to inhomogeneities, doping, and defects. These hinder domain wall motion and contribute to a higher coercive field. B) In addition, in magnetic materials the measurement axis plays a role in the shape of the hysteresis curve, as well as the domain wall mobility. The illustration shows the difference between the easy axis (f) and the hard axis (e), which is due to magnetocrystalline anisotropy. (d) Represents the hysteresis for a single domain magnet. Due to the measurement techniques used, the shape of hysteresis in ferroelectrics is influenced by the degree of *leakage* in these materials, discussed in Sec. 3.3.1.

2.3.6 Domains

At the phase transition, the rearrangement of the static energies (Sec. 2.1) gives rise to the alignment of ferroic order. At the same time, the field alignment has an energy cost associated with the stray fields. Consequently, as a result of the balance between the various kinds of energies related to the crystal structures, domains are formed in both classes of ferroic materials. These domains are volumes of ferroic material with the same polarity. Domain formation occurs due to the minimization of the magnetization/polarization energy associated with the magnetic/ferroelectric material [34].

Ferromagnetic domains: P. Weiss postulated that upon the onset of spontaneous magnetization, a ferromagnet would not necessarily order into its saturated magnetic state. He concluded that spontaneous magnetization splits into different directions inside the ferromagnet. As a result of this, it forms a demagnetized state. Subsequently, the existence of a demagnetized domain state was confirmed by the observations of Bitter (1931). Moreover, Landau and Lifshitz (1935) explained it using the concept of energy minimization. The hysteresis reflects the domain behaviour in this context as it represents the overall domain configuration for the size of the applied field. Consequently, the hysteresis is portraying the nature of the domain energies, Sec. 2.8, if the material is assumed to be a homogeneous, defect-free, single-crystal ferromagnet with cubic symmetry, Sec. 2.9B. The domain formation can be explained by the minimization contest between the exchange, magnetostatic, anisotropy (magnetocrystalline), magnetoelastic, and wall energies. This formation yields a balance over the sum of the five basic energies [54]:

$$E^{\star} = E_{exch.} + E_{m.crystal.} + E_{m.stat.} + E_{m.elasticexch.} + E_{wall} \tag{2.36}$$

The parallel alignment of all the magnetic moments in a single region would minimize the exchange energy and create the domain. On the other hand, this circumstance also creates also stray fields that are associated with magnetostatic energy.

The parallel alignment of all the magnetic dipole moments in a single region would minimize the exchange energy and create the domain. On the other hand, this creates also stray fields that are associated with high magnetostatic energies. In order to reduce the energy-intensive contributions of the stray fields, the splitting of a single domain into multi-domain regions is favourable. This would lower the energy associated with stray fields. In addition, the lower permittivity of the air compared to the magnetic material, makes the presence of the field-lines inside the material energetically more favourable. This leads to the formation of domains with different orientations. Despite this, there is some energy cost inside the material since the direction of the coupled spin-orbit alignment needs to be changed, which will work against the exchange energy minimization. As a result of this, the contribution to the total energy increases as it splits the region of the same alignment by creating a boundary region, the domain wall, where the rotation of field direction takes place. For the process of domain wall formation, the demagnetizing field is decisive, as it reflects the tendency of the field to reduce the total magnetic moment, Fig. 2.9A. It can contain 10 - 100 unit cells until the change is fulfilled. This, however, depends on the anisotropy of the system, which determines the possible angle of rotation between the neighbouring domains. It is part of the overall trade-off between the competing energy contributions, which are competing in order to minimize the total energy. As a result, all these small particles (20 nm) tend to be single-domain, whereas larger particles form domain walls in order to reduce the demagnetizing energy.

The width of the domain wall is determined by the balance between the exchange energy, and the magneto-crystalline energy. The exchange energy prefers wide walls to align the magnetic moments parallel to each other as, on the other hand, the magneto-crystalline energy prefers narrow walls so that the magnetization is aligned as close as possible to an easy axis.

Ferroelectric domains: Similar to the understanding of domains in magnetism, the findings were carried over to ferroelectric crystals. In this case, the minimization of the system overall energy drives the formation of the domains. However, in this case, domains are formed as the perovskite crystal transforms from a non-ferroelectric cubic to a ferroelectric tetragonal phase. The uniform alignment of the dipoles throughout the crystal along the same direction leads to a domain region (polarized region). Moreover, inside the crystal, at certain surfaces bound charges can be found. Due to the electrical and mechanical coupling of elementary dipoles, associated elastic energy arises as well. The electric field of the surface charges competes with the polarization energy, and this tends to reduce its electrostatic energy. The corresponding field, the *depolarizing fields* E_d (Fig. 2.9), which is of the order of $MVm^{-}1$, can become strong enough to completely suppress the polarization. Leading rearrangement of the single-domain state of the ferroelectric, which is energetically unfavourable and this leads to the formation of ferroelectric domains.

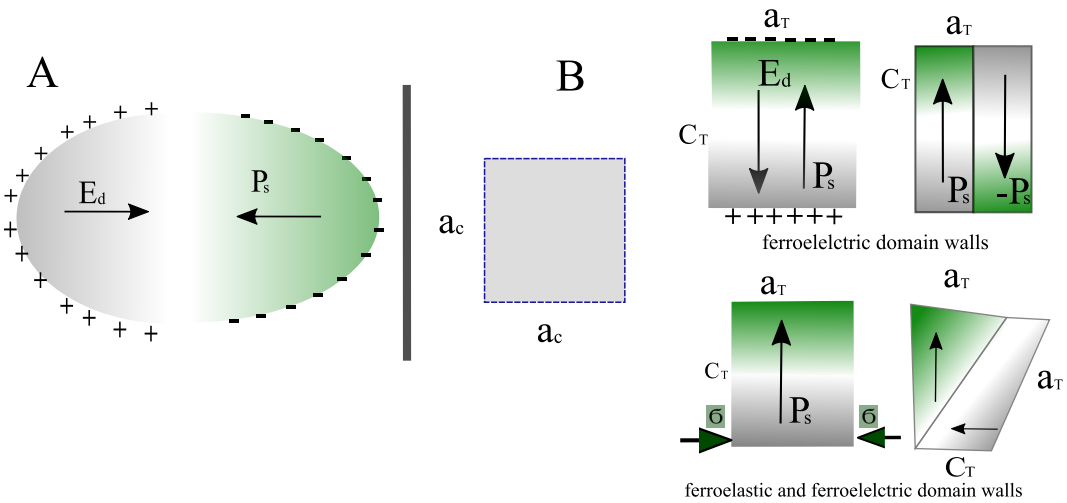

FIGURE 2.9: The bound surface charge generated by spontaneous polarization causes a field alignment in the opposite direction. This depolarization leads to the formation of domains. The equivalent to this in magnetic material is the demagnetization field. B) The emergence of 180° and 90° domain walls due to different conditions for the minimization of electrostatic energy. The 90° domains in both phases are associated with stress σ, drawn in accordance with [55].

The electrostatic energy of the depolarizing field is minimized (i) if the ferroelectric splits into domains with oppositely oriented polarization, 2.9, or if (ii) the depolarizing charge is compensated by electrical conduction through the crystal, 2.9. The region between the two domains is also called a domain wall, since its formation creates a polarization gradient. The establishment of domain walls due to the rotation between dipole moments also increases the system energy, so the resulting domain structure in the framework of total energy minimization has to be a compromise between all energy cost contributions. For the tetragonal case, the crystal structure allows only 90° - and 180°-domain walls. Both kinds of walls reduce the effect of depolarizing fields. The formation of a 180°-domain wall leads

a more significant polarization gradient than that of a 90°. Mechanical stress can also cause domain splitting, where the formation of 90° domain walls may minimize the elastic energy.

Domain wall motion: The appearance of hysteretic behaviour in ferroic materials is an indication of domain switching. Domains are rearranged through domain wall motion. The microstructure morphology (grain-size, impurities, defects, ...) also has an impact on the domain wall mobility. In this regard, the hysteresis portrays how the switching is happening, and it depicts the energy that is required for the domain wall motion as during the switching process a specific work is done. In this respect, the coercive field reflects the amount of energy that is necessary for switching of domains, Fig. 2.8. Specifically, pinning defects and impurities impede its movement through the domain region. The common terminology for them in ferroic materials is known as "hard" and "soft" hysteresis[26].

Under an additional external field (e.g. uniaxial stress), the motion of a domain wall will be affected as well as the additional external field influences the mobility of the domain wall. Depending on the nature of the field, the domain wall undergoes a different transformation under the given condition. In this case, the switching of the polarity in domains depends on the amount of the energy to overcome the additional field compared to the energy that is required.

2.4 Mechanical effects in ferroic materials

Both ferromagnets and ferroelectrics exhibit a *spontaneous deformation* simultaneous to their polarization and magnetization at the phase transition. This occurs as a consequence of the reorganization of the structure in the crystals, and it is coupled to a macroscopic strain. Furthermore, the strain[27] of the ferroic phases can be driven by the respective fields.

In the introduction (Sec. 2.1.2), *piezoelectricity* was described as the change in polarization, with a *linear* function dependency on applied stress. Or for the inverse effect, strain is a linear function of the applied electric field. The strain behaviour of ferroelectrics, however, is described by *electrostriction*, which is a change in the strain with a *quadratic* dependence on the local electric field [56]. Similarly, piezomagnetism describes the strain as a linear function of the magnetic field, or with its inverse effect, the change in magnetization as a linear function of applied stress. Magnetostriction, however, describes the strain as a *quadratic* dependence on the local magnetic field for ferro- and ferrimagents.

2.4.1 Electrostriction

Microscopically, inside the unit cell of a dielectric, an electric field separates the charge centre of the ions inside the unit cell, with a corresponding associated displacement. Macroscopically, the electric property is coupled with the mechanical property; Strain-to-field coupling, Sec. 2.1.2.

The study of strain ε vs. E field in ferroelectric materials shows a hysteretic, so-called butterfly, loop due to its shape, see Sec. 2.10A. As previously introduced, the simplest way to describe an electrostrictive behaviour is through a quadratic dependency of it on the E-field,

$$\varepsilon_{ij} = k_{ijkl} E_k E_l \tag{2.37}$$

where k is the electrostrictive coefficient that describes the coupling. Once a sample is poled, it has for $\vec{E} = 0$ the same elongation regardless of the direction of the previously

[26] In some applications such as high-precision sensors, actuators, and capacitors, a hysteresis caused by domain wall motion is undesired.

[27] The extent of deformation over the nominal length in an axis.

applied field and the strain ε is approximately linear to the electrical field. The slope of strain vs. E at $E = 0$, gives d_{33} [57], which is a key figure of merit for a ferroelectric material when used in composite magneto-electrics, Eq. 2.52. The effect of external stress on strain is a further characterization parameter. The total strain has elastical strain and remanent portion. The field switches strain elastically[28] [58], Sec. 2.10B. E vs.ε_σ results also in the dependency of d_{33} from the amplitude of the stress as a driving field that switches the domains.

It is worth noting that there is no inverse electrostriction, as mechanical stress equally influences positive and negative ions. Consequently, it can cause no polarization change. However, polar materials exhibit a piezoelectric effect that dominates any electrostriction effects [59].

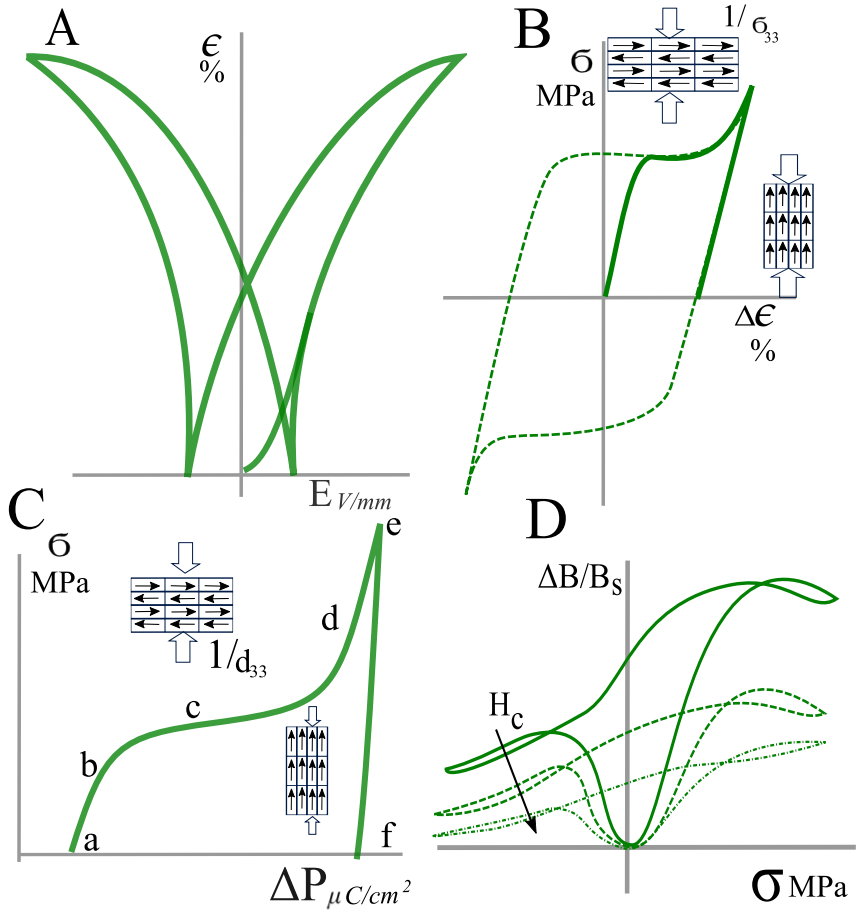

FIGURE 2.10: Hysteretic effects in ferroic materials. A) Is the illustration of ferroelectric strain hysteresis (butterfly hysteresis). B) Is the representation of the ferroelastic strain hysteresis, the dashed line shows the case for both compression and tensile stress, while the solid lines illustrate the only a compressive stress. C) Depicts the depolarization curve of a poled state under uniaxial stress parallel to the poling direction, b-d is the regime of domain switching. In both B), and C) the domain switching process is illustrated as well [60]. D) Magnetization-stress curves illustrate the difference between tension and compression for a demagnetized magnetic material subjected to a small constant magnetic field [61].

[28] The remanent portion of strain is un-switchable.

2.4.2 Magnetoelastic properties: Magnetostriction

Magnetostrictive materials are currently used for various sensor applications[29] [62]. Furthermore, the time response of the magnetostrictive material is also a relevant parameter for its use in a composite magnetoelectric material, Sec. 2.6.3, given the dynamic nature of the magnetoelectric effect in composite.

From the measurement of magnetostriction, it is possible to obtain the magnitude of strain $\frac{\delta l}{l}$) of a ferromagnetic material in response to an applied magnetic field as its coupling coefficient $q_\sigma = \frac{d\lambda}{dH}_\sigma$. Hereby, the piezomagnetic coefficient $q_{33} = d\lambda/dH$ -strain derivative- is the corresponding figure of merit in this case[30] [50], see Sec. 2.11. In particular, their utilization as a pseudo piezomagnetic material at certain bias magnetic fields offers interesting strain sensitivity, which makes them interesting for magnetoelectric composites. The length change, as a result of domain reorganization, is a consequence of the magnetization process, see Sec. 2.11 and Sec. 2.3.6 [46, 64]. The magnetization M obeys the $\lambda \sim M^2$ relationship to strain [65]. On the crystal level, the magnetostriction is linked with a rotation of the local magnetization, see Sec. 2.11A.

The spin-orbit coupling of the electron with the crystal lattice gives rise to the emergence of strain, as long as a dependency of the magnetic anisotropy energy on magnetization exists in a material. As the magnetic moments are aligning with the magnetic field, it induces an internal strain of the crystal lattice (magnetocrystalline anisotropy, Sec.2.3.4, p.19) [66]. As the magnetic field is increased, the domains rotate more and align along the direction of the field until saturation with regard to the expansion is reached, denoted as λ_s, see Sec. 2.11. It displays the main magnetostrictive effects for an applied H-field. Given that volume is conserved delivers the relation for the magnetostriction between perpendicular and parallel field directios $\lambda_{\parallel} + 2\lambda_{\perp} = 0$ given. If θ is the angle between the magnetization and the easy axis as illustrated in Sec. 2.5 , the relation is in Eq. 2.42 [47].

Sec. 2.11B illustrates the magnetostriction of a polycrystalline material over the field range up to saturation. The dashed curve displays its relation to compressive stress according to the Jiles-Atherton-Sablik model [67, 68]. Further, the *strain sensitivity*, which is given as the variation of a strain derivative upon an applied magnetic field ($d\lambda/dH - H$) is displayed. The strain sensitivity can be tuned by atomic substitution in magnetostrictive crystals, and with that, the magneto-electric effect can be tailored [69]. Stress also affects the strain sensitivity and, thus, the piezomagnetic coefficient.

The conservation of volume for a magnetostrictive material means that there is a corresponding decrease of the diameter as the length grows. Moreover, reversing the magnetic field changes the configuration of the domains, which causes hysteresis in the strain curve for ferromagnets in field direction.

Furthermore, magnetostriction λ_s depends on stress σ. For uniaxial stress, the saturation field shifts to higher magnetic fields, however with lowerλ_s^σ. The opposite occurs for electrostrictive strain, where the saturation decreases with the field [72].

In order to trace back the origin of magnetostriction, it is useful to derive the Legendre polynomial expansion of the interaction energy ($\mathcal{E}$) of the spin pair (Eq. 2.38) in terms of its inter-atomic distance "r", with ϕ the angle between magnetization and the line the pair of atoms. This will show that the interaction between the *atomic magnetic moments* is the main driving force for this effect. The expansion is:

[29] Also other technical applications like in micro-motional control or ultrasonic sound generators.

[30] The effect of sensitivity in the magnetostrictive coefficient (the slope) at certain bias fields is used in acoustic- magnetic surveillance at e.g stores, with magnetic tags made of two strips, one magnetostrictive. However, the focus of modern research in magnetism is dominated by the investigation of zero thermal expansive and low magnetostrictive magnetic compounds. This is due to the importance of dimension stability which is required in precision instruments and data storage devices [63].

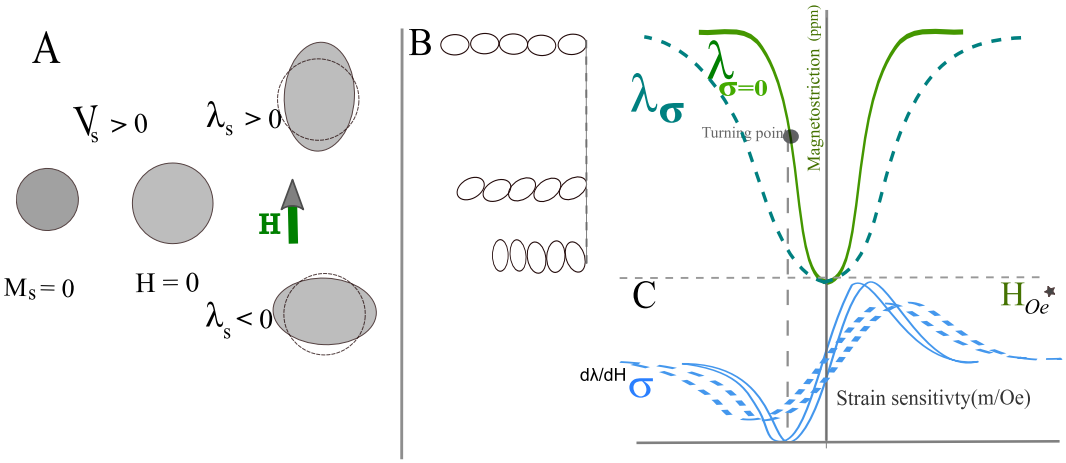

FIGURE 2.11: A) displays the main magnetostrictive effects; I. the spontaneous volume magnetostriction V_s (Isotropic, at $\mathbf{H} = 0$), and II. the field magnetostriction (anisotropic, with a field $\mathbf{H} \lesseqgtr 0$). [47]. Sec. B) illustrates the magnetostriction of a polycrystalline material. C) Displays the *strain sensitivity [70, 71]*.

$$\mathcal{E}(r, cos\phi) = \hat{\mathcal{E}}_{spin}(r) + l(r)(cos^2\phi - \frac{1}{3}) + ... \quad \text{with} \quad l = -\frac{3\mathcal{M}_{dm}^3}{4\phi\mu_0 r^3} \qquad \text{see Sec. 2.1.1} \tag{2.38}$$

The first term is the exchange interaction energy term of the spins from Eq. (2.38). The other terms describe the contributions of anisotropic exchange interactions and crystal field interactions [73]. Here, the direction of magnetization doesn't depend on the exchange term $\hat{\mathcal{E}}_{spin}(r)$, and the deformation caused by it would not contribute to magnetostriction. The same conclusion can be made for the anisotropy[31]. The second term represents the *dipole-dipole interaction*, Sec. 2.1.1, which depends on the direction of the magnetization and can be seen as the main origin of magnetostriction, Sec. 2.4.2. This term will also be relevant for domain formation. Its switching behaviour gives rise to magnetostriction. Magnetostriction is large in the vicinity of the coercive field as domain-wall motion and spin rotation take place within the domains, see Sec. 2.3.6.

The field-induced magnetostriction is referred to as the *Joule effect*, and its opposite as the *Villari effect*, which is the change of the magnetic state under the influence of an applied stress.

The piezomagnetic coefficient $q_{33} = d\lambda/dH$ -strain derivative- is the corresponding figure of merit in this case[32] [50], see Sec. 2.11. Furthermore, the time response of the magnetostrictive material is also a relevant parameter for its use in a composite magnetoelectric material, Sec. 2.6.3, given the dynamic nature of the magnetoelectric effect in composite.

Magnetoelastic properties: The coupling energy magnetoelasticity is the energy of a crystal which arises from the interaction between the magnetization and the mechanical

[31] Nevertheless, it plays a role in the volume magnetostriction, which is discussed in [66] *chap.* 14.5.

[32] The effect of sensitivity in the magnetostrictive coefficient (the slope) at certain bias fields is used in acoustic- magnetic surveillance at e.g stores, with magnetic tags made of two strips, one magnetostrictive. However, the focus of modern research in magnetism is dominated by the investigation of zero thermal expansion and low magnetostrictive magnetic compounds. This is due to the importance of dimension stability which is required in precision instruments and data storage devices [63].

strain of the lattice, and it is obtained by summing (Eq. 2.38) over all the nearest neighbours of each atom in a deformed magnetic solid. Magnetostriction inside the material causes internal stress. Conversely, applied mechanical stress can change the dimension of domain structure and, correspondingly, the total length, see Sec. 2.11. The change of the magnetization state by an applied stress depends also on the remnant magnetization, or magnetic field offset, as discussed by Jiles [74] in the theory of the magneto-mechanical effect, Sec. 2.10D.

The magnetic field affects the overall elastic properties of the material, see Sec. 2.10, 2.13B, which results in a dependency of the materials Young's moduls Y_{mod} on its magnetization state. This is known as "Δ-*E effect*"[33], which is related to the difference of the Young's modulus (ΔY_{mod}) between the originally demagnetized and saturated states [75].

A further **magneto-mechanical effect** defines the change in magnetization of a magnetic material resulting from the driving stress field. Here, domain switching depends on the state of magnetization that is given by the constant applied field [76]. Moreover, the uniaxial stress σ induces uniaxial anisotropy, Eq. 2.44, Sec. 2.13 [49]. This stress affects how the magnetic domains are reoriented and results in a preferential strain orientation inside the material [54].

Moreover, the stress affects the domain wall movement, and at smaller length scales, it distorts the crystal lattice as it alters the relative positions of atoms within the lattice. As the axes and the atoms move relative to each other, this affects the spin-orbit coupling, which determines the magnetocrystalline anisotropy. Consequently, the changes in anisotropy energy and exchange energy (that both depend on the relative separation of atoms), modify the energy required to keep the magnetic moments pointing in any given direction [72]. This leads to the formation of a new source of magnetic anisotropy. With regards to hysteresis, *Jiles* argues, that stress dependency results in an additional field, see Eq. 2.40, Jiles1995.

$$H_{eff} = (1+\alpha)H + H_\sigma \quad (2.39) \qquad with \;\; H_\sigma = \frac{3}{2}\left(\frac{d\lambda}{dM}\right)(cos^2\theta - \upsilon sin^2\theta) \quad (2.40)$$

It is an empirical equation to predict these changes in magnetization, with υ being Poisson's ratio.

[32] In most of the literature, Young's Modulus is denoted with the letter E_{mod}. In order to avoid confusion with energy terms E, the letter Y_{mod} is used instead.

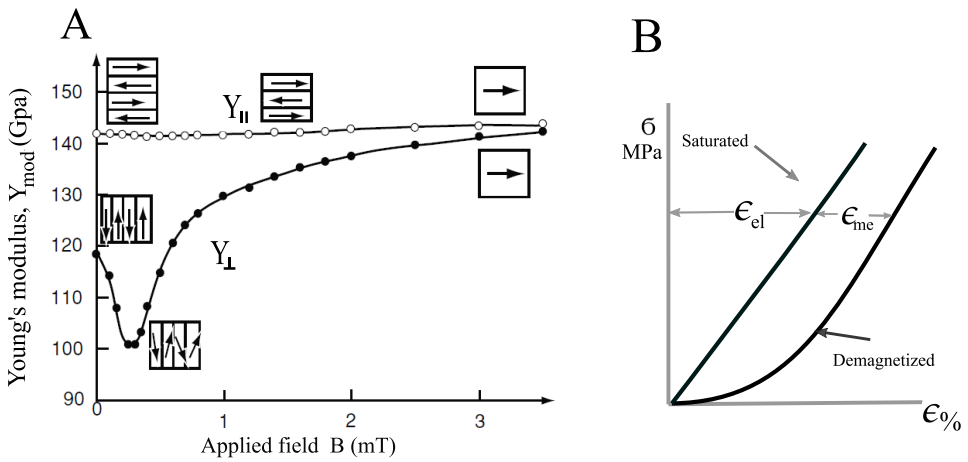

FIGURE 2.12: The uniaxial stress σ gives rise to strain-induced anisotropy. A) Reorientation of the domain along the direction of applied stress. Depending on stress and the sign of λ in the material, Young's modulus evolves differently, [77], reprinted from [47]. B) Displays the contribution of the magnetoelasticity ϵ_{me} to strain, as on demagnetized FM-material two kinds of strain are produced upon stress. The ϵ_{me} is zero in the saturated state because no domain reorientation occurs. In contrast, the demagnetized state in response to a uniaxial pressure deforms differently. The curve differences in the schematic have been exaggerated, redrawn from [49], p. 270.

The elastic energy density for a polycrystalline magnetic material is:

$$E_{elast} = -\lambda_s(\frac{Y_{mod}}{2})(3cos^2\theta - 1)\epsilon + (\frac{1}{2})Y_{mod}\epsilon^2 \quad (2.41) \qquad \text{with} \quad \begin{matrix}\theta \text{ Angle btw. } M \text{ \& } \lambda_s \\ Y_{mod} \text{ Young's modulus}\end{matrix}$$

By taking into account that a material fails at high stresses, which gives an upper limit to the applied stress, it can be determined, if sufficient stress can be applied to a sample in order to induce stress-related effects. For the case of applied pressure, the generated magnetostriction can also be calculated. The minimization of the elastic energy (Eq. 2.41) with respect to strain with $\frac{\partial E_{elast}}{\partial \epsilon} = 0$ gives:

$$\lambda(\theta) = \lambda_s(3cos^2\theta - 1)/2 \qquad \text{see Sec. 2.5} \qquad (2.42)$$

In case of zero stress, the saturated strain is: $\epsilon = \lambda_s$. With $\sigma = \epsilon Y_{mod}$, for an isotropic material, the uniaxial stress energy as follow:

$$E_\sigma = -\frac{\lambda_s\sigma}{2}(3cos^2\theta - 1) \qquad (2.43)$$

and by inserting the uniaxial anisotropy energy of Eq. 2.35, delivers :

$$K_{ani} = \frac{3}{2}\lambda_s\sigma_{ij} \qquad (2.44)$$

From this, the given magnetostriction of iron can be calculated to generate a pressure of 1.4 Mpa [47][34].

[34] If no stress is applied, with $\lambda_s \approx 7 \cdot 10^6$ and $E \approx 200$ GPa.

2.5 Secondary ferroic effects

According to the classification of Newnham and Cross, the continuous changes of the physical effects at a phase transition belong to a second-order transition [78]. The 2^{nd} line of the partial derivative in equation 2.25 of H_i and E_i, respectively, leads to the following equations:

$$\begin{aligned} (i) \qquad P_i^{ME} &= \left(\frac{\partial F}{\partial E_i}\right) = P_i^s + \varepsilon_0 \chi_{ij}^e E_j + \alpha_{ij} H_j + ... \\ (ii) \qquad \mu_0 M_i^{ME} &= \left(\frac{\partial F}{\partial H_i}\right) = M_i^s + \chi_{ij}^m H_j + \alpha_{ji} E_j + .. \end{aligned} \tag{2.45}$$

2.5.1 Electric and magnetic susceptibility

Here, the 2^{nd} terms on the right of Eq. 2.45 (i) and (ii) are the susceptibilities, as introduced in Sec. 2.1.1.

$$(i) \qquad P_i = \varepsilon_0 \chi_{ij}^e E_j \quad \text{and} \quad (ii) \qquad M_i = \mu_0 \chi_{ij}^m H_j \tag{2.46}$$

Electric susceptibility χ_{ij}^e, is a second-rank tensor of the dielectric susceptibility. It describes the ability of a substance to be polarized by an external electric field. It is also the linear term added to the hysteresis curve of the spontaneous polarization, see Sec. 2.7. The *relative dielectric constant* ε_{ij}^r establishes a direct connection between the induced electric field E and electric flux density. In this case, the electric flux density is induced by a surface-charge density, which is given by a dielectric displacement vector, $\mathbf{D}$. The relation is: $\chi_{ij}^e = \varepsilon_{ij}^r - \delta_{ij}$[35], and with equations 2.11 and 2.46(i), it leads to:

$$D_i = \varepsilon_0 \varepsilon_{ij}^r E_j = \varepsilon_{ij} E_j \tag{2.47}$$

In practice, the relative dielectric constant of a material, $\mathcal{K}_{ij} = \varepsilon_{ij}/\varepsilon_0$ is a more commonly used term than the term dielectric permittivity.

In the case when a dielectric material is exposed to an alternating electric field $E(t) = E_0 cos(\omega t)$, with frequency f, $\omega = 2\pi f$, it is expected that the electric flux density Eq. 2.47 will be time-dependent. Due to the inertia of the charge carriers involved in the polarization process, a frequency-dependent phase shift $\phi(\omega)$ may occur:

$$\begin{aligned} (i) \qquad D(\omega, t) &= D_0(\omega) cos(\omega t - \phi(\omega)) \\ (ii) \qquad &= \underbrace{D_0(\omega) cos\phi(\omega)}_{\varepsilon_1(\omega) E_0} cos(\omega t) + \underbrace{D_0(\omega) sin\phi(\omega)}_{\varepsilon_2(\omega) E_0} sin(\omega t) \end{aligned} \tag{2.48}$$

In Eq. 2.48 two dielectric constant terms ε_1 and ε_2 are introduced. The first term of the electrical flux density oscillates in phase with the electric field and a 2^{nd}one is shifted by a phase of $90°$. This can be summarized in the complex representation: $\varepsilon(\omega) = \varepsilon_1(\omega) + i\varepsilon_2(\omega)$.

The real part of the dielectric constant describes the strength of the charge movements, while the imaginary part is a measure of the dielectric losses. The frequency-dependent

[35] Kronecker's symbol, which $\delta_{ij} = 1$ for $i = j$ otherwise zero.

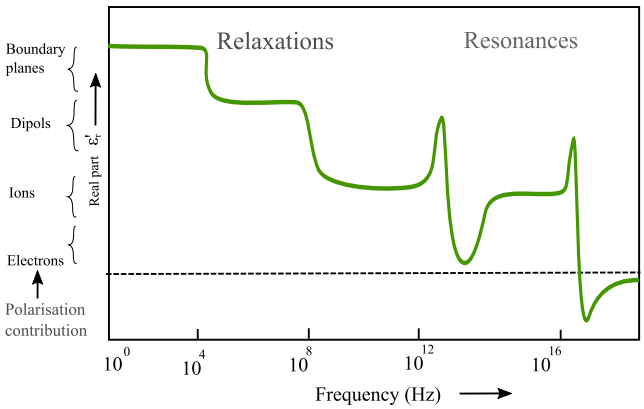

FIGURE 2.13: Frequency-dependent contributions to the polarization of the dielectric function $\varepsilon_1(\omega)$, redrawn from [79]. In the relaxation regime, the boundary planes and the dipole, coming from molecules, are contributing to total polarization. At resonance, the ionic contribution arising from the displacement of a charged ion and the electronic contribution, arising from the displacement of the electrons relative to the nucleus, are contributing to the polarization.

complex term is related to the ability of the charge carriers to follow an external alternating electric field, E_{ac}.

The processes contributing to macroscopic polarization as a function of E_{ac} gradually disappear up to 10 MHz. Here, electrons oscillate with E_{ac} relative to the atomic nucleus. A permanent microscopic dipole vanishes as ions are not shifting out of their equilibrium position, given the high frequency, see Sec. 2.13.

Magnetic susceptibility: There are several contributions to magnetic susceptibility χ^m_{ij}. They include diamagnetism, Pauli paramagnetism, and Van Vleck's paramagnetism. In paramagnetic compounds, the magnetic moment only aligns with the magnetic field in a preferred direction, which leads to a macroscopic magnetization in this direction. The Curie-Weiss law describes the resulting paramagnetic susceptibility. Its treatment goes beyond the scope of the topic. It is considered in more detail in the literature [47].

2.5.2 Linear magnetoelectric effect

The terms in the 3^{rd} line of Eq. 2.25 and in the free energy function link the electric and magnetic polarizabilities of the Materials. These can be interpreted as the second-order magnetoelectric coupling "susceptibility", which is also referred to as the *linear magnetoelectric* coupling tensor α_{ij} [36]. It is the cross-coupling property of the phases in magnetoelectric materials caused by each respective field. Therefore, it is associated with the induction of polarization by a magnetic field, or of magnetization by an electric field [17]. It is designated as being linear since the magnetoelectric cross-coupling responds in a linear a fashion. The magnitude of the cross-coupling effect is limited in materials with intrinsic coupling by:

$$\alpha_{ij} < \chi^e_{ii}\chi^m_{jj} \approx \varepsilon_{ii}\mu_{jj} \tag{2.49}$$

By using the concept of composite multiferroics magnetoelectric coupling, Sec. 2.6.3, it is possible to overcome this limitation. The coupling takes place mechanically at the interface between the phases, as the two are not intrinsically coupled [35]. As a consequence, the effect is related to the effective interaction between the order parameters that originate in each phase.

2.6 Multiferroics

As introduced in the previous sections, magnetic ordering is governed by the exchange interaction of the electron spins. In contrast, the ferroelectric ordering is driven by the

redistribution of charge density inside the crystal unit cell. Therefore, the coexistence of spontaneous magnetic moments and polarization does not contradict the general criteria for the appearance of ferromagnetism and ferroelectricity [80]. The possibility of such an effect in materials with a magnetic structure was first pointed out by Landau and Lifshitz.

2.6.1 A brief historical review

However, long before that, in 1894, Pierre Curie based on symmetry considerations predicted magnetoelectric coupling phenomena. Despite this, it took 60 years until the effect was observed in antiferromagnetic Cr_2O_3, as it was predicted by Dzyaloshinskii [81], and measured by *Astrov* [82]. He measured the electric-field-induced magnetization change, ME_{InD}; $M_i = \alpha_{ki}E_k$, while *Folen* [83] measured the magnetic-field-induced Polarization, ME_D; $P_i = \alpha_{ki}H_i$. Since then, Cr_2O_3 belongs to one of the most intensively investigated and well understood single-phase magnetoelectric [82]. The initial early-stage works on this topic are summarized by O'Dell [84]. The modern understanding of multiferroics is based on Hans Schmid's definition where crystals with " two or more of the *primary ferroic* properties united in the *same phase*" (1994) [33].

After its discovery, interest in the research of magnetoelectrics has decreased as scientists have encountered difficulties in developing useful applications. Primarily, due to the limited choice of compounds with the coexistence of ferri/ferromagnetic and ferroelectric properties that show reasonable coupling at room temperature. Moreover, the poor understanding of the microscopic sources of ME behaviour was another reason for the decline of research activity over the last two decades [17].

The new enthusiasm for the multiferroic research field was triggered by the concept *"pseudo Multiferroics",* a product property[36] of magnetoelectric multiferroics. This was supported by progress in theoretical understanding and modelling strategies, enabled by high computation power. In addition, on the experimental side, advances in novel instrumentation techniques for probing and preparation of thin films, which allow tailored properties, boosted further interest.

Van Suchtelen [85] proposed the concept of a product property in 1972. It suggests that the coupling between two *elastically sensitive* phases of magnetostrictive, and piezostrictive constituents, should be combined in a single composite material. The synthesis is carried out in particulate composite fashion by combining mixtures of a microscale magnetic and ferroelectric powders, which are sintered together as ceramics. Based on this idea, over the following years at the Philips research laboratory, many experiments were conducted, which will be considered in more detail in the following sections [86–88].

By harnessing this new concept, it was no longer impossible to overcome the lack of degrees of freedom with regard to the tuning and optimization of ME behaviour, which was previously the issue in single-phase materials. Furthermore, this inspired scientists to increase the sensitivity of the constituents in each phase by doping [69] and preparing layers [89] with the doctor-blade method. In particular, the opportunity to use thin films opened the possibility of further tailorings, such as epitaxial growth, which allows stress to be induced via lattice mismatch of the two constituents [90–92].

2.6.2 Composite Multiferroics:

Undoubtedly, intrinsic multiferroic properties bring more richness to scientific research since they link two ordered states and the mechanism leads to a direct interaction between the magnetic and electric order parameters. Moreover, it would be useful for applications since it is *not a dynamic effect*, as the change in crystal by any bias field would induce a

[36] product property refers to effects which are present in the composite, but in none of its compounds.

change in others, whilst being kept dynamically activated. Further details and mechanisms regarding intrinsic interactions are discussed in the following reviews [33, 80, 93–95]

Currently, the vast majority of work on multiferroics is being conducted on composites. It is primarily due to their enhanced ME-coupling coefficient, as they don't need to follow the reciprocity relations that limit single-phase multiferroics, Sec. 2.5.2, Eq. 2.49. The origin of magnetoelectric coupling in composites lies at the *interface* between the magnetic and ferroelectric phases. The theoretical physics behind it is considered as clearly separated since mechanical concepts are involved. In addition, the properties of each phase can be studied beforehand without taking cross-coupling effects into account. Such an approach also offers broader design flexibility and gives many opportunities for material engineering. This allows devices to be developed for magnetoelectric transducers, actuators, and sensors [12].

The details of the coupling mechanism in the composite can be challenging to quantify as the magneto-electric coupling encompasses the study of magnetically (electrically) induced inversion or rotation of a ferroelectric (ferromagnetic) *domain* polarization (magnetization). For composite materials, different approaches have been established, an overview of the established different physical mechanisms for magnetoelectric coupling so far are:

1. ***Strain mediated elastic coupling*** happens at the interface, where the magnetic and electric order couple with each other via strain caused by piezo-, electro-, and magnetostrictive [37] effects. This can be accomplished with different connectivity schemes, where detailed descriptions of this can be found in the next section.

2. **The exchange bias coupling** between the antiferromagnetic, ferroelectric and ferromagnetic components of the composite. With improvements in the controlled growth of multilayer systems through epitaxy and self-assembly, such effects became more accessible [35]. The coupling in these systems takes place between the electric order and the antiferromagnetic spin configuration. The mechanism offers the possibility of controlling the magnetic properties of the ferromagnetic layer through the exchange anisotropy effect [96].

3. **Charge-mediated or correlated effect:** The magnetic state of specific systems is related to the presence of charge. Mainly this is the case in strongly correlated oxides. For the case of multiferroics, the charge-related sensitivity of the magnetic state is exploited. As a consequence of this, an applied voltage can modulate the charges in the heterostructure composite by introducing these through the ferroelectric gate oxide. This is possible since the polarization state of the ferroelectric delivers an enormous number of charges into the system [35].

4. **Other multiferroic multifunctional behavior:** The charge transport properties in multiferroic heterostructures deliver in addition to magnetoelectric coupling another tunnelling magneto-resistance phenomena. The dependency of charge transport on the electric and magnetic field control would suggest new possibilities to control charge transport and is attractive from an applied physics point of view.

2.6.3 Strain-mediated composite multiferroics

From the above discussed-mechanisms used to understand ME coupling, only strain mediated coupling is relevant for the scope of this thesis. The concept of a product property [85] suggests that the strain induces deformation in the *crystal*. This can be induced either in

[37] Ferrite used in ME composites are not piezomagnetic, in a pseudo-piezomagnetic fashion.

the magnetic phase through the converse piezoelectric effect, or in the ferroelectric phase through magnetostriction.

$$\mathbf{ME}_{effect} = \frac{electrical}{mechanical} \times \frac{mechanical}{magnetic} \tag{2.50}$$

By recalling the constitutive equations Eqs. 2.18, 2.21, and 2.19 from Sec. 2.1.2, the above relation for the magnetoelectro-mechanical response can be written as a linear approximation using direct notation of the tensors, in accordance with Nan *et al.* [97] as:

$$\begin{aligned} \sigma &= \mathbb{c}\epsilon - \mathbb{d}^T\mathbf{E} - \mathbb{q}^T\mathbf{H} \\ \mathbf{D} &= \mathbb{d}\epsilon + \varepsilon\mathbf{E} + \alpha_{ME}\mathbf{H} \\ \mathbf{B} &= \mathbb{q}\epsilon + \alpha_{ME}^T\mathbf{E} + \mu\mathbf{H} \end{aligned} \qquad \begin{array}{l} \text{Rank of} \\ \text{tensors, its} \\ \text{(corresp. mats.)} \end{array} \qquad \begin{array}{r} \mathbb{c} - 4(6x6), \mathbb{d} - 3(3x6), \mathbb{q} - 3(3x6) \\ \varepsilon - 2(3x3), \alpha - 2(3x3), \mu - 2(3x3) \end{array} \tag{2.51}$$

In order to attain a satisfactory solution for the constitutive equation of ME-coupling, six different variables are at least required. The variables are attributed to the constituents, which are the magnetic, electrical, and mechanical properties. [38].

The Green's function technique, developed by Nan *el at*, is used to solve Eq. 2.51. As a consequence, for the calculation of the effective constitutive coupling ME-coefficient α^* a mean-field approach is adopted. To this end, the properties for σ, ϵ, $\mathbb{d}$, $\mathbf{E}$, $\mathbf{B}$, $\mathbf{H}$ are approximated by their average values. A further advanced approach takes the linear and nonlinear contributions to the equation (Eq. 2.51) into account [98]. The magnetostriction as in ferrites is a nonlinear magneto-mechanical effect($\propto \mathbf{H}^2$) [99], unlike in piezoelectricity, which is a linear electromechanical effect $\propto \mathbf{E}$.

The coupling parameter k [100] is a more useful parameter, which was added to the calculation of heterostructures ($2-2$ connectivity), as it also takes the interface properties of the two constituents into account. It involves the transverse in-plane bulk modulus and transverse shear modulus. This parameter improves the model by Harshe *et al.* [30], as the coupling parameter gives the degree to which the deformation from the constituent layer transfers into another layer by considering a correction for the intrinsic deformation. The parameter k reveals which combination of piezoelectric and magnetostrictive material would have the most promising coupling [101], see Table 2.2. As a result, the overall ME properties can be tailored by choosing suitable materials for both phases [102].

The k parameter enables the formulation of a simple formula for the measurement of the product property, Eq. 2.50, which can be used to determine the coupling coefficient experimentally. For a bilayer, the amplitude of the voltage (V_{ac}) is given as the measurement the effective magnetoelectroelastic moduli of multiferroic composite and it is known as a direct effect (V/m)/(A/m). When a magnetic excitation field (H_{ac}) is applied, a change in polarization would be detected:

$$\frac{\partial E}{\partial H} = \alpha_{ME} = \left(\frac{\partial P}{\partial H \frac{1}{\varepsilon_0 \varepsilon_r}}\right)_{eff} = \left(\frac{\mathbb{d}}{\varepsilon_0 \varepsilon_r}\, k\, \mathbb{q}\right)_{eff} \tag{2.52}$$

[38] As reminder to the notation: σ stress, $\mathbb{c}$ stiffness, ϵ strain, $\mathbb{d}$ piezoelectric and $\mathbb{q}$ piezomagnetic coefficients, $\mathbf{E}$ electric and $\mathbf{H}$ magnetic field, $\mathbf{D}$ electric displacement, ε dielectric constant, α_{ME} ME-coefficient and μ magnetic permeability.

In pursuit of high ME coupling in composites

In addition to the coupling parameter k, the optimization of the volume ratio of the two phases and their connectivity schemes give further possibilities to improve their ME-coupling. According to Newham et al. [103], various connectivity schemes can be used to achieve interface coupling in bulk composites, Fig 2.15. Correspondingly, the micro-geometric arrangement of the constituent *affects* the magnitude of ME response. The $0-3$–type, which is a particulate composite system, is easy to prepare. In this connectivity scheme, a particle phase (ferrite) is embedded in the matrix of another phase (piezoelectric). The $2-2$–type is formed by laminated composites layers, consisting of piezoelectric and magnetic phases, and the 13–type composites are rods (ferrite) embedded in the matrix of the piezoelectric phase.

Particulate Composites

A straightforward method for the engineering of particulate composite multiferroics is based on the solid-state reaction route[39]. In a subsequent step, the standard ceramic production methods are used, as the mixed oxide powders are sintered, and magneto-electric composite ceramics pellets are produced. The solid-state reaction method is simple, in contrast to the sol-gel processing method (Appendix A.2), where the number of possible parameters contributing to the ME-coupling during the synthesis is high. Consequently, the method is error-prone as it involves a lot of randomness fluctuations in the parameters of each step, Sec. 3.2.

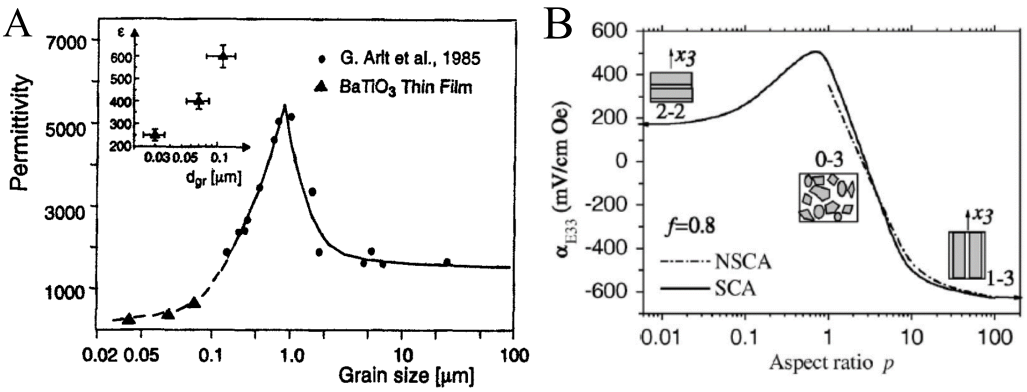

FIGURE 2.14: Two of many contributing factors in engineering of ME-composites. A) Grain size dependency of permittivity in BTO ceramics [104], and the polycrystalline thin film of different grain size [105]. B) Theoretical maximum magnetoelectric coupling coefficient of the composites for different connectivity.

From the point of view of engineering the functionality of such a composite, a larger interface would result in a higher exchange of strain/stress between the phases, as is the case for $0-3$ particulate composite ceramics, Fig. 2.15, [97].

In this regard, theoretical calculations predict a higher ME response for 0-3-particulate composite ceramics compared to composites with different connectivity, Fig. 2.14. The experimental values for 0-3 are in contrast to their theoretical values, which are discussed in Chap. .3 and Chap.5.

The experimental realization of the $0-3$ composites suffer from several pitfalls that yield α_E values, which are two to three orders of magnitude smaller than the theoretical

[39] Technical details on synthesis based on solid-state reaction are covered in, Sec. 3.1.1, its discussion and its modification scope are covered in Sec. 5.1.

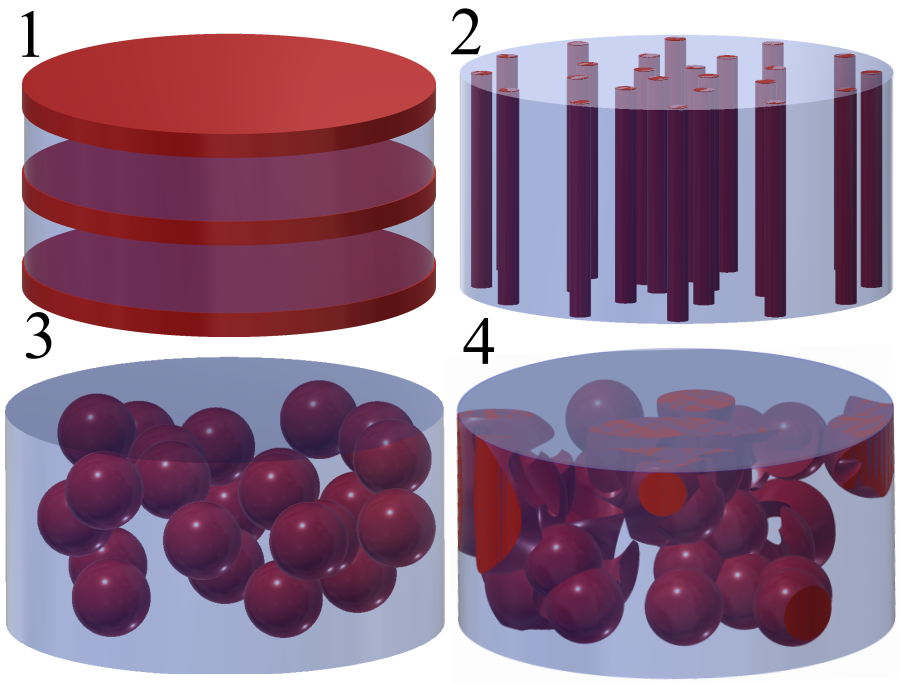

FIGURE 2.15: Diagrams of possible connectivity schemes for multiferroic composite structures. 1) Depicts a 2-2 connectivity scheme of laminated multi-layer structure [100, 106, 107]. 2) Represents a multiferroic composite pilar structure [108]. 3) Homogeneous mixture of electric and magnetic phases. The composite made of magnetostrictive particles is mixed in a matrix, simulation of this case is presented in Fig. 5.7. (4) Agglomerated magnetic phase that would lead to the percolation of electric current in the multiferroic composite. This combined with pores is the most realistic scenario, Fig. 5.7, which contradicts the theoretical calculation in 2.14B.

prediction for the ME-coupling. These pitfalls include as the particle size decreases, the degree of tetragonality in BTO decreases as well. Since, below a critical size ($0.3\mu m$), the particles tend to be in the cubic phase, the dielectric permittivity almost vanishes in this case, see Fig. 2.14, [114, 115]. The electric energy of the tetragonal phase in small particles is large enough to destabilize the tetragonal phase in favour of the cubic phase [116].

In general, an awareness of the limiting factors affecting the ME coupling coefficient is essential for improving the high ME-coupling. In addition to the choice of material for each phase, the following parameters need to be specified:

TABLE 2.1: Specification of relevant aspects for high ME-coupling that need to be taken into account.

Aspect	Implication and Conditions
• Chemical stability	Acquiring the right sintering parameters to avoid a chemical reaction, that could form parasitic phases at the interface, e.g. $BaFe_{12}O_{19}$ from BTO and CFO [86, 87].
• Sintering	The effect of sintering temperature (T_s) and time (t_s) and in particular, the cooling rate, and sometimes the ambient oxygen partial pressure have to be controlled [109–111], Fig. 3.1.
• Thermal expansion / shrinkage	The mismatch between the phases during high sintering temperature T_s causes cracks and pores. A low cooling rate would improve quality.
• Dispersion of magnetic phase	While applying the electric field on the sample (e.g., poling), it is required to avoid percolation due to the low resistivity of the magnetic phase.
• Grain size	The effect particle size has to be identified. Each phase requires a different size for a large ME coupling in the composite. E.g. nano-size of magnetic particles hinders percolation [112]. Or the effect of ferroelectric particle size on the dielectric constant, Fig. 2.14.
• Crystallinity	Crystalline quality of the ceramic powders (XRD data in Sec. 5.2, Fig. 5.1) has to be verified.
• mechanical contact	The choice of constituents can be optimized by considering the coupling parameter k between the piezoelectric and the magnetostrictive phases [113].

A good principle for reaching high coupling is to optimize the room temperature performance of the parameters, d_{33},q_{33}, and the resonance frequency of each phase independently [16].

2.6.4 Choice of materials

In addition to the specifications highlighted in Table 2.1, the choice of material is essential, if a high ME-coupling is to be achieved. Gains in the strength of the magnetoelectric coupling can be achieved by choosing the suitable magnetic and piezoelectric materials.

On the magnetic side, the ferrites, from the family of spinels, are considered as the most promising ones. Not only due to their relatively high electric resistance but also because of being magnetostrictive. Using a soft magnetic (nickel ferrite) nanocrystalline with a low coercive

Piezoelelctric phase	Magnetic phase
$BaTiO_3$(BTO)	$NiFe_2O_4$ (NFO)
$PbZr_xTi_{1-x}O_3$ (PZT)	$CoFe_2O_4$(CFO)
$PbTiO_3$ (PTO)	Yttrium iron garnet(YIG)
Pb(Mg,Nb)O_3 (PMN)	Li, Mn, Cu ferrite
(Sr, Ba)Nb_2O_5	(La, Ca/Sr)MnO_3

TABLE 2.2: Any combination of piezoelectric and magnetostrictive materials are possible [35].

field, high relative permeability, and high saturation magnetization is preferred.

From the engineering point of view, their stability with regard to chemical, thermal, and structural properties makes them suitable to be incorporated in composites together with a piezoelectric material, see Table 2.2. Piezoelectric perovskite, in particular the ferroelectrics, possess similar stable properties. Some representative compounds are presented in Table 2.2.

Another critical aspect of acquiring an excellent coupling is to consider that each phase is independently optimized with regard to its coupling parameters. This contributes to the coupling (d_{33},q) and room temperature performance, as their composite product cannot be varied afterwards.

Following on from the stress mediation concept, elastic coupling losses at the interface between the constituents of choice should be as low as possible. A critical factor in this respect is the comparability of Young's moduli in each phase, see Table 5.1.

Aside from this, a high field sensitivity at a low field for each phase enhances the coupling. For instance, the PZT-CFO composite shows a weak ME-coupling despite the high magnetostriction of the CFO phase because it has a relatively high Young's modulus. In comparison, the combination PZT-NFO exhibits a higher ME-coupling due to its "softer" magneto-mechanical properties, despite having low magnetostriction [69]. In addition to the high field coupling of a ferroelectric with its d_{33} coefficient, its dielectric property is also decisive for the figure of merit of the ME-coupling in the ferroelectric phase [117].

$BaTiO_3$: In 1946, Wul [118] reported that barium titanate (BTO) ceramics exhibit a high dielectric polarization which varies strongly with temperature and peaks with a high maximum value. Its phase transition behaviour on the crystal lattice level has been discussed in Sec. 2.3.2. As this material is a piezoelectric with ferroelectric character, it is suitable for use as a constituent of magnetoelectric composites. It is a member of the perovskite crystal group and has the general formula ABO_3. Its conventional cell is a face-centred cubic (fcc) structure, consisting of an oxygen octahedra (O_3). The *covalent* bonding in perovskites between B and A originates from the easily ionized A atom electrons. Consequently, A is bonded *ionically* to B and O units. This complex structure enables ferroelectricity and maintains an internal dipole moment, which is associated with displacement, as introduced in 2.3.2 [119]

Ferrites have the composition AB_2O_4. Extensive studies have been made of the Co- and Ni-ferrites. Their inverse spinel unit cell structure is built-up of eight face-centred cubes of oxygen, and each cube has eight tetrahedral (A) and four octahedral (B) cations, with Co^{2+} ions, occupying octahedral sites (B sites) and the Fe^{3+} ions on both tetrahedral (A sites) and octahedral sites, see Fig. 2.16. This corresponds to a cubic crystal structure with oxide anions arranged in a cubic close-packed lattice. For its synthesis, many methods are used, e.g. thermal decomposition and co-precipitation techniques [120], hydrothermal method, microwave calcination, as well as sol-gel processes. For the case of ferrite-based magnetoelectric composites those containing CFO and NFO are interesting. They combine a relatively high electrical resistivity of the ferrimagnet, despite being a magnetic material, with a piezomagnetic coefficient q, which provide a high magnetostriction. This can be tuned further to a higher sensitivity with the use of Cu, Zn, and Cr substitutions, which are added in order to increase the electrical resistivity [109]. With regard to the mechanical characterization of its magnetic properties, its mechanical stiffness allows the measurement of its magnetic response by uniaxial stress without risk of fracturing at low stress, see Fig. 5.8.

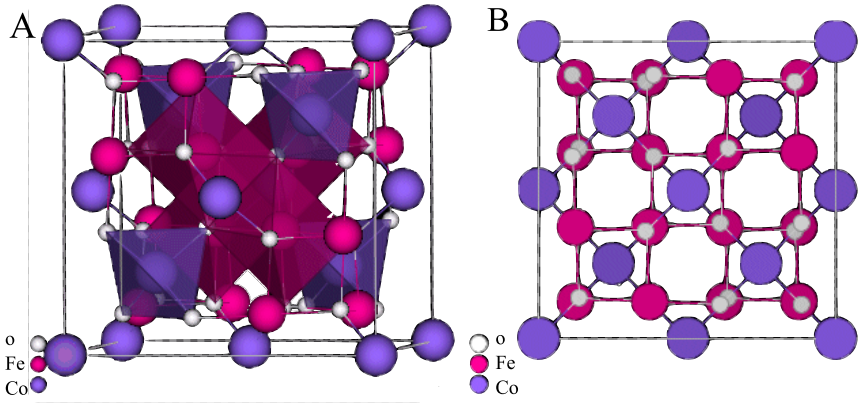

FIGURE 2.16: A)3D view of spinel AB_2O_4 structure unit cell B) projection along [001]. Figures are illustrated with ⇒JCrystalSoft.
A Software for Crystallography.

The grain size of ferrites determines the magnetization saturation and permittivity. The grain size of the sintered ceramic also influences its resistivity. By reducing the particle sizes, more grain boundaries are created, which increases the resistivity.

3

Materials and Characterization Methods

This chapter is divided into two main sections. The first one focuses on the sample preparation techniques and the ideas behind the evolved approaches in the work used for the solid state powder preparation involving *different powder size mixture and successive adding*. The second section is dedicated to the standard characterization methods and instruments used to identify the sample morphology and structure. Furthermore, it covers the response of magneto-electric composites to a single field and cross-field coupling effects.

3.1 Requirement specification for composite ceramic

The synthesis of suitable magnetoelectric samples is required in order to prove the functional principles of the developed setups (Fig. 4.3). For the measurement of its mechanical performance in a multi-field environment. This needs a dense composite ceramic that can sustain large tensile stress without cracking and the enhanced coupling between the phases. Therefore, a new approach is required to obtain a denser and high-quality (= higher stiffness) composite[1]. For this purpose, enhanced mechanical stability can be achieved in 0-3 connectivity by using a matrix phase of large ferroelectric grains [111, 122], see Sec. 2.14, including embedded CFO nanoparticles. The choice of a CFO-BTO composite is primarily based on the chemical stability of both phases during 0-3 connectivity sintering, and their enhanced mechanical endurance under stress.

The high loss rate of samples during preparation and poling, uniaxial stress-dependent characterization of the strain, polarization, and stress-dependent ME-effects requires the production of batches with a large number of samples (minimum 10 samples). Therefore, any Therefore, an optimized preparation route, Sec. 3.2, for a large number of samples per batch with high reproducibility is needed. This implies a controllable and standardized routine in order to avoid random variations in the processing route.

In order to standardize the routine, a commercial CFO powder (particle size 40 nm, 98% purity) was purchased (PI-KEM Ltd.). However, the delivered particles were found to be agglomerated, as their sintered SEM image reveals, see Sec. 3.7. Since it is necessary to keep the CFO particle size as small as possible, a ball milling step was applied. This contributes to homogenization of the particle size, remedying agglomeration. Further, in the second step, powders of different sizes were used to keep the agglomeration to a minimum. This step can be seen in the flow chart for the synthesis route Sec. 3.2.

[1] In the range of mechanically suppressing electric polarization [57] or mechanical domain switching [121].

3.1.1 Synthesis

An array of methods are available to prepare materials with functional properties. Four main methods (with some sub-categories) are usually used, these are:

(i) Solid-state reactions, (ii) Film deposition, (iii) Sol-gel method, and (iv) Crystal growth[2].

The method of choice for the synthesis of polycrystalline solids like bulk ceramics is the *solid-state reaction route*. It has the advantage of being relatively simple, scalable, and low cost. The engineering of bulk composite magnetoelectrics consists of the synthesis of microscale and nanoscale mixtures of magnetic and ferroelectric particulate ceramics.

Compositions and powder processing

A central aspect of the synthesis is focused on the engineering of the initial powder in a way that both phases do not suffer from the common issues listed in Table 2.1.

Usually, in the first step, each phase of the magnetoelectric composite is separately synthesized. For this purpose, high purity starting materials are mixed in accordance with their stoichiometric ratio. This is followed by a grinding step using a pestle and mortar. A subsequent ball milling step ensures to obtain close contact among the nanopowder particles with the purpose of large contact between the powders. In a further step, the powders are heated at elevated temperatures for a fixed time (calcined [3]). During the first calcination, CO_2 is liberated from the mixture. Afterward, the powder is sieved using a specific sieve size in order to maintain uniform particle size. However, many steps make the sample preparation error-prone (powder size, phase formation, secondary phases)[4]. Further, the laboratory mixtures were not showing satisfactory results, as visible for the tested sol-gel approach.

Given the fluctuations in the quality of the self-made starting powders (via the sol-gel methode), commercially available final powders of each phase (CFO: PI-KEM Ltd- 98%, BTO: Alfa Aesar) were used. The XRD diffractograms of both commercial BTO and CFO are a good match with the literature values, Sec. 5.1. Commercial powders guarantee a specific range of particle size distribution. With this, the approach of using *different powder size mixtures with a successive adding variety of mixture ratios* as a process method can be applied. The mixing of two different BTO powder sizes allows better powder compaction, as depicted in the flow chart of Sec. 3.2. This is required, as ferroelectric particles with larger sizes possess a better electrostrictive response [104], see Sec. 2.14, and smaller particles would fill the gaps and enclose any possible pores. Consequently, the mixture of different particle sizes, partially 50 - 100 nm and 1-3 μm, significantly contributes to the improvement of the pure BTO phase properties in terms of its resistivity, electrostrictive behaviour, density, and associated mechanical properties. Such improvements have been observed in the measurements of the polarization and strain under uniaxial stress of these samples, see Sec. B.7.

On the other hand, for the magnetic constituent of a magnetoelectric composite, a better coupling is generated if the CFO particle size is between 50-100 nm[5]. Smaller particle sizes would have a higher contact area between the surfaces of the constituents compared to

[2]However, many other routes aside from Sol-Gel (wed chemical method) for powder processing exist. Spark Plasma and Autoclave- methods, etc. are available.

[3]Here carbonates, nitrates, sulfates decompose on heating to yield oxide precursors.

[4]Given this, the desired particle size might not be achieved. Besides that, this first step of the preparation process is time-consuming.

[5]lower than 50 nm decreases the melting point.

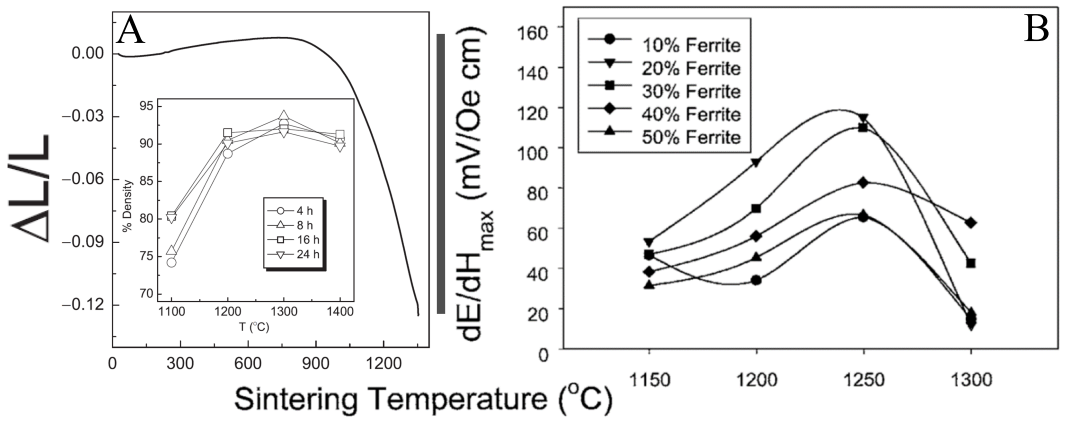

FIGURE 3.1: Literature overview of sintering temperature and time related to ME composite synthesis. A) Magnetostriction dependence on sintering temperature for cobalt ferrite. The inset shows how the sintered density varies as a function of sintering temperature B) Magnetoelectric response voltage coefficient for various ferromagnetic/ferroelectric ratios of the composites as a function of sintering temperature [111]

larger particle sizes, even with the same weight ratios of the initial mixture. The question of obtaining a homogenous distribution of CFO in the BTO matrix with the solid-state route remains unanswered.

Initially, in order to avoid the issue with the agglomeration of the CFO particles, the ansatz was to ensure a core-shell structure composite by using the sol-gel approach (Appendix A.2), however, it failed to meet the requirements, Sec. 3.1.1. An approach to realize the complete coverage of the CFO particle with the BTO phase would be to "mimic" the core-shell structure with the solid-state route. This would involve multiple steps. At the start adding a low CFO content and higher BTO content to the composite would allow distributing of the CFO better in a composite powder, Sec. 3.2. Here, a pre-sintering stage with low CFO content powder mixture ($CFO_{15\%}$-$BTO_{85\%}$ was applied, followed by ball milling at 400 rpm for 4h. The mixture was subsequently pressed uniaxially into a big pellet (⌀25mm) and sintered at 900°C for 4h. Afterward, the pellet was crushed and milled at a low rotational speed of 200 rpm for 1h. This is expected to increase the probability of encapsulating CFO particles inside the BTO.

A second powder mixture with a high content of CFO was produced as well. This had a composition of $CFO_{50\%}$-$BTO_{50\%}$, with the BTO particle size of 50-70nm. This mixture was ball-milled at 400 rpm for 4h. This composition, and the composition with lower CFO content powder, were mixed in accordance with the desired final composition in the last step of the powder preparation.

Technical details

For the preparation of the batches, the same mixing parameters were used. In the powder preparation phase, a ball milling step is applied in order to improve the homogenization of the particle size. The grinding zirconia balls had diverse diameters of 3, 5, and 10 mm, and were used with a weight proportion of 50%, 30%, and 20%, respectively. The weight ratio of the balls to the powder to be milled was $\times 15$. For grinding, a zirconia container with ethanol as the grinding solvent during the milling process was used[6]. After the milling step, the ground powders were dried in a jar together with the zirconia balls. For the separation step afterwards, they were manually shaken to separate them easily from the balls, and then

[6]RETSCH planetary ball mill machine is used, Sec. 3.2.

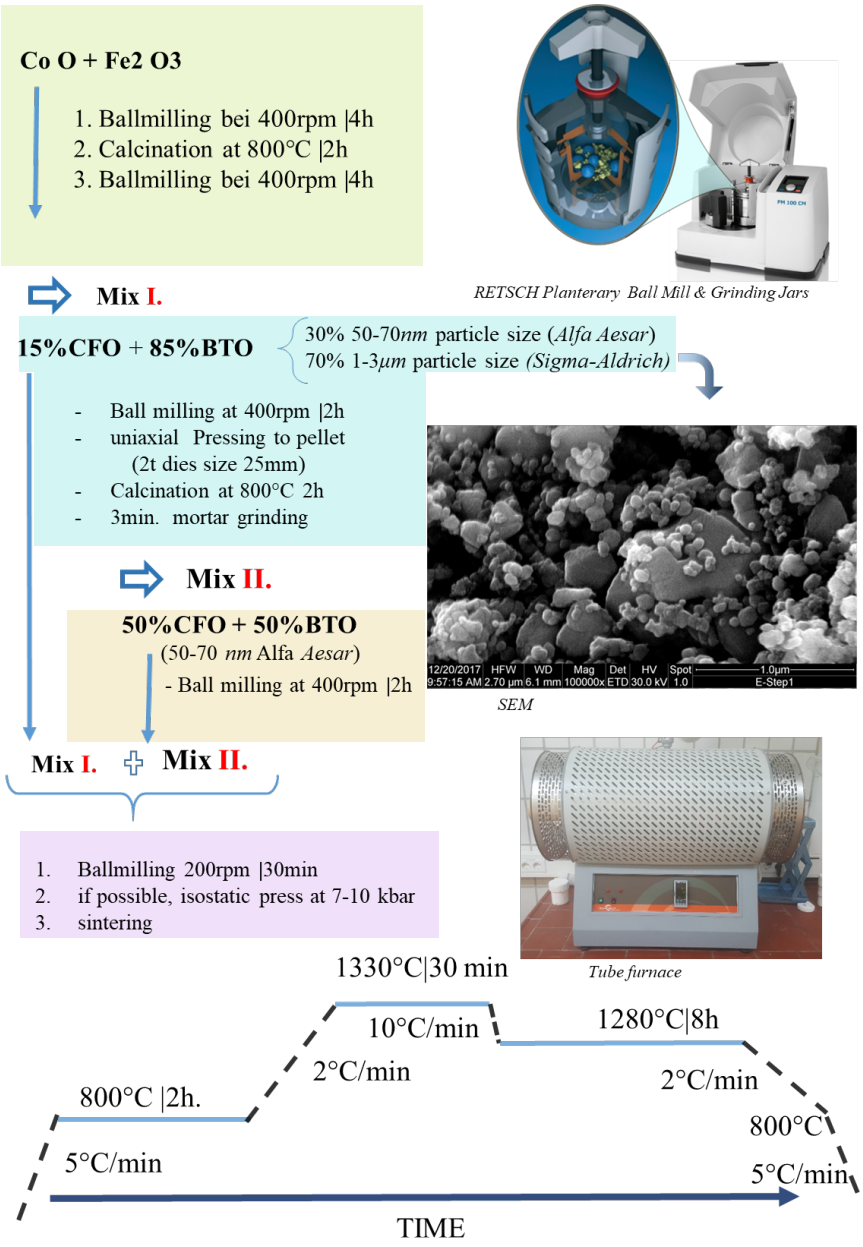

FIGURE 3.2: A heuristic synthesis route developed to mimic the core-shell approach. It involves multiple steps in order to achieve a dense, well distributed magnetic phase with a low percolation threshold. The use of commercially available, high-purity end material minimizes possible errors. Several ball milling steps are used to resolve the agglomeration of the CFO nanoparticles (commercial ones); additionally, the mixing of CFO with BTO powders (consisting of two different particle sizes: - SEM- inset) are processed. The sintering temperature was kept at 1280°C, a trade-off for better mechanical stability in accordance with Sec. 3.1. For a pure phase of BTO, a better result is achieved at 1350°C.

they were mortared in an agate mortar. From the finished BTO-CFO powders, green-body pellets were pressed at 100 MPa in a uniaxial press. In a following step, the green-bodies were sealed in plastic bags and then pressed in a cold isostatic press at 7 kBar.

Sintering

The final properties of magnetoelectric ceramics are partly determined by their porosity, grain size [123, 124], and the existence of secondary phases. Control over the pore-size, or their avoidance, is an important aspect of sample preparation. In some materials, pores are intentionally desired to increase the surface area, such as for catalytic applications. For the performance of magnetoelectric materials, the appearance of pores is undesired. Their existence affects the ME-coupling more than the formation of secondary phases or grain size effects, as pores impede the concept of strain meditation for the ME-effect, as there is no meditation of strain in the vicinity of pores. The study of mechanical properties of ferroic materials reveals the increased likelihood for appearance of cracks if stress is applied or generated. The simulations in Sec. 5.7 demonstrate that micro-cracks show up around pores when the sample is exposed to uniaxial stress fields. Therefore, understanding and analyzing pore formation at the sintering stage is essential for proper composite engineering, as compact ceramic compounds are needed see Sec. 3.3.

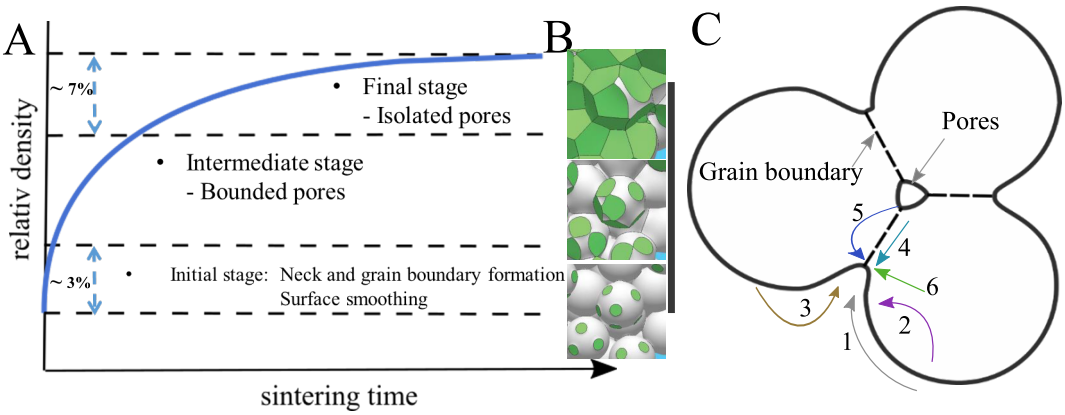

FIGURE 3.3: A) Schematic representation for a green body of the compaction curve dependence on sintering time. It is divided into three sintering stages: initial, intermediate, and final stage. B) Shows the microstructure evolution in simulations, taken from [125]. C) Presentation of the six paths for the mechanisms of mass transport in a simplified Three-Ball Model: Path 1 - Surface Diffusion, Path 2 - Lattice Diffusion from the surface, Path 3 - transport through the gas phase, evaporation, and condensation, Path 4 - grain boundary diffusion, Path 5 - lattice diffusion of the grain boundary, and Path 6 - plastic tiles, redrawn from [126].

The compaction of ceramic occurs in two different stages. The first step involves pressing of the green body in a dry condition as a pellet or desired form[7].

Each stage can influence the final property of the ceramic material. At the powder processing stage, the control parameters are related to, amongst others, the particle size, chemical composition, and powder distribution. In composites, these parameters determine the final morphology, as well as the degree of agglomeration. At the sintering stage, external parameters related to the heating process, exposure time at a specific temperature, atmosphere, pressure, and temperature control (heating and cooling rate) play a decisive role in tuning a particular property.

[7] As slurry, it is referred to as plastic mass, however for scientific purposes, they are pressed in cylindrical shaped dia.

In a second step, *sintering*[8], a process of solidification initiated by heat compaction of the green bodies, takes place. This process forms the grain boundaries while pores are eliminated at temperatures below the melting point, leading to the final densification and macroscopic shrinkage of the green body, see Sec. 3.3. The underlying mechanism behind the compaction is the tendency of the system to reduce its total energy $E = \gamma A$, with $\gamma = \frac{\partial G}{\partial A}$, stating that the free energy G increases as a new surface A is formed. Here, the reduction of interfacial area is accompanied by mass transport, as the system's free energy tries to achieve a thermal equilibrium, which is the driving force behind the compaction process.

Three stages have been identified during the sintering process: initial, intermediate, and final. In the first stage, the distance between sources and sinks determines the densification kinetics during the mass transport in the first stage, see Sec. 3.3A. In this stage, the diffusion mechanism can be altered with particle size and shape. Consequently, there is a more pronounced interfacial diffusion for a higher specific interface area. This diffusion consists of the surface diffusion, grain boundary diffusion through the grain boundaries, and vapour transport, see Fig 3.3C.

The *grain* size distribution also determines the kinetics of grain growth. For a *broad size-distribution*, the diffusion-pressure difference between the smaller and larger grains is higher, leading to the growth of larger grains at the cost of the smaller ones at a faster pace than in the case of narrow size distribution. In light of this, mixing two different particle sizes of BTO achieves higher compaction with comparatively large particle sizes of 1-3 μ, Sec. 3.2. These effects contribute to the sintering of *denser* BTO-CFO composites.

3.1.2 Sample preparation

Sample preparation consists of polishing and grinding. It is a crucial part of this work as uniaxial mechanical stress requires a high degree of planarization and flatness to guarantee homogenous stress on the surface. It is also necessary to measure the sample properties and further process the pellets as a bilayer. Polished cross-sections are needed for SEM (Fig. 5.2), and piezo-force microscopy (PFM, Sec. A.4) surface probing. There needs to be 1μm parallelism and flatness for the polished surface. The sample with a (2-2) laminate connectivity Sec. 2.15C) between piezoelectric and magnetostrictive layers requires a flat surface between the layers in order to achieve enhanced coupling, see Sec. 5.18.

Plane parallelism and flatness The use of a flat grinder is necessary as the samples, due to the sintering process, are slightly deformed. Therefore, a flat surface grinding machine (Gerh10) was re-activated. Herefor, two diamond grinding wheels (grit sizes 90μm and 20μm, *Lach Diamant*) were used.

At the start of the process, the samples were fixed via crystal bond on a flat iron plate, see Sec. 3.4. After grinding both sides plane-parallel, the samples underwent several polishing steps manually in a sequence of grit sizes 15μm, 9μm, 6μm, 3μm, 1μm, and 0.25μm [9].

After mechanical processing, the samples were annealed for thermal edging (30 minutes at 740°C) and slowly cooled to ensure they were completely uncontaminated. This ensures that no internal stresses occur due to the mechanical processing.

The sample preparation for mechanical load measurements requires burning a 10μm thick layer of silver on both sides of the sample in a furnace (450°C, 30min). Subsequently, the surface is cleared with 1000 grit size sandpaper to avoid conductive residues or bumps

[8] For sintering, various other methods are exciting, like Spark Plasma Sintering (SPS), in situ formations of Ceramics by unidirectional solidification, as a eutectic liquid of the phases [87], are existing too.

[9] Depending on the experiment, as under mechanical load, where sliver past need to be burned, the polishing step can be counterproductive.

that could lead to electrical shorts. The curved edge surfaces were also ground for sample poling.

Poling

of the samples was performed by the process of field cooling. For this purpose, ferroelectric and composites samples were heated on a temperature-controlled hot plate under an applied E-field inside a jar filled with high-temperature resistant silicone oil.

For BTO the temperature was raised to 120°C, for PZT it was 150°C. The respective electric field of 1,5kV/mm^{-1} for BTO and 2.5kV/mm^{-1} for PZT were applied. After heating, the oil bath is cooled within 15 mins to below 45°C, and only then is the electric field withdrawn. Typically, an electric leakage current of 300-400 μA is measured at T_c.

Laminated layers:

A laminated trilayer is made of two magnetostrictive layers, and a single piezoelectric layer (BTO or PZT) sandwiched between them. The bi-layers are comprised of one layer of each phase. The laminate composites were fabricated by bonding layers together using a silver epoxy resin, followed by an annealing step on a hot plate for 60°C under a slightly reduced pressure of 0.1 MPa. The ME-coupling value of laminates depends on these processing parameters, see Sec. 5.18.

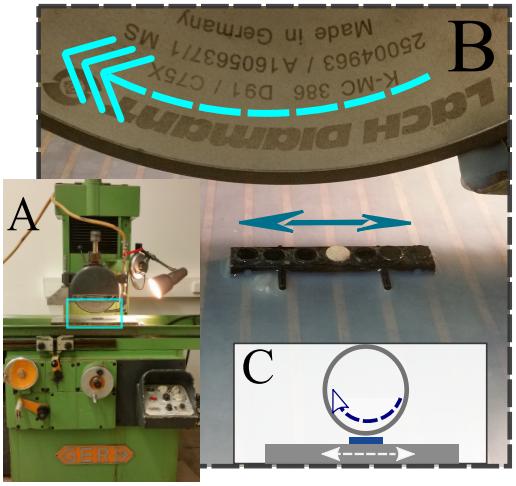

FIGURE 3.4: A) Displays a flat-bed grinder for sample preparation. B) and C) display the direction of the motion for sample and grinding wheel

3.2 Characterization devices

Like many other multiphase materials, magnetoelectric materials also require a broad array of characterization devices in order to specify the full range of their properties. These measurements provide key information as they can help to confirm the existence of a multiferroic phase by detecting at least two co-existing ferroic order states. A typical set of employed experimental characterization techniques would involve microscopy, structural measurements, dielectric/ferroelectric characterization, and magnetic measurements. For advanced characterization, additional measurements as the variation of frequency, temperature, mechanical and external field-dependent conditions might also be required. Typically, such measurements would yield magnetization (M), polarization (P), strain (ϵ), microstructure characteristics, images of ferroic domains (with PFM[10]), crystallographic structure, phase transitions, resonances, and relaxation effects.

Each phase of the CFO-BTO composite requires many characterization steps, which necessitates a limitation on the number of characterization methods used for the mechanical testing and magnetoelectric coupling measurements. Therefore, in this work, a selection of suitable methods for the study of CFO-BTO was made. Several devices will be introduced for the pre-characterization of the precursor materials at the synthesis phase, and some characterization devices for the functional properties of the ceramic sample will be introduced afterword.

[10]Piezo Force Microscopy

3.2.1 Structural Characterization

X-ray diffractometry (XRD) is used at the powder processing and final stage of the synthesis process in order to confirm the crystal structure in materials [127]. As a scattering method, XRD utilizes the periodic structure of crystals to determine whether a material is crystalline or not, regardless of whether the specimen is polycrystalline or a single crystal. Moreover, XRD measurements provide information about the bulk structure as the X-ray penetrates through the crystal. This is possible since the X-ray has a weak interaction cross-section with the solid-state, leading to its large mean free path [128].

The conditions needed to obtain Bragg diffraction underpin the XRD method, Sec. 3.5. It states that an incident plane X-ray wave on the crystal is scattered by its electrons. The high symmetry of the unit cells over the Bravais lattice allows the scattered waves to superimpose constructively. Consequently, the sharply defined geometrical conditions give rise to an intense scattered signal, which provides feedback on its crystalline state. This is mathematically captured in Eq. 3.1:

$$2dsin\theta_B = n\lambda \tag{3.1}$$

where d is the inter-planar spacing θ_B is the Bragg angle, n is the diffraction order and λ wavelength.

From the diffraction patterns, the inter-planar spacings can be determined.

For this, it is essential to know the distance of the reflection points r. There is also the assumption that only small diffraction angles are used.

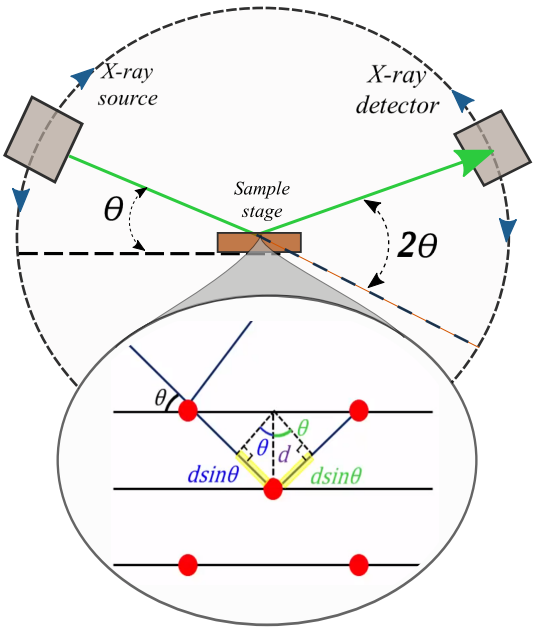

FIGURE 3.5: Schema of the Bragg geometry and its technical realization. Both, the X-ray beam source, and detector are moving from grazing incident angle to higher incident beam angles during the measurement. In the inset an illustration of the condition necessary for diffraction of the X-ray beam.

The diffraction pattern of the diffractograms represents a fingerprint for each material. The positions and intensities of the peaks deliver information about the arrangement of the various atoms within the unit cell. Besides, the relative intensity of the lines gives details about the crystal structure and the symmetries associated with it. Furthermore, the

evaluated information allows further statements about the existence of secondary phases in the material and the percentage of each phase in a composition.

For the analysis of the data, there are many software and visualization tools available[11]. They are connected to reference databases[12], which makes the XRD method an indispensable analysis tool for structural characterization. The measurement data presented in this work was obtained on a *Bruker D8*.

3.2.2 Topographical imaging

In contrast to XRD, which characterizes the bulk crystal structure over a volume and delivers averaged information about long-structural ordering in a crystal, *SEM (Scanning electron microscopy)* as a characterization method delivers only localized real space images. It is used to probe the surface morphology and 2D cross-sectional images of bulk materials as the polishing process provides a cross-sectional cut of the bulk material.

The high spatial resolution of an SEM facilitates the acquisition of an overview of the particle arrangement of the CFO-BTO. It allows the user to see, if the composition is agglomerated. It can deliver the grain size distribution for various compositions, sintering temperatures, and, importantly, the state of porosity. In particular, the latter makes the use of SEM essential and enables a particle size dependency study of the effects to be made. Consequently, it is possible to evaluate the particle morphology at each stage of the syntheses.

The operational principle of an SEM is based on the control and focusing of an electron beam. An SEM is made up of a cathode, anode, and one or two magnetic lenses, which function as condensers, see Sec. 3.6. The cathode generates the electron beam with a beam energy ranging from 2-10 keV. The beam is accelerated through the anode and condensed by a condenser lens.

Furthermore, the condenser aperture beam constricts the beam and focuses it to a very sharp point on the sample, along with an objective lens.

The focused electron beam scans the sample surface and interacts with the material surface. This leads to the emission of electrons from the probed material surface. These are sensed via backscattered and secondary electron detectors and yield information about surface topography and composition. The intensity of the emitted signal determines the brightness of the scanned spot, which is displayed on the screen. Thus, the observed topographical image results from local variations of the electron emission from the surface [127].

The scanned areas are controlled by the joystick manually. The scanning process happens automatically once setting values are entered in the related software.

Energy-Dispersive X-ray Spectrometry (EDX): SEMs often have another integrated option that can be used for chemical analysis which allows, within the limits of its resolution, to identify an elemental of the image. However, for the 0-3 composite, due to the nature of its structure (mixed distribution), the significance of the results obtained with this measurement is limited. Nevertheless, it can identify, if a region is rich in certain elements. Such measures were made on the BTO-CFO samples, see 3.7. The recorded spectra were evaluated with "EDAX Genesis" software.

[11] Fullprof, GSAS, Topas and X'pert.
[12] Crystallography Open Database, FIZ Karlsruhe.

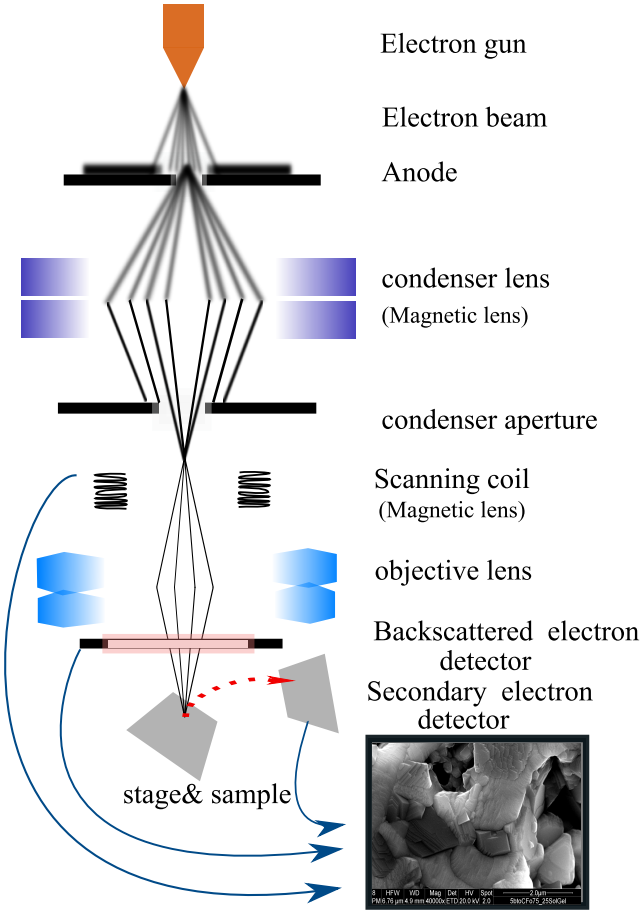

FIGURE 3.6: Illustration of the basic structure of the SEM setup and its operational principle. Inset image: Sol-Gel prepared bulk ceramic, revealing its porosity state and grain size.

3.3 Electrical characterization

In the section on theoretical introduction to ferroelectricity (Sec. 2.3.5) , it was pointed out that the hysterical behavior was a nonlinear response that can be used to reveal the behavior of ferroic materials to applied fields. The switching of domains dictates its shape as the polarisation (P) is reversed by applying an electric field (E). Even though the measurement of the hysteresis is a macroscopic electrical characterization, its evaluation delivers information about the domain behaviour and motion of domain walls as the growth and shrinking of domains takes place. This characterization method and the one used for the dielectric properties are standard techniques. A further section on the design of a customized setup with an integrated interferometry setup will consider the implementation of this technique, see Sec. 4.4.

3.3.1 Ferroelectric hysteresis

Two methods are mostly used to measure the ferroelectric hysteresis: The Sawyer-Tower circuit and the current-voltage method. The current-voltage method[13] [129, 130] is used to measure the static current response to a slow cyclic triangular voltage. For this measurement, the integration is done over time in order to obtain the hysteresis loop.

[13] A low-cost method as a high voltage and high-frequency power source is not needed.

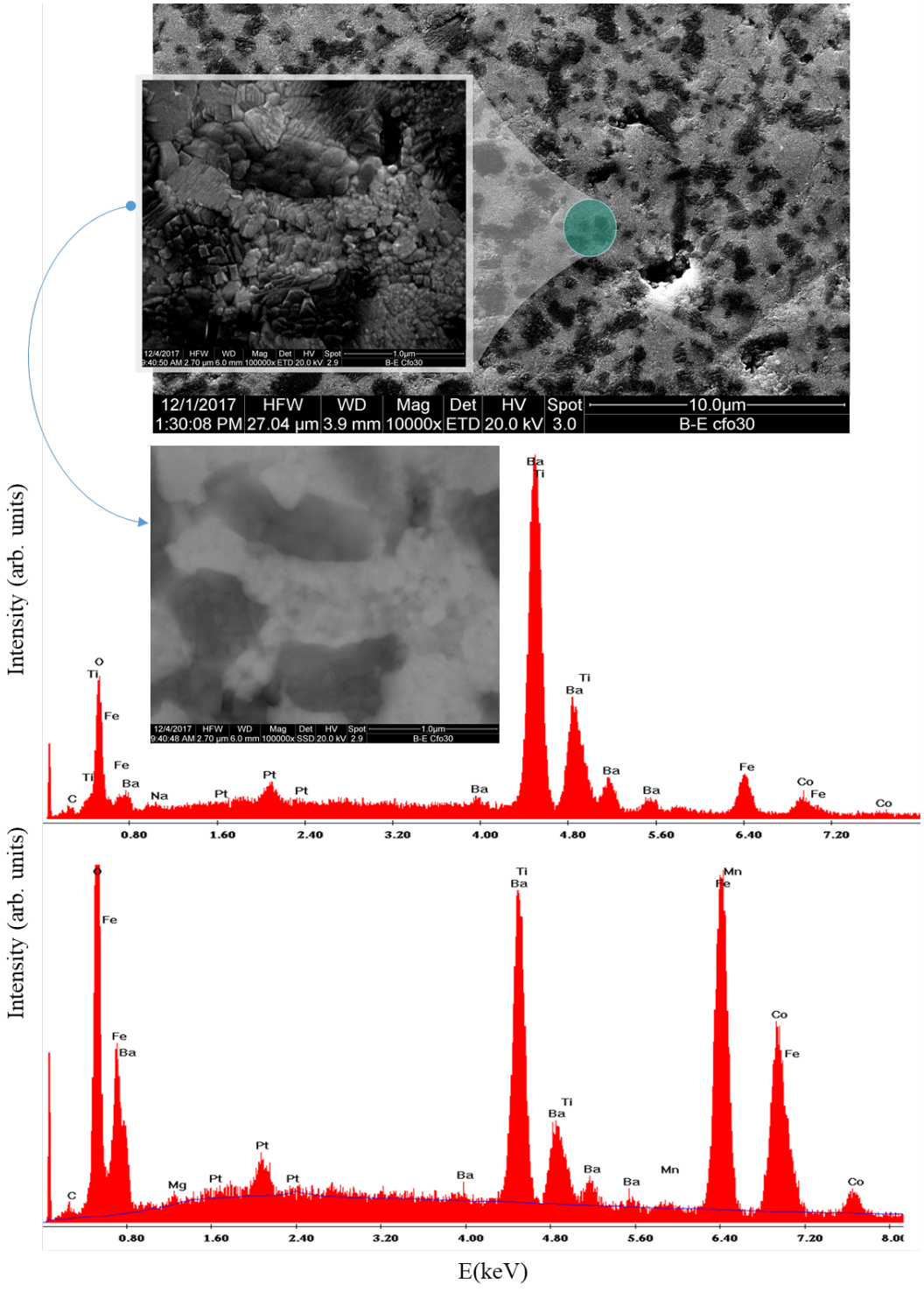

FIGURE 3.7: Comparison of the EDX spectra obtained from particular regions shown within the SEM image of $BTO_{70\%}$-$Cfo_{30\%}$ composite. The sample was prepared via a solid-state route (Fig. 5.1 shows the correspondingg XRD Data. The comparison of the EDX spectra of different sites contrasts with those selected for the EDX examination for the respective phase of the chosen regions.

For the case of leaky samples, a more straightforward method is the Sawyer-Tower circuit [51], and an improved version of it [131]. A Sawyer-Tower circuit is considered a charge-voltage measurement type, as a high ac driving voltage is applied to the sample. The measurement circuit is a capacitance bridge, where the two capacitors in series have the same charge (Q). For measurement, the ferroelectric sample is arranged to be the first capacitor in the circuit. This is followed by a second well-defined larger sensing capacitor, across which the voltage is measured (see Sec. 3.8), which corresponds to the voltage of generated charges on the sample. The polarization (charge per area) is calculated from the relation between the measured voltage on the known capacitor divided by the sample thickness. The polarization (ac-voltage value) is plotted on the y-axis as a function of the driving E-field in order to obtain the hysteresis loop. For its calculation, it is assumed that $\chi = \epsilon$. Therefore, the polarization of a cylindrical sample in poling direction is given by the charge Q and the area A of the sample:

$$P_3 = \frac{Q}{A} \quad \text{and} \quad C_{sample} \cdot V_{sample} = Q = C_{ref} \cdot V_{ref} \quad \Rightarrow \quad P_3 = \frac{C_{ref} \cdot V_{ref}}{A}$$

The given larger reference capacitor ($C_{ref} = 5\mu F$ compared to $C_{sample} = 50nF$) ensures that most of the applied voltage drops over the sample as it has the higher capacitive reactance $\frac{1}{\omega C}$. Due to this, the value of the voltages over the reference is also in the working range of oscilloscope, and it can be measured safely.

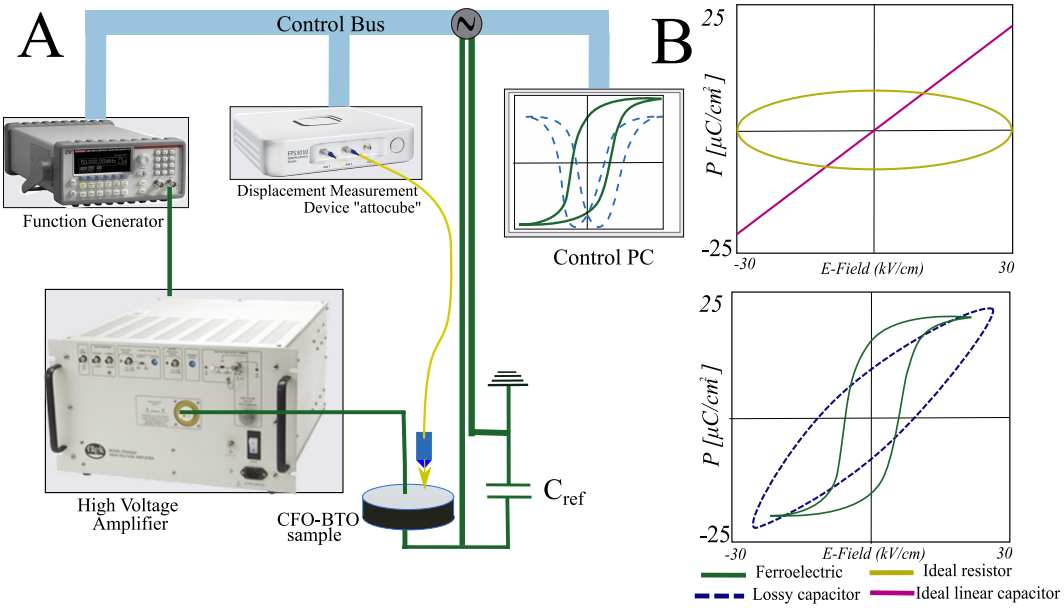

FIGURE 3.8: Schematic of P-E, and S-E loop system in Sawyer-Tower configuration and interferometric sensor integration. B) Displays the material-dependent characteristic behavior in the Sawyer Tower measurement setup.

The Sawyer-Tower method is suitable for this work, as its high ac driving voltage allows the parallel measurement of the correlated strain (ϵ) for a given polarization. The system for performing P-S-E measurements is shown schematically in Sec. 3.8, and further details about the device engineering for parallel strain measurement in constant magnetic fields are presented in Sec. 4.4.2. The Sawyer-Tower circuit for recording P-E and S-E-loops has been further designed to integrate stress as an additional parameter aside from the magnetic field.

Idle time:

As already noted, magnetoelectric materials tend to be leaky. Therefore, when high frequency voltages are applied, the samples heat up due to dielectric losses. This calls for measures to prevent overheating, as temperature influences the hysteresis. Hence, an automation routine was implemented in LabView (Fig. B.8) to adjust the excitation period, Figs. 3.9.

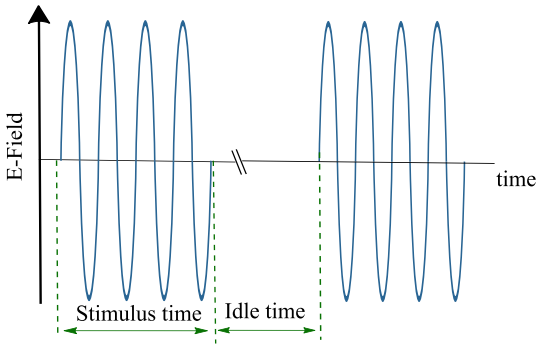

FIGURE 3.9: Idyle time implemented in the control setting of the automation for the excitation period of $E(t)$. The number of cycles and length of idle time can be chosen by the user, see. Fig Appx. B.8

3.3.2 Dielectric measurements

While the hysteresis measurement covers the high voltage excitation behaviour, another aspect of electrical characterization involves the study of the transport mechanism in bulk solids, as introduced in Sec. 2.5.1.

It involves measuring the frequency-dependent signal response of the dielectric measured by impedance spectroscopy [132]. For this purpose, a small, well-defined alternating voltage is applied to the sample, and a sweep over a broad frequency range is performed[14].

The measurement setup consists of a Solarton impedance analyzer, a temperature controller unit, and a chamber. The sample is placed inside the chamber, ensuring a homogeneous temperature distribution and heating and cooling of the sample. By using the Solarton, it is possible to determine the frequency-dependent conductivity $\sigma(\omega)$ and the frequency-dependent electric permittivity $\varepsilon_r(\omega)$ of the sample. From the obtained spectra, one can make conclusions about the long-range mobility of ions in the sample and gain a deeper understanding of the transport mechanisms, comprising of the grains and grain boundary responses, which cause different signal contributions in the ceramic samples.

3.4 Mechanical characterization

The ferroelasticity of the multiferroic magnetoelectric composites mediates the coupling between the ferroelectric and ferromagnetic components (Sec. 2.6.3). This presupposes sensitive elastic properties for the participating constituents. Consequently, mechanical characterization is essential in order to derive the coupling parameter "k", Eq. 2.52.

Standard mechanical characterizations are performed by applying external forces on ferroic samples while the stress-strain hysteresis-curve is recorded. The measured hysteresis describes the effect of mechanical switching between at least two orientation states of domains in crystals [58]. The ferroelastic properties, such as the stiffness value (Young's Modulus) can be determined by stress-strain measurements as it determines their coupling. However, the microscopic coupling origin is established in the crystal and by the chemical binding properties between the atoms inside the unit cell, where other ferroic properties also have their origin.

Depending on the measurement conditions, there are various methods to apply uniaxial stress. One approach is to utilize a piezo-actuator clamped inside a stiff metallic frame. Another approach can be to use a screw inside a fixed frame to apply the stress, as in the case of magnetization measurements under uniaxial stress, pressure cells can be used,

[14]The small excitation is required since the response of the sample needs to be completely linear, reversible, and free of hysteresis. This ensures that only the reversible contribution of permittivity is measured.

Sec.4.5.1. However, for this work, primarily a universal spindle based testing machine is used.

3.4.1 Ferroelastic hysteresis

Defining measurement condition: Similar to electrical excitation, the mechanical loading of a ferroic sample can cause a highly non-Hookian strain curve, yielding ferroelastic hysteresis, see Sec. 2.10 and 5.6. Unlike electrical excitation, a compression test is regarded as a constant stress experiment, given the propagation speed. The deformation response to the stress field takes time since the strain propagates at a speed similar to the sound speed [25].

Furthermore, an understanding of ferroelasticity can be obtained by varying the stress cycle of the stress-strain curve within an interval. For instance, at a certain stress level, an incremental increase of stress and a partial relief would allow conclusions about changes in the property. Especially if an additional parameter, such as a constant magnetic field, is involved. With this possibility the direct effect of the additional field on the stress-cycle test can derived. This has been performed in this Sec. 5.3.2. Additionally, by inserting a hold time at maximum stress, creep effects under the application of an additional field can be investigated.

Spindle testing machine

In this work, a spindle testing machine (AGX-V, Shimadzu) was acquired and integrated into the setup assembly, see Sec. 4.2. An universal testing machine is suited to deliver a high precession force control or displacement detection. Furthermore, with the spindle testing machine, the repetition accuracy, e.g., for cyclic loading, is given. In addition, for uniaxial stress conditions, its axial longitudinal parallelism and its high linearity for the crosshead movement make it the method of choice.

The rigidity of the frame facilitates the static loading condition. In addition, it also meets the requirements for low-cyclic effects, as it is possible to capture minor hysteresis loops under small stress variations. Such conditions are essential for fatigue tests, creep rupture tests, and fracture mechanics studies with Compact Tension (CT) samples.

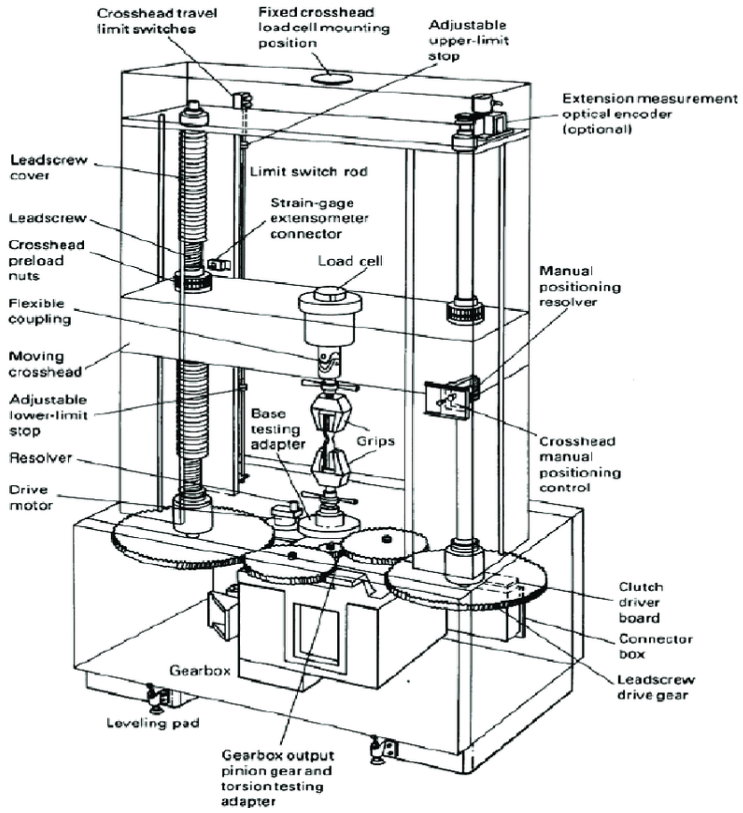

FIGURE 3.10: Schematic of spindle testing machine. The main advantage of the screw-driven testing machine lies in the use of a backlash-free ball screw, which facilitates high linearity and precision. Schema is taken from [133].

The construction of the testing machine is as follows (Fig. 3.10): The load cell is positioned in the center of the moving cross-head, which is connected to the load arm (loading path). As a result, during the test, a direct force path on the sample is achieved. The mechanical force is driven via a central spindle motor. The lead screw on this is only for lateral guidance and is not stressed in the bending experiment. The force "F" and strain are recorded by the testing machine software (TRAPEZIUMX-V, Shimadzu) and, locally, by the integrated Attocube interferometric sensor, see Sec. 4.2.

3.5 Magnetic characterization

Magnetization is an essential characterization quantity of a magnetic material. It gives insight into the degree of alignment of the magnetic moments in materials. This is the case because a magnetic field -internal and external- interacts with matter, Sec. 2.3.5. Several characterization methods are available to study the induced change of magnetization. Here *magnetometry* techniques such as, the Vibrating Sample Magnetometer (VSM) and a Superconducting quantum interference device (SQUID)[15], are applied to probe the volume magnetization.

More novel methods, such as spin-polarized scanning tunnelling microscopy, are also suited to study spins in low dimensions [134]. This technique allows the imaging and manipulation of individual spins with atomic spatial resolution. X-PEEM (X-ray photoelectron

[15]For the sake of completeness MOKE, magneto-optic Kerr effect measurement method, also belongs to this family.

emission microscopy) is a further advanced method. This uses the x-ray dichroism effects of polarized light from synchrotron sources to record the image of the specific element of magnetic domain structures [135]. It quantitatively measures the ground state of spin and orbital magnetic moments of elements with a high temporal resolution. It also allows the imaging of transient processes due to their interaction with synchrotron radiation [136].

In the scope of this work, an MPMS-5S[16] (Magnetic Property Measurement System) SQUID, manufactured by Quantum Design, and a PPMS[17] (physical property measurement system) - VSM, manufactured by CRYOGENIC were used to measure the magnetization M(H) hysteresis of the magnetoelectric ceramic samples. The SQUID was further customized by Borisov et al. [137] for the measurement of the magnetoelectric coupling coefficient, and the VSM is additionally used to measure the stress-dependent magnetization, Sec. 4.5. Both characterization devices are customized beyond their primary setup. The SQUID device has an additional custom built option for measuring the magnetoelectric coefficient $\alpha_{conv\,ME}$. On the other hand, the higher stability of the CRYOGENIC PPMS system is customized for using pressure cells to measure stress-dependent magnetization, Sec. 4.5.

3.5.1 VSM

Simon Foner [138] developed the first VSM to measure the variation of the magnetic flux as a function of an external magnetic field in magnetized materials. Since then, more advanced versions are available in the market. Depending on the manufacturer, these devices can reach a sensitivity of 10^{-8}emu[18]. The VSM option of the CRYOGENIC PPMS has a noise floor sensitivity of 10^{-6} emu, at 10 s integration time, Fig. 3.11. This resolution is certainly required to study magnetic nanostructures, as the amount of magnetic material deposited in the form of a thin film is low. This high sensitivity is not necessary for the study of bulk ceramics[19]. However, when the effect of additional parameters has to be quantified, indeed sensitivity of the magnetometer is crucial.

The VSM comprises a cryogenic chamber with a static pair of pick-up coils and a superconducting magnet with a cylindrical bore integrated inside the chamber, see Fig. 3.11. The magnetic field orientation is along the axial direction of the inner bore and pick-up coils. Therefore, the pick-up coil is only sensitive to the stray magnetic fields of the sample. In contrast, the homogeneous contributions from any external fields are canceled out by the coil arrangement. Additionally, the system has a temperature control unit that regulates the temperature of the sample via helium cooling and heating via a filament built inside the chamber. Outside of the cryogenic chamber, there is a motorized vibrator with a sample holder tube-rod system attached to it. The *rode-tube system* is utilized to evacuate the vacuumizable loading chamber as the tube functions as a vacuum protector. It is made of carbon fiber that is rigid, light, thermally stable, and non-magnetic. The sample is mounted on the rod, allowing it to slide into the superconducting magnet's bore inside the cryogenic chamber.

The sample-rod unit is connected to the vibration motor. The assembly is moving freely inside the tube, as it is located in the vacuum. Further, the vibrator is mounted on a motorized Z-positioner, which enables the precise positioning of the mounted sample in the middle of the static pair of pick-up coils. This step is necessary, as otherwise, the measured

[16] Located at University Duisburg-Essen, Faculty of Physics, - AG Wende, maintained by Dr. Salamon.

[17] Located in TU Dresden, supported by Dr.-Ing. Richard Boucher.

[18] The higher versatility of CRYOGENIC PPMS-system for customization compared to *Quantuum Design* PPMS make it favorable.

[19] Ferrites, the magnetic material used in the frame of this work, exhibit a saturation magnetization in the order of 10-100 emu/g.

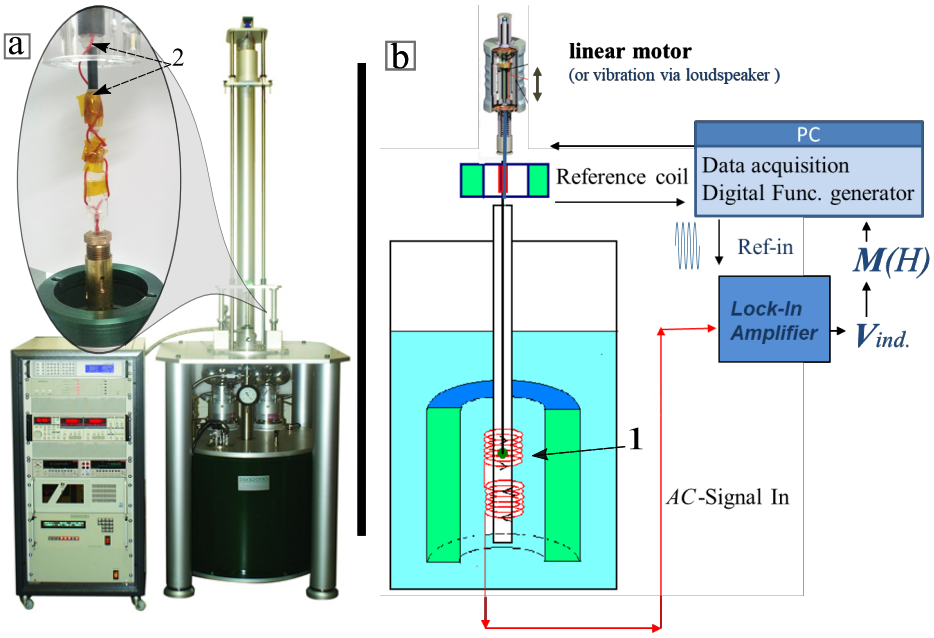

FIGURE 3.11: a): A Cryogenic PPMS, the inset shows the mounting rod-tube system connected to the pressure cell, see Fig. 4.24. The VSM lifting assembly can position the sample inside the measurement space. b) Illustrates the construction of the VSM assembly, and a schema of its operation, 1) shows the sample in the measurement space, located between the pickup coil and inside the superconducting solenoid magnet.

hysteresis would be shifted. The vibrator typically oscillates at 21 Hz, with a peak-to-peak amplitude of 2 mm. It logs the value with an optical sensor housed in the vibrator. The oscillation of the sample (magnet) in the middle of the pickup coil will induce an AC signal, which is used to calculate the sample magnetization, see Eq. 3.2. In order to improve the signal-to-noise ratio, the AC signal detected by the pick-up coil is cleared out of the noise by tuning a lock-in amplifier into a reference of the oscillation frequency signal. This detects the in-phase voltage from the pick-up coils. Furthermore, the cryogenic VSM has a strong vibrating motor, which can sinusoidally oscillate a 100 g heavy load, which gives it an advantage over other systems.

The motion of the magnetized sample induces a voltage in the pick-up coil. Here, a varying external field causes a change in a magnetic moment that is detected as a corresponding difference in the induced voltage. The magnetization is calculated from the voltage following Faraday's law of induction. Regarding the interpretation, it is important to consider that the measured values are an average over the volume, as reflected in the unit [m/V].

$$V(t) = -N\frac{d\Phi}{dt} = -N\mu_0 A\frac{d}{dt}\,(H + M(t)) = \underbrace{-N\,\mu_0}_{\alpha} A\frac{d}{dt}\,M_0\,sin\omega t - \underbrace{-NA\mu_0\frac{dH}{dt}}_{=0,\text{ coil geometry}} = \quad ...$$

$$= \alpha_m M_0 \omega\, cos\omega t \quad \Rightarrow \text{ moment} = \frac{V_0}{\omega\alpha_m} \quad \text{with; } \alpha\text{: coupling constant} \tag{3.2}$$

In the early stage of this work, magnetization measurements of composites under a static electric field were performed. For this purpose, the pins belonging to the AC-susceptibility

option of the PPMS were used for further customization. Consequently, two electrical leads were incorporated into the VSM rod-tube system to enable a E_{DC}-field to be applied to the sample. However, due to a lack of high resistive samples, it was not possible to acquire reproducible data, and during the latter stages of this work, due to limited accessibility, it couldn't be retried, see Fig. 3.11a. It needs to be noted, however, that a E_{DC}-field can affect a single-phase multiferroic, as is discussed in the outlook chapter.

3.5.2 SQUIDS

SQUIDS are part of another magnetometry based method, where these are used to measure the variation of magnetization as a function of magnetic flux of a magnetized sample with a detection "coil". In the case of a VSM, it was a pick-up coil that converts the change in magnetization into a voltage. In a SQUID, however, it is a superconducting ring that operates based on the Josephson effect and associated flux quantization. This makes it the most sensitive detector of magnetic flux known. It can reach quantum-limited sensitivities.

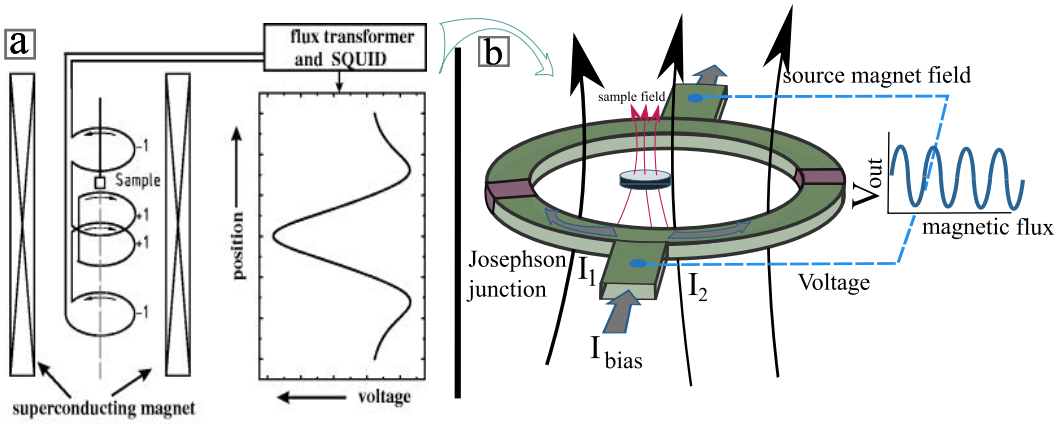

FIGURE 3.12: Schematic of the pickup coil geometry in the SQUID and SQUID VSM systems used, where the arrows indicate the direction of the current. a) The sample indicates the direction of sample travel during a measurement while the voltage is measured. (b) Double junction SQUID (left) with the output voltage as a response to a change of flux (right) The dc SQUID is simply a ring of superconductor containing two Josephson junctions

The working principle is as follows: flux quantization is a feature of superconductors, when electrons are circulating as Cooper pairs around a closed path (ring), they quantiz32 according to integral $\oint d\theta = n2\pi$. This states that each pair of electrons represented by a quantized *magnetic flux* moment, where the magnetic flux Φ through a superconducting ring is the multiple integer (n) of the quantum magnetic flux $n \cdot \Phi_0 = n \cdot \frac{hc}{2e}$. The Josephson effect describes this quantized tunnel current between two superconductor materials separated by a thin, non-superconducting layer, the Josephson contact, see Fig. 3.12b [139].

Combining both ideas makes it possible to deduce that a change in the magnetic flux through the ring induces a current in the range of the quantum flux. Therefore, the superconducting current through the ring is proportional to the change in the magnetic field.

Operational principle

In a SQUID magnetometer, the magnetic flux is initially measured by a series of pickup coils. These input coils are coupled to the SQUID loop, as displayed in Fig. 3.12. A voltage appears in the presence of the magnetic field through the ring as the bias current splits and

passes through each arm of the ring. If the two junctions in the SQUID are identical, as in the absence of a magnetic field, the current will divide evenly, and half will pass through each junction before recombining.

Similar, to VSM, the SQUID uses a rod to slide the sample through the bore into the location of the pick-up coils. In the SQUID, the magnetic moment of the sample induces an electric current in the coils. The geometry of the pick-up coil is only sensitive to the stray magnetic fields of the sample. Since the detection coil, the connecting wires, and the SQUID input coil form a closed superconducting loop, any change in the magnetic flux in the detection coil produces a change in the persistent current of the detection circuit. Depending on the magnitude of the induced current, the voltage drop across the Josephson junctions is measured. Therefore, the ring of the SQUID sensor is at the heart of this magnetic flux to voltage converter device [140].

3.6 Magnetoelectric measurement devices

The magnetoelectric coefficient α_{ME} describes the strength of the magnetoelectric *coupling*, Sec. 2.6.3. The discovery of single-phase multiferroics and later the concept of composites gave rise to the development of an array of methods. The measurement of the magnetoelectric coupling coefficient is considered as the figure of merit of the ME-composites regarding the performance of ME-composites. A setup that characterises the ME-composites provides an understanding of the syntheses of magnetoelectric materials[20]. Thereby, it provides quantifiable feedback in order to improve the quality of the sample material.

Initially, the existence of ME-coupling in Cr_2O_3, based on the theoretical prediction made by Dzyaloshinskii [81], was measured by Astrov. He developed the first concept for the dynamic measurement of the ME effect [82], where the ME-coefficient was measured in response to an electrical excitation field. Vopson *et al.* [141] cover all the major techniques and setups used for macroscopic characterization. Lately, given the increasing number of nanostructure-based concepts, the local mapping of the ME-coupling effect has become relevant[21].

3.6.1 Measurement principle and materials

The measured value of the magnetoelectric effect coefficient depends on the amplitude of the excitation field Eq. 2.52. The induction of electric polarization by applying a magnetic field is coined as the direct ME-effect, ME_D: P = αH, and the effect, which is measured by applying an electrical excitation field, is termed the converse ME-effect, ME_C M = αE. The nature of the excitation field implies how the measurement technique principally needs to be designed. Essentially, the setup requires a stimulus field (magnetic or electric) and the possibility to detect any change of polarization or magnetization.

For the characterization of composite, both techniques are necessary. Given that the effect is a mechanically driven pseudo-coupling at the interface, both methods require an active AC- exciting field. This activation field needs to correspond to the concept of the coupling in composites, see Sec. 2.6.2. A further point of consideration in composites is the nature of the magnetostriction curve. It has a constant value at near-zero fields (up to 40 mT), which needs to be considered in the measurement since a small excitation at a near-zero field doesn't induce a strain response due to its zero slope, see Sec. 3.13. This implies

[20] E.g. the effect of different sintering temperature and grain sizes.

[21] The locally resolved ME-coupling, Sec. A.4. Such experiments were implemented and conducted by Dr.Trivedi at University-DuE [142].

that the field needs to be tuned to the strain-sensitive regions. Therefore, an offset H_{dc}-field is applied, in order to shift the magnetic phase of the composite with a working-bias field, to a range where a more linear and larger magnetostriction effect is measured. The H_{dc}-field is generated by an electromagnet, and it is typically run in a sweep mode cycle up to $\pm$1.5T. The field range covers the characterization of the ME effect over the full range of the magnetostriction curve and identifies the optimum working field. With this data, it is possible to engineer application-specific composites.

The activation of the ME-effect occurs in the *presence* of either a magnetic field H_{ac} or an electric field E_{ac}. The small AC field superimposed on the working-bias H_{dc}-field induces a proportional ΔP_{ac} or ΔM_{ac}, which is detected as a polarization voltage or magnetization change. For the latter, a pick-up coil is used to convert the change into a voltage.

For direct and converse measurements, the ME coupling value also depends on the geometrical arrangement of the DC- and AC field's, as the effect relies on the mutual orientations of polarization, electric field, and magnetic field. Furthermore, the ME coupling has a frequency dependency on the activating AC fields, as the induced magnetization and polarization properties vary with the excitation frequency. Moreover, the AC field makes the measurement error-prone as there is some cross-coupling between the excitation field and the response signal[22].

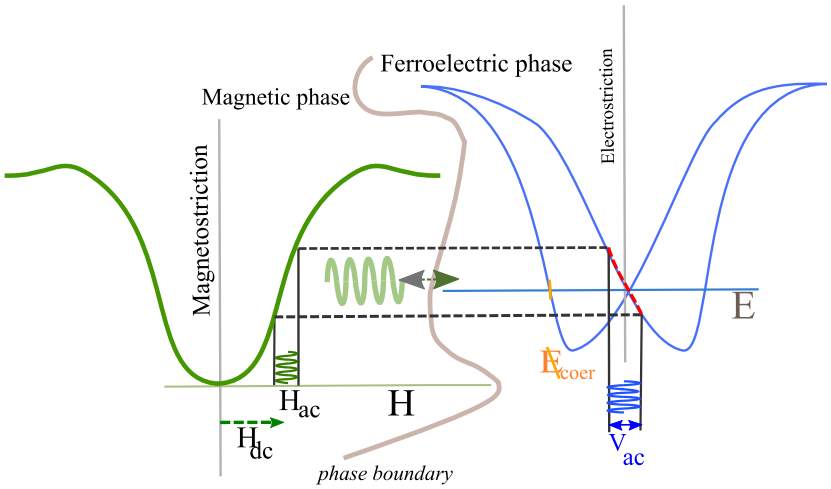

FIGURE 3.13: Schematic illustration of the ME effect in composites as a product property of two phases. Here, the ME-effect needs to be "activated" initially. In the direct method (ME_D), a low amplitude H_{ac} field (1 mT), and in the converse method (ME_C), a low amplitude E_{ac}-field is superimposed on a H_{dc}, see Sec. 3.15. The H_{dc} shifts the magnetic constituent into the strain-sensitive range to utilize a pseudo piezomagnetic behavior (linear dependency). The application of the H_{ac} generates a mechanical wave in the samples, where the active phase transfers vibration into the sensing phase. In the direct method, the slope of the ferroelectric strain curve around E_{dc}=0 reflects the amplitude of the generated voltage. Therefore, it needs to be poled in order to overall exhibit pseudo-piezoelectric properties. The related measurements are shown in Sec. 5.14.

[22] The pick up coil would measure due to E_{ac} polarization change (charge movements) and ME-magnetization change at the same time.

3.7 ME-coefficient measurement with Lock-In amplifier

The voltage response plays an essential role in designing magnetoelectrics for applications. The relationship between the magnetically *induced* polarization in a magnetoelectric sample and the deduced *voltage* is given by Eq. 2.52. Using $E = V/d$ with V being the voltage and d the thickness of the ferroelectric layer, yields [89]:

$$\alpha_{ME}^{H} = \frac{V_{measured}}{H_{ac} \cdot d} \tag{3.3}$$

Eq. 3.3 implies that the voltage response of a multiferroic varies linearly with the amplitude of the applied AC-magnetic field. Furthermore, it also indicates that the magnetoelectric coupling coefficient α_{ME}^{H} is determined by the slope of $\frac{Response}{Stimuli}$ divided by the thickness of the sample (dielectric). The DC bias magnetic field, which tracks the response behaviour over the full range of H-fields, is not involved here.

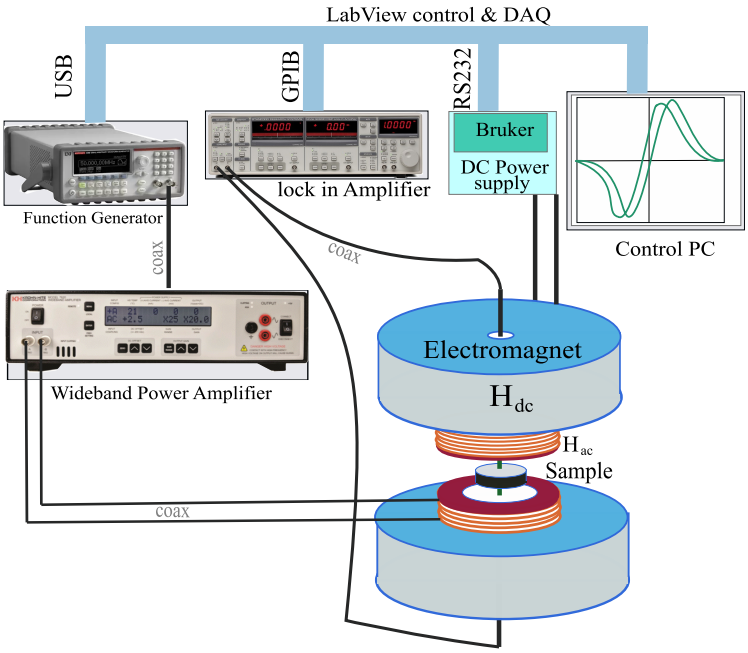

FIGURE 3.14: Schematic plan of the direct ME setup. The system allows the simultaneous application of DC and AC magnetic fields while electrically induced signals are amplified and detected via a lock-in amplifier, see Sec. 3.15. In addition, a simultaneous mechanical stress field, as a modular option, has been implemented into this instrument, see Sec. 5.13. This gives the device a unique measurement option for ME measurement.

The related setup, see Sec. 3.14, consists of an electromagnet[23] that generates the DC bias field, a pair of Helmholtz coils used for driving the AC field, and a sample holder that can allow the measurement of both the longitudinal and transverse coefficients. Furthermore, the measurement process has been automated with a LabView program that controls the devices and processes the output signals generated by the samples.

Despite the measurement possibilities, the technique has some technical issues to overcome. It is easy to measure the low output AC-voltage of the magnetoelectric sample, as a lock-in can resolve μV and nV signals that match the reference frequency. However, given

[23]The DC field bipolar electromagnet (Bruker "Forschungsmagnet" B-e25 B8, Sec. 4.2 and 5.13) generates a magnetic field of up to about 2 Tesla, depending on the distance between the poles (Airgap). The ferromagnetic core has a large permeability which increases the field by four orders of magnitude. Further, the soft magnet core has a low coercive field, so a negligible amount of magnetic hysteresis arises.

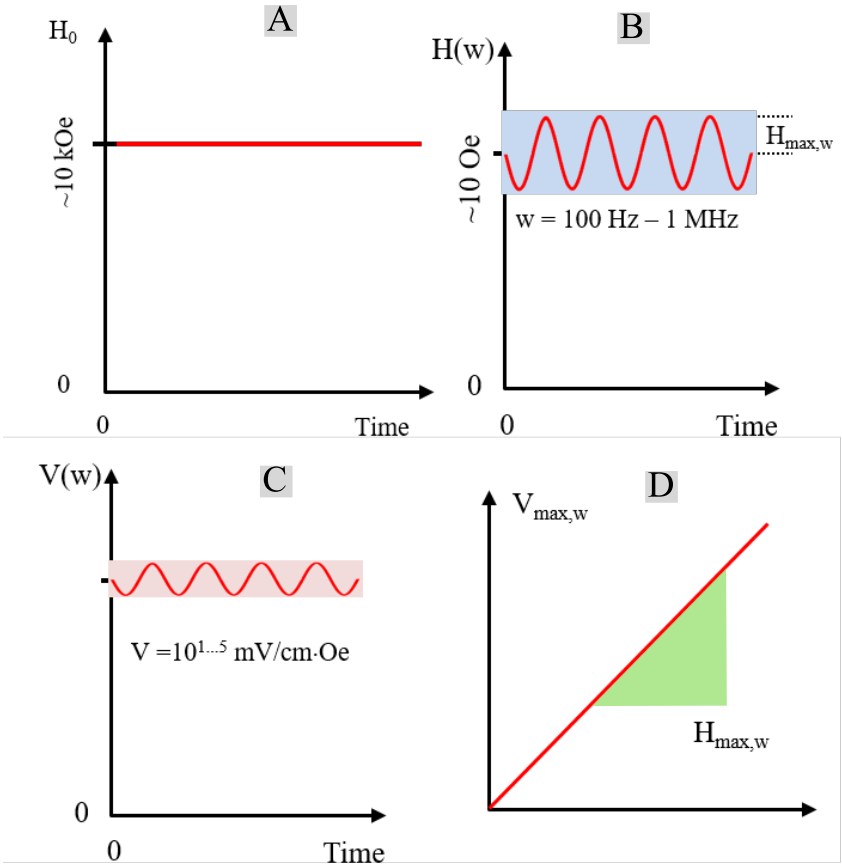

FIGURE 3.15: The experimental procedure for the measurement and calculation of direct ME-effect related to Fig. 3.14. A) A magnetic DC field is applied. B) An AC-excitation field superimposed on the DC-field. C) Shows the induced voltage over time, while D) shows the proportional to H_{ac} induced voltage, from which the ME-coefficient is calculated according to the Eq. 3.3

that the excitation H_{AC}-field has the same frequency as the output signal, a primary issue is related to the electrical connection to the sample, and stray field pickup by electrical leads to the sample from the excitation H_{AC}-field. Effectively, as the wires are connected to a dielectric (ferroelectric sample), it constitutes an open-loop, and the signal pickup is regarded as an antenna effect. Therefore, the lock-in cannot filter out the additional parasitic signal as it has the same frequency as the reference signal. In order to overcome this, there are two solutions: first, the geometry and amplitude of the AC driving magnetic field, H_{ac}. The centered sample position in the H_{ac} field and the centered, orthogonal electrical connection through the AC driving magnetic coil to the sample pads, as it taps the V_{ac}response signal, reduce noise pickup. Furthermore, a low H_{ac}-field of only 1mT is enough to induce a measurable voltage response[24]. In this case, the broadband current amplifier can be omitted, as it causes a time delay which leads to phase mismatch. Instead, the function generator can be used to generate the H_{ac} as its power is sufficient for a 1mT AC field, and its signal can be supplied as a reference to the lock-in.

A further point of consideration is using coaxial cables for the alternating field. The standard coaxial cables have an impedance of 75Ω and capacitance of 100 [pC/m], arising from the insulation between the wires. This implies that α_{DME} is decreased by the factor

[24]This parameter depends on the quality of the sample.

derived from:

$$V_{sample} = V_{measured} \cdot \frac{C_{wire} + C_{sample}}{C_{sample}} \tag{3.4}$$

If the AC magnetic excitation signal matches the electro-mechanical resonance frequency of the sample, the voltage output has a sharp and enhanced resonant response for α. Therefore, the measurement setup for the coupling coefficient requires a characterization option that can be used to identify frequency dependency. This can help with the development of tailored multiferroic devices.

In addition to the measurement above, a modified version of this device also characterizes stress-dependent α^{σ}_{DME}. For this purpose, the setup is positioned in a mechanical testing machine. The setup concept for it is discussed in the next chapter, in which the setup modularity and adaption are considered.

3.7.1 Converse-ME technique with SQUID

Based on the measurement proposal by Kita [143], Borisov [137] *et al.* modified an MPMS squid from *Quatum Design* to measure the converse ME- effect. The proposal is based mainly on Astrov's approach [82]; however, it takes advantage of the modern SQUID with its high resolution, as introduced in the previous section. The modification involves the diversion of the leads in the MPMS[25], which would typically send current to the magnetic AC field solenoid, for AC-susceptibility measurement option[26], in order to use them to apply an electric field E_{ac} on the sample. The SQUID records the resultant change of magnetization via a lock-in amplifier, which corresponds to the electrically induced moment. The E_{ac} tracks the magnetostriction curve in sweep mode up to 5 T applied biased H_{dc} field.

A detailed description of the method measurement system is presented by Dr Salamon [144, p. 83].

[25] Magnetic Properties Measurement System.
[26] The solenoid is shorted to avoid parasitic signals.

4

Development of a multi-purpose modular setup

" I happen to have discovered a direct relation between magnetism and light, also electricity and light, and the field it opens is so large and I think rich."
– Michael Faraday, *The Letters of Faraday and Schoenbein*

This chapter continues the study of the mechanics of magnetoelectric composites to derive underlying constitutive behavior. As elucidated in the Heckman diagram, the interrelationship of the ferroic functional materials shows how the magnetoelectric effect manifests itself, see Fig. 4.1. It illustrates the cross-coupling properties of the three quantities. This illustrates the required equipments and capabilities for the setup design to characterize the composite samples. This chapter discusses the considered parameter space for the setup and the compatibility of its characterization methods in detail. In particular, a proper technique has to be determined, which detects the strain when external fields are applied. Furthermore, given the versatile properties and cross-couplings in magneto-electric composites, the modular design of the setup and the many characterization options are discussed in detail.

4.0.1 Probing functional materials

Conceptually, functional materials transfer one physical quantity into another. The magnetoelectric composites, convert the energy of a specific field into mechanical properties. In this context, magneto-electrics couple to multiple external fields and respond with multiple physical quantities to each field. Thus, their study necessitates simultaneous control across multiple fields and corresponding response detection instrumentation. From a broader perspective, having simultaneous multiple fields may interfere with the detection instruments, which makes the overall instrumentation design a demanding task. This limits the selection of available methods. The engineering task is to bypass the difficulties of multiple field arrangement and incorporate the detection instruments in the experiment space. Moreover, numerous fields also put limitations on the handling of the sample, as it sets constraints on the sample size.

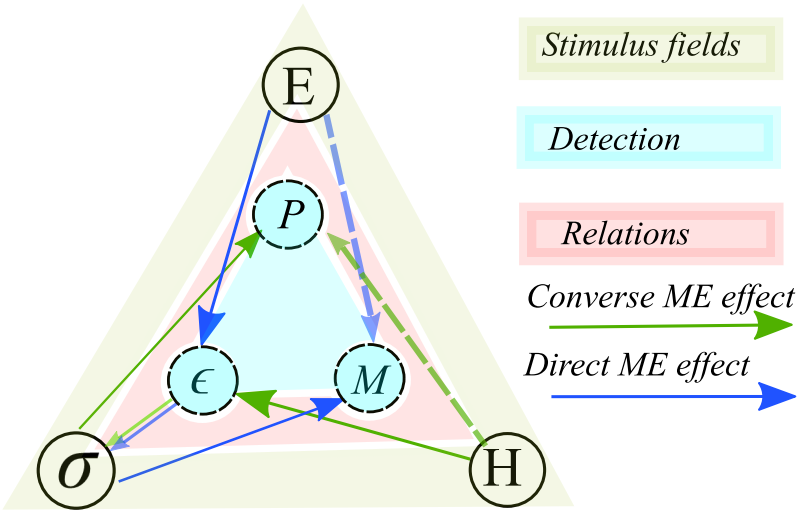

FIGURE 4.1: The Heckmann diagram illustrates which fields- the external physical quantity represented by the outer corners - and material response - inner corner- are required to measure the ME-effect. Understanding of stress-strain effects in the characterization of magnetoelectric materials would help to improve the ME-effect.

4.1 Requirement analysis for the setup

The benchmarks of the instrumentation need to meet the requirements for the underlying mechanism of the functional properties [107, 145–147]. In this regard, the analysis of the setup requirements comprises defining the stimulus technique and its parameters, such as the field range, resolution, and control precision. Likewise, a requirement for sensitivity and compatibility needs to be set for the detection techniques. For the onset of the effects, the related fields need the possibility of applying all three fields in an AC mode, Fig.4.9, superimposed with a DC field.

Furthermore, to characterize the coupling effects quantitatively, it is required to have a resolution for the detection device that is better than the measurable effect amplitude itself. A minimum requirement criterion would be a resolution of 10% of the total expected effect amplitude. The precision of the resolution is determined by the standard deviation of the noise floor, which needs to stay within 10% of the resolution range. The minimum resolution is required for the control of stimuli fields in order to be able to tune the field step in a range such that it would not exceed 10% of the total effect. It is also crucial that the detection instrument can collect at least 10 data points within the effect range. For instance, the detection of the mechanical response of strain requires the capability of resolving a strain for each field step.

Given the multi-field dependencies of ME materials, the characterization setup requires three field modules: magnetic, mechanical, and electrical field. The design should enable each field to be applied independently and in multi-field arrangements to determine the contributing parameters of different fields.

This section will discuss the setup options and configurations in detail. The overall construction needs to be applicable for the characterization of other functional materials beyond its primary use for measuring ME composites.

Modularity: The broad range of properties of the ME-materials need differing experimental characterization settings. Hence, during the conception phase, great importance is

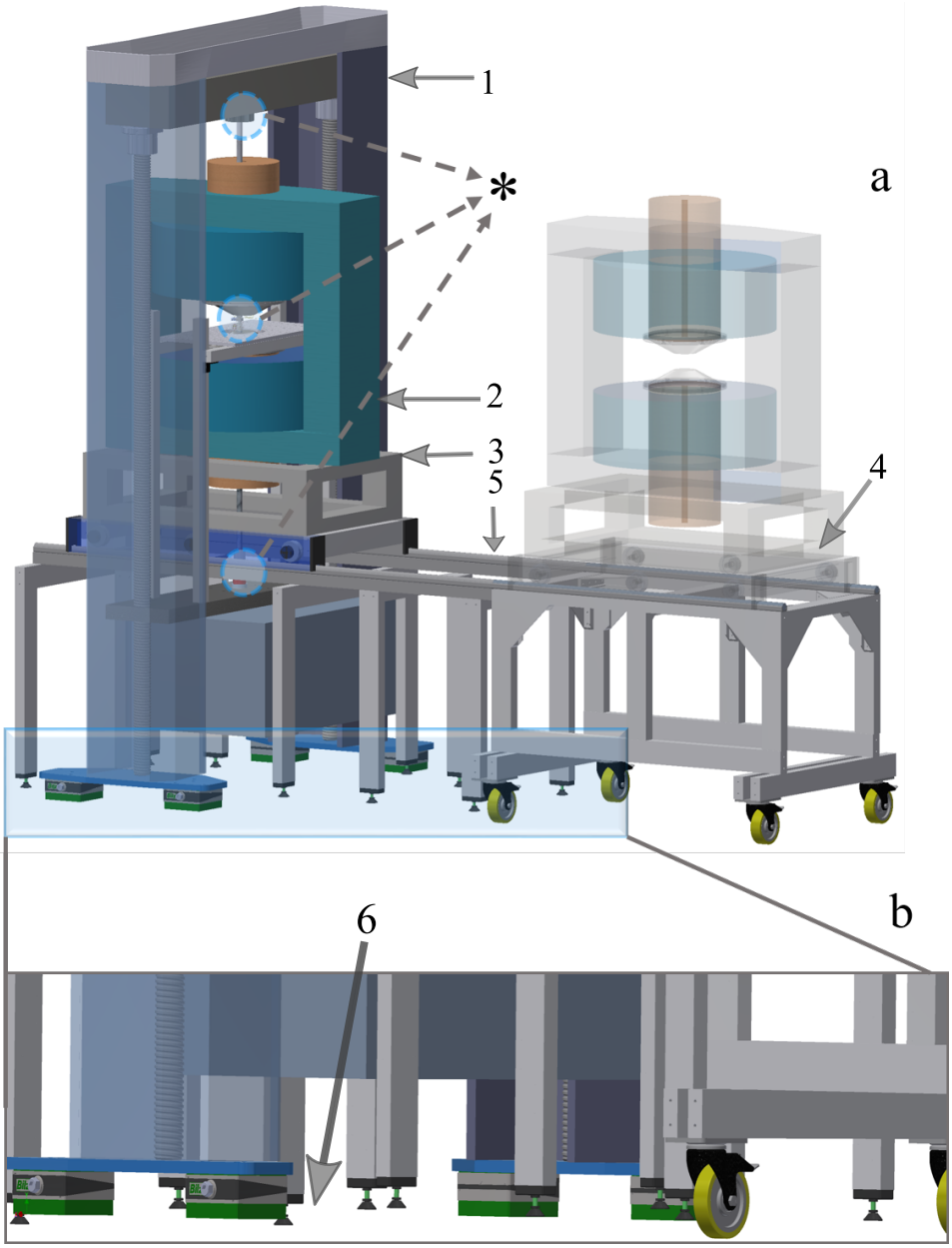

FIGURE 4.2: CAD design of the assembly of the modular units. a) The overview illustrates (1) the universal testing machine for precise load control, (2) the bipolar electromagnet sitting on a frame (3). (4) A rolling carriage with track-line, enables the positioning of the magnet on the fixed track (5), allowing modularity. b) An angle alignment mechanism has been installed for both the testing machine and magnet in order to align the drilled hole (6) with the rod system, see Fig. 4.3, and for different modules between the pole shoes Fig. B.6. * Denotes the visible parts of the alumina mechanical load rod (details , see Fig. 4.3).

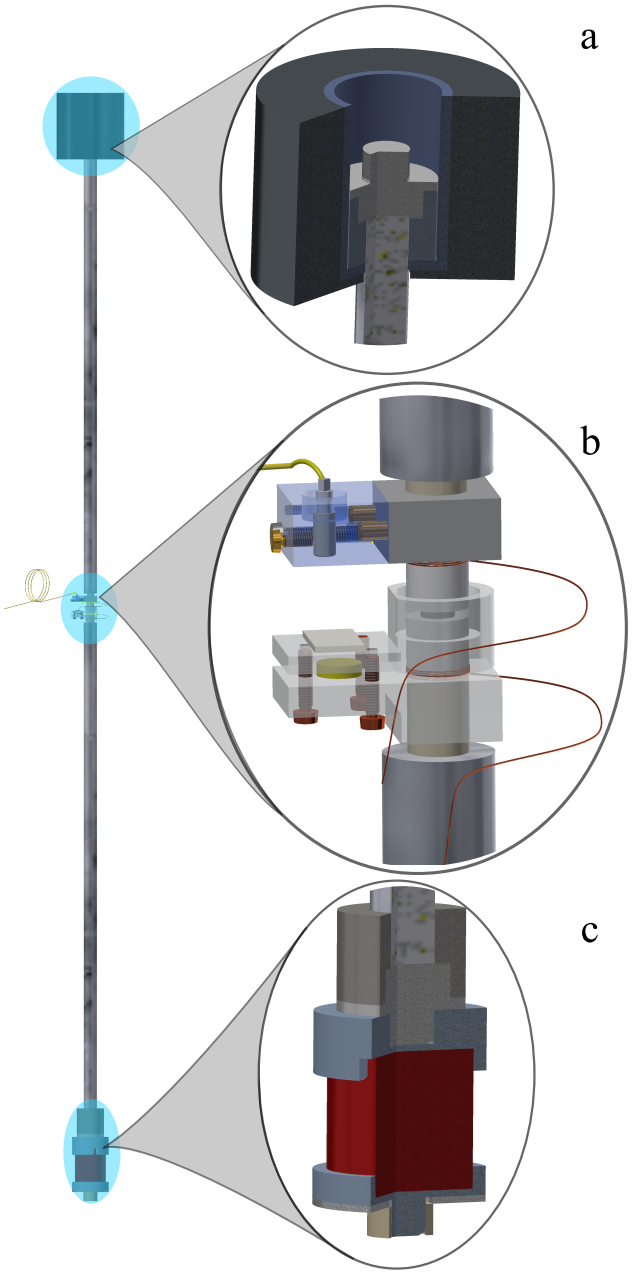

FIGURE 4.3: Alumina-rod system attached to the testing machine. a) The shielded screw is attached to the traverse. It transfers the load through the hole in the sample space. It consists of a flat frontend screw, where the rod is glued onto it with two-component epoxy-adhesives and housed in a mu-metal shielding case. b) An illustration of the sample space arrangement for longitudinal strain measurements during uniaxial compressive loading. The sample area with the sensor is described in detail in Sec. 4.4.2, Fig. 4.18. This means, even in the case of ambient vibration, that the relative position of the sensor and the mirror position would not be affected, see Fig. 4.3. c: Shows the AC-loading option with an actuator for AC mechanical loading. It is fixed at the bottom of the testing machine.

assigned to realizing a modular setup. The setup incorporates the mechanical characterization option that influences the ME properties, see Fig. B.6.Also, the setup was developed around a pre-existing bipolar electromagnet with a weight of approx. 2 tons, see Fig. 5.13.

This considerably limited the design and needed to be integrated into a modular configuration concept. Given the dimensions of the magnet, an oversized mechanical testing machine was required to be able to insert the magnet into the frame. Furthermore, the field orientation was fixed once the setup was organized. For it to be still modular, a solution was required for the mobile handling of the two-ton magnet. For this purpose, two options were considered

I. Handling via gantry crane or II. Rail track.

It was found that the rail track-supported maneuvering is more advantageous since this not only exposes the user to less danger but also allow more accurate and easy positioning of the magnet. The necessity for this solution becomes more evident when the other components are considered in Sec. 4.1.

Requirements of fields: Probing the magneto-mechanical properties of functional materials requires both magnetic and stress fields. The options for applying mechanical stress are numerous. The integration of a universal mechanical testing device (Shimadzu AGS-X 100kN, Sec.3.4) is a standard approach way for achieving constant loading rate (independent of displacement). It further offers the option for velocity control mode (independent of loading rate). Moreover, its feasibility for the investigation of functional electro ceramics has already been shown by several groups [148, 149] and it inspired its use for this work as well, Fig. 4.3c. Alternatively, uniaxial stress can be applied in a setup consisting of a stiff frame with a screw or a piezo actuator for the loading of the sample inside the frame.

The choice of the universal testing machine is due to its precise control of the loading process and repeatability of the settings, which fulfils the necessary requirements[1]. For its integration, the mechanical testing machine of choice had to have a dimension that it would allow the magnet to pass through its frame.

The possibility to apply ***cyclic mechanical loading,*** was a further option integrated into the setup, see Fig. 4.4. A cyclic module for mechanical loading is integrated in the setup, if the characterization requirement of the functional material requires it. Such excitations are required to characterize *fatigue* or d_{33} under a uniaxial preload. The ME-effect shows an enhanced coefficient at the mechanical resonance of each ferroic phase beside the mechanical coupling factor between the two components. Accordingly, probing the mechanical resonance frequency bandwidth of each phase involved in the composite provides a further possibility to tailor this property [122]. Moreover, adding a magnetic field to the cyclic mechanical module under stress makes the setup compatible for fatigue studies under complex environments [150].

For this purpose, the incorporation of an actuator (PI: P-016.40P[2], driven with Piezo Amplifier/Servo Controller PI: E-482)

could be a suitable approach. It allows a broad range of frequencies and high load excitation amplitudes, even under high blocking forces, as required in a preload case. The module is integrated into the load path by a rod system, as displayed in Fig. 4.3.

The mechanical specification of the rods is a crucial aspect. It presupposes that the rod material has a higher stiffness than that of the tested material, as during the experiment

[1] For detailed description and arguments for its use see Sec. 3.4.1.

[2] Specifications: Travel Range: 60μm, Diameter 16mm, Length L 58mm, Blocking Force 5600N, Static Large-Signal Stiffness 94 N/μm, Capacitance 510 nF $\pm$20%, Unloaded Resonant Frequency 20 kHz.

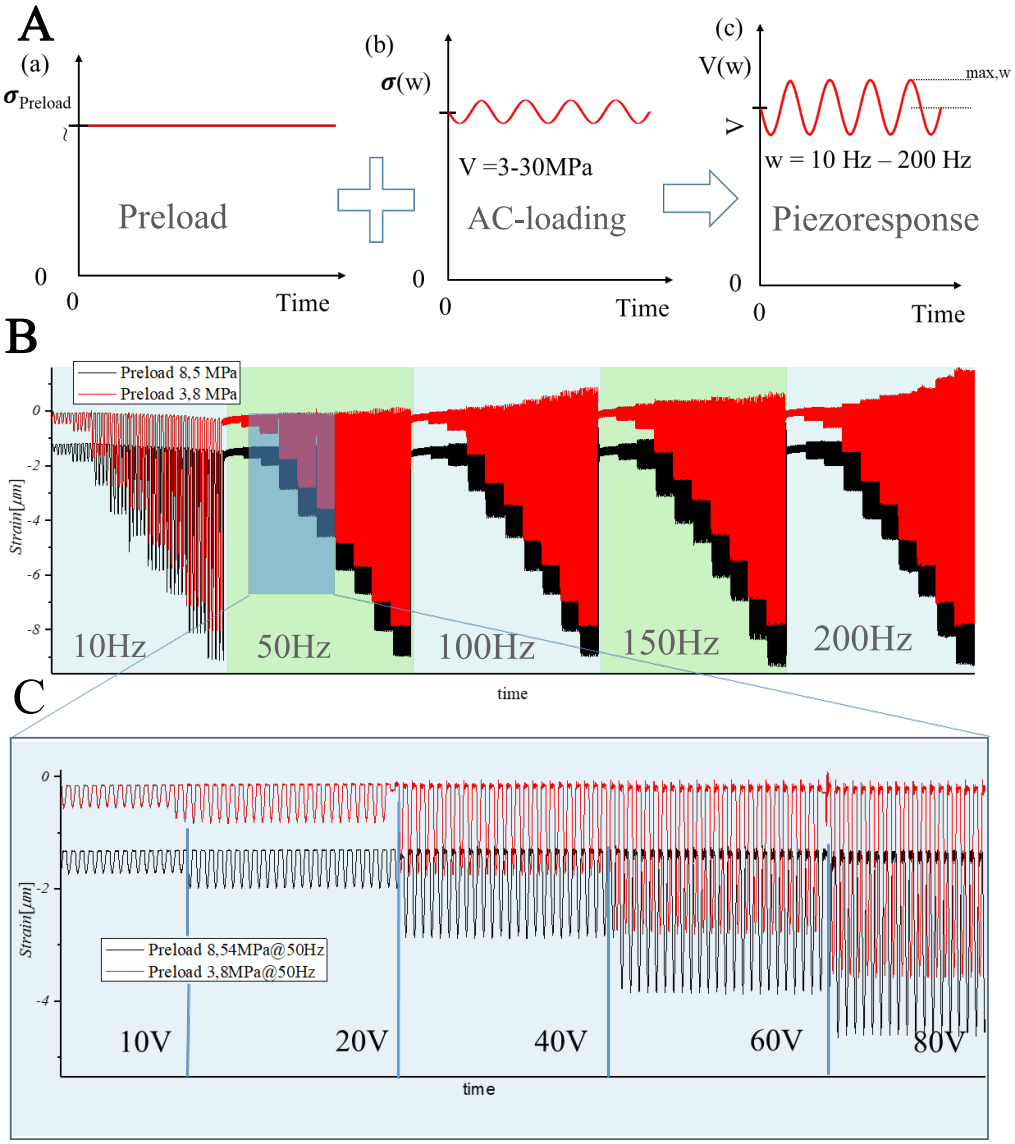

FIGURE 4.4: Feasibility of the setup with AC-mechanical loading. It demonstrates the performance of the actuator integrated into the setup, as displayed in Fig. 4.3. Here, a sinusoidal excitation for different oscillation amplitudes, frequencies, and two different preloads are applied. The characteristic measurements have been performed on a PZT sample ($h = 0.5mm$, $\varnothing = 10mm$). A) Illustration of the experimental procedure. The mechanical testing machine applies the preload (a), and AC-loading is applied by the actuator (b). c) The voltage is recorded as a response to both parameters, shown in Fig. 4.5A for a piezo stack. B) Demonstration of the recording of the displacement as a result of excitation for different frequencies and two preloads on the PZT sample, with a setup used that is shown in Fig. 4.3 while C) Shows excitation at 50Hz with different amplitudes (given as a voltage value of the function generator that drives the amplifier), as depicted in Fig. 4.9.

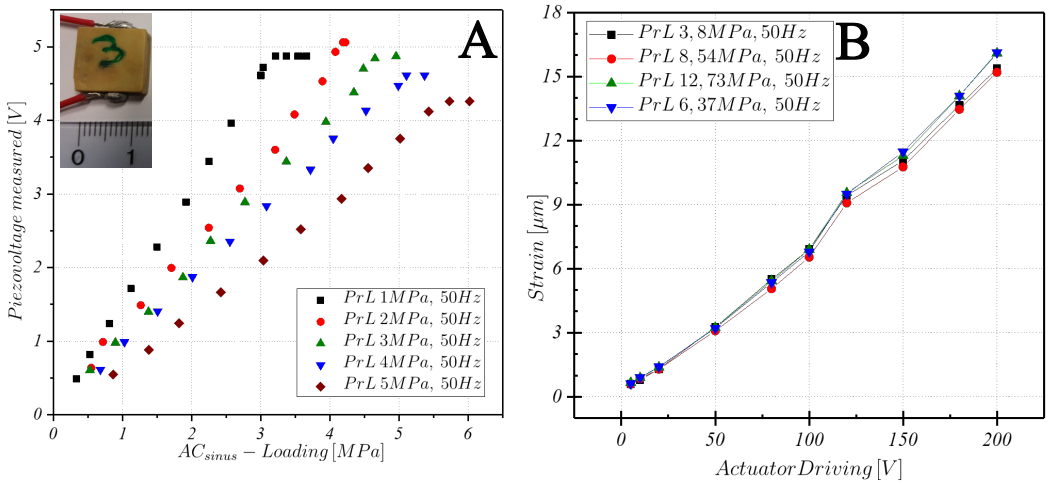

FIGURE 4.5: Illustrative measurements of when the actuator is used for cyclic loading with the configuration shown in Fig. 4.3. A) The voltage response of the piezo stack (depicted in the inset; Dimension:$12mmx12mmx6mm$) is measured under different preloads (PrL). They were provided by Dr.P.K.Panda -*CSIR-NAL*-. B) A PZT sample ($h = 0.5mm$, $\varnothing = 10mm$) under cyclic loading with different preloads at 50Hz. The displacement caused by the actuator is measured with an interferometer sensor.

the rods are exposed to static and cyclic load. Therefore, the stiffness of the rods must remain unchanged throughout the experiment. Moreover, a multi-field set-up requires a non-metallic rod so that it is not affected by the presence of a magnetic field.

Also, a ***magnetic AC-field*** option was integrated as a module in the setup using a Helmholtz coil. This option was extensively used to measure the ME-coupling coefficient of the magnetoelectric ceramics, see Fig. 5.13a.

Adaptation: Integrating different field sources in the same space requires the consideration of their compatibility with each other. Specifically concerning aspects of how the fields are generated and if the mechanism of one field source could cause an error in another. For instance, the stray magnetic field could disturb the spindle thread rod of the testing machine. However, in the devised, the stray magnetic field setup doesn't create any risk for error since the high permeability of the magnet frame conducts most of it. At the concepts phase of the setup, various design was considered to align the load path parallel to the magnetic field (Appendix B.2[3], Fig. B.1).

Here, a hole is drilled through both poles. The load path is guided via alumina rods through it. The trade-off is a lower magnetic field homogeneity, which is, however, sufficient for probing magnetoelectric, see Fig. 4.6.

This approach requires a balance between a minimum hole diameter for obtaining a high homogeneity of the magnetic field and a large enough one in order to obtain the necessary mechanical stiffness of the rods so that their strength is not exceeded while applying pressure.

[3]This would be a custom-made testing machine with special traverse, for which the cost would outweigh the feasibility aspect.

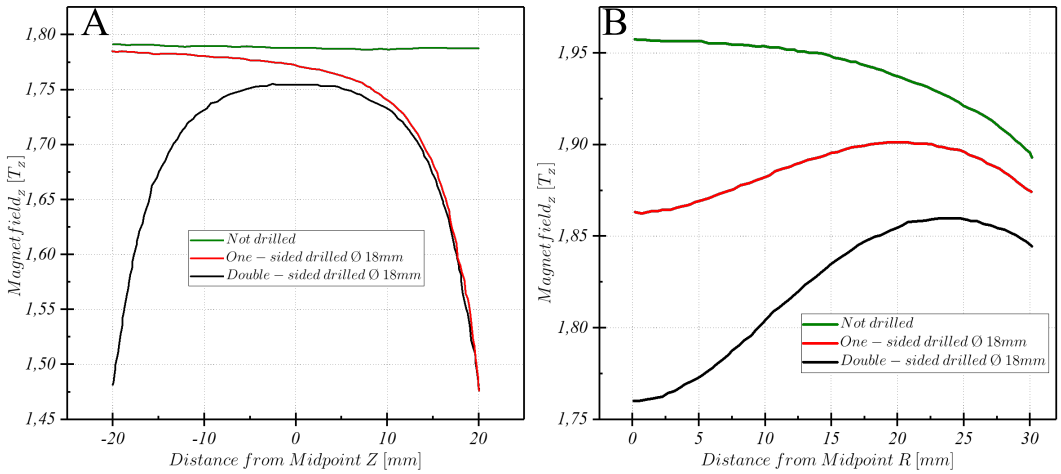

FIGURE 4.6: The effect of hole on the magnetic field in the sample space. The calculation for a pole shoe with about 120mm diameter of the face and air gap 50mm. The diagrams show the behavior of the Bz magnetic field component in the radial direction at z = 0 and axial direction at r = 0 for the cases without bore, with an 18mm bore on both sides and an 18mm bore on one side only.

The total length, from one pole of the magnet to the other that needs to be drilled is 1.20m. However, the total length of the two rods that are fixed to the frame of the test ing machines, that need to meet each other in the centre of the magnet is longer. It is 920mm for the fixed rod from the bottom of testing machine and 720mm for the movable rod connected to the traverse and load-cell of the testing machine. The critical force needed to cause buckling of the rods was calculated according to Euler's column formula, Fig. 4.7.

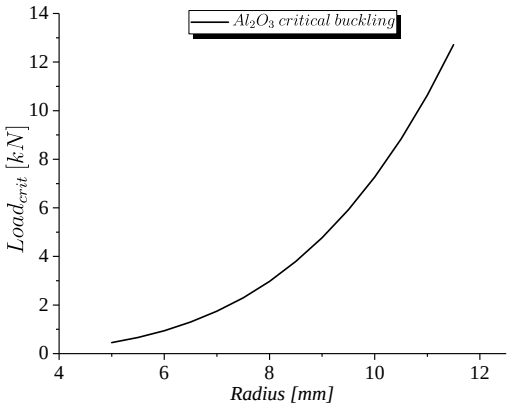

FIGURE 4.7: Critical force for the total lenght of Al_2O_3 rod before it fail due to buckling

$$F_{Eueler} = \frac{n\pi^2 Y_{mod} I_{ner}}{L^2} \tag{4.1}$$

where,

F_{Eueler}	is the *critical buckling load(N)*, n = factor accounting for the end conditions, in this case, one end is fixed, and one end is free $(n = 0,25)$
Y_{mod}	is the modulus of elasticity of alumina, 375GPa
L	is the length of the column (m) and
I_{ner}	is the moment of inertia $I_x = \pi r^4/4[m^4]$

By taking this argument into account, the trade-off concerning the rod's diameter for the total rod length is that the rod diameter must not fall below 16mm. Otherwise, there is the danger that the bar will break under stress.

Given the requirement for precise maneuvering of the magnet inside the frame of the testing machine, the position of the drilled hole ($\varnothing$ $21mm$) needs to match the location of the alumina rods ($\varnothing$ $19 - 20mm$) that is attached to the frame of the universal testing machine while it is positioned on the rail track. The match over the whole length of 920mm

from the bottom point of the testing frame, and over 720mm from the traverse to the middle of the sample space (between the pole shoes), requires a precise angle alignment. In other words, the angle accuracy for the drilling precision through the magnet needed to be better than $tan^{-1}(1/800) < 0,1°$. This also requires an angle alignment mechanism between the magnet and the rods (attached to the testing machine) during the positioning process, as they are separate units. This is achieved for the rail track using of adjustable feet under the part holding the magnet. The adjustable feet have a spindle thread with an angle compensation via a ball joint (a product of *Item* GmbH). In addition, a screw-driven precision wedge shoe was mounted underneath the testing machine, allowing it to be tilted (a product of *Bilz* GmbH), Fig. 4.2b.

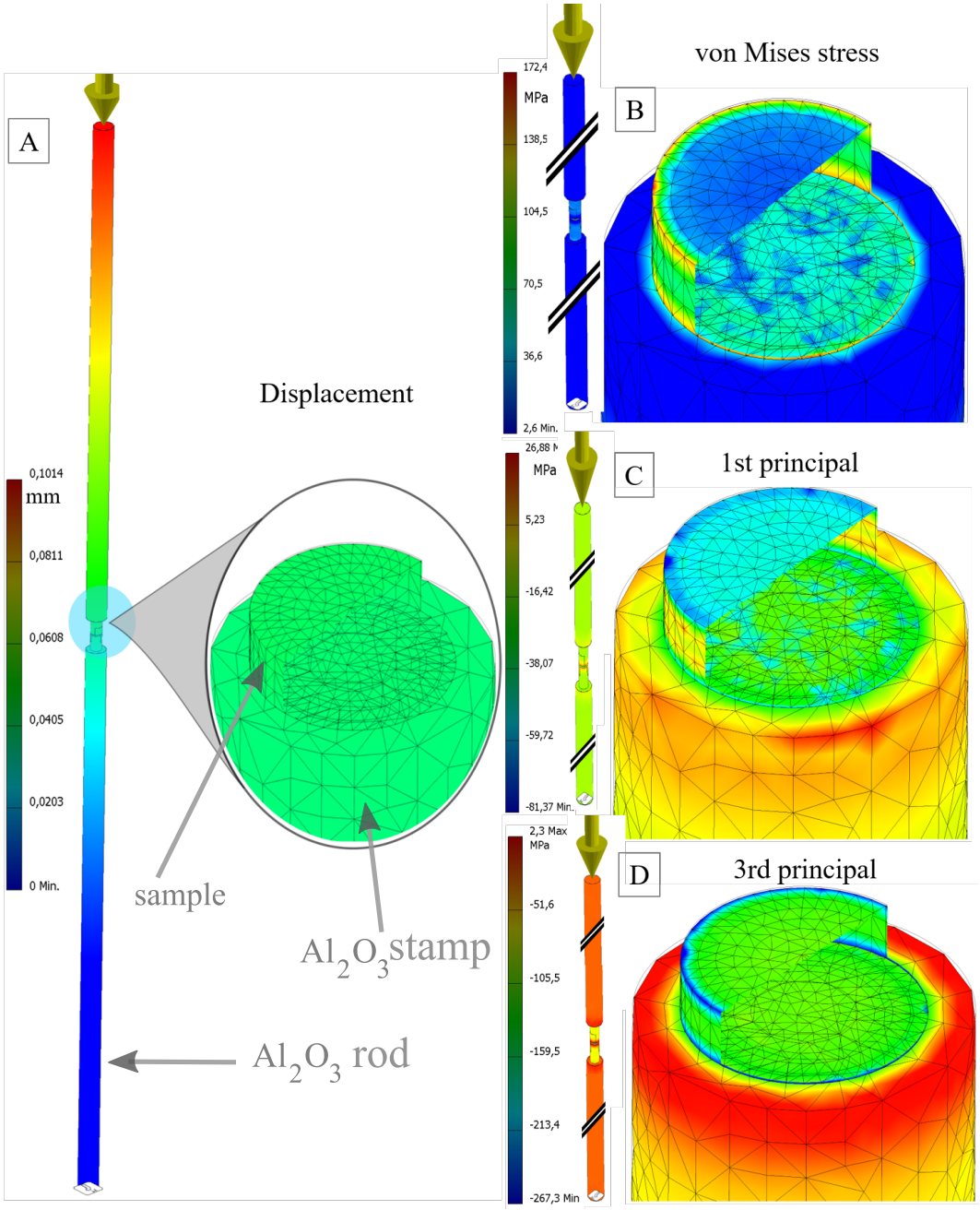

FIGURE 4.8: FEM simulation of stress in the rod system with the sample in place. A 200 MPa stress field is applied. The boundary conditions are the same as in the experiment, with the bottom rod being fixed and the thrust rod loading from above. The input values of the simulation are the standard literature value of Young's modulus for a CFO sample and alumina. A.) The simulation shows that most of the strain occurs in the thrust rod over the entire length of the rods. However, the interferometer is mounted in a limited sample space to measure the strain from the sample. B) Von Mises stress shows the likelihood of sample destruction due to high stress. As expected, the highest risk is at the edges. C) and D) show the stress that occurs in the direction of the force and the lateral stress caused by the same force. Details of the simulation parameters: Sec.Appx.B.1

Handling: A rolling carriage with an integrated rail system was designed to keep the magnet agile. It was also required for changing the ceramic rods. Furthermore, this enables modularity, as it keeps the possibility open, if necessary, to use the magnet or the testing machine separately for other purposes, see Fig. B.6. For other purposes, the magnet must be able to be moved out of the testing machine. An additional safety feature is an arm mounted on the carriage to position the rods during the movement of the electromagnet. Once the electromagnet is placed, the magnet is fixed by screwing four aluminium plates to lock the carriage with a magnet at the four fixed points on the rail track. A wheel rail track is used to decouple the magnet from the fixed track line inside the universal testing machine. This option is crucial as the fixed rail track construction with its adjustable feet needs to be positioned precisely inside the testing machine frame, see Fig. 4.2. The two rail track systems have the same height and track width. Nevertheless, the adjustable feet offer the possibility to compensate for any height differences. In order to ensure that the two rail constructions can be correctly docked together and that the two rail systems are screwed to each other, they are fixed with aluminum plates on each side. In this manner, the magnet can be manually transferred from one rail system to the other.

Avoiding vibration noise Strain measurements are exposed to various sources of noise. The background vibration noise in the setup is coming from the building, water-cooling, room ventilators system, etc. Given the requirement for strain measurements of nano-scale movements, it is crucial to avoid noise sources as much as possible. These problems were partially solved by placing the setup in a room decoupled from the basement[4].

A further route to mitigate any errors caused by vibration and structure-borne noise involved the *decoupling* of the magnet and testing machine. For instance, this would occur if both were placed on the same pedestal[5]. The noise caused by the water-cooling cycle of the magnet could transfer into the strain measurement space. Additionally, damping pads[6] had to be installed under the testing machine in order to ensure optimum damping properties under dynamic loading.

The strain sensor head is located in the close vicinity of the sample in order to keep the ambient noise level low. The nearest possible point to the sample is the load stamp position: Therefore, the sensor head holder is designed as one separate unit with the stamps integrated with them, see Fig. 4.18. Furthermore, the integration of strain measurement geometry *on the load path reference* ensures the correct measurement, given that it is installed on the same reference axis. Otherwise, if the measurement is performed in the frame reference with a fixed point decoupled from the load path, the strain measurement would be erroneous since tilting compensation/adjustment is not given as they are not in the same reference frame. Being on the same reference axis configuration makes the measurement insensitive to tilting and up and down movement.

In general, the traverse in a screw-driven testing machine is stiff. This is the reason for high precision in strain measurement, as the sensor head and mirror are *clamping* in the same frame of reference inside the measurement system. Since the sample is clamped under uniaxial stress, most of the noise due to background vibration would not have much effect on the clamped axis configuration. The observation is that the noise level decreases as the uniaxial pressure increases since the loading frame functions as a fixture frame. This is in opposite to how a cantilever-based scanning technique (AFM) behaves, as the detection is not fixed in the same frame and, therefore, it requires damping measures, like massive concrete blocks.

[4] Originally this room was designed for sound experiments.
[5] Fig. B.2, illustrates all the alternative as a collage of ideas integrated in a different setup assembly.
[6] Made from a combination of nitrile rubber and cork particles embedded in a composite of cotton fibers.

4.2 Automation of data acquisition[7]

The motivation behind the automation of a measurement task is manifold. First and foremost, automation significantly contributes to time saving. It furthermore supports confidence in the measurement, as the procedure is defined, which is essential to ensure the repeatability of the measurement. With this, accurate and precise control of the devices contributes to avoiding random errors in the data. The control of the devices is mainly demanded in multiple field environments, as additional fields mutually influence the other measured parameters. Here, time synchronization is a significant issue, and the excitation fields are causing changes with different rates in the sample and can cause latency. Moreover, the knowledge of the measurement procedure is secured in the source code. With this, the know-how on the operation of the instruments is not necessary to be acquired.

4.2.1 LabVIEW©

Due to its graphical functionality and libraries, LabVIEW offers modular programming in an object-oriented manner at a high abstraction level. Therefore, the programmer gets a rapid understanding of the development environment. Furthermore, given the demand for multiple field environments, the multithreading capability of LabView is an essential benefit of its implementation. For each option of the setup, a LabVIEW application can be programmed. Consequently, the complete task can be divided into smaller modules called functions or procedures. These are available in LabVIEW in a library, VIs (Virtual Instruments). The VI functions enable rapid program development as they handle one particular responsibility. The main idea is that as long as the programmer sticks to using the interfaces between the module blocks, he has the advantage of instrument interchangeability without being forced to change the source code. This lends itself to the automation of a modular setup, as realized for the setup in this work, Fig. 4.9.

National-Instruments (NI) offers LabVIEW with the NI-Max framework, which provides a control framework for timing issues and the ability to synchronize operations at a very low level of the system, as this is included in all National Instruments drivers.

For the setup in this work, two measuring PC stations were configured to take full advantage of modular coding for the modular setup. The intention behind this is to develop an agile automation and debugging process. Consequently, while one station measures, the other can be dedicated to further development and debugging different modules. This configuration proved to be a very productive arrangement during this work. The related modules for measurement in this work are presented in the Appendix, see Figs. B.9, B.8, B.10.

Regarding Fig. 4.9, it displays the automation of the measurement environment of each module using the single responsibility principle for each function. The developed applications allow the user to enter the settings of the experiment parameters. The risk assessment for the stress parameter at this stage of program development was high. It is manually applied as a constant value for multi-field experiments.

[7] The automation task has been done mainly by Yang Lai and Zhouchen Xu in their master thesis. [151, 152]. Their contribution and those from Daniil Lewin regarding debugging and improving the measurement routine are greatly acknowledged and appreciated.

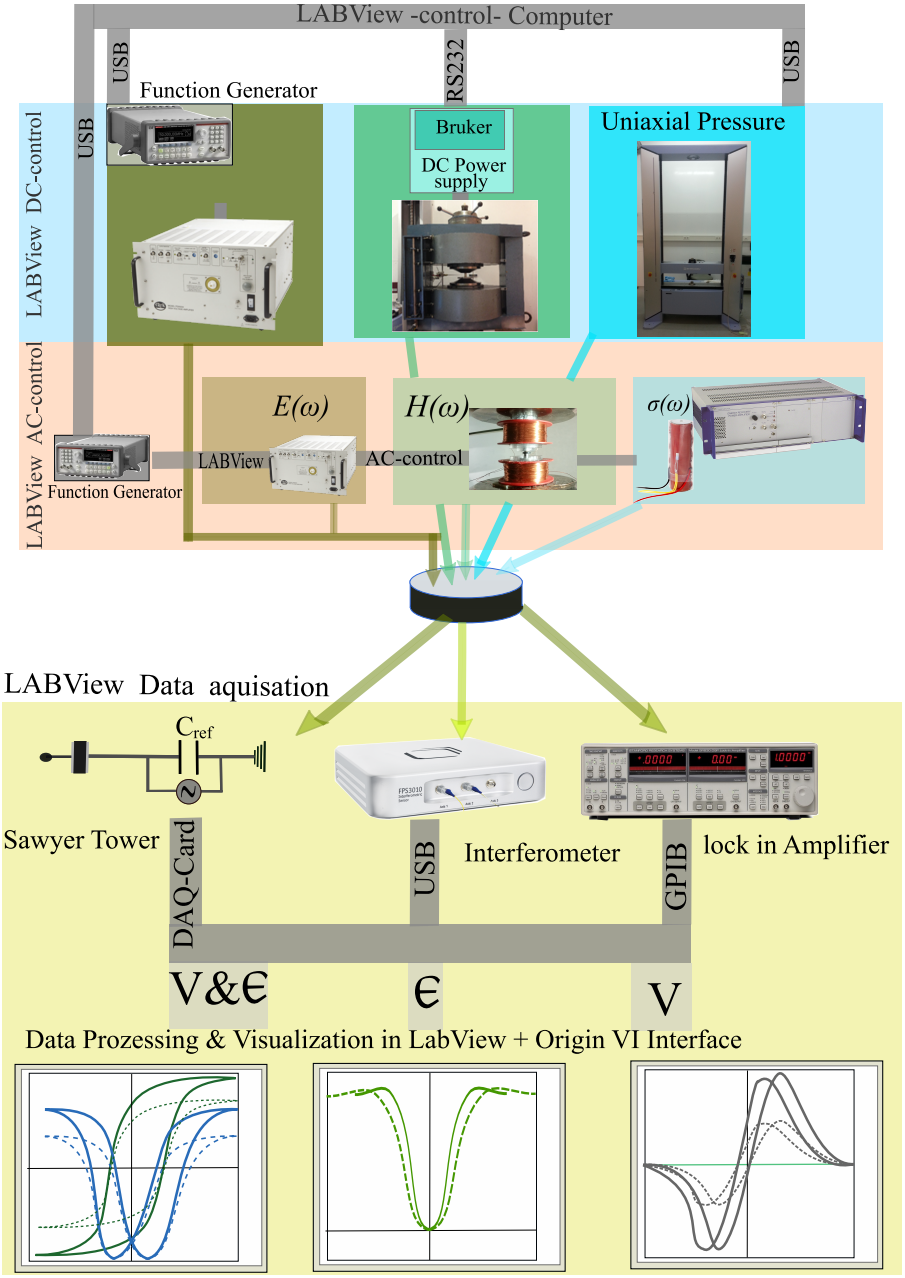

FIGURE 4.9: LabVIEW-based automation concept layout for all modules. Moreover, the measured data are visualized in real time and can be used to calculate the final physical values. On the control side, in the LabVIEW Front Panel, Fig. B.9, the parameters for the magnetic field H_{dc}(amplit.), and the electric field E_{dc}(amplitude, frequency) can be configured. The AC-modulus of the three fields is controlled through the function generator (Keithley and HP), which has its corresponding LabVIEW-VI module. On the data acquisition side, LabVIEW records the values for the strain ε (magnetostriction λ and electrostriction) from the attocube interferometer over a USB interface. The polarization (P) is recorded as a voltage from the Sawyer Tower circuit via a DAQ-card. The induced magnetoelectric coupling coefficient α_{MED} is acquired by a LockIn-amplifier connected to the PC by GPIB bus.

4.3 Strain measurement

Magnetoelectric multiferroic materials respond to magnetic, electric, and stress fields with a strain since the involved phases possess ferroelastic properties [58]. Depending on the strain sensitivity of the material to a corresponding external stimulating field, the strain measurement method can be chosen. An easy-to-use method, such as a strain gauge, Linear Differential Transformer (LVDT), or capacitive-based method, can be applied to measure the strain with single-field stimuli. They are mostly sufficient in terms of their resolution and dynamics, see Fig. B.2, [148, 153].

For the measurement of the relationship between stress and strain, mostly a strain guage is used. This is also utilized in mechanical testing machines as they are often attached to its load cell. In addition, the strain gauge-based method (being calibrated ahead in a magnetic field) is commonly used for magnetostriction measurements. However, it is not suitable to be used in a dynamic and multi-field environment. For instance, as required for the measurements of the ferroelectric butterfly hysteresis with low thickness samples (1-2mm) under stress [60, 148] attaching the strain gauge becomes practically impossible.

In this case, an LVDT as part of a contact method[8] is commonly used[9] [153]. However, due to its functional principle, it is impractical to use LVDTs in a magnetic environment. Optical strain measurement techniques, as non-contact methods, offer more benefits with regard to their resolution and frequency bandwidth [154]. However, they are error-prone as they are susceptible to mechanical noise. Therefore, they need engineering in order to be adapted to the setup. They are also suitable for measuring thin-film samples in contrast to the strain-guage and LVDT-based methods. The scope of this work requires integrating a strain measurement technique compatible with the multi-field environment and providing a resolution below $5nm$, see Fig. 4.10. Strain measurements compatible with the multi-field environment provide the basis for comparing strains originating from different stimulus fields. Moreover, the fields can be applied simultaneously. It is crucial as the functional composite materials respond to the presence of each field with varying amplitudes of strain. In terms of experimental feasibility, the method of choice needs to be practicable, as is partially discussed in Sec. 4.4.

The properties of the materials and their characteristic form (as a thin film, bulk, single or polycrystalline) play an essential role in choosing a method for the strain measurement in a given geometry of the experiment and it also determines the measurement design. Moreover, single crystals possess a defined response axis upon interaction with the corresponding stimuli field, which gives them an inherently defined property direction. In contrast, the properties of polycrystalline are averaged. They don't possess a preferential direction. [10]. The following section will cover the essentials for the appropriate choice of strain measurement.

4.3.1 Analysis of a suitable method

Various measurement methods exist for recording the magnetostrictive behaviour of ferromagnetic/ ferrimagnetic materials, Sec. 2.4.2. The literature values measured for magnetostriction are diverse due to the various factors which play a role: grain size, sintering route, and measurement method. Therefore, awareness of the common source of error in

[8] With a mirror and spring combination in contact with the sample, Fig. B.2.

[9] Used in differential dilatometer arrangement resolving displacements of 10nm [148] .

[10] That is due to its structure since it is made up of grains with random orientation. This fact will affect the nature strain as the material interacts with external fields. Especially in the case of magnetostriction, Sec. 2.4.2 .

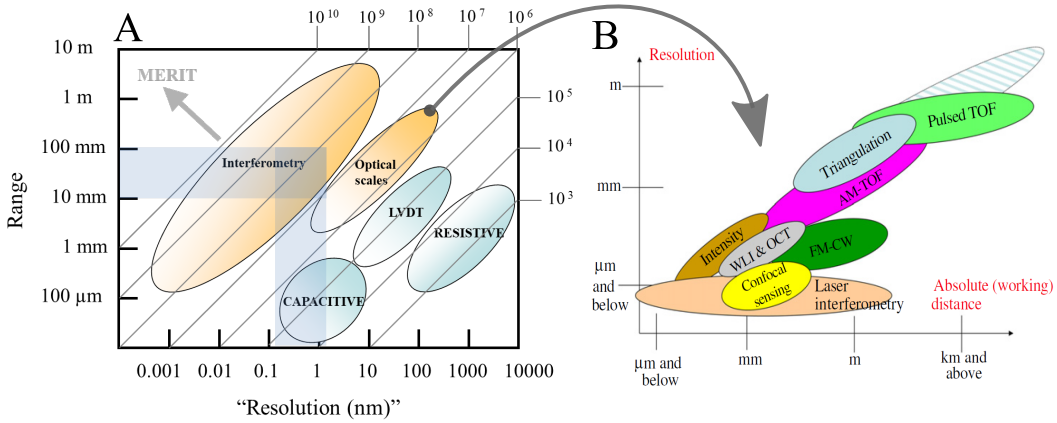

FIGURE 4.10: Position and Displacement Sensors arranged considering their figure of merit, courtesy of Attocube, Haar, Germany. B) Displays the variety of optical strain measurement methods [154]. Reprinted with permission from OSA Publishing.org

TABLE 4.1: Specification of relevant aspects for strain measurement instruments

Aspect	Arguments
• Resolution	The device *integration needs to achieve a* minimum resolution of 5nm and a drift time stability of over 1sec. [155]
• Environment	Need to be unaffected by electric and magnetic fields. Especially, the sensor head is required to be nonmagnetic.
• Size	Space confinement due to the mechanical loading nature and the small air gap between the magnet pole shoes requires a small size for the sensor-head.
• Fiber optic	Guidance of the laser beam into confined space, in contrast to other interferometry method and optical in general.
• Non-contact	Contact method can cause erroneous measurement due to incompatibility with the field, and displacement range.
• Multiaxial	3 measuring channels allow coverage of all axes.

the measurement facilitates the proper method choice. In the following, the example case of a strain guage is discussed to cover some of the issues related to strain measurements.

The strain gauge-based method is widely used for displacement measurements of magnetic and ferroelectric materials [156, 157]. A strain guage is a comb-like wire structure that is attached to the tested material. The strain is measured as a change in electric resistivity of the fine guage wire as it distorts when the material undergoes deformation under the influence of an external stimulus. A Wheatstone bridge is used to measure the very small variations of resistance. Its simplicity makes this method a straightforward technique. However, it suffers from various limitations and drawbacks, which make the technique error-prone. A proper measurement requires good practical skills and experience of the user [158]. The problems start with installation techniques such as surface preparation, bonding, wiring, and how the protective coating is applied.

Furthermore, suitable adhesives and the right cure temperature are needed to ensure reliability. These are some of the critical aspects that need to be mastered to realize the potential high performance of a resistance strain gauge. In addition, the measurement of the resistivity in the wire is sensitive to the ambient temperature, which is a common source of error and a cause for divergent values. An awareness of the wide range of materials used for the strain-guage alloy is crucial since different materials apply to particular experimental conditions. For instance, during magnetostriction measurements, a magnetic strain-guage alloy would interact due to the current with the magnetic field or even experience magnetoresistance, causing spurious resistance changes. This would tend to change their length in the magnetic field, which causes additional measurement errors.

Concerning the scope of this work, the strain measuring technique is not constrained to pure magnetic materials but needs to be able to measure composite magneto electrics. This implies that the device of choice needs to meet the requirements set of the bulk magnetoelectric composite ceramics. They possess low magnetostriction and a relatively low sample thickness due to the confined measurement space[11].

4.3.2 Strain method for multiferroics

Strain is the most relevant characterization quantity for any field with mechanical dependency. The strain measurement of multiferroic composites requires a metrology tool suited to measure displacement under the influence of high magnetic and electric fields. Furthermore, it needs to fit in a highly confined space due to mechanical load for uniaxial stress measurements. After a detailed analysis for a suitable method that would meet the requirements, it turned out that the fibre-optic Fabry-Pérot interferometer would achieve the objectives of this work, see Fig. 4.10 [159]. All other strain measurement methods would neither achieve the resolution nor the universal applicability of the Fabry-Pérot interferometer. Given the dimension and low effective strain in composites and thin films, and the vulnerability of contact methods, the use of an interferometry-based method is crucial for measuring composites and, consequently, is the method of choice [155]. In addition, other optical methods would not be suited, see Fig. 4.10B.

4.3.3 The use of interferometry

Regarding precision and versatility in metrology, interferometry is the method of choice. A laser, as a source of coherent light, is essential for its technical realization since the interferometry method takes advantage of properties inherent to wave interference. In the method, the light of the coherent source is split first into two paths, where one acts as the reference and the other as the detection path. Both paths are eventually joined back together where they interfere, as illustrated in Fig. 4.12A.

The information extracted from the changes in wavelength, phase, intensity, frequency, and bandwidth gives information about the nature of the displacement. A laser source has all the necessary input information to perform such multifaceted measurements. It is also, at the same time, meticulously controllable. Additional improvements that contribute to the richness of this technique, besides the laser, are the incorporation of fast and precise electro-optical detection of the interference fringes and an associated computer-assisted automatic evaluation.

The interferometry technique allows precise measurements in a broad dynamic range, given its phase sensitivity, which is reflected in the intensity of the interference pattern. It facilitates a high resolution for the strain measurements compared to all the other optical

[11] Compared to the dimension of a strain gauge, all samples lower than 3 mm thick are difficult to measure.

methods see Fig. 4.10. Additionally, due to its nature of being electromagnetic waves, it is a multi-field compatible technique.

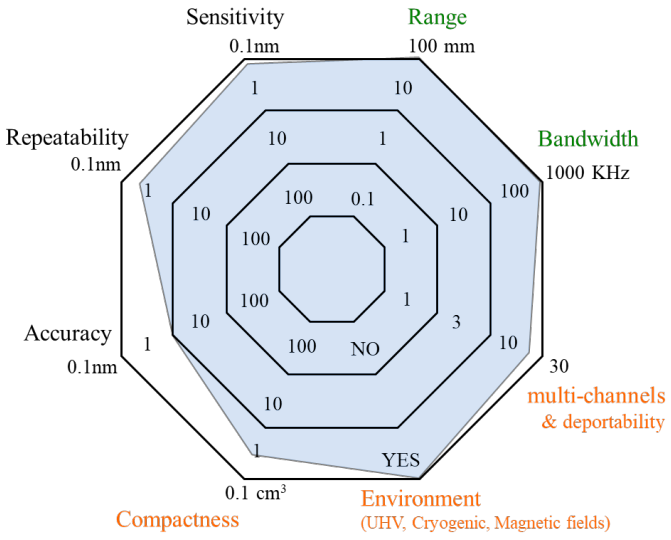

FIGURE 4.11: Illustration of the multifacetedness and technical specs of Fabry-Pèrot fiber optic interferometry as a spider chart. The degree of complexity of the instrumentation grows outwards from the center of the chart. The blue coloration covers the specification of attocube's FPS3010 interferometric sensor [Haar,Germany].

The emergence of the optical fibre played a pivotal role in the evolution of interferometry, regarding its technological utilization [160, 161]. In this case, the merging of fibre optics with interferometry methods brought more robustness to the technique. It also expanded the range (Fig. 4.11) for the Attocube's FPS3010 interferometric sensor, (Haar Germany), as the state-of-the-art realization of the technique.

The essential features of an optical fibre are compatible with the requirements for a strain measurement technique in the setup of this work. Its high flexibility for the guidance of light into confined spaces and its small form factor enable its integration. In the fibre the waves are guided in accordance with Snell's law, which allows more adaptability. It preserves all the inherent properties of a laser due to its multiplexing, high accuracy, and low propagating loss [162], Fig. 4.11.

A further advantage of an optical fibre is the use of only one sensing path, as, at the cut-face of the fibre, some portion of the light is reflected into the fibre. This is used as a reference before it propagates in the air see Fig. 4.12. It gives interferometry the ability for simultaneous sensing while its immunity to electromagnetic interference has persevered. With all these attributes, the optical fibre makes deflection mirror elements redundant, enabling remote sensing in the present setup.

Operating principle of interferometry: Michelson interferometry demonstrates the physical principle behind the interferometry technique in an illustrative manner. In this case, the incident plane wave is divided into two halves, see Fig. 4.12A.

In the figure, wave (a) passes through optical path 1, and the mirror M2 reflects wave (b). After the beam splitter, the two waves are reunited, and consequently, they interfere with each other (5) and thus form an interference fringe pattern. Because of its geometry and the requirements for its usage, the Michelson method is impracticable and too error-prone for most applications[12]. Therefore, using optical fibre is a convenient route to overcome all difficulties.

[12]It requires vibration isolation via an optical table, a fixed path length as a reference, optical elements, and temporal stability.

Fabry-Pérot interferometer sensor:

This method is also based on the interference of two optical paths. However, the optical paths are different from those in the Michelson interferometer, see Fig. 4.12A. In the Fabry-Pérot configuration, the optical fibre is the crucial element for the optical path guidance, see Fig. 4.12B, allowing a compact size. In addition, the beam from the laser diode doesn't need to be split by a beam splitter, and there is no need for a reference arm.

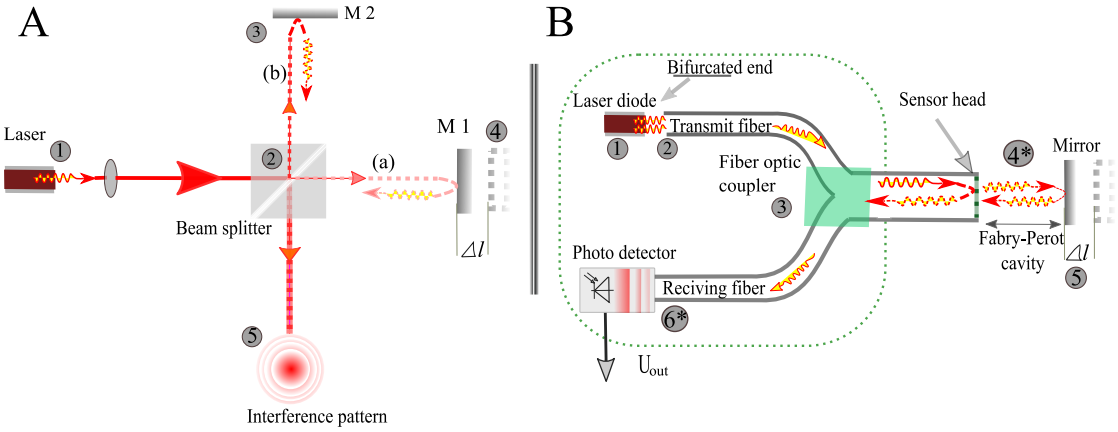

FIGURE 4.12: A) Formation of interference fringes in a *Michelson interferometer.* A beam of monochromatic light is split so that one beam strikes a fixed mirror and the other one a movable mirror, resulting in an interference pattern as they are brought back together. B) In Fabry-Pérot Interferometer, the beam spiting is done inside the devices, and the light is guided inside the fibre optic.

Principle of operation A laser diode[13] Fig. 4.12B(1) serves as a source of a coherent beam. Inside the device, the laser beam is coupled into the fibre (2) and guided through the coupler into another fibre (3). The beam is partially reflected at the end face of a cleaved[14] optical fiber (4).

However, a larger portion of the beam is transmitted into the air, which works as a sensing path, see Fig. 4.12B. The beam subsequently reflect back into the fibre from the target (5), which has a mirror attached to it. The distance between the target and the fibre end builds an air cavity. By utilizing this technical configuration, the requirement of a Fabry-Pérot -Interferometer is achieved [159]. Such an interferometer arrangement functions as an optical resonator[15], see Fig. 4.13A.

As the beam passes across the cavity, it reflects from the mirror (5) at one end and partially from the cut end of the fibre optic at the other. It resonates in the cavity and forms a standing wave, partially injected back into the fibre (4). Its transmission spectrum shows a narrow transmission maximum for wavelengths, where the optical path length of the resonator is a multiple of half the wavelength of the incident beam, see Fig. 4.13B. In other words, it meets the resonance condition and shows an interference effect in the resonator, while the other spectral regions in the transmission are almost entirely extinguished. For a displacement (Δl) the pattern fringes periodically change, depending on the distance x_0

[13]Mostly, a tunable DFB laser is used (distributed feedback laser). Attocube* FSB is using the standard telecom wavelength (λ = 1550nm). All the additional optical lenses can be purchased based on the wavelength property.

[14]The process by which an optical fiber is "cut".

[15]An array of mirrors that serves to reflect the light as often as possible.

between the fibre end and the mirror. This results in the variation of intensity of the interference fringes, which are detected by an InGaAs photodetector (5), and the real displacement amplitude is calculated, see Fig 4.13C.

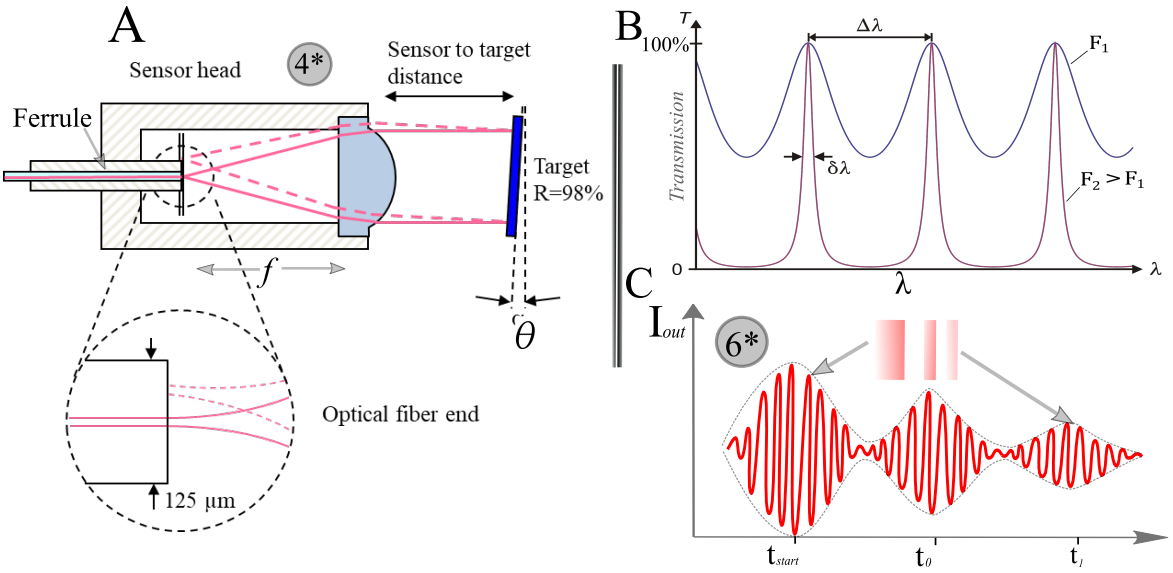

FIGURE 4.13: A) Illustration of a detailed view of the optical coupling, consisting of a confocal system with a highly reflective plane mirror on the target and a lens that collimates the light emitted from the fibre. A technical realization of the sensor head with its lens is depicted in Fig. Appx.B.4. . B) The transmission in a FB cavity as a function of wavelength. F stands for the finesse of the optical resonator (cavity). A high-finesse reflectance shows sharper peaks and a lower transmission minimum than a low-finesse mirror. The free spectral range is $\Delta\lambda$ (shown above the graph). C) Detailed illustration of Fig. 4.12B. The interferogram shows an oscillation period of half the wavelength and width corresponding to the coherence length of the source. The interferogram gives the position of the sensors.

The role of sensor heads:

The Fabry-Pérot functioning principle, when applied to a displacement measurement device, also has some disadvantages. These are mainly related to its low back coupling efficiency. Once the beam is transmitted into the air, it disperses in all directions, and only a small portion of the beam is redirected into the fibre. Therefore, a collimator placed in the optical path would help to guide the beam to the moving target and back into the fibre, as it reflects from the target. Its use additionally improves the alignment process.

The alignment procedure is a critical issue for this method, a common problem for interferometry techniques. The realization of an alignment tool in a hostile and confined environment is a challenging task[16], which requires additional measures. The use of an optical lens to focus the beam, see Fig. 4.13A, can help to some extent, solve the alignment difficulties. There are different sensor heads available in the market. However, they are all made of titanium alloy[17]. For this work, several sensor heads based on plastic materials have been designed, see Appx. B.4 [18].

[16] Examples are magnetic fields, cryogenic environments for temperature-dependent measurement, and Vacuum chambers.

[17] And expansive to purchase.

[18] They are intended to verify the sensor head's compatibility with the magnetic field, as in the course of work, some of the sensor heads exhibited attraction to the magnetic field.

The use of a collimator lens makes, on the one hand, a larger angular tolerance possible, and on the other hand, it allows the use of an optimum working range, which depends on the focal length of the lens. Furthermore, a higher beam recoupling permits the use of a polished sample surface as the reflector and eliminates the use of a mirror, which is desired in confined spaces.

Implications for the measurements:

A technical realization of a displacement measurement device based on the Fabry-Pérot - principle is made by the *Attocube Systems AG*. In this case, any tilting of the optical axes in the cavity away from the aligned configuration, like lateral displacements of the target during target movement, would lead to a lower intensity coupling into the fibre, see Fig. 4.13. In data processing, a change in intensity is treated as a cavity length change. During the alignment procedure, the device calibrates a particular setting as zero displacement for a given cavity configuration in order to deliver an initial finesse coefficient [161], Fig. 4.13B. The device computes length changes due to the displacement based on changes in the transmission coefficient and interference intensity. The displacement computation is accurate, assuming that the cavity configuration changes only along its length. However, changes that cause a decrease in the constructive interference intensity due to any tilting or lateral movement can cause an influence on the data. For the integration of the sensor head from an engineering point of view, the angle dependency can be further reduced by focusing the beam such that it needs smaller working distances. As a result, the system will be more tolerant for misalignment. In addition, lower reflectance materials can be used due to the shorter length, which provides a higher flexibility regarding surface reflectance quality.

4.4 Strain sensor integration

In the context of magnetoelectric materials, the strain needs to be recorded as a response to all three relevant field couplings.

For this purpose, a range of setup configurations is necessary to achieve strain characterization with an interferometer. In this work, the integration of the sensor head for three different configurations was undertaken. These were for the case of:

1. Magnetostriction measurements of composites
2. Strain curves as a function of the electric field (butterfly hysteresis) & polarization with the possibility of applying a magnetic field (P-E & S-E)
3. Butterfly hysteresis & polarization under constant pressure & magnetic field (P S E_p = const)

Integration of FB-sensor head for electrical characterization: Macroscopic characterization of the *mechanics* in ME-composites requires, among other things, the simultaneous measurement of polarization and strain as a response to an electric field excitation. One primary method of testing the switching behaviour in ferroelectric materials is the measurement of the ferroelectric polarization hysteresis P(E) and its corresponding strain hysteresis S(E), see Sec. 2.4. These measurements can also be applied to ME composites[19].

In this work, it was essential to determine, if an external magnetic field can influence the butterfly hysteresis measurement. However, this demands a device compatible with the

[19]The measurement method doesn't deliver the same information as the ferroelectrics since ME composite is leaky and can not be poled.

relevant experimental boundary conditions. In order to acquire all the necessary parameters for the development of a sample holder, the use of all fields and their related effects on the sample holder need to be considered.

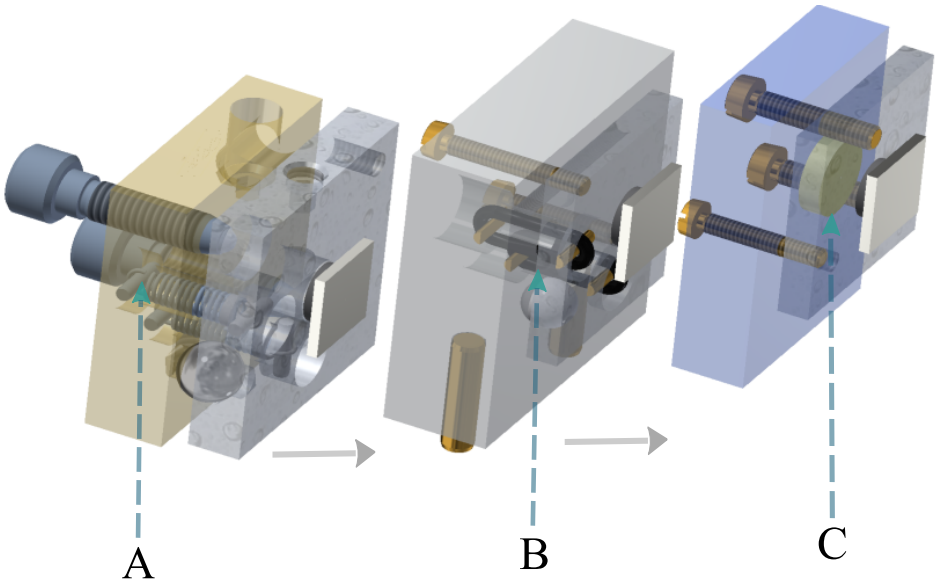

FIGURE 4.14: Evolution of the → non-magnetic beam alignment inserts. (A) Inserts inspired by OWIS GmbH, however, due to its metallic components is not useable in this application. (B) An evolved version of A, in which the metallic parts in A have been replaced. (C) Insert based on an entirely new concept and final version of the non-magnetic alignment insert. It uses the elasticity of silicon, and a round cylinder see schematic, Fig. 4.15. It has been integrated into all strain measurement options. See Fig. B.4C for the proof of concept.

All fields compatible alignment inserts: An aligned and focused beam would have a higher reflected signal coupling into the fibre. Therefore, it is necessary for the strain measurement with the Fabry-Pérot interferometry method, see Fig. 4.13A, to have an exact alignment procedure for the laser beam (sensor head), see Fig. 4.14. Furthermore, this method must have measures to encounter noise vibration and provide long-term stability. The commercially available optical adjustment inserts are unsuitable for this work.

For this work, an adjustable *nonmagnetic* and *miniaturized* alignment insert to align the laser beam has been developed. It is designed to allow a beam alignment of under 0.1°. During its development, two different versions were tested, see Fig. 4.14.

For the insert, Perspex was used as the base material. The first developed version of the alignment insert used a rubber sealing ring as a replacement for a spring and a ceramic ball as a replacement for the metallic one. Two brass screws were used in the contact plate to align the angle of the surface plate with the faces of the beam from the laser. However, it turned out that the rubber under tension tended to become brittle with time and needed frequent replacement.

A further drawback of the first design and the commercial ones is that the alignment must be achieved with two aligning points, as the ballpoints are fixing the plane in a position given by the point of contact with the ball. This makes the process of alignment time-consuming (5-15 min), Fig. 4.15.

An entirely new alignment insert concept was developed in order to counter the one-fixed point constraint for the mirror-plane adjustment, Fig. 4.14C. The latest version consists of two Perspex plates: a bulk plate is fixed on the reference line to the sensor head, and another smaller plate (15x15mm) is screwed on the front of the fixed one, with a circular silicon rubber glued between them (∅ 6mm, height 1mm), see Fig. B.6B and C. The three screws (brass) tighten the two plates to each other on the edges. Here, by using different tightening levels on each screw, an offset of the edges relative to each other is achieved due to the soft silicon rubber. This allows the plane to be tilted to some degree, depending on how far each edge is tightened to the fixed plate, see Fig. B.6B.

An advantage of this improvement was the rapid alignment of the signal in less than 3 minutes. The absence of a fixed point dictated by the ball and its replacement by a screw, gave the mirror plane an additional degree of freedom, as now the signal can be aligned by three screw points.

Moreover, the alignment is tightened with screws, which provides better shock and vibration protection than a spring, Fig. 4.15.

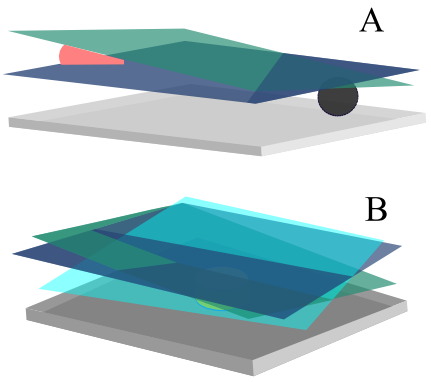

FIGURE 4.15: Illustration of the different mechanisms of the angle for adjustment with different inserts. The ball gives a fixed point for the planes in A (representing the inserts in Fig4.14A and B). B) A soft silicon rubber sandwiched between two plates with, see Fig. 4.14C, three screws for adjusting offers more degrees of freedom for the plane to be aligned compared to version A.

4.4.1 P-E$_H$& S-E$_H$-loops measurement with interferometry

Various experimental approaches have been developed in the ferroelectric community to simultaneously record the P-E & S-E ferroelectric hysteresis, Fig. Appx. B.2. As previously discussed, the method of choice for strain measurement depends on the resolution, accuracy requirements, and environmental conditions[20]. The integration design of the strain measurement device requires ingenuity with regard to the experimental conditions and is a substantial aspect of the setup design.

Concerning the measurement of P-E$_H$& S-E$_H$ of magnetoelectric composites, a suitable setup has not been reported yet in the literature. Such a strain measurement concept must be compatible with the application of a magnetic field. It also needs to record displacement effects as low as 30-50[nm/mm], given the maximum strain of a ME composite. Compared to the displacement effects in ferroelectrics (approx.1-3 [μm/mm]), the strain effects in magnetoelectric composites are two orders of magnitude lower. In this case, following the discussion from Sec. 4.1, a device with a minimum resolution of 3-5 nm is necessary[21].

The existing setups for the measurement of ferroelectric butterfly-loops, for example, those in the group of Prof. Rödel (Fig. Appx. B.2), are too large to fit between magnetic pole- shoes. Furthermore, their contact springs and other metallic parts exclude their use in a magnetic field. In addition, integrating an *alignment insert* is not possible in existing setups, so incorporating the Fabry-Pérot interferometry is not feasible.

[20] As introduced already, various types of exits: fibre optic probe, laser interferometry, capacitance probe, and strain gauges. Also, a commercial one for the measurement of strain and polarization with a double beam laser interferometer technique from aixACCT Systems GmbH is available.

[21] Rule of thumb: minimum 10% of the effect.

A Perspex container was designed to meet the boundary conditions which are displayed in Fig. 4.16. The container fits between the magnet poles in a parallel configuration, as depicted in Fig. 5.13, Fig. B.6A and the perpendicular configuration as depicted in Fig. B.5). In the case of electrostrictive characterization, the sample needs to be immersed in a silicon bath inside the container[22].In addition, a copper-lead contact passes through the container wall to an electrode contact nipple (7). It is positioned in the centre and slightly elevated above the bottom of the container (Ø2 mm, approx. 0.3 mm above the container ground). This ensures contact with the sample leads, as depicted in Fig. 4.16 (7) and (10).

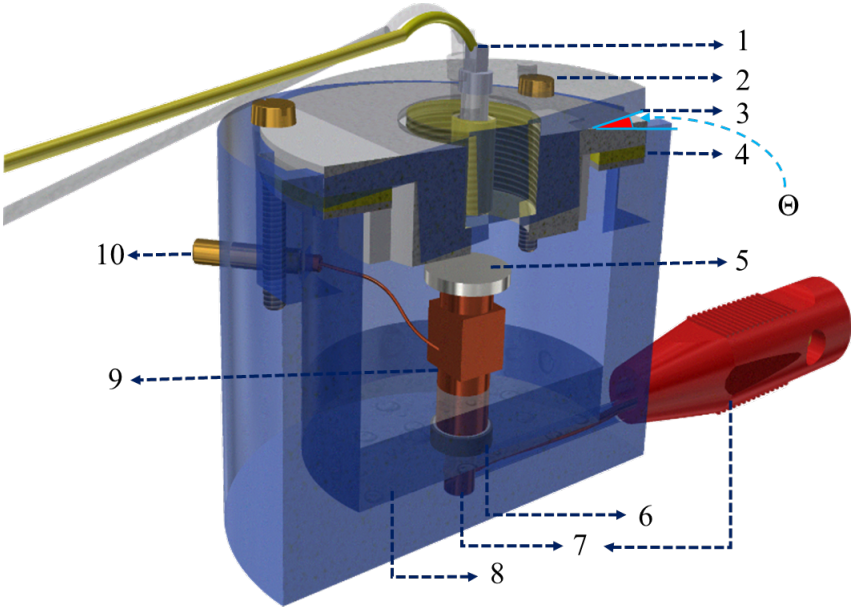

FIGURE 4.16: CAD sectional view. The design of the concept for the integration of the interferometer strain measurement sensor-head. It is integrated in a nonmagnetic container for the P-E_H & S-E_H-Loop measurements. An annular silicone rubber band (yellow) allows an angle alignment of the sensor head (4) to be made. Furthermore, the sample is immersed in a silicon bath and connected to the copper block, where an electric wire is soldered to it. The block (9), given its height, keeps the attached mirror out of the silicone oil bath, thereby enabling the cavity configuration. The numbered items are discussed in the text.

The sample (Ø6-8 mm) is placed in the middle of the copper electrode contact (Ø2 mm), and its edge is glued with two-component adhesive (UHU plus) to the bottom of the container[23]. This ensures a fixed position of the sample[24] (6). In addition, the adhesive approach allows elongation to occur in the field direction, which means that the interferometric alignment is maintained even for the sinusoidal motion of the sample under an electric field excitation. In order to remove the sample, acetone can be used to dissolve the two-component adhesive.

The cavity with the mirror (5) needs to be established for the interferometry applications in the first step. For this, a cylindrical copper block (height = 15 mm) is glued to the upper electrode surface of the sample (9). A copper cylindrical block is used for two reasons: it

[22] It is required to avoid any flash-overs caused by the high voltage. needed for the Sawyer-tower configuration. See the section on Sawyer Tower.

[23] Acetone dissolves the two-component adhesive so that the sample can be removed.

[24] A capacitive measurement is performed to ensure that electrical contact with the sample is available. Given the high resistivity of the sample, a resistivity check would not make it clear whether the sample is contacted electrically.

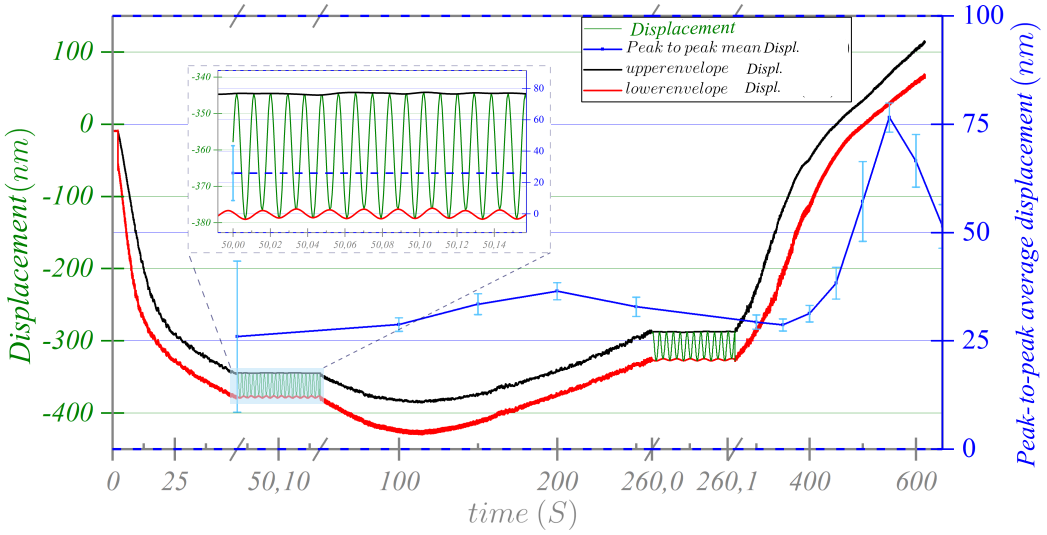

FIGURE 4.17: Displacement measurement with Sawyer-Tower method Sec. 3.8 at a fixed driving voltage for CFO_{25} BTO_{75} composite sample in the non-magnetic cavity Sec. 4.16. It is showing time-dependent oscillation measurement curve , with a peak to peak average value. The corresponding polarization and strain under magnetic field measurements are covered in Sec. 5.5.1. In a similar manner to the calibration measurements performed on the piezostack, see Fig. B.7, it confirms the functionality of the device.

holds the mirror above the silicone oil bath (8) since the use of silicone oil is required due to the application of a high excitation voltage. Secondly, it establishes a contact between the surface electrode of the sample and the thin wire soldered to it without disturbing the contact with the mirror.

As previously mentioned, the integration of a beam alignment arrangement is crucial for the strain characterization device. In this case, the particular solution is achieved by placing an annular silicone-rubber band (2 mm thickness) in a milled space around the inner edge of the container (4). The sensor head is integrated into the centre of a disc made of Perspex which fits in the milled edge (3). This functions as a cover and tilt alignment mechanism as the round disc is tightened by using three screws (2), which are offset by 120° to each other. The tilt angle θ for the incidence beam is adjusted by changing the tightness of the screws on each corner. The screws couple mechanically to the sensor-head and sample on the same optical path, stabilizing the cavity configuration against vibration, as they have the same reference system.

In the scope of this study, the device functionality was proven by making strain measurements on composite samples, Fig. 4.4.1[25]. A sinusoidal (56 Hz) electric field (25 kV/cm) was applied for these tests. The displacement response was detected, as shown by an upper- and lower envelope of the displacement[26]. The blue curve in the figure shows the mean peak-to-peak displacement over the recorded time. The nature of the displacement is shown

[25]The measurement and data processing by "R"-routine was performed by Daniil Lewin. R is a free programming language for statistical calculations and graphics.

[26]It is displayed as an envelope as otherwise the course of excitation would not be visible.

in more detail in the inset of Fig. 4.4.1. During the measurement, the overall displacement displays a drift over time, although the peak-to-peak displacement stays constant. This can be caused by Joule heating as the applied electric fields heat the sample, and some portion of the heat transfers into the copper bar. Further measurements were carried out to prove the long-term stability of the Attocube sensor while using an actuator. This enables more disturbance-free measurements and excludes device-dependent errors, Fig Appx. B.3.

4.4.2 Setup option for P-E$_{\sigma H}$ & S-E$_{\sigma H}$-loops

Given that device development is an iterative and incremental process, the steps toward the development of a device for $P_{\sigma H}$ - E, $S_{\sigma H}$ - E measurements will be discussed in detail in this section. In order to fulfil the compatibility requirement for enabling strain resolution below 10 nm, it is essential to avoid structure-borne noises in a multiple-field environment. The design for the strain detection requires that, besides being compatible with the magnetic field, the sensing device has to be installed close to the sample and within the shortest possible distance on both sides of the clamping stamps. A selection of discarded ideas that were tested in the development process is presented in Sec. Appx. B.1. In this section, the final version of the module is described.

Applying mechanical stress and an electrical field to a sample necessitates direct contact with the sample. Given this, measuring the strain while the surface is blocked makes an indirect strain measurement inevitable, see Fig. 4.18$_{\rightarrow(1-8)}$. The strain sensor head (1) is attached in the vicinity of the sample[27](4), as the contact between the load piston (3) and the sample surface confines the space.

The sample shape, size, and handling are all part of the design consideration. The thickness of the sample is limited maximum applicable electric field strength by the power supply. Given the specification of the voltage source (7.5 kV, Trek voltage Amplifier), a sample with a thickness of 3 mm can be tested, with 2.5 kV/mm.

Another point of consideration is the choice of piston material. For the simultaneous application of mechanical stress and electric field, it is necessary f to have contact. In contrast, the application of magnetic fields requires no contact. For the case where contact is needed, the contact material should be non-magnetic. A metallic contact would either add a magnetic field or possibly shield the magnetic field. Hence, given the mechanical testing requirements, the piston material has to be non-magnetic but electrically conductive and stiff. A further reason to exclude the use of a metallic material for the piston is the considerations about plastic deformation. The reasons why the load paths need to be stiff, as for in the case of the rods Sec. 4.1, also apply to the stiffness of the piston.

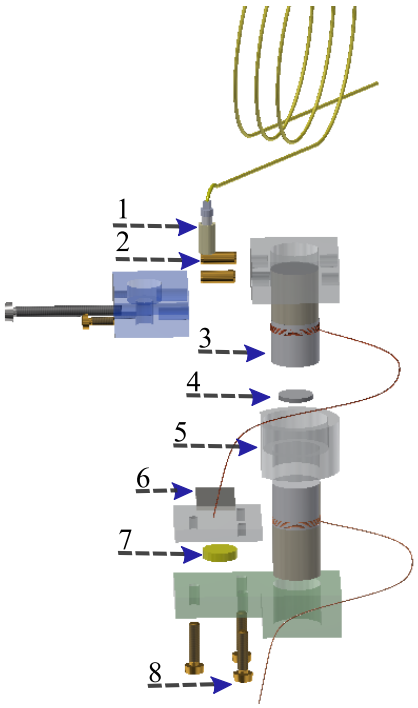

FIGURE 4.18: Detailed view of the construction of the sample space from Fig. 4.3b. It shows the lens holder with the piston upper part(1-3), and the integrated alignment insert, see Fig. 4.14 in the lower part(6-8). The measurement results obtained with this option are presented in Fig. 5.11

[27] Which is also a requirement for the precision of the related interferometry method in use.

In conclusion, in order to reduce the possibility of errors to a minimum, is to use aluminum oxide for the piston material. Its non-magnetic nature and high stiffness[28] make it suitable. It can be made conductive by painting silver paste over its surface and, subsequently, firing this at high temperatures, see Fig. 4.18.

The solution: Considering the proximity of the interferometric sensor head with the piston, the use of Perspex for the sensor head holder is a suitable solution. The advantages of Perspex, besides being an insulator and non-magnetic are: it is easy to process, transparent, has low thermal conductivity[29], and is rigid. The sample holder assembly consists of two parts. The ceramic piston is integrated with the sensor head holder attached to the thrust rod in the upper part. In contrast, in the second part, around the lower piston, built-cavity has been designed. The construction around the piston allow the sample to immerse to into silicon oil bath in order enable an electric field (Fig. 4.18 ,5. In addition, the alignment mechanism (6-8) for a mirror (6) has been incorporated into the lower piston.

The sensor head holder connected with the upper piston will be disturbed, if the traverse of the mechanical testing machine moves up. This is since the piston attached to it would touch the magnet pole-shoe and damage the fibre optics of the sensor head, Fig. B.6. Therefore, as a protection measure to avoid damage of the sensor head fibre-optics, the holder has been divided into two parts and assembled, once the piston reaches the sample surface(2).

The transfer of ambient noise in the measurement space is limited by the integrated design of the sensor into the reference frame. The climbing nature of the experiment, as pressure is applied to the sample, enables to achieve high accuracy due to the stiffness of the frame.

Moreover, the experimental procedure for using the interferometer requires a self- calibration, which involves an automated alignment process to evaluate the intensity. The self-calibration must be performed each time, as a new stress is applied, Sec.B.3.1. The measurement results obtained with this option are presented in Sec. 5.5.2.

4.4.3 Magnetostriction measurement of composites

> What we observe is not nature in itself but nature exposed to our method of questioning.
>
> Werner Heisenberg

As for all hysteresis measurements, the magnetic materials need to be magnetized to saturation in bipolar directions. In terms of setup capability, it means applying fields higher than the saturation field. Otherwise, minor hysteresis loops will be measured, which does not reflect the intrinsic magnetic properties of the material. In the present setup, an integrated electromagnet can generate a bi-directional magnetic field of up to 2 T, which suits this purpose to saturate the studied CFO. Furthermore, the magnetic field must be uniform in the sample space to detect the strain in magnetostriction measurements. Otherwise, field gradients will induce forces that alter the strain distribution, leading to erroneous results and distorted magnetization curves. For a reliable measurement, the setup is required to be free of active magnetic elements (screws, holders, etc.). In this regard, some measures were taken to avoid possible sources of errors, the details of which are presented in the Appx. B.3.1.

[28] Needed to exclude any strain absorption while an AC-electric field is applied.
[29] If not, a thermal drift of the holder would be caused.

Also, for the magnetostriction measurements, the Fabry-Pèrot interferometer is used. Thus, the configuration ofg cavity-geometry must be fulfilled, as displayed in Fig. 4.12B.

In this case, the same arrangement as it is used for verifying of the interferometer with the piezostack is applied. Here, a mirror is attached to the sample facing the sensor head, see Sec. B.3. Additionally, the piezo stack is replaced with a cylindrical CFO sample. Both sample surfaces were ground to assure its plane parallelism, see Sec. 3.1.2.

An initial approach involved a measurement using a piezo-actuator-like geometry, see Fig. Appx.B.3. However, this resulted in erroneous results, despite the setup construction being free of metallic parts. Nevertheless, from the initial measurements, there were indications of problems due to the use of this geometry. In general, the measurement shows a hysteretic behaviour, Fig. 4.22B . Still, the values and shape of the graph are not consistent with literature values [46, 68, 163], even though the measurement geometry was placed in the homogenous space between the pole shoes[30].

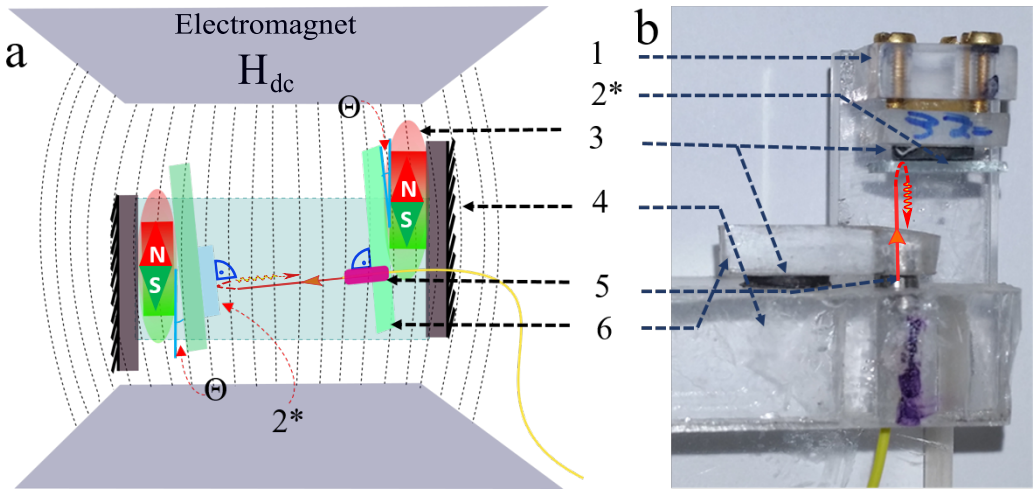

FIGURE 4.19: Interferometry-based magnetostriction measurement principle. A) Demonstrates the final concept, reached after conducting heuristic case studies, as shown in Fig. 4.20 and 4.21. B) Design of the device: *Two* samples (3) are glued in a rigid frame opposite to each other. on one side with the mirror (2) attached to it on the alignment insert (1). The sensor head (5) is fixed to the Plexiglass arm (6). This is connected to the frame (4) via a compensation sample (3). The sensor head fiber is guided through the hole in the frame (4).

Plausibility explanation

A series of case studies was performed to evaluate the nature of the error in the experiment design. Herefore, the following figures are interrelated with each other: Figs. 4.20, 4.21, 4.22. This error occurs when the measurement geometry is as in Fig. B.3, schematically depicted in Fig. 4.20 1-3. In this configuration, a sample is attached to the mirror, which faces the sensor-head, see Fig. Appx.4.12, and consequently forms an air cavity for the interferometry. The magnetostriction measurements were performed for different sample locations between the pole-shoes, as depicted in Fig. 4.20, cases 1-3. Each case represents a measurement at a particular degree of magnetic field homogeneity[31] during the field sweep.

[30] Since, in case of any slight field inhomogeneity, it would lead to misalignment of the Fabry-Pérot cavity configuration.

[31] Magnetic field line exposure of the sample, especially regarding the homogeneity of the magnetic field.

The likely explanation for the error can be inferred as follows: It is hypothesized that when a magnetic field is applied, there is a concurrent misalignment of the optical axis. One plausible cause for this misalignment could be attributed to a minor surface curvature present in the sample[32].. This hypothesis is drawn from the observed behavior of the magnetic nanopolycrystalline material when subjected to a uniform magnetic field. To illustrate this mechanism in a simplified manner, we can compare the behavior of the polycrystalline sample to that of a ferrofluid [33].

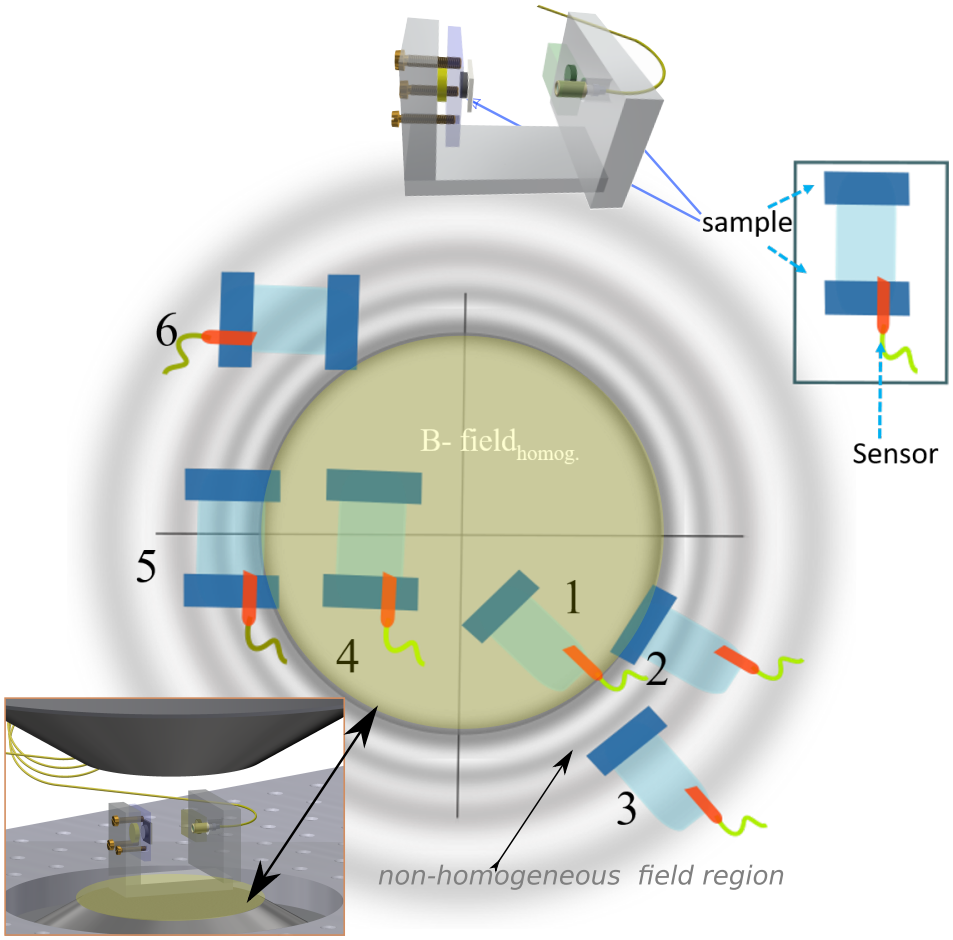

FIGURE 4.20: The design of experiment for case studies conducted in different location between the pole shoes. 1-3; uncompensated (i.e., a second sample is not attached to optical sensor head) optical axis of interferometric cavity, 4-6 compensated optical axis. The centre of the figure marks the homogenous magnetic field zone between the pole shoes, as shown in the inset in the bottom left corner. In the "fringing fields" zone the magnetic field is not homogeneous. Its value declines with increasing distance from the homogeneous edge, so the field strength is less than in the core. It is marked with a wave-like pattern. The case studies, as well as their configuration and position, are marked with numbers, the blue area represents the CFO sample. In Fig. 4.19a (4-6) the 2^{nd} sample, which functions as a compensation mechanism is shown. Cases 1-3 show the states without compensation. The related magnetostriction measurements for the configurations as presented in Fig. 4.21 and 4.22.

[32] As the reason for Fig. 4.21 B is inexplicable in the frame of this work.

[33] They consist of a few nanometers of large magnetic particles that are colloidally suspended in a carrier liquid. The particles are usually stabilized with a polymeric surface coating.

The orientations observed in a single crystal doesn't directly apply to a polycrystal, where grain orientations are entirely random. Therefore, the cumulative effect of all magnetostriction λ_{sat} of the polycrystal is given by the average over these orientations, Fig. 4.19a. A plausible cause of the surface curvature is related to non-uniform strain at the grain boundaries, assuming the limiting case of uniform stress throughout the sample body. This assumption is made as the grain boundaries confine the sintered polycrystalline grains. The magnetic domains inside the grains do not fully align with the field direction due to mechanical restrictions on their expansion. Each crystal grain is influenced by its neighbors, leading to strain behavior different from that purely in the direction of the applied field. Empirically, such non-uniform strain can be correlated with the polycrystalline nature of the samples. There are two limiting cases to consider: either stress is uniform throughout the sample, while strain varies from grain to grain, or strain is uniform, and stress varies [49, p. 254]..

Any surface deformation creates aberration in the Fabry-Pérot cavity arrangement, see Fig. 4.13. Consequently, any misalignment of the optical axis, as discussed earlier (see Fig. 4.13A), alters the portion of the beam recoupling into the fiber optic. This discrepancy results in erroneous computations by the interferometer device compared to its optically aligned state. The device cannot differentiate between intensity changes caused by misalignment and those resulting from a supposed change in distance. This misinterpretation leads to reduced laser-light intensity recoupling into the fiber optic Sec. 4.3.3.

The tilting of the reflective surface in the cavity was suspected as a source of error. Here, an educated guess is to install a tilt compensation mechanism to keep the optical reference axis aligned in the direction of the field. Given that the exact nature of the deformation of the magnetic sample (with a mirror on it) is unknown, any measure for its compensation is also unknown. An important idea for solving the misalignment issue is to mimic the deformation on the sensor head position in order to stay in alignment with the sample with the mirror attached to it. This is only possible by assuming that any sample of the s ame size and form would undergo an identical deformation. This solution requires a practical approach to the design.

This solution requires a practical approach to the design. In the new approach a 2^{nd} sample of the same kind is attached to the sensor head, see Fig. 4.20 cases 4-6. After analyzing the case configurations, a new case configuration as the experiment design for the interferometer was devised, as depicted in Fig. 4.19. This approach was guided by the results of the measurement data related to the measurements depicted in Fig. 4.20 and 4.21.

The first tests on the new construction revealed that the assumption was correct. The values and the shape of the measured curves for a standard sample were found to match the literature values. The results are displayed in Fig. 5.5, confirming the literature value for CFO as in [46, 68, 163].

Case studies to verify magnetostriction: An optical table is built between the pole shoes to place the magnetostriction setup arrangement in the magnetic field, Fig. 4.19. As a result, the magnetostriction setup can be positioned in any arbitrary place between the shoes. The numbers in Fig. 4.20 illustrate the measurement positions between the pole shoes.

The course of the magnetic field and the magnetostriction are simultaneously plotted in the time domain, Fig. 4.21.

In the time domain, the magnetostriction behaviour depends on the configuration and position that is used. Using different ramping times and maximum field strengths allows an evaluation of magnetostriction for different positions and configurations. In the case of A), Fig. 4.21A, the location dependency of the setup is explored. The measurement positions (2 and 3) have different distances from the centre of the homogeneous fields, as displayed in Fig. 4.20. Both measurements are performed with the same field-ramp and

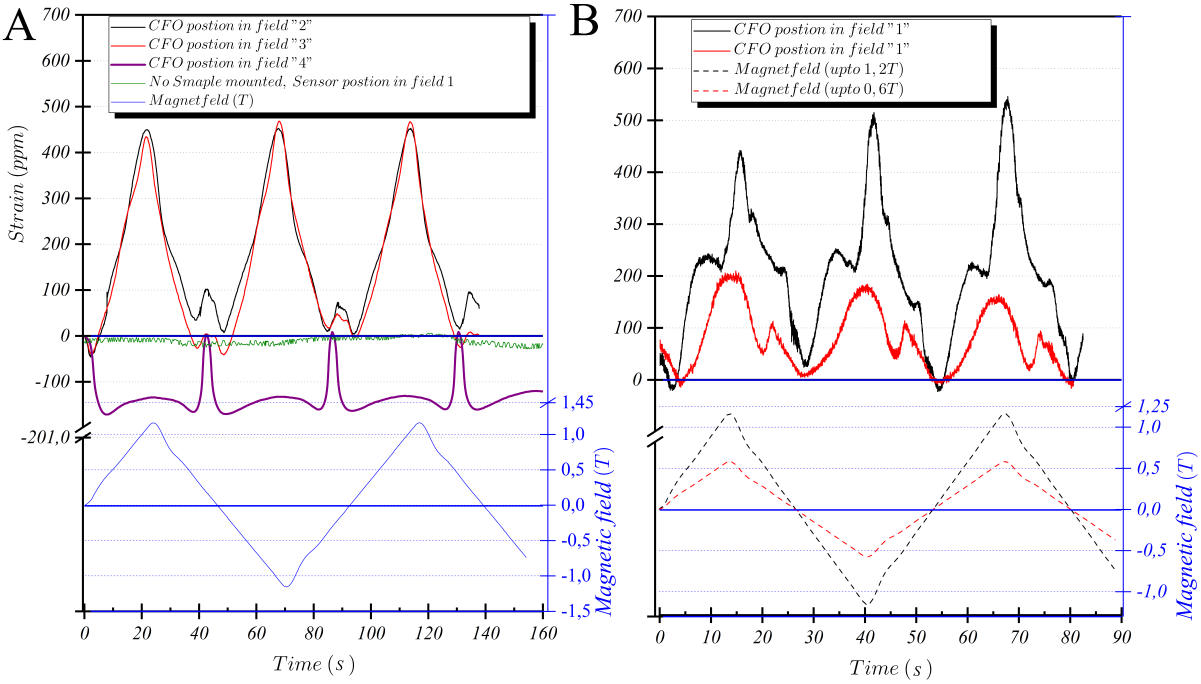

FIGURE 4.21: The magnetic field variation and magnetostriction curve over time are displayed. In both graphs, the left axis displays the magnetostriction values, while the right axis shows the magnetic field values. A) Results of the magnetostriction measurement of CFO for the different cases depicted in Fig. 4.20 with the corresponding magnetic field changes shown below. B) Strain displacement measurements in position 1 with different max. field strengths, but with the same period,see Fig. 4.20.

strength. Moreover, both are performed with an uncompensated configuration with one sample attached to the mirror. An analysis of the data shows that position (3) is more exposed to misalignment due to the higher magnetic field curvature as it is further away from the centre than the location for case (2). A consequence of the inhomogeneity of the field, in case (3), is the distortion of the aligned optical axis. This can be deduced from the data, as the measurements in case (3) supposedly show that a "larger strain" is taking place. Any distortion leads to lower recoupling of the light intensity into the fibre optic, see Fig. 4.13A. The interferometer interprets the lower light intensity feedback as the mirror moving away from the sensor head. However, the higher angular tilting of the optical axis is the reason for that.

Case B of Fig. 4.21 represents the settings without compensation for two different maximum fields; $0.6T$ and $1.2T$. However, both measurements were conducted in the homogenous field region with the same position (1) and period for the field sweep. These measurements show that increasing the field has a more substantial distortion. Both magnetostriction curves behave the same up 0.6 T[34].

Another study was performed to investigate the compensation of tilting misalignment by *another sample of the same kind* when the device is exposed to the same sweeping magnetic field. The second sample was attached to the sensor head holder, Fig. 4.22. In the compensated configuration, the measurement shows a negative strain value. Furthermore, the saturation field for strain is as expected for an applied field of 0.2 T, Fig. 4.21(4), Fig. 4.22A.

[34]The magnetostriction curves are not overlapping as depicted in the time domain, where each field has a different ramping slope setting, coming from the maximum field 1.2 T and 0.6 T for the same period.

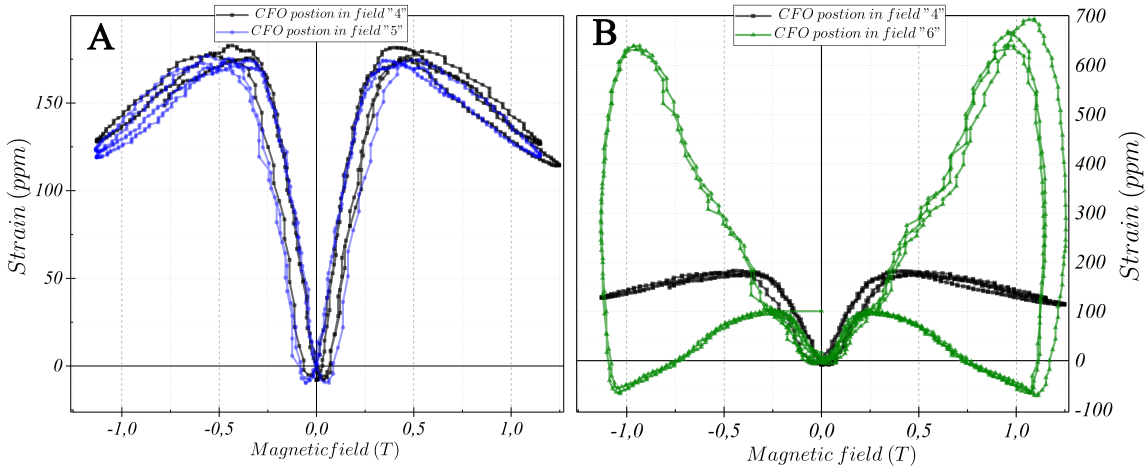

FIGURE 4.22: The measurement configurations refer to the case studies shown in Fig. 4.20. The cases displayed are tilt-compensated with a second sample. The cases displayed are tilt-compensated with a second sample. The left graph compares measurements made in positions 4 (homogenous region) and 5 (inhomogeneous region). Due to the compensation by the sample on the sensor head, the field inhomogeneity in the measuring point location doesn't affect the measurement (5). In both cases, the device configurations are simultaneously exposed to the same field. On the right: The measurements compare case (6) with the compensation sample on the sensor head with case (4). In case (6), due to the distance from the homogenous region, the samples on the sensor head and mirror are ex- periencing different fields simultaneously. This leads to erroneous results in contrast to those obtained in position (4), where both are always sensing the same field.

This finding indicates that the magnetostriction measurement is independent of the field homogeneity of the field. The decisive factor is that both samples are experiencing the same field at the same time. As a consequence of this, the optical axis of the mirror and the one on the sensor remain aligned. This finding can be used for a sensor, which can be used to investigate the homogeneity distribution between the points of interest.

4.5 Magnetization under Stress

In many applications, avoiding any change in the magnetic state caused by stress is also necessary through proper material engineering, such as magnetic data storage or GMR[35]-based geomagnetic sensing. The stress dependency in ferromagnets is crucial concerning the characterization of functional materials. This makes it necessary to investigate the stress dependency of magnetic materials with an instrument.

The stress sensitivity of magnetic materials is utilized in diverse applications such as actuators and transducers. They present an equivalent effect to the piezoelectric effect, with the additional benefit of being driven in a contactless manner by the magnetic field[36] [164]. Among other materials, the magnetic shape memory alloys as a material class, with their large magnetostrictive behaviour, are interesting given their stress-related properties [165].

A large magnetostriction gradient and stress sensitivity make magnetic materials suitable candidates for strain-mediated magnetoelectric composites, Sec. 2.6.4 [166].

[35] Giant magnetoresistance

[36] However, the longest elongations are one order of magnitude lower than those achieved for ferroelectrics.

Another feature of stress sensitivity in magnetic materials is the ability to tune their magnetic properties [167]. Further, the permeability of a material can be regulated with applied stress as there is a stress dependency of magnetic anisotropy [168].

There is also considerable interest in utilizing the magneto-mechanical effect for strain sensors because magnetic sensing does not require electrodes and electric leads [169].

4.5.1 Pressure cell for VSM

Stress (or pressure) is one of the ordering parameters in the phase diagrams of materials [170]. It affects the structural phase transitions of crystalline materials and other ordering states associated with a crystalline structure. In the case of magnetic materials, aside from the magnetic order, stress also influences the lattice parameters in the crystals. Consequently, it changes the magnetization and the elastic modulus [74], which can be as high as 90% [47], Sec. 2.4.2. This topic has been also discussed in the section on magneto-elastic effects[37]

Due to the operating principle of VSM as a vibrating magnetic characterization technique (Sec. 3.5.1), the generation of stress inside the VSM tube is challenging. In general, The application of stress requires a rigid clamping structure, which contradicts the concept of using vibration at first glance. A practical solution would be to isolate the stress space into a small cavity and integrate the cavity into the vibrating device. Isotropic pressure-dependent magnetization measurements can be made by using pressure cells, which have been only realized for squid devices but not for a VSM [172, 173].

Initially, pressure cells were used for the study of pressure-induced superconductivity phenomena [174–177]. In particular, understanding highly correlated electron systems under high pressure, in large magnetic fields and low temperatures, has driven the community to develop pressure cells. Pressure cells are also used to investigate stress effects on the magnetic and structural properties of magnetic shape-memory alloys, in particular, this concerns the piezoresistance and magneto-resistance properties of Heusler alloys [171]. Furthermore, research on the magneto-caloric effect has shown that the combination of stress and a magnetic field can improve the impact, highlighting the need for magnetization studies under stress [178]. The purpose of the study in this work is related to the investigation of the uniaxial stress-induced magnetization change and other physical properties of magnetoelectric materials.

The study in this section investigates the uniaxial stress-induced magnetization change of magnetoelectric materials. Sofar, no study has been conducted on the pressure dependency of magnetization in multiferroics. In this regard, however, the Heckmann diagram illustrates how the stress relates the two phases in the magnetoelectric composites, sec. Sec. 2.4.2, [35]. The measurement of the directional stress dependency of the magnetization necessitates the development of a pressure cell. It also needs to consider the simultaneous ability to apply an electric field to stress. The pressure cell would enable to derive the *constitutive behaviour* belonging to the tested material class. In this case, external stress can tune the level of offset stress as an add-on field to improve the ME coefficient in magnetoelectric composite since certain stresses enhance the d_{33} value [57, 149].

The stress-induced variations in magnetization gradient data provide crucial insights into the stress-sensitive range of the magnetic phase. Understanding this parameter facilitates the selection of the most suitable ferroelectric material, ensuring it possesses the requisite stress field strength to optimize electrically induced magnetization changes[38].

[37] An effect associated with domain alignment, where uniaxial stress induces an easy axis of the magnetization (Sec. 2.4.2, [49, 171]).

[38] For 0-3 composite, sufficient insulation property of the magnetic material is required, as it is the case, e.g. for $NiFe_2O_4$ nanoparticles.

Design and challenges: Most of the existing pressure cells are for hydrostatic pressure studies, which are well suited for isotropic material properties. Here, the diamond anvil cell approach is typically used to pressurize a sample. In this case, the pressure is hydrostatically transmitted by compressing a liquid such as a spindle oil, isopropanol, etc. [175–177]. Another method to apply pressure uses the specific volume increase in some materials during their solidification process, e.g., gallium, which is diamagnetic [172]. Furthermore, on the pressure detection side, the pressure is commonly measured in real-time by a Manganin [39] gauge wire, which is placed in the liquid cavity with the sample [179].

Measuring the change of magnetization as a function of pressure requires a low magnetic background noise. Therefore, the background signal originating from the pressure cell itself needs to be minimized by building it using low-diamagnetic materials with low magnetic susceptibility. As low diamagnetic materials are rare, this is one of the main reasons why few materials are suited for manufacturing cells. Other limitations are related to the need for a material with high tensile strength and high fracture toughness to withstand the desired high pressure. Ideally, the magnetic properties of the material should not be affected by temperature, and its mechanical stress should not induce any magnetization in the cell. The same requirement is needed for the mechanical stiffness over the temperature range. Hence, material selection needs to be the subject of critical consideration.

Materials that support the above conditions are, among others, titanium alloys like CuTi alloy, $Ti_6Al_6V_2Sn$ [172, 180], which has extremely low magnetic susceptibility [181], a NiCrAl alloy for the design of a 4 GPa class pressure cells [174] and a beryllium copper (BeCu) alloy with a very low susceptibility($\chi \approx -2{\cdot}10^{-6}$). Both Be and Cu are diamagnetic elements [179].

The material used for this work is BeCu with 2 wt.% Be[40]. Unlike the other materials, its plasticity even increases at low temperatures, giving it a unique mechanical property. Furthermore, it is commercially available in a standard rod shape. However, it doesn't have the tensile strength of the others, but it is fully sufficient for the requirement of this work, where a maximum of 0.5 GPa will be used.

The uniaxial stress characterization is required for materials that show anisotropic properties. The $CoFe_2O_4$ nanoparticle ceramics exhibit isotropic magnetic properties due to the *polycrystallinity* of the sintered ceramic samples. At first glance, the isotropic nature of the magnetic phase in magnetoelectric composites contradicts the magnetoelectric effect. However, in the interaction with the field, the magnetic response is anisotropic, and it has remnant magnetization at zero fields. Furthermore, given the electrically poled direction in the ferroelectric phase, the coupling properties of the 0-3 magnetoelectric composite are measured to be directionally dependent. Given that the direction of the exciting field mediates the magnetoelectric effect, uniaxial stress affects both constituent phases and their combined properties.

Kamarad et al. [173] developed a uniaxial pressure cell to study magnetic materials by neutron-diffraction. Due to its size, it is not suitable for a VSM, aside from its non-compatibility with the pressure calibration method. The technical requirements for uniaxial pressure cells are, unlike hydrostatic cells, more complicated, which will be elaborated on in the following section.

This section covers the properties of a pressure cell developed for applying a B-field in parallel and perpendicular to the stress and for use in a VSM. The developed design allows a comprehensive measurement of the change of magnetization by uniaxial stress for all the tensor elements with respect to the constitutive of the material.

[39] manganin posses low strain sensitivity but high hydrostatic pressure sensitivity, and at the same time its electric resistivity has low-temperature dependency.

[40] http://www.ngkberylco.co.uk

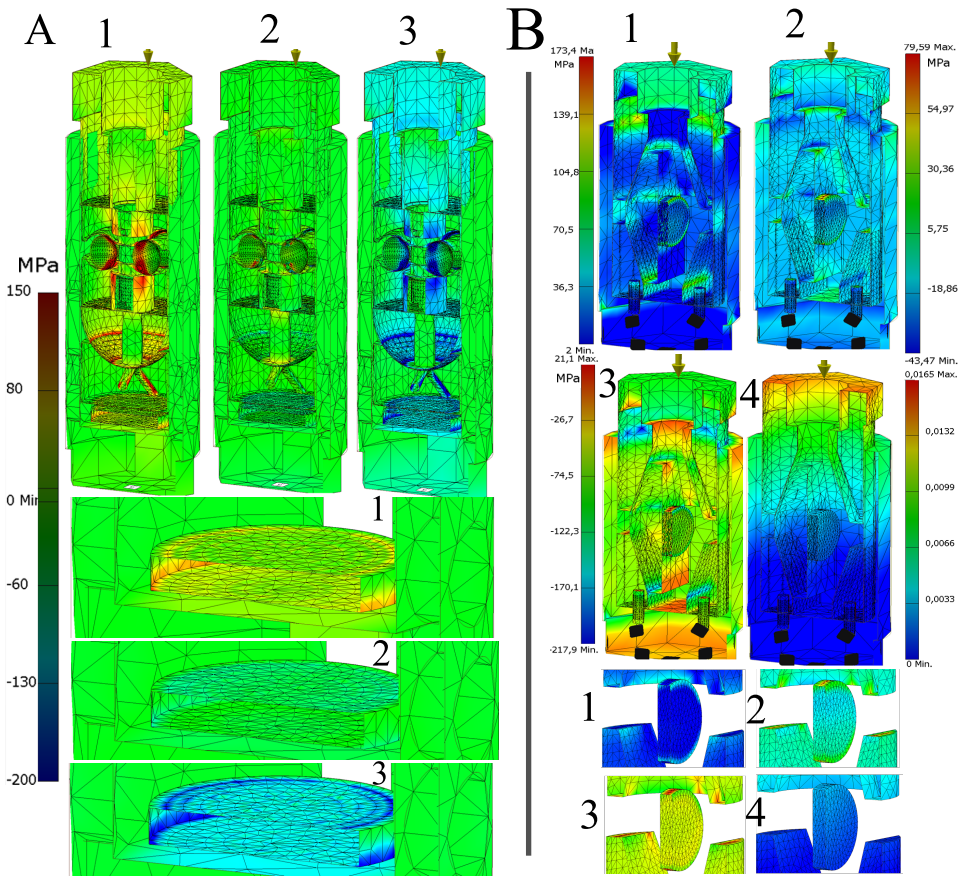

FIGURE 4.23: FEA (details of the simulation parameters: Sec.Appx.B.1) stress analysis of the pressure cells, see Fig. 4.24. A) B-Field is parallel to uniaxial stress geometry. B) Geometry of B field and uniaxial stress are perpendicular to each other. Numbering of analysis specification: (1) Von Mies yield stress, (2) First principle, (3) 2 Principle, and (4) Total strain. In both cases, a 10kN force has been applied.

The challenges: For applying uniaxial pressure inside a cell it is necessary to clamp the sample on both sides. Two methods are identified in this work. This can be achieved by closing the cell with a bolt screw or clamping with a suitable non-magnetic piezo stack inside the cell. The pressure applied by this method allows the stress direction and the magnetic field to be parallel[41]. Each method has its specific drawbacks and benefits. The screw technique causes issues related to shear stress that need to be handled, and the piezo-stack method adds more weight and needs electrical connections.

In order to realize a perpendicular orientation of the stress to the magnetic field, wedges can be used to redirect the force by 90°, Fig. 4.24B. In this case, the pressure is applied on the top edges of the two wedges by a screw bolt. As the screw bolt is tightened, the space between the wedges is confined. As it has an angle to redirect the force, stress is then created, and the sample in the space between the wedges is pressurized.

The design of the cell in the VSM module is influenced by the geometry of the setup. Specifically, the inner bore of the cryogenic PPMS inlet has a maximum diameter limit of 13.5 mm [42]. This limitation sets boundaries for both the sample space and the wall thickness of the pressure cell. Additionally, the presence of threaded holes further impacts the wall

[41] Sec. 3.5.1 on the VSM, the inner-bore direction is the magnetic field direction, see Fig. 3.11.

[42] This is still larger than the one of the *Quantuum Design* device, but the Cryogenics's PPMS loses resolution over the Quantum Design device with its 8mm diameter.

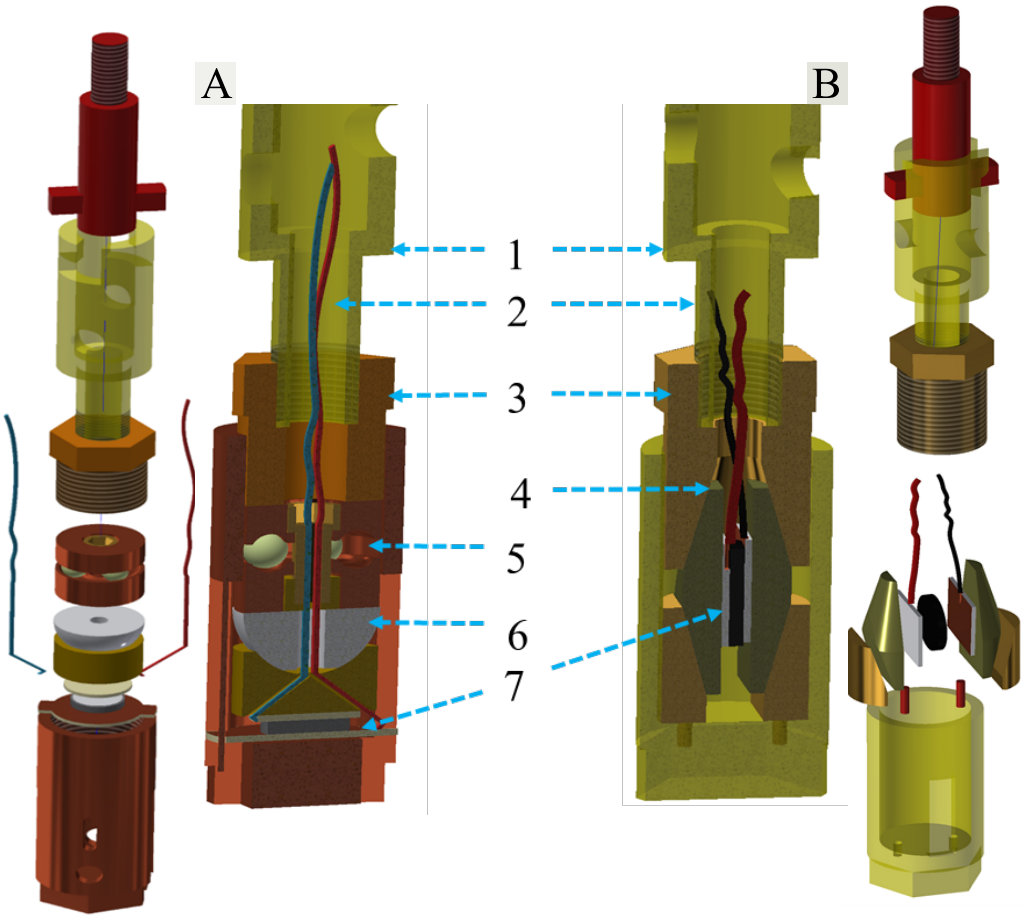

FIGURE 4.24: Cross-sectional view and CAD-assembly design of the uniaxial pressure cells for two field orientations: The parallel (A) and perpendicular (B) orientations of the $B_{\updownarrow}$-field and $\sigma_{\downarrow\&\rightarrow}$-fields inside the same cell. A cell consists of 4 main parts: one of which is the BeCu-cell, the closing bolt screw (3), which generates the pressure. A twist turn-lock fastener system (1), to mount the cell on the rod of the VSM magnetometer in a vertical position, Fig. 3.11. An axial bearing and half-ball zirconia in the hemispherical cavity (56) are used for tilt compensation. In order to avoid rotary motion on the sample while the screw is turned, the hemispherical cavity has two sliding pins on its side, which follow the drilled holes in the cell outer casing. All the parts involved have holes in their centres intended to feed the leads through all parts and, thereby, enable the application of an electric field on the sample. The sample is placed on a PCB material (conductive, nylon), which is glued to pressure stamps (7) see Fig. 4.23. After each stress level has been applied, the mounting is done with the twist turn-lock fastener system consisting of a groove on one part and a tenon on the other. Otherwise, after each remounting process, an error would be generated, and the position would be lost.

thickness and determines the maximum load capacity of the pressure cell, as well as the linear range of applied force.

Moreover, the pitch of the screw thread on the cell wall plays a critical role in determining the maximum pressure tolerance of the cell. A low pitch may compromise the tensile strength of the pressure cell, while simultaneously offering finer control over stress settings on the sample. Consequently, a balance must be struck between achieving lower precision control and ensuring optimal strength, linear range, and maximum load capacity.

A key consideration in pressure cell development is the method of pressure measurement, especially for uniaxial loading scenarios. This presents a significant challenge as it involves integrating a load cell within the cell itself, while ensuring compatibility with the cryogenic VSM module and its isolated environment within the vacuum tube.

Furthermore, the selection of a non-magnetic load cell is essential, taking into account both its weight and size constraints. Additionally, electric leads are necessary for in *in situ* pressure monitoring. Unlike hydrostatic pressure cells, utilizing manganin gauge wire or MEMS pressure sensors is not feasible due to their sensitivity to hydrostatic pressure [136].

This calibration method is simple and accurate enough to be the method of choice, Fig. 4.27. It requires the design of a new setup. It consists of a torque wrench meter with a scale display, load cell, bolt, and fixture construction. This was used for the case when the stress was applied parallel to the magnetic field. The mechanism of torque-to-force transfer is presented schematically in Fig. 4.25. In this design, the cell calibration unit is integrated into the fixture, simulating the pressure cell's closing process. The force translation is detected with the load cell in the universal testing machine. The load cell (fixed on the traverse) is attached to a rod pin that touches the cell's bottom. The elastic deformation of the cell in the process doesn't play any role. The force is measured as the bolt is tightening in the cell. The exact force translation depends on the pitch of the cell thread.

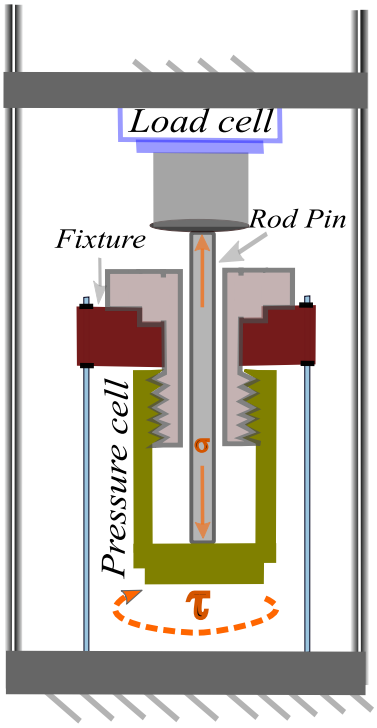

FIGURE 4.25: Schematic of the exsitu setup for the pressure cell calibration. The device is also shown in Fig. 4.27A.

In this construction, the resolution of the torque wrench is decisive for precise calibration. This, however, depends on the full working range of the torque wrench. Initially, the calibrations, as displayed in Fig. 4.26 are made with a torque wrench that had a working range of up to 30Nm, which leads to a lower resolution. However, for smaller torques, a torque wrench with a smaller working range of up to 10Nm was purchased. The 10Nm wrench offers higher precision and better resolution.

Another challenge arises from the tilting of the sample, particularly concerning the application of uniaxial pressure via a screw. This issue necessitates countermeasures, as illustrated in Fig. 4.24(5 & 6). Moreover, the unevenness of the sample surface must be addressed. To tackle both concerns, a non-magnetic axial bearing composed of CuBe with zirconia balls was developed, as depicted in the inset of Fig. 4.27B. One end of the axial bearing features a spherical surface designed to compensate for surface irregularities.

In addition, the feasibility of simultaneously applying an electrical field alongside pressure is also taken into account during the design phase. The presence of the electric field would distort the the crystal structure of the ferroelectric phase.This effect is particularly

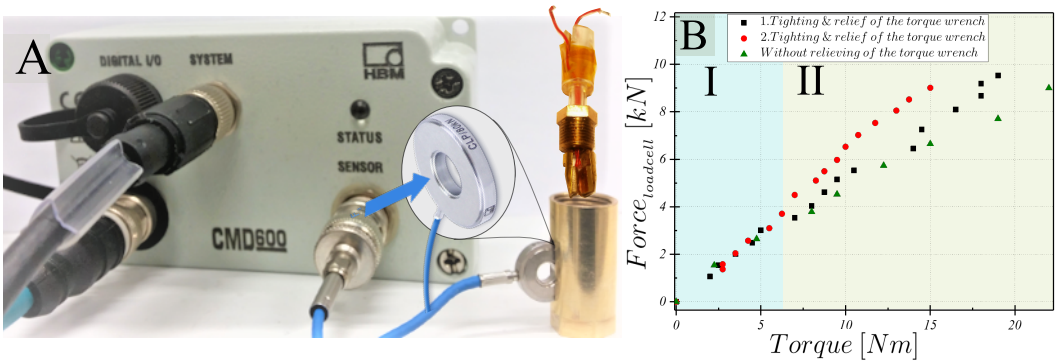

FIGURE 4.26: Applying stress perpendicular to the B-field inside VSM-tube. A) Displays the small load cell (CFTplus, force sensor,- piezoelectric force transducers- and CMD600, a charge amplifier, HBM) used for the stress calibration inside the cell. B) The highlighted area is the range of interest as the system attains a force up 4kN within the linear range

significant in single-phase materials, where the ferroelectric properties of multiferroics can be adjusted with a constant offset induced by an applied electric field.

To facilitate this capability, electric leads were routed through the bearing and locking bolt, as depicted in Figure Fig. 4.24. This feature sets the pressure cell apart from most previously designed hydrostatic cells. However, its application for composite magnetoelectrics may be less compelling due to the absence of a continuous AC stimulus.

As part of the design process, stress-strain analyses with FEM simulations were carried out to identify the load tolerance of the pressure cell and its limits, Fig. 4.23. Furthermore, the simulation confirmed the sample's homogeneity of the stress distribution in the sample. It indicates that the applied force is redirected from the top screw into the sample space through the adjoining body elements. Moreover, following the simulation, lateral bulges within the sample appear, which are not related to the mechanism of uniaxial stress. The simulation also illustrates that while applying stress within the cell, some parts, like the ball-bearing, are exposed to excessive stress. This doesn't, however, affect the stress distribution in the sample. Instead, the related strain is absorbed by the plasticity of the CuBe.

The experimental procedure to apply pressure requires the mounting and demounting of the pressure cell on the VSM-rod in order for the next stress level to be applied, see Fig. 3.11A. This change is achieved by tightening the bolt screw when it is fixed in a vise. The remounting of the pressure cell is a critical issue as the initial position of the cell inside the tube between the pickup coils needs to be preserved. In this case, in the processes of tightening, the total height of the pressure cell together with the bolt screw needs to be measured by a caliper before and after the tightening process. This is required as the total height of the cell decreases after the screw is tightened. The difference in the total length of the cell compared to its initial length needs to be compensated by adjusting the Z-stage height of the VSM vibrator relative to its initial position. Otherwise, the pickup coil will produce an inaccurate signal. With this problem in mind, a rotating-lock unit between the rod and cell was considered during the redesign.

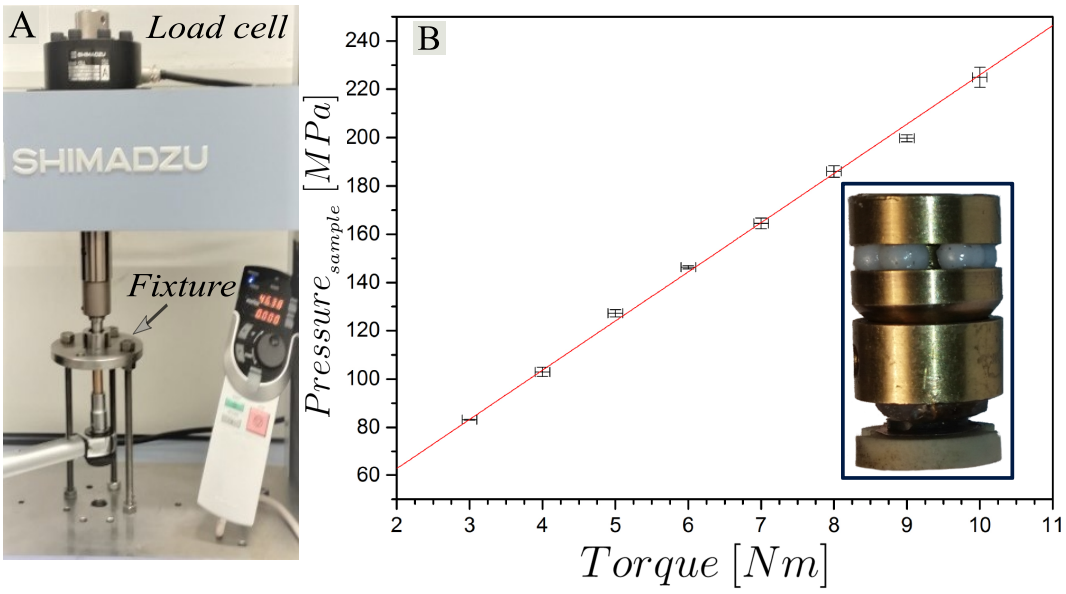

FIGURE 4.27: Applying load parallel to B-field. A Torque wrench is used for the pressure calibration, a reliable way to create pressure in the cells. When applying a load perpendicular to B-field, the torque is redirected into the force

5

Results and Conclusions

The overall goal of this work was to characterize the parameters related to the mechanics of magnetoelectric composites and to prove the functional concept of the new setups. As a consequence, model measurements[1] were made in order to test the modularity and functionality of the various measurement modules belonging to the setup.

n particular, strain measurements were performed to showcase the integration of the interferometer across multiple field conditions and demonstrate its ability to achieve sub-nanometer resolution. The initial part of this chapter outlines the requirements for composite samples, emphasizing their mechanical testing. Subsequently, the results encompass structural, morphological, and coupled properties of the composites. Additionally, strain measurement data under various field conditions are presented.

Finally, the characterizations of the magnetoelectric composite under uniaxial pressure are analyzed, providing insights into its behavior under applied mechanical stress.

5.1 Studying 0-3 connectivity composites

The $CoFe_2O_4$-$BaTiO_3$ magnetoelectric composite has proven to be a suitable candidate for the mechanical study of the composites, as both phases possess similar mechanical properties [182]. In particular, the 0-3 particulate system has been well studied experimentally, even though the 0-3 connectivity does not provide the highest ME-coupling value [64, 87, 183–187].

Also, many modelling studies on the mechanisms behind the interaction of the constituents have been conducted [188, 189]. In these studies, the mechanical behaviour between inclusion and matrix is modelled. The composite system provides an inclusion model for a three-dimensional embedded formulation.

Experimental determination of the relevant parameters facilitates the calculation of constitutive laws, which dependent on the inclusion and matrix interaction.

Mechanical experiments on composites are necessary, as most mechanical models for 0-3 particulate systems use values that originate from the pure phases of these composites. Moreover, these models contradict the experimental values[2]. The addition of a phase mixed in pure materials alters the properties of the constituent phases, see Figs. 5.6, and 5.3. As a consequence, the data cannot be used for the composites. Balke *et al.* [190] have identified several relevant publications that use unsuitable material parameters, highlighting the ambiguity in the community due to a noticeable lack of experimental data.

[1] The measurements are relevant to the functionality setup and measurement capability. They are not a complete analysis of the composite magnetoelectrics.

[2] E.g. hysteresis of magneto-electric composite Fig. Appx.5.11C versus pure ferroelectric material Fig. B.7A.

Optimization of syntheses

The previous work on the synthesis of magnetoelectric composites at the Institute of Materials Science - University of Duisburg-Essen - was driven by the desire to achieve high coupling factors [191, 192]. An enhanced effect was reported for the core-shell approach, with CFO nanoparticles being the core coated with BTO nanoparticles as the shell [193–195]. *Etier* [185] created this structure using sol-gel synthesized nanoparticles, where a single magnetostrictive particle is surrounded by an electrostrictive phase. This approach is well suited to the local study of the nature of the ME-coupling by synchrotron methods [196] or by high-resolution techniques such as MFM[3]. Both techniques enable to depict the domain state at the interface[4].

In this work, the mechanical properties of the composites are the subject of investigation. Given the low mechanical stiffness of the core-shell composites and the destructive nature of compressive stress, core-shell composite samples suffer from failure before any significant stress effect is measurable. The reasons for this are manifold; A major one is porosity, as reviewed in Appx. A.2. This arises mainly from how the nanoparticles were sintered. In this process, they accumulate to form bigger grains, leaving nano-size pores behind, see Fig. 3.3B. Additionally, the high surface energy related to the small particle size of the initial powder (≈50 nm) lowers the melting temperature of the composites and impedes uniform densification at higher sintering temperatures [5]. This additional energy leads to premature melting of the sample and hence a poor densification of the mixed-phase material [64].

In the mixed oxide processing route, composites formed by an optimized synthesis process are needed to fulfil the criteria for highly effective ME coupling and a high density[6]. The latter is required to improve the mechanical stiffness of the composite. Furthermore, the composite sample requires high electric resistivity on the order of $G\Omega$ for a high coupling value, see Tab. 2.1. Common reasons for low cross-coupling in composites are the agglomeration of CFO particles (which leads to leakage) and porosity in composites. Other aspects of the sintering stage, like interdiffusion, interphase formation, and mismatch in thermal expansion between the piezoelectric and ferrite phases, further deteriorate the microstructure [122].

In order to achieve successful synthesis and high ME coupling, all the above obstacles need to be limited. To reduce the porosity, mixing different particle sizes in the initial powder was considered, as discussed in Sec. 3.1.1. The related results are presented in the following section. The effect of porosity on mechanical yield strength for 0-3 composite is demonstrated in the FEM simulations presented in Sec.5.4.1.

5.2 Composite Characterization

This section shows the results of characterization measurements made on composites and their related pure phases. These were obtained with characterization methods introduced in Sec. 3.2. The measurements were conducted to verify the crystal structure of the ceramic

[3] Magnetic Force Microscopy

[4] Subsequently, the mechanical coupling at the interface, which is responsible for the mediation of the magnetoelectric coupling, can be derived [197, 198].

[5] Etier chose 1150°C for sintering, which is lower than many literature values used for the high densification of CFO [199].

[6] High density doesn't imply high stiffness; however, it is the precondition for composites with high Young's modulus.

composites, microstructural morphology, and compositional integrity. They contain the necessary information and parameters for the composite that can be used to prove the existence of the ME effect in the composites. For this task the crystal structure is investigated using XRD and the distribution of the inclusion phase in the BTO matrix is confirmed with SEM measurements. Furthermore, the magnetic and ferroelectric properties are investigated.

The XRD diffraction patterns of BTO and CFO, as displayed in Tab. 5.1, were taken at room temperature. The pure phase samples were sintered using the same route, see Tab. 3.2, as the composites, Tab. 5.1B.

"Match! software"' was used to evaluate the diffraction data[7]. The matching analysis shows an agreement for BTO with reference CIF ID no: 1525437 [43]. The splitting of the BTO diffraction peaks at 45° and 66° confirms the tetragonal structure of the unit cell. A match with the reference CIF ID no:1540973 [200] for the CFO phase confirms the hexagonal spinel structure. For both pure phases, the XRD data, together with their reference data and intensity relations, are displayed in Tab. 5.1a. The XRD results of the composites indicate that the individual compositions of the components within the bulk CFO-BTO sample correspond very well with their pure phases, as shown in Tab. 5.1b. Furthermore, a Rietveld refinement was performed for the composite with the 27% CFO volume fraction, which confirmed the phase content of composite to be a 27%-volume fraction for CFO 5.1c, with an R score value of 3.

The presence of crystalline and secondary phase-free XRD diffractograms is a precondition for reasonable coupling between the phases. However, it is also essential to know, whether the 0-3 composite inclusions display a well-dispersed phase distribution in the matrix. More importantly, it is also crucial to know the porosity state in ceramic composites Therefore, SEM imaging is required. This is displayed in Tab. 5.2. It shows 0-3 connectivity in the samples and confirms a good distribution of the constituents. The EDX spectra of the CFO-BTO composite, see Tab. 3.7, were used to verify the regions which correspond to the phases of CFO and BTO. These form the dark and the bright areas, respectively.

[7]The software is used to compare the diffraction pattern of the sample to the COD reference database in order to identify the presence of know phases. Further, it allows a quantitative analysis using Rietveld refinement with FullProf (by J. Rodriguez-Carvajal) running as the engine in the background

[8]M.Schmuck performed measurements. His efforts are highly appreciated

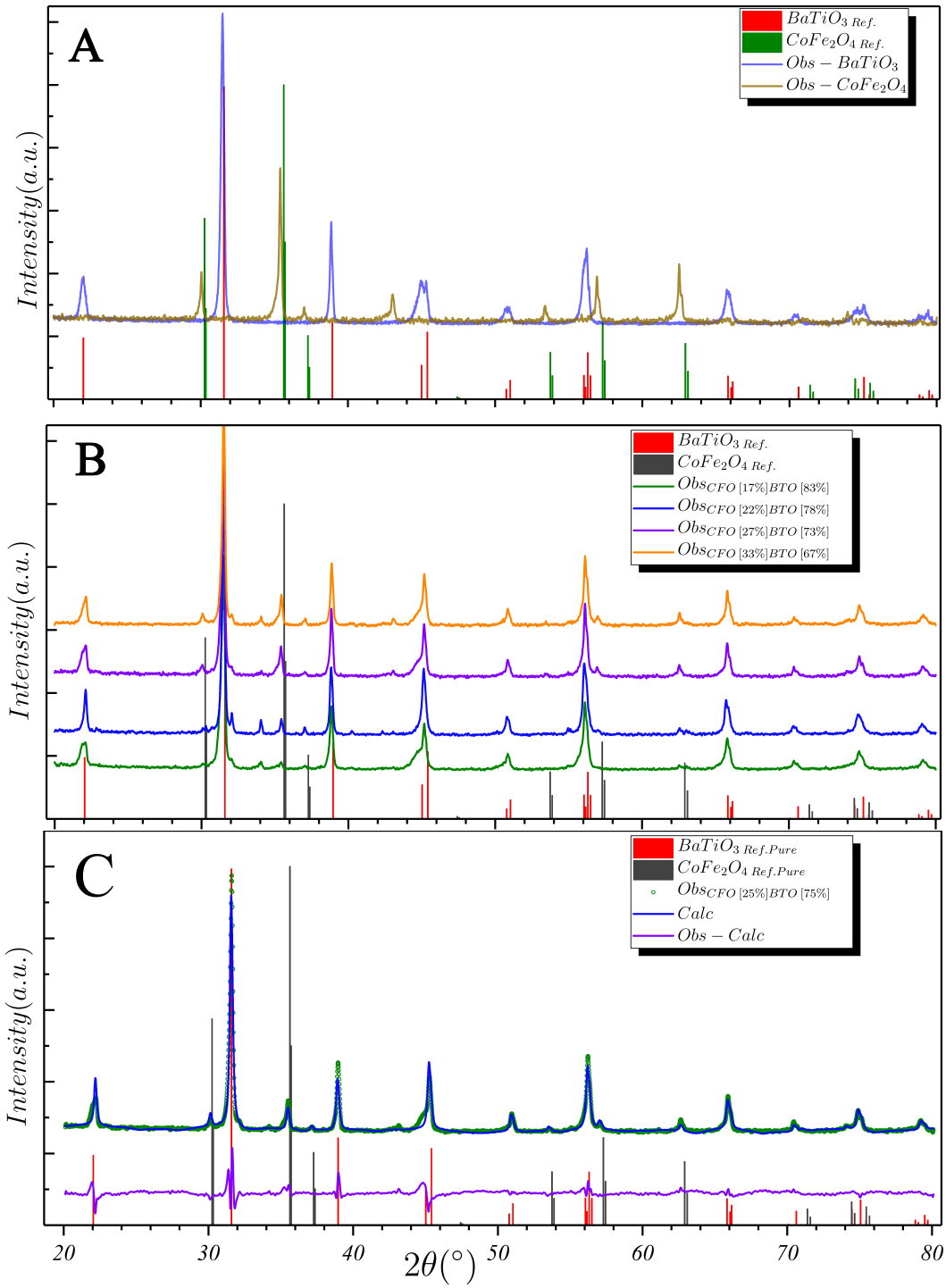

FIGURE 5.1: A) The pure phases of CFO and BTO are synthesized according to the established route, Tab. 3.2[P.46], Sec. 3.1.1. The vertical bar lines mark the peak positions in the reference data, which correspond to the relative peaks of BTO. [43] and CFO [200]. B) Results for the sintered composite with different volume fractions of CFO. C) Results of the Rietveld refinement for the sample with CFO 27%-volume fraction

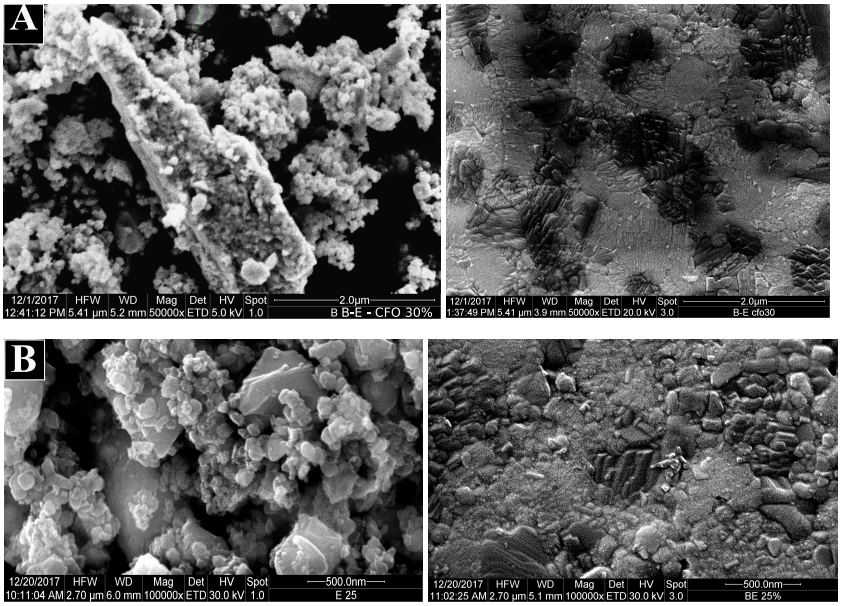

FIGURE 5.2: Examples of SEM surface images of composites with (A) 27% and (B) 33% CFO volume fraction acquired at room temperature after two different preparation stages. The left images show the green bodies of the pressed powder, and the right images show the sintered samples of both composites[8]

The left images in Tab. 5.2A and Fig. 5.2B are the microstructure images of the green bodies of composites containing a 33%, and 27% CFO-volume fraction, respectively. They display the different initial particle sizes involved in the synthesis following the flowchart illustrated in Fig. 3.2. The 1-2 μm BTO particle (*Aldrich*) are present and well dispersed with the smaller particles of BTO (*Alfa*) and CFO powders. Fig. 5.2A & B confirm that the used production approach (Fig. 3.2) successfully synthesises the crack- and defect-free ceramic samples. There are some agglomerates of the CFO phase present in the sample. However, these regions are well separated and homogeneously dispersed

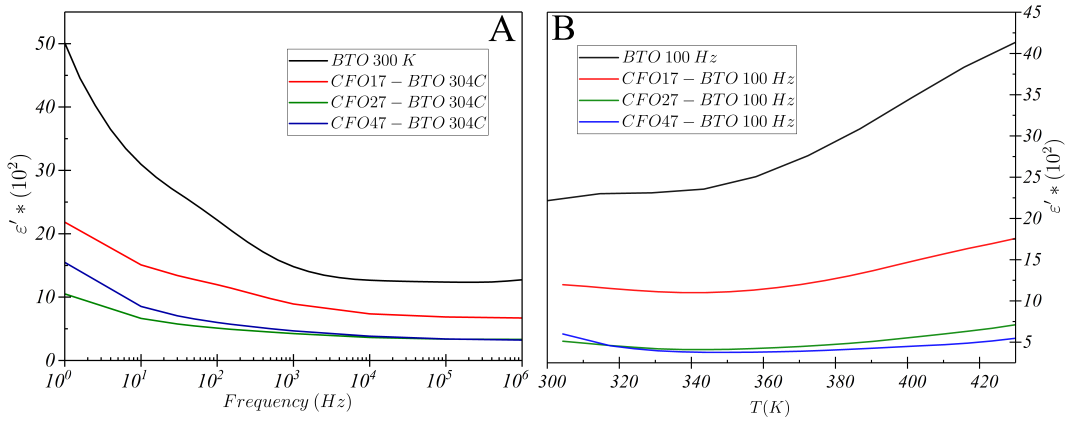

FIGURE 5.3: Permittivity (ϵ) [9]of the ME composites synthesized via solid-state route, Fig. 3.2[p.46] A) The dielectric dispersion at room temperature for different composite compositions and pure BTO. B) The temperature dependency of the dielectric permittivity measured at 100 Hz, over a range relevant to the measurements in this work.

The electrical characterization of the performance of the coupling of the composite requires an investigation of the dielectric constant[10] ($\epsilon_r = C \cdot d/\epsilon_0 A$.), as it is the parameter that describes the amount of charge needed to generate one unit of electric flux. The evolution of the dielectric constant (the real parts of electric permittivity) with increasing temperature and its dependency on frequency are presented in Fig. 5.3. The temperature range from 300K-400K is relevant in this work, as the performance of the composites is investigated in further measurements that are carried out within this range[11]. In Fig. 5.3 the correlation between a higher concentration of cobalt ferrite (CFO) and increased conductivity is evident. This phenomenon, attributed to the presence of CFO, leads to the applicability of Maxwell-Wagner relaxation in these samples, effectively resulting in an increase in electric permittivity. Similarly, this trend is observed throughout the temperature range.

Magnetic properties

Magnetization M(H) hysteresis loops were measure to the composite magnetic properties, Fig. 5.4[P.111], The measurements were done at room temperature for both synthesis routes, as discussed in Sec. 3.5. Composites prepared via a solid-state processing route were measured with a SQUID magnetometer, in fields up to 5 T, where as the saturation is reached below 1 T. The VSM served to measure the magnetization M(H) of composites under uniaxial stress.

[9]Describes the ability of a medium to store an electric field as it is polarized.

[10]C is the capacitance, d is the thickness, A is the cross-sectional area of the pellet and ϵ_0

[11]The sample heats up during the polarization measurement.

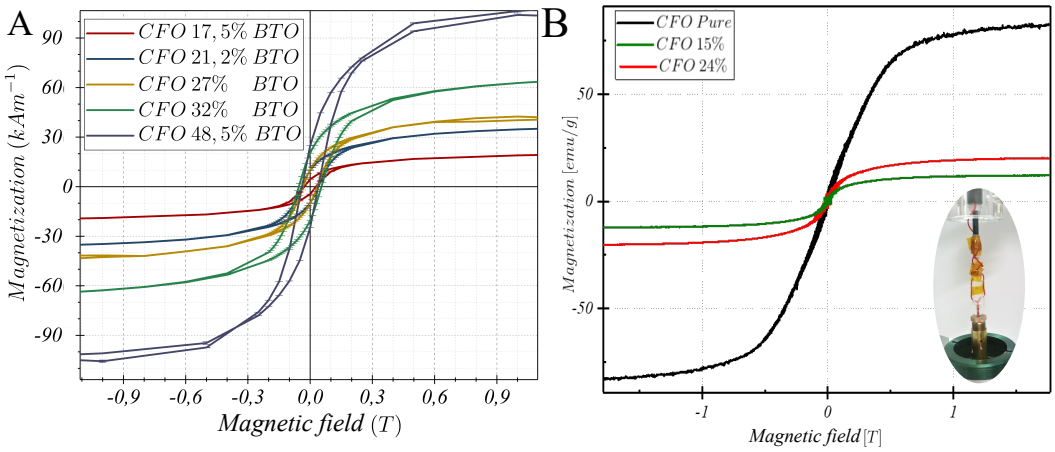

FIGURE 5.4: A) The room temperature magnetization M(H) obtained with a SQUID for the composite ceramics sintered under the same conditions but with different volume fractions. B) Magnetization measurements made with a VSM. The samples are inside the pressure cell ($\sigma = 0$), which proves the nonmagnetic nature of the CuBe cells (insert). At this stage of the measurement no stress is applied. The saturation magnetization values agree well with the literature [201].

Conspicuously, the magnetization decreases disproportionately with decreasing CFO volume fraction for composites. It can be assumed that only the ferrite grains are contributing to net magnetization, while the ferroelectric component acts as a paramagnetic matrix with a negligible magnetic response. The lower volume fraction of CFO (which means, in other terms, a decreasing number of magnetic clusters) is accompanied by an increase in the ferroelectric fraction. From a magnetic perspective, it is indicating an increase in the distance between the magnetic clusters and a more significant discontinuity of field regimes, decreasing the *magnetic self-reinforcing* effect [202]. This lowers the overall field strength as the contribution of the clusters for inducing a total magnetic flux is disrupted, suggesting that the coupling between the nanoparticles is weaker if they are further apart. However, this would not affect their saturation magnetization M_s, it means that the M_s is observable at higher fields. This can be further corroborated because the magnetic dipole-dipole interaction energy decays with r^3.

5.3 Magnetoelectric properties with new setups

The following section focuses on measurements that demonstrate the functionality and applicability of various modules of the setups. Furthermore, the results will be discussed in the context of relevant material properties.

5.3.1 Magnetostriction of the composites with interferometry

Using an interferometer for magnetostriction measurements is a viable and compatible technique, Sec.4.4.3. In this section, some representative measurements on composites are presented in Fig. 5.5b. The acquired measurement values and the profile of the magnetostriction curve obtained through this method align closely with those obtained using CFO with a strain gauge [50].

The strain measurement apparatus was positioned between the pole shoes, with its optical axis perpendicular to a DC magnetic bias H. A magnetic field range from 1.5 T to -1.5 T

was used to record the magnetostriction hysteresis. For the magnetostriction of CFO, a peak value of 180 ppm at 300 mT was obtained, see Fig. 5.5. The related *static* piezomagnetic coefficient $q_{m(trans)} = 1.4\ nm/A$ was calculated using the linear part of the curve.

This measurement underscores the capability of the setup to gauge magnetostriction with*single-digit nanometer* precision, accounting for the 1 mm thickness of the $_{73}$-CFO$_{27}$ composite.

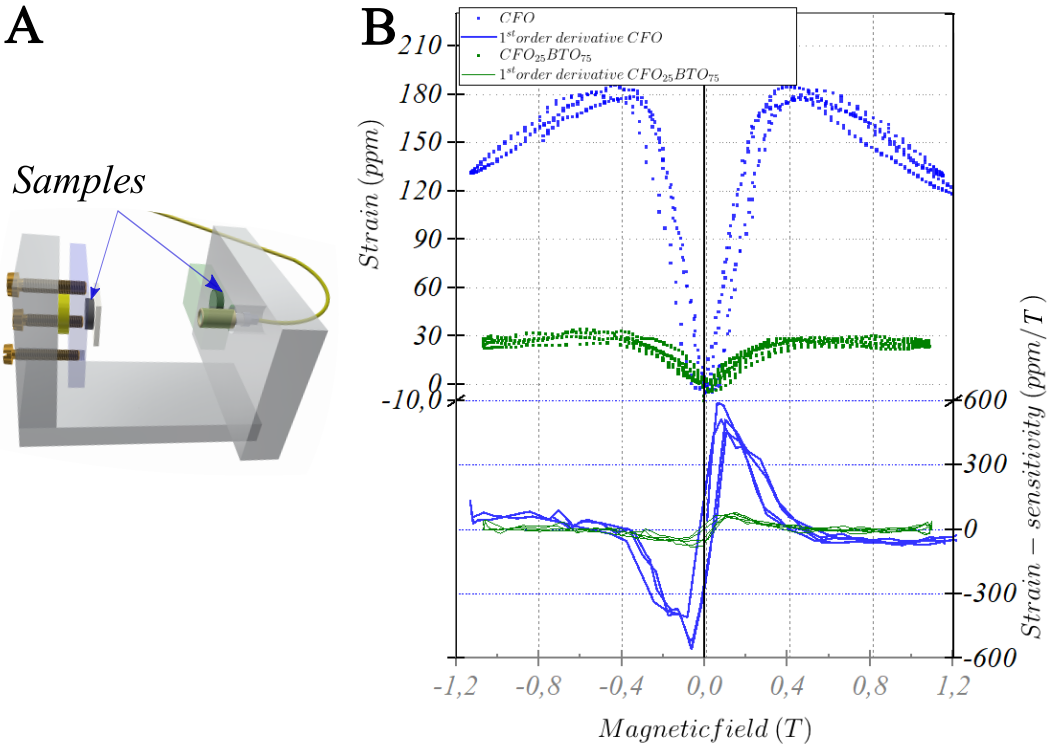

FIGURE 5.5: Interferometric magnetostriction measurement of a polycrystalline CFO and BTO$_{73}$-CFO$_{27}$ ceramic. A) Illustration of the interferometric-based device, which is positioned between the pole shoes of a bipolar magnet. It measures the magnetostriction as a volume change, whereas the strain gauge senses the surface deformation. B) Strain and strain-sensitivity dependence on the applied magnetic field, Fig. 2.11. It shows the ability of the device to resolve at total displacement of 50 nm for two samples. The subscripts of BTO$_{75}$-CFO$_{25}$ refer to weight percentage. The strain sensitivity is derived from magnetostriction above it.

Notably, the saturation strain of the composite is $\approx$ *18%* of that exhibited by the pure CFO phase, despite the composite having a *27%* volume fraction of CFO. This discrepancy can be elucidated by considering the discontinuity inherent in the CFO phase and the mechanical constraints imposed by the BTO phase. The rationale applied to the isolated magnetic regions discussed in Sec. 5.2 can similarly be extended to this scenario. Thus, the depiction of the material as *magnetically* "porous" warrants revision in light of these insights.

Moreover, polycrystalline ceramics exhibit isotropic properties[12]. Therefore, there is no specific direction of magnetostriction $\lambda(H)$ for a polycrystalline ceramic, which means, given their random anisotropy, their neighbours can limit their grain expansion.

The ferroelectric phase, though magnetically inert, serves as a boundary of confinement with a certain degree of stiffness.

[12] Aubert *et al.* [50] demonstrated that a uniaxial anisotropy could be induced with the reactive sintering SPS.

This boundary prevents the magnetic phase from expanding in the direction of the applied field, thereby enhancing the ambiguity of the strain direction along the magneto-mechanical axis. Building upon the plausible explanation outlined in Sec. 4.4.3, it is posited that any deviation from the easy axis induced by the field necessitates compensation through a second sample positioned opposite to the one with the mirror. This secondary sample, situated on the laser head, experiences the same distortions induced by the field and effectively counteracts any deviation from the optical axis, as depicted in Fig. 5.5A.

5.3.2 Mechanical characterization

The elastic properties of the ferroic phases play a pivotal role in mediating the magnetoelectric effect in composite magnetoelectrics. This mechanical attribute is notably intertwined with both magnetic and ferroelectric properties and derives its significance from their microscopic origins within the unit cell. Any exertion of force causing distortion to the unit cell affects the properties of both phases simultaneously [60, 72].

With respect to the calculation of the coupling of the magnetoelectric effect, the value of "k_c"(Sec.2.6.3) depends on the stiffness coefficient for the in-plane and the transverse shear [113, 122]. In the case of the longitudinal orientation[13], k_c depends only on the value of Young's modulus $Y_{mod} = k_c$. Correspondingly for Eq. 2.52 $\alpha_{ME} = \frac{d_{33}}{\varepsilon_0 \varepsilon_{r,ij}} k_c \, q_{33}$ is applicable [203].

In order to determine the general stiffness of the material and get an idea of its dependency on electric or magnetic parameters, the measurement of the stress-strain curve, as introduced in Sec.3.4.1 is required.

Stress-strain: Representative cyclic measurements were carried out on a composite as shown in 5.13B. For this purpose, the mechanical testing machine, which is integrated into the setup, was used. The measurements were made using a cyclic loading mode with a constant loading rate of (0.75MPa/sec). As is shown in the inset of Fig. 5.6B, initially, the load is applied until a defined pressure limit is reached. Afterward, the testing machine begins to unload down to 1MPa, and it starts to load again.

By loading in a cyclic mode the material behaviour, in terms of its plastic properties, is revealed. As seen from Fig. 5.6, the first curve in the cycle does not match the second loading cycle curve. It shows a slightly flatter curve, indicating the progression of slow damage inside these brittle composites. The plastic part of the deformation is irreversible. Nonetheless, the strain returns close to the initial point where the difference is due to the plastic deformation.

From the proportionality of the stress-strain curve, the Young's modulus of the material can be determined, see table 5.1. The values for Young's modulus are three orders of magnitude lower than the literature values, which range for cobalt ferrite from about 150 GPa [204] to 172 GPa for nanoparticles [182]. However, the sample in this work for the chosen sintering path, Sec.3.1.1, reaches only 70% of the theoretical density for CFO [199].

Material Phase	**E$_Y$ [GPa]**
BTO	267
CFO at	290,3
CFO at 1,5T	289
CFO_{27}-BTO_{73}	470

TABLE 5.1: Experimentally obtained values for young modulus, data evaluated from Fig. 5.6

In contrast to this, Young's modulus of BTO varies significantly in the literature [205]. Experimental values are relatively diverse as for single crystals at 59.2 GPa [206] and 100 μm thin films at 67 GPa [207]. In other literature sources, this value is significantly higher at

[13] When all field's directions, alternating and magnetizing fields coincide with the direction polarization of the sample.

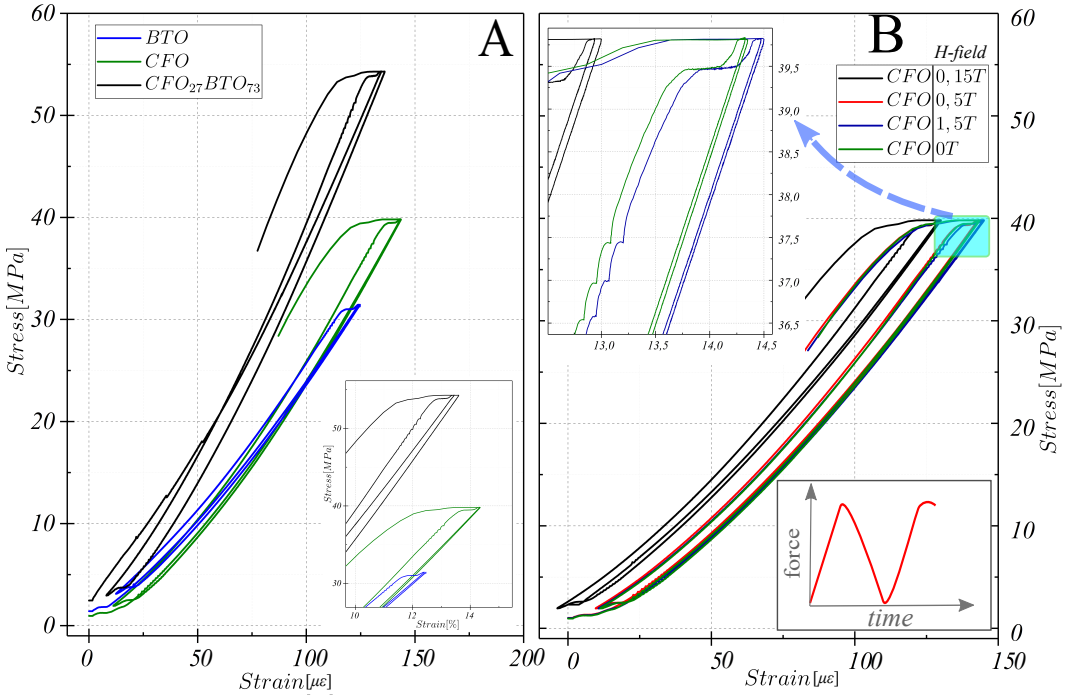

FIGURE 5.6: Identifying the elastic properties of composite and pure phases of BTO and CFO. A) Displays the stress-strain measurement of three materials, With composite showing high young modulus. B) displays the magnetic field$_{const}$ dependency of the same CFO sample during a cycle of loading, unloading, and loading for different H$_{const}$-fields. Given this, the sample experiences certain plastic deformation during each cycle. However, besides the distortion, it reveals the dependency of the elastic moduli of anisotropic materials is influenced by ferroic order as the difference between the curve at 1,5T and the subsequent measurement at $H_0 = 0$ shows; Visible in the inset on the upper left corner. (inset: The applied pressure at the rate (0,75MPa/sec) for loading and unloading)

168 GPa [205], and for ceramic discs, it ranges between 97 - 112 GPa [208]. The differences in the literature can be referred to as material impurities and variations in the used sintering routes.

The composite material has a higher Young's modulus than both pure-phase constituents, as shown in Fig. 5.6A. This can be due to the microstructure formed after densification as the composite builds a near eutectic composition [87]. Furthermore, the composite particle size has a wide range, given the different sizes of CFO and BTO, which helps to obtain better compaction in the green bodies than to that of the pure CFO or BTO phase. Such effects would lead to higher final densities.

The measurements in Fig. 5.6B show the dependency of the stress-strain curve on the external magnetic field, Tab. 5.1. The dependency is due to the correlation between the magnetic order, anisotropy, and elastic moduli, as discussed in Sec.2.4.2.

5.4 Composite effects under uniaxial stress

In the previous sections, the mechanical stress measurements were related to cyclic mechanical loading, see Fig. 4.4, and stress-driven strain measurements. The latter was made to investigate the elasticity of the ceramic samples. This section delves into the impact of constant uniaxial mechanical stress as an additional external parameter on various properties

pertinent to magnetoelectric composites. Specifically, its influence on magnetization, magnetostriction, polarization, and electrostriction are scrutinized. Of particular interest is its effect on magnetoelectric coupling α_{ME} which undergoes thorough analysis. By applying uniaxial stress, we aim to elucidate the intricate interplay of mechanical and electromagnetic phenomena in these composite materials.

The experiments conducted in this section also seek to characterize the performance of the uniaxial stress module within the setup and its interaction with other stimulus field modules. It is observed that changes in each parameter involved in the coupling coefficient α_{ME}, as described in Eq. 2.52. The experiments reveal that a change in each parameter would affect the coupling as a result of it being a product property, 5.6.1 and Sec. 5.4.2.

5.4.1 Effect of pores under uniaxial stress

In order to demonstrate the effect of stress on the mechanical behavior of porous composite, an FEA (Finite Element Analysis, Appendix.B.1) stress analysis simulation for the case of uniaxial stress has been carried out, Fig 5.7.

In the simulation, stress is applied on one surface of the cylindrically shaped sample while the other surface is fixed (boundary condition). This arrangement reflects the experimental procedure applied in the uniaxial stress-related measurements. The stress is exerted as an external force that acts from top to bottom. However, the material behaviour can be extrapolated for the case of internally induced stress. In contrast, in real magneto-electric composites, one phase is activated internally (by an electric or magnetic field) and exerts a force on the other phase. The inclusions (representing CFO) in the model are given different sizes and shapes as they are embedded in a BTO matrix (grey). The model is calculated with literature-derived mechanical values of CFO and BTO (Tab. 5.1), with 150MPa being the external stress applied on the top surface. In Fig. 5.7 the first column presents the situation with no pores in the 0-3 model and with a perfect interface between the constituents. In this case, the stress is transferred homogeneously with the initial magnitude, as applied to the upper surface, into the volume, and into the inclusions. The second column displays the results for the case of elliptic pores (depicted as transparent vesicles, with $R_1 = 0,0005mm$ and $R_2 = 0,001mm$), which are randomly distributed in the model with a total volume fraction of $\approx$ 0,1% of the overall volume in a composite of CFO $\approx$ 18% and BTO$\approx$ 81,9% volume percent. The third column shows the case when the volume fraction increases to $\approx$ 0,5%, with bigger pores and random shapes.

From this study, it can be concluded that the presence of pores results in abrupt changes, causing a discontinuity in stress transfer. Additionally, porous composites experience locally higher stress levels than the initially applied stress to the sample. The emergence of regions with elevated stress indicates potential areas where cracks may form. Similar reasoning can be applied to internally induced forces resulting from the applied cross-field. Exceeding the yield energy leads to the formation of "crack nuclei", potentially resulting in crack development during uniaxial stress. This can ultimately lead to poor mechanical coupling between phases and plastic deformation of the ceramics.

5.4.2 Influence of uniaxial stress on the magnetization

This section demonstrates the performance of the pressure cell to detect changes in magnetization, see Sec.4.5. Further, it investigates the influence of constant uniaxial stress on the magnetization hysteresis of CFO and CFO-BTO, see Fig. 5.8.

The custom-built pressure cell is compatible with the VSM used in this work, with its DC-magnet field being oriented collinear to the uniaxial stress field direction, see Fig. 3.11. The hysteresis loops were taken separately for different applied uniaxial stresses for both

composites and pure CFO, see Sec.5.6.1. Each hysteresis is measured with sequentially increasing stress until the sample is broken.

From the interpretation of the data presented in Fig. 5.8[14], it can be inferred that the samples' mechanical response consists of both elastic and plastic components, as demonstrated in the preceding section. Understanding the underlying relationship between elastic and magnetic behavior is crucial from a magnetic property perspective.

The magneto-mechanical coupling influences the change of magnetization caused by the application of stress in a constant magnetic field. Given that the hysteresis maps a non-linear behaviour of the domain switching between two "order" states given by the field directions. The switching process involving 1) domain-wall motion and 2) magnetization rotation is suppressed in the direction of the applied uniaxial field, as it necessity higher magnetic fields to surpass the

The related magnetization curves by variation of uniaxial stress are displayed in Fig. 2.10 [74]. This is due to the nature of domain formation, as it results from the interplay between the uniaxial anisotropy and demagnetizing field.

Furthermore, in polycrystalline ceramics, the behaviour of the domains is complicated by the overall structure as it is not a regular single crystal lattice, but instead, a polycrystal is made up of multiple grains. Furthermore, the structure of its crystal lattice could contain all sorts of defects and impurities. This makes the study of the switching processes an elusive task. Nevertheless, the saturation of the hysteresis is one of the key subjects of this investigation [15].

The data from Fig. 5.8 states that the stress clamps some magnetic domains inside the grains. This leads to some domains being unable to rotate to align with the high magnetic field. In other words, domain wall motion and magnetoelastic energy under pressurein those grains cannot overcome a mechanical hindrance. From this, the elastic energy in the domains can be deduced as it is related to the stress-induced anisotropy overcoming the magnetocrystalline anisotropy, see Eq. 2.44, [47].

At some stress levels, the sample cracks. A hint for the existence of crack formation in the sample comes from an increase of saturation magnetization of the hysteresis despite increasing stress, which contradicts the restraining effects of stress on the hysteresis. This occurs as the crack leads to a partial release of stress inside the sample. This would lead to a higher saturation magnetization than the previous magnetization measurement. Here, as shown in Fig. 5.8B for CFO when the applied stress increases from 25MPa to 30 MPa.

The measurements on composites show a relatively small decay of the magnetization compared to CFO, see Fig. 5.8B.

[14] The data points in Fig. 5.8B represent the normalized saturation magnetization taken from Fig. 5.8A.

[15] In a single crystal with defined uniaxial anisotropy, there will be changes expected in both coercive and remanence fields.

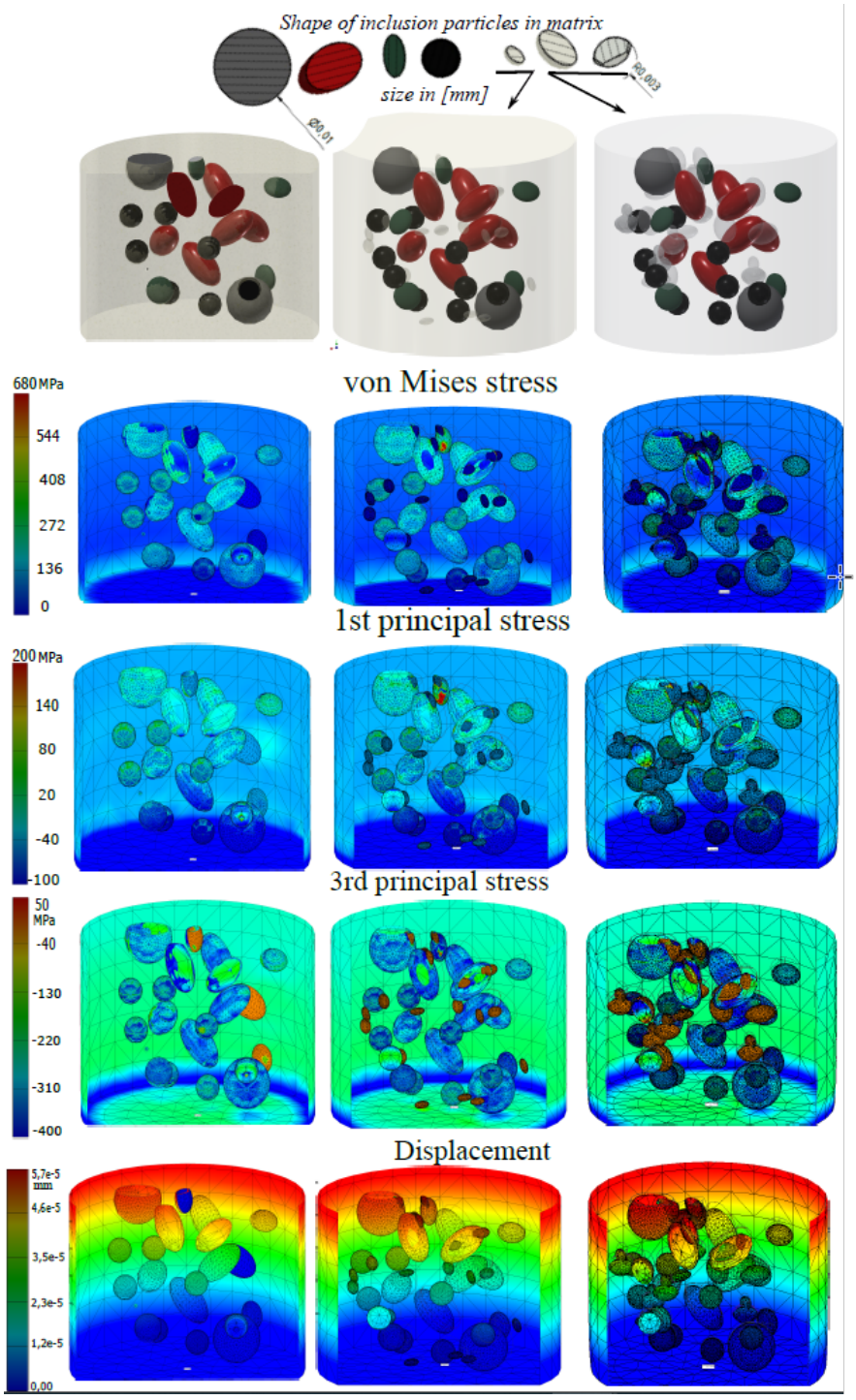

FIGURE 5.7: FEA simulations of the effect of uniaxial stress on 0-3 composite with different CFO particles embedded in a BTO matrix. The model is solely mechanical, without any ferroelectric or magnetic phases functionality. As is the case for a real experiment, the pressure is applied from the top while the sample is fixed at the bottom. The first row displays the 0-3 model with different pore volume fractions. The first *column* displays a composite with no pores and perfect interface coupling between the constituents. The second column displays the results of samples with pores with a total of $\approx$ 0,1%. In the third column, this volume fraction is $\approx$ 0,5%. Details of the simulation parameters: Sec.Appx.B.1

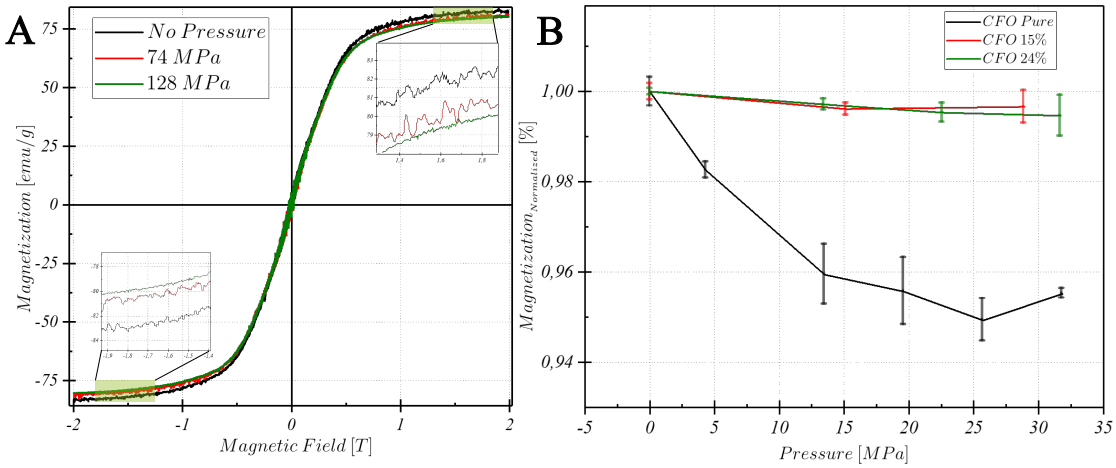

FIGURE 5.8: Uniaxial stress-dependent magnetization measurements performed with a VSM. A) M(H) measurement of CFO and composite (sol-gel prepared, as displayed Fig. A.2) inside pressure cell at different stresses σ. B) Normalized relative magnetization at different stresses σ for the CFO and composite.

5.5 Polarization and strain under constant external fields

This section describes the ferroelectric properties of the magnetoelectric composite compared to those of BTO and PZT. The measurements are performed under constant mechanical stress and magnetic field. It confirms the feasibility of the concept for the setup to measure $\epsilon_H(E)$ in a magnetic environment.

At the start, the *electromechanical* properties of 0-3 mixtures of $CoFe_2O_4$-$BaTiO_3$ are studied in the presence of a magnetic field but without applied uniaxial stress.

For this case, the Sawyer Tower configuration is utilized to measure polarization and bipolar strain-electric field hysteresis loops, employing the interferometry method integrated into the setup for non-pressure conditions, as detailed in Sec.4.4.1. Subsequently, the samples are tested under uniaxial compression stress alongside the magnetic field, using the same device configuration as described in Sec.4.4.2. Altogether, the measurements serve as a proof of concept for the integration of interferometry in the complex multi-field environment.

5.5.1 Polarization and strain under magnetic field

Hysteresis depicts the switching behaviour of the domains in ferroelectric materials. With respect to the technical utilization of ferroelectrics, it is a decisive parameter. However, here, the hysteresis is measured for magnetoelectric composites. The related device is able to resolve nanometer displacements which enables to study the effect of the external field on the strain response of composites to an electric field, see Fig. 5.9C. The S-E loops are measured together with the polarization in a *stress-free* state with the setup as presented in Fig. 4.16.

In this regard, the "butterfly" curves (ϵ_3 vs. E) represent the electromechanical properties, with their slope close to $E = 0V$ specifying the piezoelectric coefficient d_{33}. Its value is a decisive factor in the determination of the coupling coefficient of composite magnetoelectrics (Eq. 2.52).

For these measurements, given the moderate dielectric strength of the composites, an AC-electric field of 25kV/cm was applied[16].

The measured data, as shown in Fig. 5.9A, exhibit a quadratic dependency, which is expected for electrostrictive materials. At the same time, the curves show a lower strain amplitude compared to pure BTO phases due to the ferrite content Fig. Appx.B.7. This is to be expected since the charges induced by the electric field percolate in view of the low resistivity of the magnetic phase, which leads to a lower polarization. Moreover, the magnetic phase in the sample volume does not exhibit piezoelectric/electrostrictive properties.

A further notable feature of the data is its narrow hysteresis loops. This shows that these materials have low coercive and remnant fields, indicating a lower ferroelectric behaviour in terms of domain switching[17].

In order to investigate the impact of the magnetic field on the strain hysteresis of ME composites, the setup is exposed to various constant magnetic fields. In this case, the field configuration of both the electric and magnetic fields are collinear, Fig. Appx. B.6A. The resulting hysteresis shows an elongated peak-to-peak displacement with increasing magnetic field, which indicates that there is an extended alignment of ferroelectric domains in the field direction, given the support of the magnetic field, see Fig. 5.9C. Fig. 5.9C. The related error bars are evaluated for peak-to-peak displacements within a 1-second sampling

[16] In all the measurements, samples are disk-shaped with a diameter of 6.5 mm and a thickness of 1.0 mm. After polishing and lapping, the circular faces of the disk samples were electrodes with *Ag* paint, burned, and polished.

[17] The reported butterfly hysteresis for BTO are narrow as well [124].

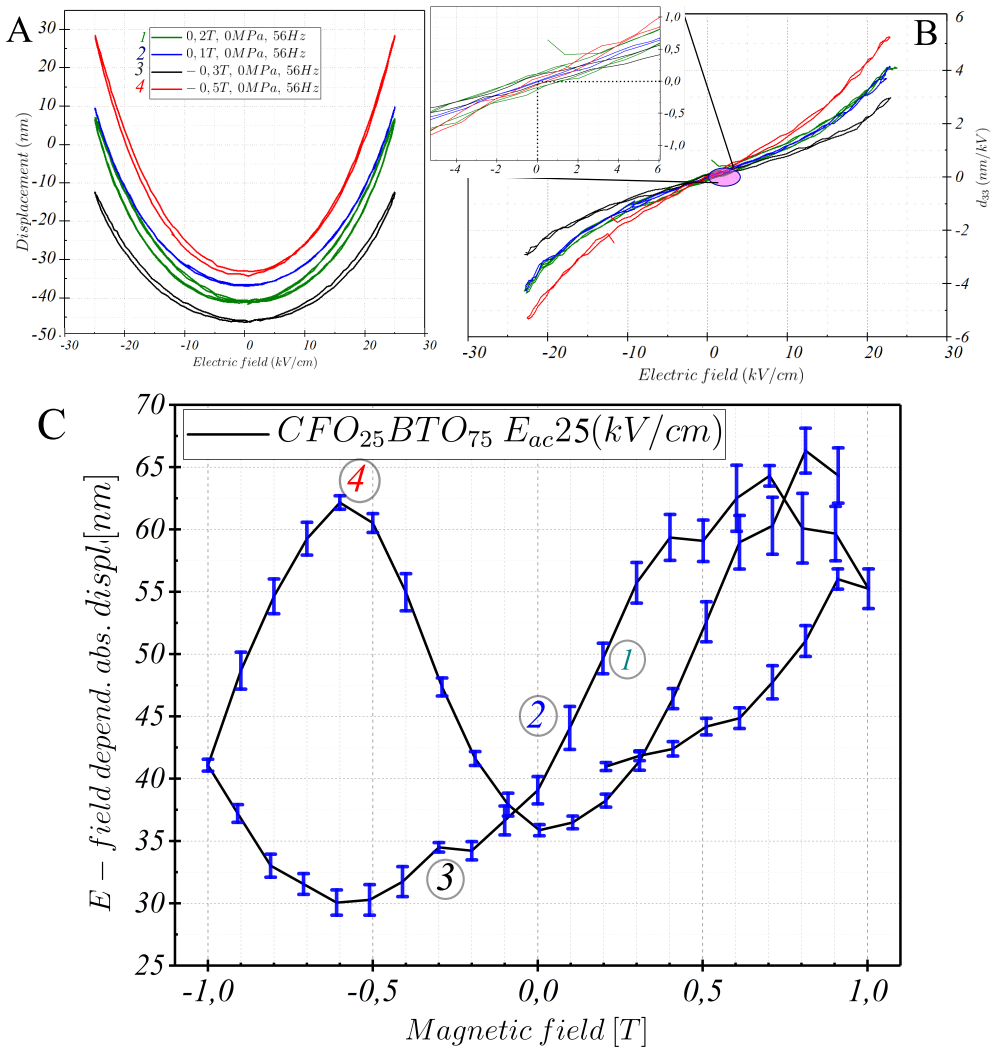

FIGURE 5.9: P-S loops of 0-3 CFO_{25} BTO_{75} composite at different magnetic field offsets, measured with the magnetic field compatible container, Fig. 4.16. A) The unclamped strain measurement loops under the influence of a constant magnetic field. The offset-shift on the displacement-axis between the strain-curves for different magnetic field is for better illustration. B) The piezoelectric coefficient (d_{33}) of the composite obtained as a derivative of the strain curve in A, it ranges between 0.1 pm/V to 0.2 pm/V. The d_{33} value is the proportionality factor to α_{ME}, Eq. 2.52. C) Represents the *average* peak to peak displacement value dependence on the magnetic field for a 1 mm 0-3 CFO_{25} BTO_{75} composite, where the numbers mark the field points shown in A, and evaluated in B in order to obtain their corresponding d_{33}.

time. The error is systematic and originates from the thermal drift of the diode laser in one part and the dissipated heat due to the applied AC field in the other. A further measurement capability of the setup is the calculation of piezoelectric constants driven from the strain curves at $E = 0$, as the derivative $d_{33} = \frac{\Delta\epsilon_3}{\Delta E_3}$ for different magnetic fields, Fig. 5.9.

Moreover, the electromechanical energy conversion (k^2, Eq. 5.2) is another essential component of the ferroelectric phase, which is correlated with the value of α_{DM} over the $d_{33}^{E=0}$, Eq. 2.52. With this value, it is possible to classify the S-E loop and decide whether the ferroelectric phase is suitable for composites. A butterfly curve with high amplitude and low coercive field would result in high d_{33} around $E = 0$, as is the case for soft PZT, which makes it a suitable candidate for magnetoelectric composites[107, 209].

In the next section, the topic of electromechanical testing under the influence of constant uniaxial stress on the ferroelectric phase and composite is compared to the zero applied stress case.

5.5.2 Uniaxial pressure device

In applications, ferroelectric-based devices are subject to *mechanical* load and *electrical* field, as is the case for actuators. Therefore, the experimental procedures to characterize the parameters related to the ferroelectric materials under both conditions apply to applications and the standard characterization route in research.

Zhou *et al.* [149] extensively investigated the effect of uniaxial stress on P-E and S-E hystereses of commercial piezoceramics (PZT). He used a hydraulic universal testing machine to apply stress. However, strain detection was made with a strain gauge. His work concludes that increasing uniaxial stress makes generating the initially pronounced hysteresis no longer possible as the domain switching process is suppressed [57]. In this case, the stress prevents the complete alignment of the domains and induces mechanical depolarization simultaneously [210, 211].

In this section, similarly, the electromechanical switching behaviour of composites is investigated under uniaxial stress and constant magnetic field. The results of the measurements are used to calculate the d_{33}. Additionally, they prove the concept of the setup for creating uniaxial stress and is compatible with magnetic field applications. The measurement procedure stays the same as in the previous section, with an AC-electric field being applied in the Sawyer Tower configuration. At the same time, the data on strain is recorded simultaneously. The measurement is performed in an automated manner, except for the application of constant stress. This is manually applied as a fixed parameter before the measurement is started. The setting for the magnetic field (steps/sweep), frequencies, and the strength of the electric fields are pre-configured in the LabView program, Appx.B.8. The samples tested in the measurements are laminated bilayer composites of $CFO_{1mm}PZT_{0.5mm}$, Fig. 5.10, and 0-3 $CFO_{33\%}BTO_{67\%}$, Fig. 5.11.

The data in Fig. 5.10A displays the typical PZT hysteretic behaviour. The slight deviation from the typical shape of the strain hysteresis is possibly caused by CFO, as it constitutes the second layer, which has a finite elasticity. The slopes of the polarization hysteresis at zero electric field yield the permittivity ε_{33}. PZT's values do not alter much with stress, which agrees with the result obtained by [149].

In contrast to the permittivity value $\varepsilon_{33}|_{\sigma_3}$, the piezoelectric coefficient d_{33} evaluated from the S-E$|_\sigma$ curves alters drastically under uniaxial stress, see Fig. 5.12. This finding *partially* explains $\Rightarrow$ the value of α_{DM} under stress as the electromechanical energy conversion k^2 is proportional to $d_{33}(\sigma_3)$, see Eq. 5.2 and Fig. 5.19.

The effect of the *magnetic field* combined with constant stress on the electrically driven strain measurement is also investigated. In this case, the peak-to-peak displacement of the

bilayer reveals that the S-E_H amplitude doesn't show any dependency on the magnetic field, Fig. 5.10C.

This was not expected, as for the clamped state, the magnetostriction of the magnetic layer exposed to the magnetic field would generate additional stress in the H-field direction. This would suppress the electrostrictive strain of PZT, or lower the stress on the PZT, depending on the sign of the λ. However, the effect originating from CFO is not measurable. The explanation for the negligible exerted stress effect on PZT is explained in the following. The magnetostriction of 1mm thick CFO generates a 180nm displacement in a stress-free state and less when under uniaxial stress. This value is less than 2% of the total strain for 1mm PZT with $_{max} = 0,8\%$, see Fig. 5.13C. Consequently, the additional stress effect on the electrostrictive displacement of PZT in the clamped state is not significant.

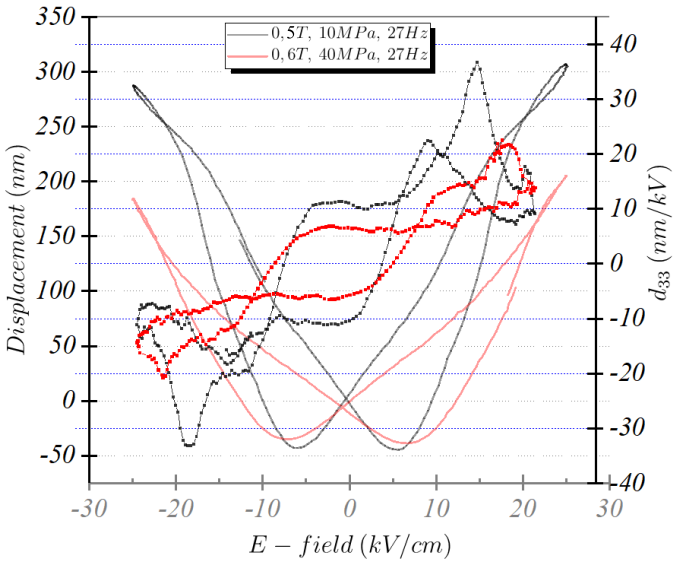

FIGURE 5.12: The effect of constant uniaxial compressive stress (10Mpa and 40Mpa) on d_{33} (dot-line) driven from the displacement (plane line), Fig.5.10, marked in the square box

Aside from the measurements on the bilayer, the same measurements were also performed on 0-3 composites, see Fig. 5.11. For these samples, also unlike the case of the stress-free state, see Fig. 5.9, no dependency on the effect of the magnetic field in the clamped state could be detected, see Fig. 5.11. Detailed investigations of these materials looking at the magnetic influence on the ferroelectric-ferroelastic switching behaviour can be very complex and require locally resolved analysis techniques, such as MFM and PFM.

The measured displacement of composites at different E_{AC} field amplitudes, see Fig. 5.11, under different uniaxial stresses, along with applied magnetic fields, gives insight into the performance of the main module in the setup, see Fig. 4.3.

The overall concept for the integration of interferometry provides the accuracy needed to perform a few nm exact characterization, as shown here in the measurements.

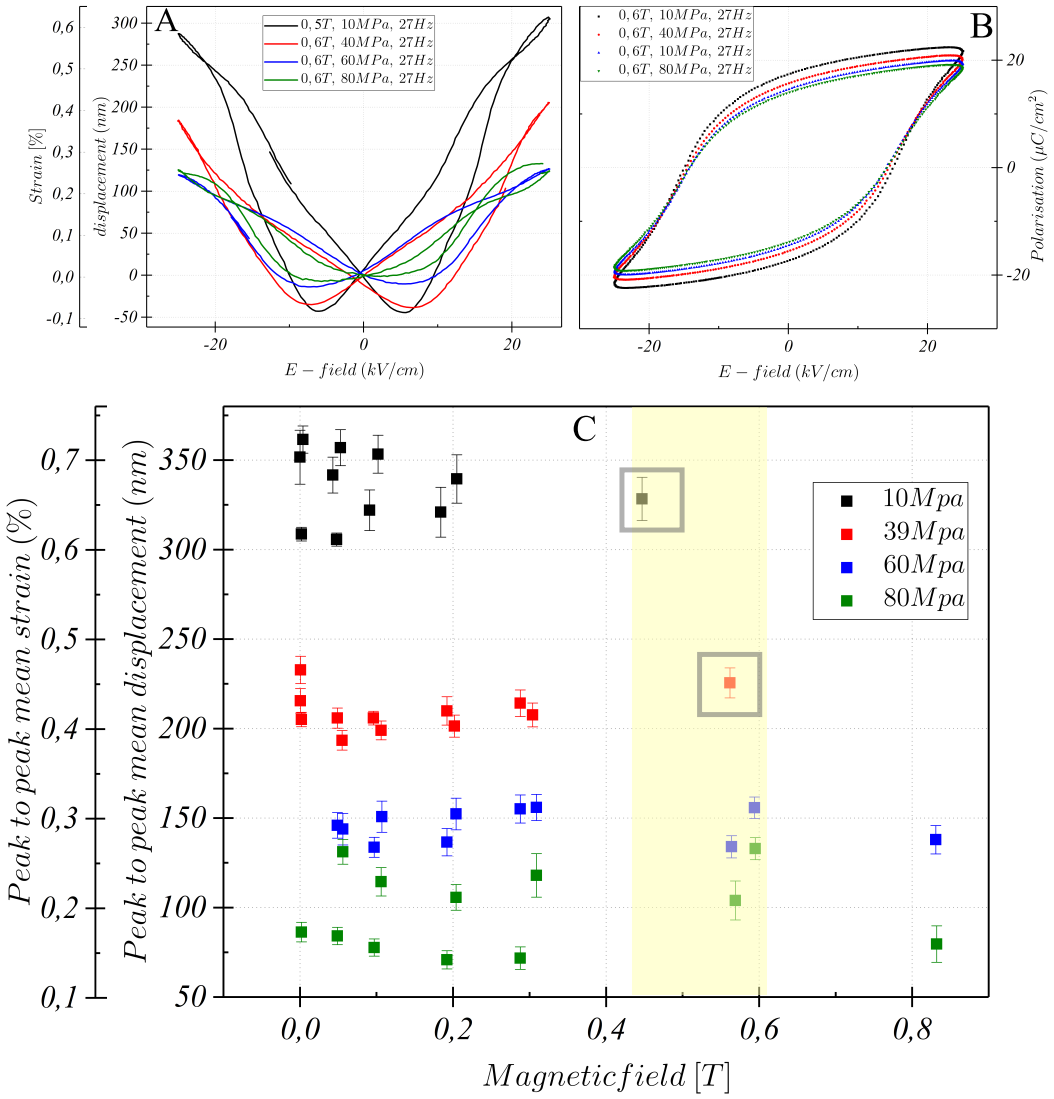

FIGURE 5.10: PZT and CFO as a bilayer system is measured under different stresses and magnetic fields with the setup module displayed in Fig. 4.18. A) Electromechanical strain properties are tested at 0.6T along with B) the polarization hysteresis for this bilayer at room temperature for various constant uniaxial compressive stresses. C) Dependency of the peak to peak displacement/strain for various magnetic fields and stresses. The data points marked in the square boxes is further evaluated in Fig. 5.12 for its d_{33} value.

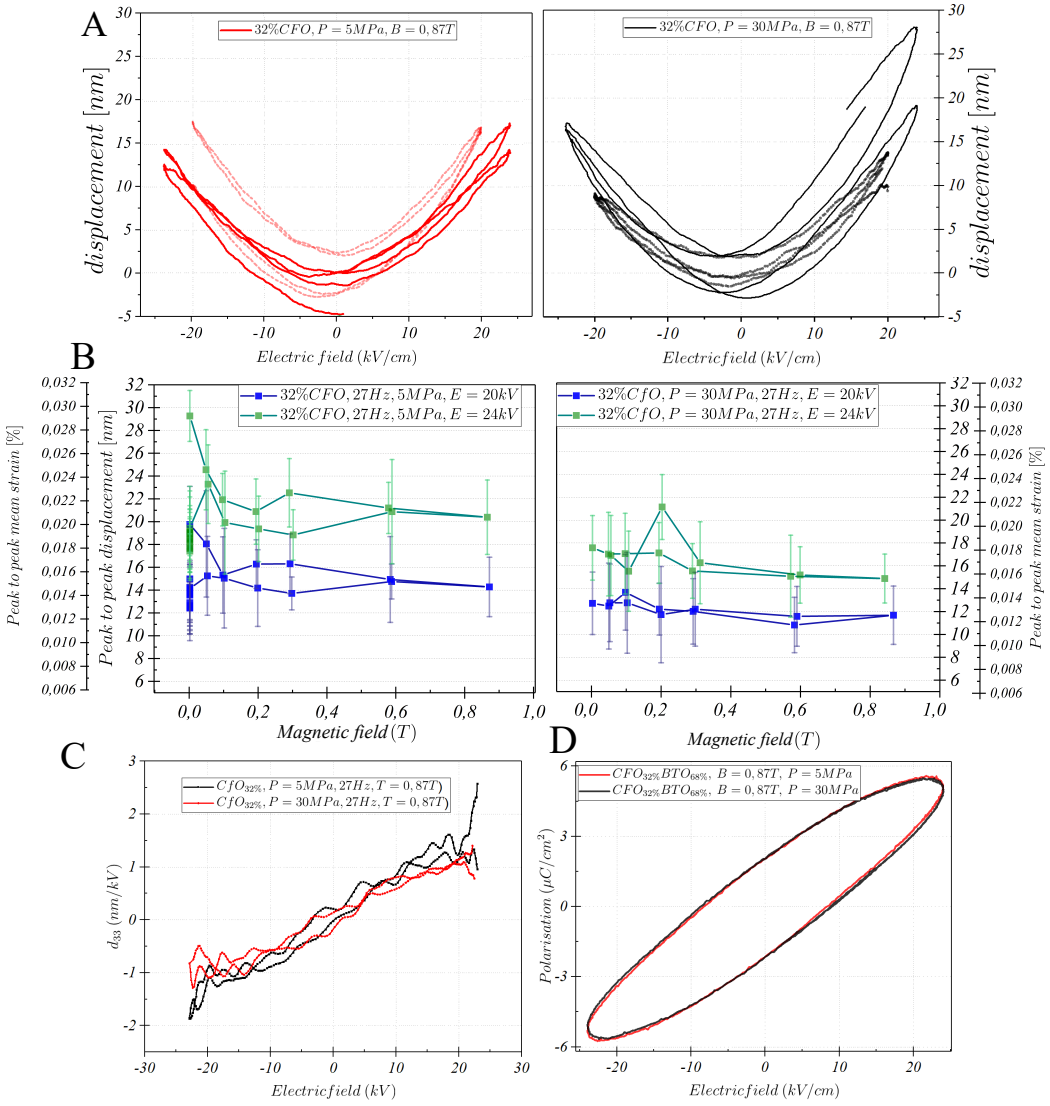

FIGURE 5.11: Investigation of the electrostrictive response of composites. For the measurement, the option shown in Fig. 4.18 is used. A) Butterfly loops under different stress fields and constant magnetic fields. This proves the feasibility of the approach. B) The peak-to-peak values of butterfly loops averaged over a 1-second integration time for a driving frequency of 27 Hz. The displacement and the absolute mean displacement axis are plotted together, showing the resolution capability of the device. The mean strain value with different excitation parameters is automatically measured at several points over a half-magnet cycle up 0.9 T for two electric fields (20kV/cm and 24kV/cm) and two constant stress fields (5MPa and 30MPa). The peak to peak calculation was made by D.Lewin. C)The related polarization and calculated d_{33} for A). D) Presents the related polarization hysteresis.

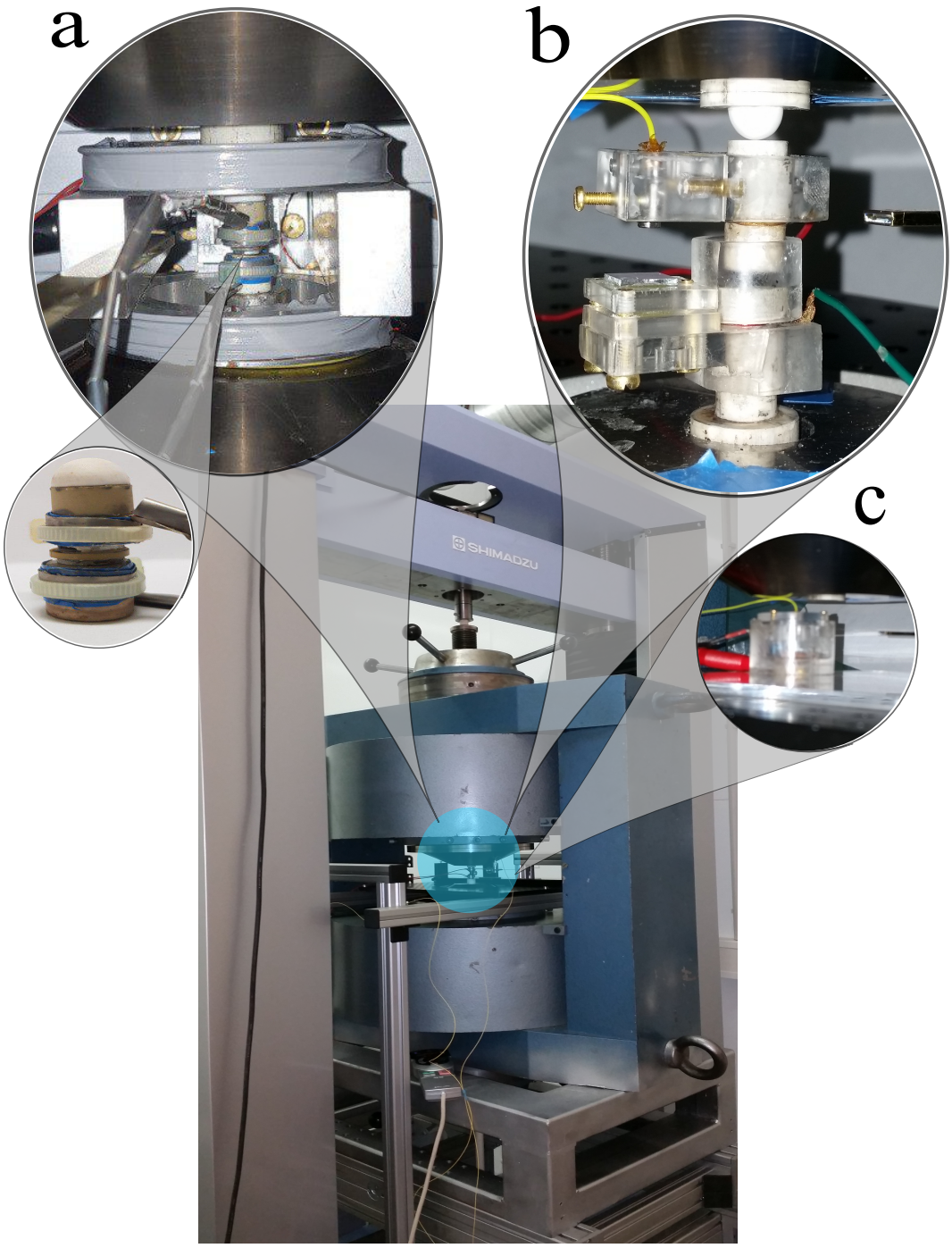

FIGURE 5.13: Demonstration of the interchangeable modules of the setup. A) The ME-effect module, with the possibility of applying uniaxial stress by placing the sample between two homogeneously flat alumina disks. B) The option for simultaneous P-E and S-E loop measurements under uniaxial stress and magnetic field. C) The compatible magnetic container for stress- free P-E and S-E measurements when placed between the magnetic pole shoes.

5.6 Magnetoeletric coupling values

The characterization of the ME coupling coefficient, as the primary performance parameter, is driven by the aspiration to utilize the magnetoelectric composite in applications. As sensor material, it is of essential importance to detect the response of one phase in composites by an acting field which is indifferent to the active field. Given this, the ME-coupling α is the foremost investigated value of magnetoelectric multiferroics. It gives them the characteristic of a figure of merit [146, 212].

Recent literature predicts that the measured magnetoelectric coefficient can be tuned by applying a certain pre-stress. An advanced setup involving all the characterization parameters would improve the coupling efficiency between the phases. Here, as introduced in Sec. 3.6 , the direct ME-measurement method is used to characterise the ME- coefficient in composites. To study the stress effect on $\alpha_D(H)$, the direct ME-measurement module is integrated as an option to the magneto-mechanical setup, Fig. B.6D. This allows the possibility of applying uniaxial stress as an additional characterization parameter to the ME-effect α_σ.

For the sample, the application of uniaxial stress is often destructive. Therefore, the necessity of excellent mechanical stability of the sample is often decisive, see Sec. 5.1. Here, CFO-BTO composite samples[18] were also required to have a ME α coupling value in the same range as reported in literature [35]. This would confirm the devicmeasurement functionality.

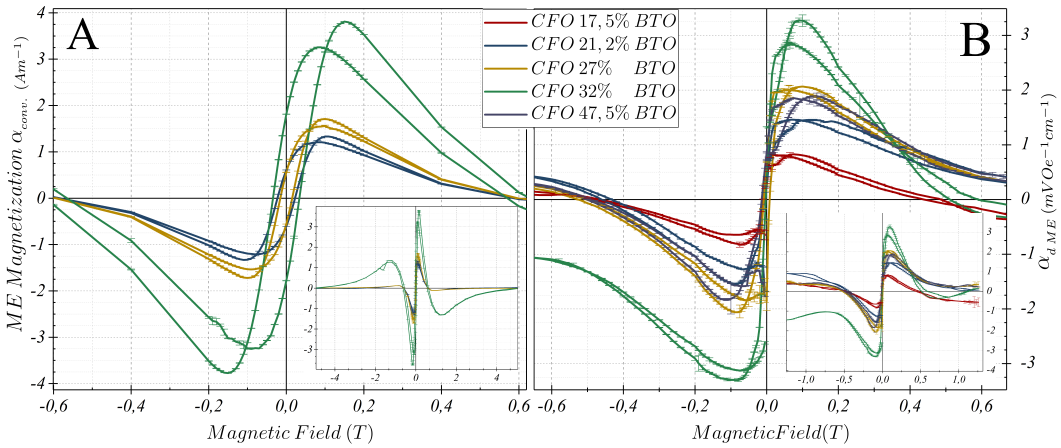

FIGURE 5.14: The data illustrates the (A) converse and (B) direct α coupling measurement of the same set of samples. Both are measured in the longitudinal configuration with a biased H_{DC} sweeping field. All the $\alpha_{ME_{D/C}}(H)$ measurements are conducted at room temperature. The direct measurement (B) requires the correction of the α value by a factor of 2.3 due to the capacitive impedance of the coax cable, calculated with Eq. 3.4. As the effect is strain meditated, the different nature of the stress-response in each phase is the reason for the different appearance of converse and direct curves. The $\alpha_C(H)$ measurements were conducted by Dr. Salamon.

ME measurements were conducted on the same CFO-BTO composite samples with both methods. The data in Fig. 5.14 reveal similar results for the methods, agreeing with literature values.

The converse method, which uses a customized SQUID setup, is already well established. By measuring the same set of samples with both methods, the functionality of the

[18] The material is well studied and serves as a “golden standard”.

incorporated *direct* ME-measurement in the assembly of this thesis can be assessed. Therefore, the measurements are conducted under the same conditions with a frequency of 96 Hz, which is much lower than the electromechanical resonance frequency (350 kHz) and at room temperature [29].

However, owing to the pseudo coupling related to the magnetoelectric effect, the curves are not similar but comparable. This pseudo coupling is due to the different nature of the response of each phase to stress, induced by the counter-dynamical excitation field, E_{ac}, or H_{ac}, see Fig. 5.14.

The direct method senses the gradient of the electrostriction of BTO at $E = 0$ by a dH_{ac} at a certain bias field H_{dc}, which depends on the degree of its poling state, as illustrated in Fig. 3.13 [p.62].

Contrastingly, the converse method senses the first-order derivative of magnetostriction ($d\lambda_{static}/dH_{dc}$), with the biased H_{DC}-field shifting it to the sensitive region. Therefore, as the shape of the ME coupling curves is α_{ME} driven by H_{dc} biased field, as presented in Fig. 5.14, these are correlated to the strain sensitivity (or strain derivative) of the magnetic phase, Fig. 5.16, [71].

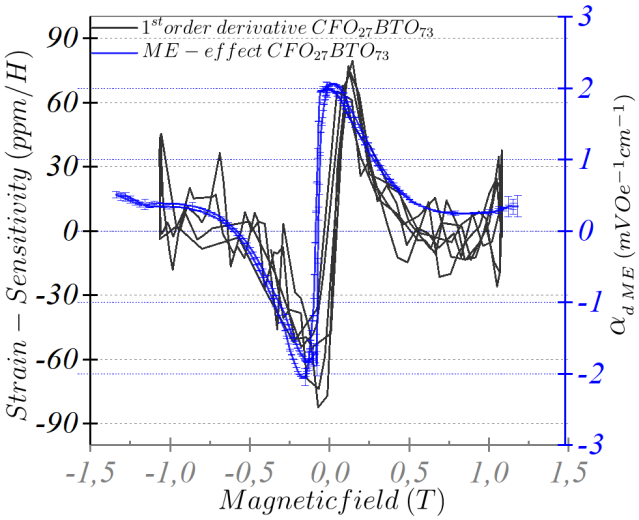

FIGURE 5.15: Magnetostriction-sensitivity as a derivative of magnetostriction (obtained from H_{dc} biased field), Fig. 5.5 plotted together with ME-coupling α (obtained from H_{ac} response), see Fig. 5.14.

The experimental procedure of measuring both $\alpha(H_{dc})$ and *strain sensitivity* is similar, however, not the same as it is done here: Here, the magnetostriction is measured with a bias DC-field[19] swept in a loop from -1.2 T up to 1.2 T and the strain sensitivity is derived from the measured strain. With this, the detection of each quantity is done differently. For the direct $\alpha_{ME}(H)$ measurement, a lock-in amplifier is used, see Fig. 4.9, and for the strain sensitivity, the presented solution in Sec. 5.3.1, with the corresponding strain detection, as presented in Fig. B.6B, is used.

Characterizing strain sensitivity as the figure of merit of the *magnetostrictive* phase in composite materials is a decisive parameter whether a material is suited as the constituent for a magnetoelectric composite. It dictates the value of the pseudo-piezomagnetic coupling ($d\lambda/dH$, see Eq. 2.52) required to engineer a composite with a high coupling coefficient as the ME effect depends on the domain dynamics and ac magnetostriction.[69]. Therefore, the characterization of a less optimal magnetic phase ahead of synthesizing the composite saves effort and time.

It is visible in the data in Fig. 5.5 that the strain response of magnetostrictive materials is generally divided into four regions. In the low magnetic field region, the strain rises slowly as the field increases. The strain increases rapidly and linearly in the field region of 0.1T – 0.25T, where the derivatives are the highest, which corresponds to the highest ME coupling in the ME-curve, Fig. 5.16. In the field region >0.5T, the magnetostriction curve value λ approaches saturation, where the coupling value falls to zero. Its appearance is notable in the inset of Fig. 5.14, for the composition ($BTO_{68\%}CFO_{32\%}$) in both direct and converse ME measurements. The field of the strain peak value can be influenced by a

[19] It is not superimposed with a constant H_{ac}.

uniaxial stress, which influences the shape of the ME coupling coefficient. This is addressed in the following section.

5.6.1 ME value under uniaxial stress

In this section, the characterization of magnetoelectric composites continues with consideration of the applied uniaxial stress on $\alpha_D(H_{DC})\,|_\sigma = const$. Especially, the contribution parameters (Eq. 2.52) to the effect are investigated.

A ME-setup with uniaxial stress possibility is not only relevant to scientific questions but also engineering. A biased dc magnetic field is generally needed for applications of magnetoelectric composite in devices to reach the maximum value of λ_{ac}/dH_{dc}. However, adding a permanent hard magnet to the device increases the size and causes cross-talk among neighboring units in an array, adding to the potential noise sources [213]. Therefore, the correct setting of the pre-stress can lower the applied magnetic bias field and improve the magnetoelectric coefficient [214]. Also, the developing of thermal stress or package stress (e.g., soldering on PCB) in magnetoelectric devices is necessary engineering requirement. These stresses may impact the magnetoelectric behavior of the laminates, necessitating quantification for the designed device. Therefore, a suitable setup is required to study and analyze these effects comprehensively.

Experimental procedure: For these measurements, the direct ME-measurement module accommodated with the universal testing machine is used, Sec. 3.4.1. The stress path is directed through a drilled hole in the magnet-core. The sample space is between the pole shoes, where the two rods from the top and bottom meet each other, as illustrated schematically in Fig. 5.16. The load path for the uniaxial stress is collinear to the H_{AC}-field and H_{DC}-field, as depicted in the setup photograph Fig. 5.13.

The sample with its electrodes is glued with conductive dual silver epoxy to plane parallel alumina disks, one on each side. The disks are painted with silver paste in order to be conductive. Hereafter they are burned, and flattened. Furthermore, on the top disk, a half-spherical (Thorlab GmbH) alumina piece is incorporated into the assembly in order to accommodate for any slight non-parallelism

It is necessary to note that the shape of the ME curves measured in Fig. 5.14 deviates from the measurement data obtained under the uniaxial stress as in Fig. 5.17. It is due to the technical acquisition of the data. The data in Fig. 5.17 are the induced ME-coupling voltage, which is tapped into Lock-in in R-mode. Technically, the R-mode of the Lock-in delivers the measured signal modulus value. Therefore, the data for the negative fields are folded up in Fig. 5.19 compared to Fig. 5.14. The reason for using this approach is the convenience that it allows the comparison and detection of any asymmetric behaviour on both sides of the H-field polarity. This can be caused by stress, e.g. for peaks and tails of the curves, Fig. 5.20.

The following measurements were performed in the clamped state under a constant stress σ_{const}, in a cyclic loop, $\pm\, H_{DC}^{max} = 1,2$ T, with H_{AC} excitation field of 1 mT driven by the function generator (Keithley). The H_{DC}-field is swept in a loop cycle of $0T \nearrow 1,2T \searrow -1,2T \nearrow 0T$) in order to close the hysteresis. The control of the fields and data processing is done with ME-modules of the LabView program, Appx.B.9.

Characterization results: For the study of stress-dependent ME|σ, the 0-3-composite of $BTO_{73\%}CFO_{27\%}$, and two 2-2 connectivity laminated tri-layer multiferroic structures CFO_{1mm}-$BTO_{0,5mm}$-CFO_{1mm} and CFO_{1mm}-$PZT_{0,5mm}$-CFO_{1mm} were measured[20].

As the compressive stress is applied, both phases of the magnetoelectric composite are affected. Both phases are well-studied concerning the manifestation of mechanical effects due to uniaxial stress. For the ferroelectric phase, the relevant studies are documented in [57, 59, 60, 217], and the ferromagnetic case is covered in [215, 218, 219][49, p. 266].

However, the effect of uniaxial stress on the magnetoelectric composite and the ME-coupling of these material systems isn't covered [220]. Therefore, a breakdown of the multiple aspects related to this is needed: The compression stress causes, on the one hand, the *depolarization*, and on the other hand, the *demagnetization* of the magnetoelectric composite. Furthermore, the stress reduces the electrostriction and magnetostriction derivatives, which causes lower piezoelectric d_{33} and piezomagnetic q_{33} coefficients.

The uniaxial stress affects the conversion[21] of energies, as the electromechanical coupling [221] and the magneto-mechanical coupling coefficients stress-dependent [76, 222]. These are given by the following:

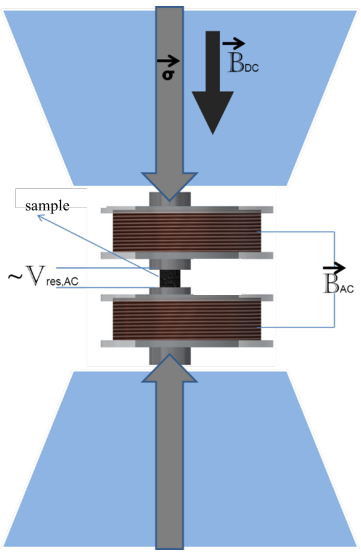

FIGURE 5.16: Schematic stress Fig. 5.13a. For each hysteresis loop, the stress is kept constant σ_{const}.

$$k^2 = \frac{Y_{mod}}{\mu_0 \mu_r} \left(\frac{d\lambda}{dH} \right)_\sigma^2 \qquad (5.1) \qquad \text{electromechanical: } k^2 = \frac{(d_{33})_\sigma^2}{\varepsilon_{33} \epsilon_{33}}. \qquad (5.2)$$

On this basis, *stress* also affects the mechanism of magnetoelectric coupling, since the magnetoelectric effect is a strain-induced product property, see Sec. 3.6.1.

Looking at the ME-curves (Fig. 5.18) under stress, it is possible to obverse that for biased H_{DC} fields of 0.1 T - 0.3,T the ME coefficient peak-value $\alpha_{\sigma=0}^{max}$ declines with increasing exertion of stress (region I).

Moreover, the ME-value merges in the biased field region 0.4 T - 1 T, region II by increasing the uniaxial stress. In this measurement, the ME-coefficient value was initially zero in the unloaded condition. Based on the experimental procedure of HDC variation, the peak of the magnetoelectric coefficient monotonically decreases, and the curves drift to the right. These overall observations are due to two main stress-induced effects, which account for the emerging shape of the ME curves under uniaxial stress. Firstly, the ME-coefficient value depends on the state of depolarization, which is $\propto$ to electric-displacement D, as shown in Fig. 5.17C for PZT, and Fig. 5.17D for BTO[22].

Secondly, it also depends on the shift of the saturation field of magnetostriction under uniaxial stress, see Fig. 2.11 and 5.17A. Both will be discussed in more detail in the following.

[20] All samples are poled in the same direction as the uniaxial stress is applied. The poling is done by applying constant E-field (E_{Pol}>E_{coer}) above the T_{curie} and cooling to T_{room} in the presence of the field.

[21] $k^2 = \frac{workoutput}{workinput}$, for the case of magneto-mechanical materials, the input energy is usually supplied by an external influence such as an applied stress or a magnetic field.

[22] The ME value of the laminate composites is lower than the literature values [69, 223, 224]. This is since they are not optimally coupled, as this requires an optimum of right mix ratio of epoxy resin, the amount of usage between layers, and curing recipe.

Regarding depolarization, *Lynch* [57] derived the proportionality relationship between strain and electric-displacement D as: $\frac{\Delta\varepsilon_{33}}{\Delta E_3}\downarrow = \frac{\Delta D_3}{\Delta\sigma_{33}}\downarrow$, where the down arrow indicates the loading path. E is the electric field that is needed to polarize a sample without stress, σ_{33} is the stress needed to depolarize the sample without an electric field. The slopes on both sides of the equation appear equal if extracted from the experimental data, see Fig. 5.17C.

Consequently, the derivative of the electrostriction (at E=0) depends on the polar state of the ferroelectric phase. Its value reflects the magnitude of the ME- effect, making the poled state essential. Following this, the application of compression stress depolarizes the domain state of the ferroelectric, as the orientation of some domains switches by 90°[23], see Fig. 2.9. Hence, the stress level affects the slope of electrostriction and with this, the value for d_{33} decays. This mainly leads to the decay of the ME-coefficient in the ME- peak region-I-.

The second effect contributing to the ME-coefficient decay caused by stress is attributed to changes in the magnetostriction derivatives under stress. It is necessary to know the effect of stress on the magnetostriction at each field point in order to portray the expanded nature of the ME-curve to the sweeping bias field when under stress.

Uniaxial stress influences the appearance of the ME-curve in two ways. Firstly, it reduces the magnetostriction sensitivity (λ/dH) over the full ME-curve, in both regions I and II. It also plays a (minor) role in the decay of the peak ME-coefficient in the region -I-, see Fig. 5.18B. Secondly, it can be used to explain why the ME curve stretches to higher fields (Fig. 5.18), which explains mainly the tail part of the ME- curve, region II, which is also reflected in the dependency of piezomagnetic coefficient under stress 5.17B.

In Sec. 2.4.2, Eq. 2.40 the formulation by *Jiles*, stress can be viewed as an additional field H_σ, which acts as a delay field until the saturation magnetostriction $\lambda_{sat(\sigma)}$ is reached. Its influence can be seen in the data in Fig. 5.17A for Terfenol-D[24]. The curves in Fig. 5.17A and B explain the case for the tails in the measured data in Fig. 5.18B-region II. By looking at the data for the CFO/BTO/CFO trilayer, after the removal of the constant stress field ($24MPa \mapsto 0Pa$), it is clear that only a decreased value of the remnant "poled state" contributes to the ME-effect. Therefore, for a subsequent measurement of the ME-curve with $8MPa$, region I doesn't display any difference. Under increasing stress levels, the magnetostriction reaches its saturation at increasingly higher H-fields as more energy is now necessary to overcome the stress. This lowers the piezomagnetic coefficient, which is needed to convey the magnetoelectric effect. In other words, the slope $\frac{d\lambda_\sigma}{dH}$ of the magnetostriction decreases, since now $\lambda_{sat(\sigma)}$ is located at a higher fields, with that the magnetoelectric range is also extended to higher fields, however, with a lower coupling coefficient.

[23] In the case of a tetragonal crystal structure.

[24] a low Young's modulus, high magnetostrictive alloy $TbxDy_{1-x}Fe_2$ (x ≈ 0.3) . Naval Ordnance Laboratory (Ter-fe-nol-D: Terbium-Iron-Naval Ordnance Laboratory).

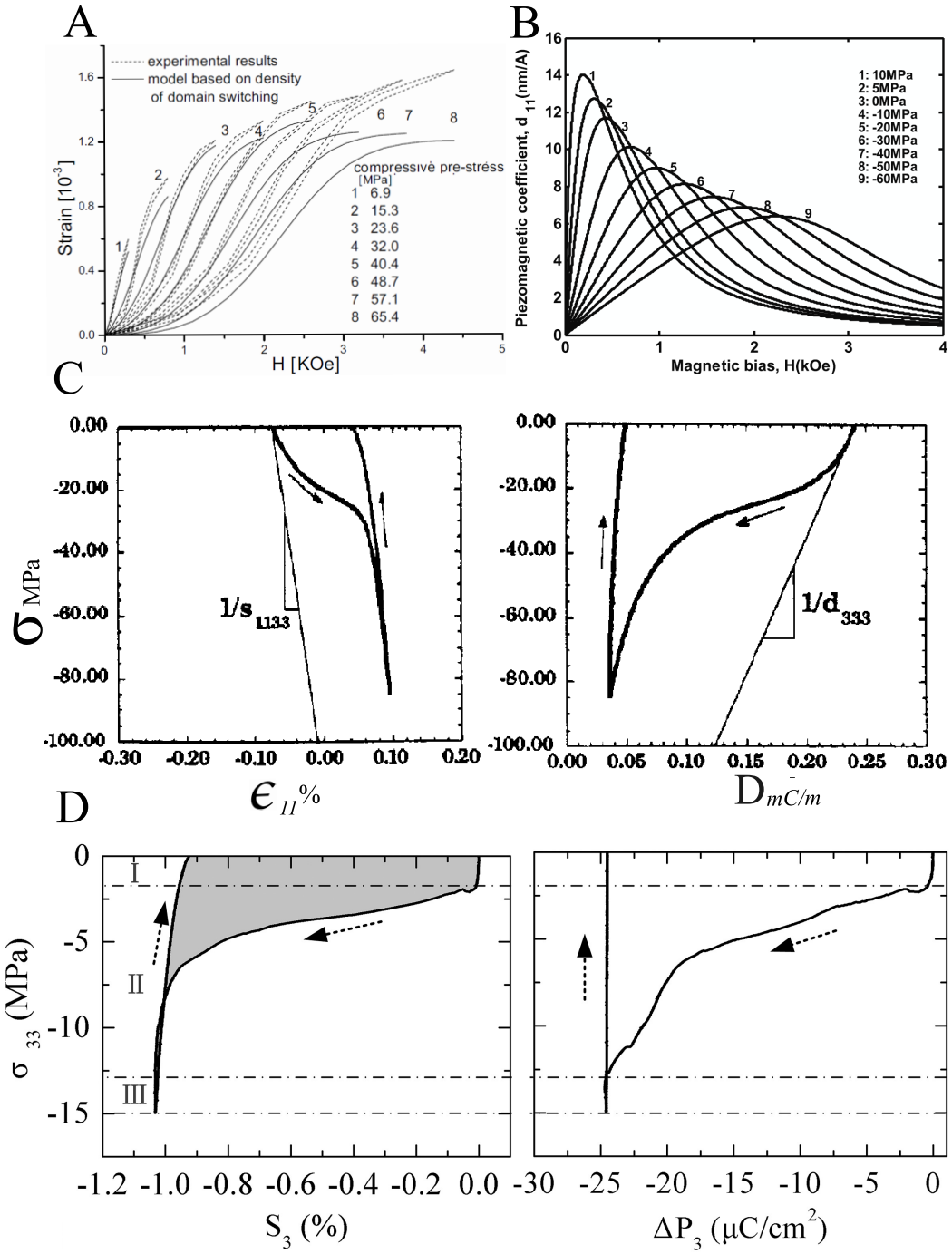

FIGURE 5.17: Uniaxial compression stress effect on magnetostrictive and electrostrictive phases of magnetoelectric composite. A) Presents the magnetostrictive $\lambda_{sat(\sigma)}$ behavior of the Terfenol-D rod under uniaxial stress over H-field until. This yields a lower λ/dH value with increasing compressive pre-stress [215]. The data is modeled based on the density of the domain switching method in a non-linear constitutive approach [216]. B) Shows the piezomagnetic coefficient under different pre-stress over the magnetic bias field [214]. C) Shows the measured depolarization by stress as a result of the switching process at zero electric field for PZT [57]. D) Displays the stress-induced depolarization curve for BTO ceramics due to mechanical stress [217]. Both C) and D) are showing a strain decay as a consequence of depolarization. Further, the amplitude of dielectric displacement in both materials are different, which is accountable for the differences in the peak ME-coefficient value of both layered composites Figs. 5.18 and 5.19.

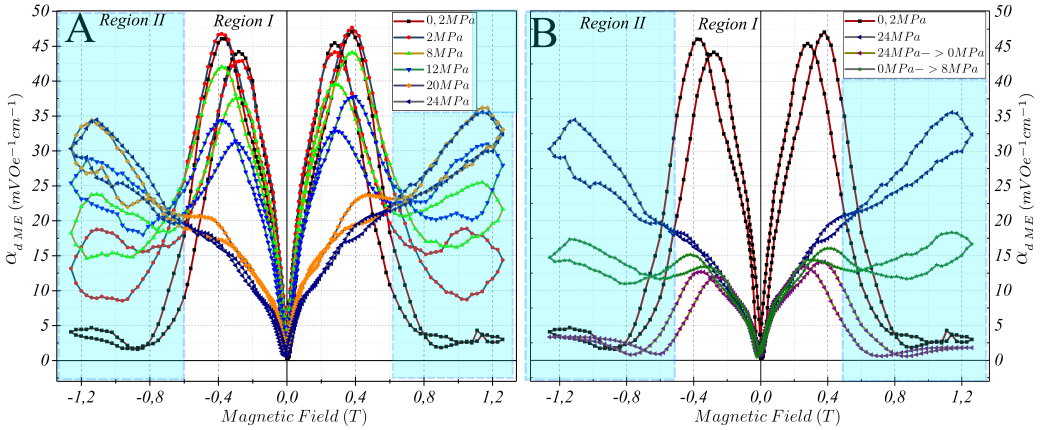

FIGURE 5.18: A) Effect of uniaxial stress on the 2-2-connectivity laminated tri-layer of $CFO_{1mm}/BTO_{1mm}/CFO_{1mm}$. Stress affects the mechanism that coveys the magnetoelectric effect for the measured ME-curves in two ways: 1) the depolarization of the ferroelectric phase, and 2) stress induces an additional field H_σ in the magnetic phase. The data in B) examines scenarios involving load application, removal, and subsequent load application. Following stress removal to the non-loaded state, the measured ME coefficient peak value does not reach the initial ME-coefficient peak value. $\alpha^{max}_{\sigma=0}$, since the depolarization is in accordance with *Kamlah* [59] an irreversible ferroelastic domain switching processes. Further, the tail value disappears to zero once the stress is removed and emerges as it is applied again, $0MPa \mapsto 8MPa$. This is as the subsequent stress excites the magneto-mechanical impact that shifts the saturation region of magnetostriction to higher H_{DC} fields.

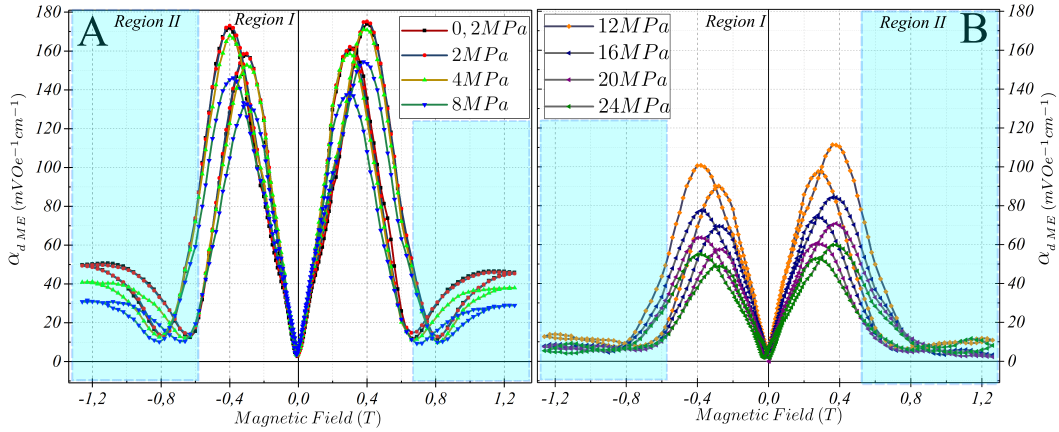

FIGURE 5.19: Magnetoelectric effect study under the compressive stress for 2-2 trilayer of CFO_{1mm}-$PZT_{0,5mm}$-CFO_{1mm}. The R-mode in the lock-in amplifier measures the modulus of the signal, therefore the tails of curves are folded up. With 24 MPa compressive stress the value of the ME-coefficient is reduced by 60%. Even though the depolarization of PZT doesn't decrease by this percentage with stress [225]. If the sample is completely depolarized, the ME-value drops to zero as it is a product property.

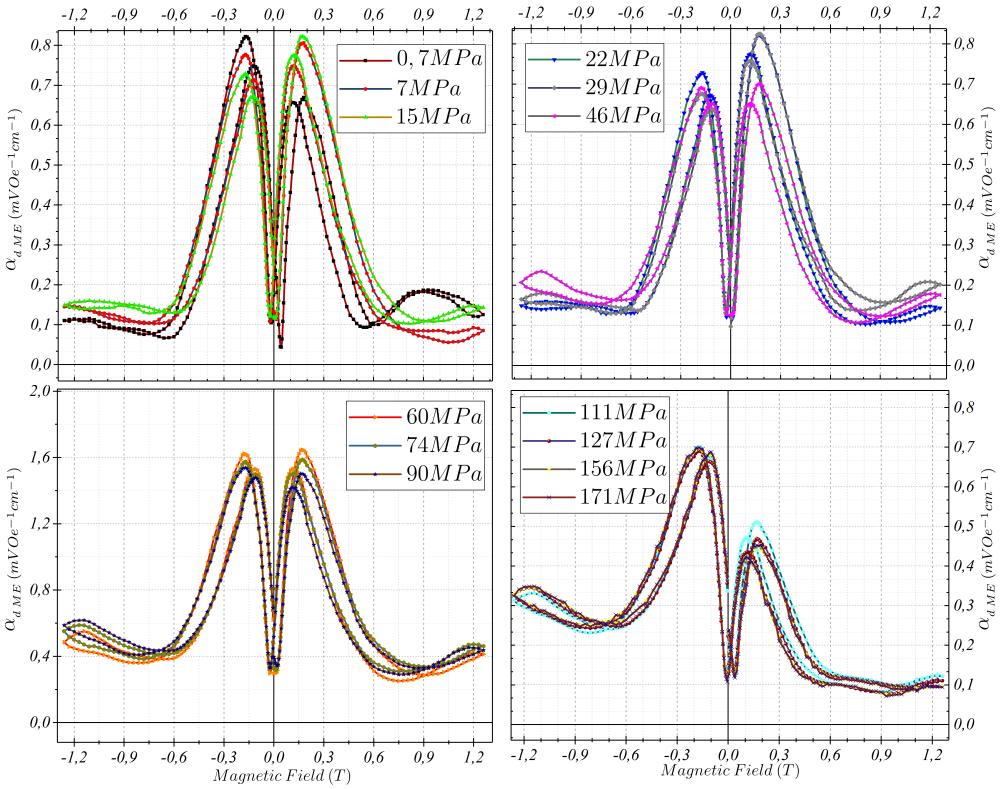

FIGURE 5.20: ME effect study of 0-3 composite of $BTO_{73\%}CFO_{27\%}$ under uniaxial compressive stress. The applied stress depolarizes the generally low poled state of ferroelectric constituent in the 0-3 composite. Consequently, most of the decay can be attributed to a stress effect on the magneto-mechanical coupling.

5.6.2 Comparison of different composite systems regarding $\alpha_D(H)\,|_\sigma$

When comparing the $\alpha_D(H)\,|_\sigma$ values under stress for CFO/BTO/CFO (Fig. 5.19) vs. CFO/PZT/CFO (Fig. 5.19), both systems exhibit similar responses to the magnetic bias field and stress. Due to their typical CFO phase, both systems demonstrate a decrease in magnetostriction derivative upon the application of uniaxial stress. Therefore, the effect of a lower piezomagnetic coefficient in the ME effect over the range of the magnetic field is also the same. Comparing the $ME_D(H)$ behaviour under stress would boil down to the piezoelectric coupling coefficients of BTO and PZT. Zhou *et al.* [214] derived a model predicting that the decay of ME-coupling under stress is due to the complex effect on the piezomagnetic coefficient. However, the data shows that the degree of depolarization in both systems is crucial, so the model needs to be extended by this parameter. Given the product property coupling of the composite (Eq. 2.52), the outcome of each system is different under axial stress. The depolarization of the softer BTO is more pronounced at the rise of stress, Fig. 5.17B, which allows the piezomagnetic coupling coefficient to be the more dominant factor in the Eq. 2.52. However, for the $CFO/PZT/CFO$ laminate system, beside the depolarization, the piezoelectric coefficient stays the dominate factor, as it depolarizes at higher stress fields.

On the other hand, comparing the ME value of the 0-3 composite of $BTO_{73\%}CFO_{27\%}$ (Fig. 5.20B) to the 2-2 tri-layer composites, it is not decaying at the same rate as the tri-layers are doing. Primarily, this is attributed to the difficulty in poling the 0-3 connectivity composite compared to the pure ferroelectric, and secondly, leakage leads to the decay of the existing poling.

6

Summary and outlook

Understanding *functional* correlations in materials requires extensive exploration of the various features of the underlying properties. Depending on the degree of correlation, the characterization requires several setups with multiple options. In this context, the design and development of any setup providing a complex and stable measurement platform is an iterative and incremental process involving a learning curve consisting of trade-offs, challenges of unknowns, and setbacks.

In this work, a modular magneto-electro-mechanical setup has been designed, constructed, and automated to conduct multifaceted studies on the properties of composite magnetoelectric ceramics from a mechanic point of view. For this purpose, dense magnetoelectric composite samples with a high coupling coefficient consistent with the reference literature were synthesized. However, given that mechanical testing is a destructive approach, an additional requirement for high Young's modulus of the samples was preassigned. As a consequence, the standard sintering route has been modified.

Here, the direct ME measurement method is integrated into the setup to provide a fast and reliable way to get feedback on the synthesis quality for the chosen CFO-BTO composite system which facilitates the optimization of the process. Additionally, the ME-measurement device determined the composition with the highest ME-coupling value. In addition, conventional characterization methods such as XRD, SEM, impedance spectroscopy, SQUID, and both ME-measurement methods confirmed the material structural, compositional, and phase basis for the functional properties of the composites.

Given that the functional response of composite materials to the electric or magnetic field is weak compared to the pure phases, instruments with better performance factors in terms of accuracy, resolution and precision were integrated into the setup.

Thereby multi-field compatible detection instruments are integrated into the sample space of the setup. Here, especially regarding the mechanical characterisation, a miniaturized magnetic field-compatible Fabry-Pérot interferometer sensor for strain measurement is integrated. Its utilization required the development of a nonmagnetic alignment insert to obtain a stable alignment of the cavity condition required for sub-nanometer resolution. The special alignment insert was integrated into three further strain-measurement-related modules of the setup. These modules enable electrostrictive characterization of composites in the presence of fields, as the integration concept has proven to be compatible with the magnetic environment. Therefore, some representative measurements were conducted to show the functionality setups. Furthermore, another module measures the electrostriction of the sample whilst under a mechanical load in addition to a magnetic field. The integration approach can resolve a stress-induced peak-to-peak electrostriction change below 5 nm at two constant stress levels. However, in this constellation, the effect of the magnetic field is not measurable or not present.

The measurement of the magnetostriction with the interferometer is another new achievement of this work. It was ascertained from literature that the deformation due to magnetic field exposure of polycrystal CFO ceramics is unknown. Such measurement requires tilt

compensation of the optical axis for the detection arm of the interferometry setup, which is an optical cavity. This is achieved by attaching a second sample to the sensor head to mimic the specific nature of the deformation behaviour of the mirror sample. The integration of the interferometer facilitated the measurement of total magnetostriction of 25 ppm ($\propto$ nm) for a 1mm thick CFO_{27}-BTO_{73} pellet. In this case, the signal drift is 10 nm in 20 sec, confirming the integration approach as an excellent low-noise optical measurement method.

The measurement of the effect of uniaxial stress on magnetization was another challenging undertaking of the thesis. The measurements were conducted in a VSM.

To perform them, a non-magnetic pressure cell was developed that meets the geometric requirements of the VSM inlet. In addition, stress control within the cell proved to be a challenging task for which a new approach to ex situ calibration was developed. For this purpose, a universal testing machine with a special built-in fixture was used. The fixture mimics the closing process of the cell. The stress-induced effects for CFO were small. However, it was shown that the tests performed were limited by the material and not by the test setup.

Additionally, a stress-strain measurement in the setup with an interferometer was performed to determine the effect of the magnetic field on the elastic modulus. The integration of the interferometer with the electromagnet and the universal testing machine made it possible to obtain this effect.

The most novel finding of the work is related to the effect of uniaxial compressive stress on the coupling coefficient of magnetoelectric composite ceramics. This measurement module is an assembly of the universal testing machine and a ME-measurement module. The measurement with the direct method shows a new product property behaviour, which reveals the change in properties of each constituent by uniaxial stress. For the electrostrictive phase, it is the degree of depolarization, and for the magnetostrictive phase, it is the change in strain sensitivity. The direct magnetoelectric effect exhibits a new curve by sweeping the magnetic DC field depending on constant uniaxial stress. Consequently, the peak value is biased, smaller, and at a higher magnetic dc-offset field

6.1 Ideas for further investigations

This section presents some recommendations for further research on magnetoelectrics and other functional materials with the developed setups.

The role of dynamical piezomagnetic coefficient: The piezomagnetic coefficient ($d\lambda/dH$), as the magnetic phase parameter of the magnetoelectric composite, is one of the three performance factors related to the coupling coefficient α, Eq.2.52.

In most model studies, the coupling coefficient α is calculated along with the constitutive value of piezomagnetic coefficient q_{33}, which is deduced from the *quasi-static* magnetostriction curve of the pure magnetic phase. However, for the measured value of α_{MED} an excitation field H_{AC} is applied, see Sec. 3.7. In this case, the corresponding dynamical piezomagnetic coefficient is much lower than the quasi-static strain derivative [226]. In order to measure this more effectively, the constructed magnetostriction setup Appx.B.6B of this work can be placed between the AC excitation coils. This configuration would allow a measurement of the dynamical value for λ/dH_{AC}, Fig. B.6B. Given that the interferometry allows measurement over a wide frequency range, the optimum frequency and working bias field can be determined.

Magnetoelasticity studies: Having a large magnetic field up to 2 T and the interferometer incorporated in the spindle testing machine would allow the study of minor hysteresis loops

under small stress variations in a constant magnetic field and uniaxial stress. This would allow the precise strain study of magnetic shape memory alloys.

Additional information from a stress-strain curve can be obtained by varying the load cycle. For instance, the other parameter of a constant magnetic field at a certain stress level, with an incremental load increase and a partial relief, would allow conclusions to be made about the change in the properties. The creep behaviour under the magnetic field can be investigated by inserting a hold time at maximum load.

By choosing the direction of the crystal system in single crystals, it is possible to probe the switching processes in a very specific manner[1].

Extending the automation for ME- coefficient by frequency The ME coefficient has an ac- magnetic/electric field dependency. Given the mechanical nature of ME-coupling in composites, the electrical (magnetic) energy converts the input energy into mechanical most efficiently at the resonance frequency. Correspondingly, at resonance, the magnitude of the ME- effect exceeds the low-frequency value by more than an order of magnitude[203].

Typically, a frequency impedance analyzer would determine a given electro-mechanical resonance of the sample by performing a frequency sweep and analyzing its response. For the ME-coupling coefficient, this behaviour can also be measured with the ME option of the setup. All the requirements needed to determine the resonant ME-coupling coefficient with the setup are fulfilled, except for data acquisition. In this case, only a sweep frequency routine in LabView needs to be implemented to scan the excitation response by the AC-magnetic field over a certain frequency range. Given that the routine for the function generator[2] is already implemented, the task is feasible and would deliver the optimum working frequency of the composite.

The sweep frequency scan mode can also be used to determine the highest dynamical piezomagnetic coefficient amplitude, as introduced before, Sec. 6.1.

Conclusions on pressure cell: The investigation into the magnetization change of polycrystalline CFO under uniaxial stress revealed several key findings. Despite the isotropic nature of polycrystalline CFO, applying uniaxial stress did not significantly alter the magnetization at zero magnetic field ($B = 0$).

Therefore, the saturation magnetizations were investigated, and small changes in magnetization under stress were measured. These measurements led to the conclusion that, due to the brittleness of the ceramics, the samples failed at a uniaxial stress level below the threshold required for any noticeable onset of magnetization change. Noteworthy magnetization changes were only observed at high-stress levels exceeding 100 MPa, provided the samples were durable enough.

In general, the performance of the uniaxial pressure cell needs to be tested by investigating systems with uniaxial pressure dependency (or directional anisotropy), as it is mostly the case for single crystal materials, as they show a directional dependency in contrast to isotropic polycrystalline system. In addition, thin-film properties are susceptible toward stress and well suited for an investigation with the pressure cell. Another use-case of a pressure cell combined with a VSM facilitates the measurement of the shape memory effect, such as in Ni–Mn–X(X = Ga, In, Sb, Sn, Al,...), which are sensitive to directional stress [171].

The pressure cell, combined with the possibility of applying electric DC- offset fields at various temperatures (3 K–500 K) in a VSM, opens up many research possibilities on known

[1] This is due to the absence of grain boundaries, which decreases the contribution of the interaction between domain walls and the internal defect structure.

[2] The function generator drives the power source.

single-phase multiferroics crystal systems such as Cr_2O_3 and $BiFeO_3$[3][227]. Provided that the samples have a resistivity in the range of three-digit MΩ, this would distort the crystal and the magnetocrystalline anisotropy by applying an electric field. There has been no study performed in such a fashion. Furthermore, the developed pressure cell opens research possibilities on the transport properties of functional material under uniaxial pressure and magnetic fields.

Applying an electric DC-offset field on single-phase multiferroic crystal systems would lead to rearrangements inside the crystal. This contrasts with composite magnetoelectrics, where the offset DC field combined *with AC-excitation fields* would evoke any ME-effect.

[3]Composites requires besides the DC-biased field additional a dynamic expectation field, which would create magnetization noise as a response.

Acknowledgements

On both professional and personal levels, the challenging nature of the PhD journey requires the support of kind and encouraging people. I want to take the opportunity to thank everyone who has contributed to the completion of this work. My special thanks go to Prof. Doru Lupascu for the trust he showed by offering me the opportunity to do the doctorate thesis on this project. During this time, his door was always open to discuss ideas. I appreciate his treatment at eye level is encouraging and providing the necessary mental support. Many thanks for this.

I want to thank Prof. Dr.-Ing. Marc Kamlah for taking over the second review. I appreciate his insight on this work, which I have experimented with in many conferences and conversations. I would also like to thank the students Zain Bin Ali, Daniil Lewin, Yang Lai, and Zhouchen Xu, who closely worked with me on their theses as a team. Their commitment and efforts were essential to the successful completion of the project as they also stimulated me professionally.

Great thanks also go to Mr Bruemm, Mr Fischer, and their team at the mechanical workshop of the Essen campus for their efforts concerning the manufacture of the assembly parts and the countless modifications of the parts. This enabled the development of all the setups and complimented my work perfectly. Many thanks also go to Dr Richard Boucher for his excellent support and care during the VSM measurements in Dresden and Dr. Salamon for the measurement with the SQUID. I would also like to thank the technical staff at the institute of material science for their support. Especially, I appreciate the discussion on technical issues as well as the pleasant private talks with Mr Dubray, and I thank Mr Menze for his advice and experience on electrical-related questions and solutions, Mrs. Escober for her support on the questions of chemical synthesis, Mrs. Kriegel for all the efforts on paperwork, and Alfred Gäbel for being my vitamin C in all the workshops.

Further, I would like to thank also PD Dr. Shvartsmann for his critical scientific views and his effort to teach scientific thoroughness. The great time in Essen was also possible with great personalities like Dr Hans-Joachim Keck with his calm, devoted, and easy-going nature which made the arduous periods endurable as he is an encouraging person through his presence.

Further, I would like to thank H. Trivedi for proofreading and discussing the results of the measurements and Mohammad Sayad for reviewing the theory part of this PhD with his in-depth knowledge. In particular, the proofreading of Dr Richard Boucher helped to give the text the necessary flow. Without their cooperation, the work would not have been possible in this state. Also, my friends, Nawid Najafi, Patrick S. and Stevan V., I am grateful for the supportive talks and encouragement during crucial moments of the PhD. My special thanks and appreciation go to my PhD friends and fun-family Danka G., Harsh T., Morad E. Naveed Ul-h., Maryam Kh., Mehmet S., Kevin V., Alexey Fedorchenko, and Gabriel.C., with whom I built great friendships. I thank them for many professional and private discussions and fun together.

My family is a great pillar for any step I take. My mom taught me persistence and modesty, and my father reminds me that keeping the bigger picture in mind is the base of my achievements. I am grateful to my brothers Khesy and Noor for their patience and

unique nature, giving me strength and guard. My sister Sahar is an outstanding gift for cherishing any challenging moment and changing any mood into joy.

Appendix A

Complementary topics

A.1 Symmetry and phase

The ***phase*** of a substance represents a state, where the structure, the chemical composition, and the physical properties are in an equilibrium condition. Since a material can have multiple stable states over a certain range of the underlying parameters, the overall state map under different conditions is denoted as the *phase diagram* of the system. In order to quantify a phase for mathematical modelling, the state variables of the microscopical homogeneous system need to be characterized, where these describe a point in the phase diagram. The state of a ferroic material is described by 3 variables, which consist of 2 control parameters (= intensive state variables) and an order parameter e.g.in a magnetic phase H| M|T, and for a ferroelectric phase E| P|T Any other state variable of the system can be derived from Maxwell's relations of the system[1].

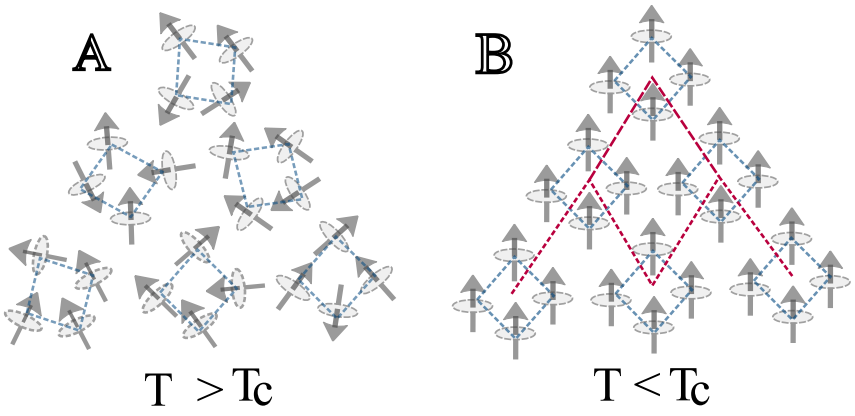

FIGURE A.1: Paramagnetic-ferromagnetic phase transition. A) Statistically averaged system over time, each position is occupied by an atom, making the system symmetric in terms of the property. In B), the symmetry is broken as the system aligns itself along energetically favourable states. Thus, it becomes, for instance, a ferromagnet as the *phase* temperature falls below the Curie temperature T_c. The new state forms an additional crystal structure, which carries the property of the new order.

The phase of a thermodynamic system may transfer into another phase as the phase interacts with external variables such as temperature, pressure, chemical composition, electric field, or magnetic field and exceeds a certain phase-related parameter range. In such a case, the degree of symmetry between two phases marks the difference. The reasons for lowering the symmetry group due to the external parameter are as diverse as the number of possibilities that exist. Therefore, as a result of the field interaction, the higher symmetry of the disordered phases transforms into the ordered phase with lower symmetry, Fig. A.1.

[1]Further treatment of the relation and transformation between phase orders, consulate [25].

Due to the emergence of a new order parameter in the system, it is necessary to introduce one or more additional variables in order to describe the new property associated with the new state. The new order parameter is the measure of the degree of order of the new phase across its parameter ranges. This is coupled with a macroscopic physical property, and with an increase of *tensor components* of its new property tensor. If the driving parameter is temperature, the high-temperature phase is almost always more disordered, hence, it has a higher symmetry than the low-temperature phase. The temperature dependency of ferromagnets and ferroelectrics reveals a marked difference above and below a critical temperature T_c. They are characterized by accompanying jumps of the macroscopic quantities in the case of first order Phase transitions.

A.2 Sol-gel Synthesis Route

In the initial stage of this work, a sol-gel method was employed to synthesize core-shell composites. The aim was to achieve a higher coupling coefficient using this method. By incorporating ferroelectric nanoparticles in the shell (starting powder size 50 - 100nm [186]) and ferromagnetic nanoparticles in the core (50 nm), it was anticipated that the larger interface between constituents would lead to enhanced coupling. Specifically, the coating of the low-resistance magnetostrictive core-particle (CFO) by the ferroelectric constituent contributes to improved electrical isolation. This, in turn, facilitates better poling of the ferroelectric phase, thereby enhancing the coupling between the CFO and BTO constituents.

There are several drawbacks to this approach. The synthesis process involves multiple steps, each requiring precise control of parameters such as ball-milling rates and calcination time [191, 228]. Any deviation in these parameters can introduce randomness into the process, leading to irreproducible results. As shown in Fig. A.2, even slight changes in processing parameters after calcination of the sol-gel result in different material properties. A comparison of two different results reveals visible differences in polarization curves and microscopic images.

In general, polarization tends to be low for nano-particle sizes of the initial powders. Additionally, particles smaller than 50nm exhibit high surface energy during sintering, causing them to melt at temperatures around 1200°C. This phenomenon impedes the mechanical stability of the ceramics. Furthermore, BTO nanoparticles tend to sinter into "random" stripe formations, which contribute to poor mechanical stability. Despite this, they can still exhibit local core-shell structures.

The SEM images in Fig. **??** clearly depict the overall porosity of the material. Moreover, sintering nanoparticle powders leads to increased porosity due to shrinkage during the sintering process, further compromising the mechanical stability of the ceramics..

Another downside of the *nanoparticle* preparation route is related to their nonoptimal ferroelectric properties. This occurs due to the permittivity of ferroelectrics, with particle sizes lower than 200nm, dropping to zero, resulting in a low polarization value, see Fig. A.2, Fig. 2.14, [229]. Furthermore, the small grain-size gives rise to the emergence of a larger density of grain boundaries in ceramics, which leads to a low percolation threshold[2]. Moreover, due to the mechanical instability of core-shell composites, they are not suitable for mechanical testing experiments.

[2] Also, PTCR (positive-temperature-coefficient-resistor) is strongly controlled by the density of grain boundaries[230].

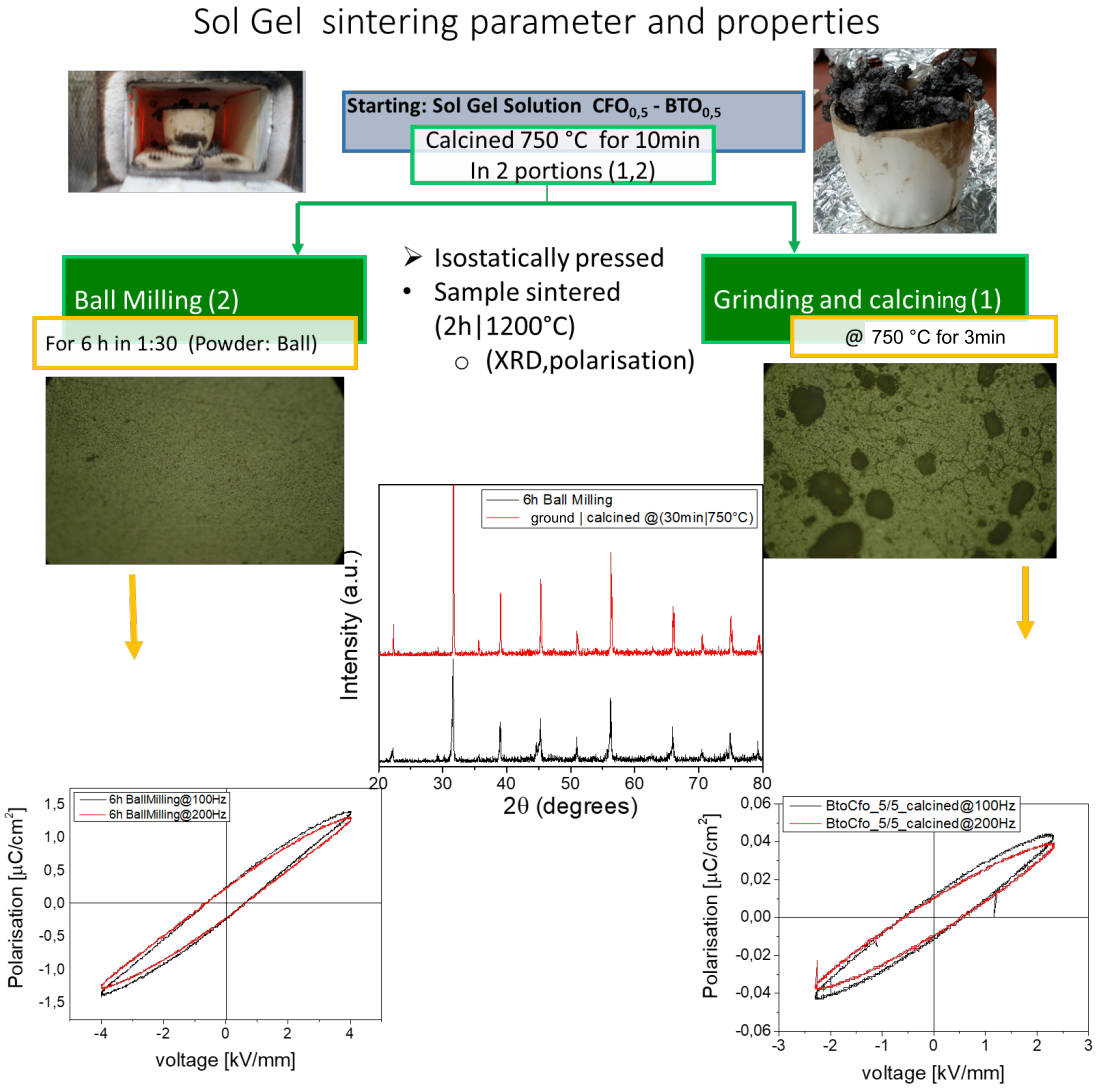

FIGURE A.2: This graph compares the effect of processing parameters after the burnout of sol-gel solvent on the final properties. As visible from the data on the processing chart, the different parameters on the left and right side have a significant impact on the final properties of the composite.

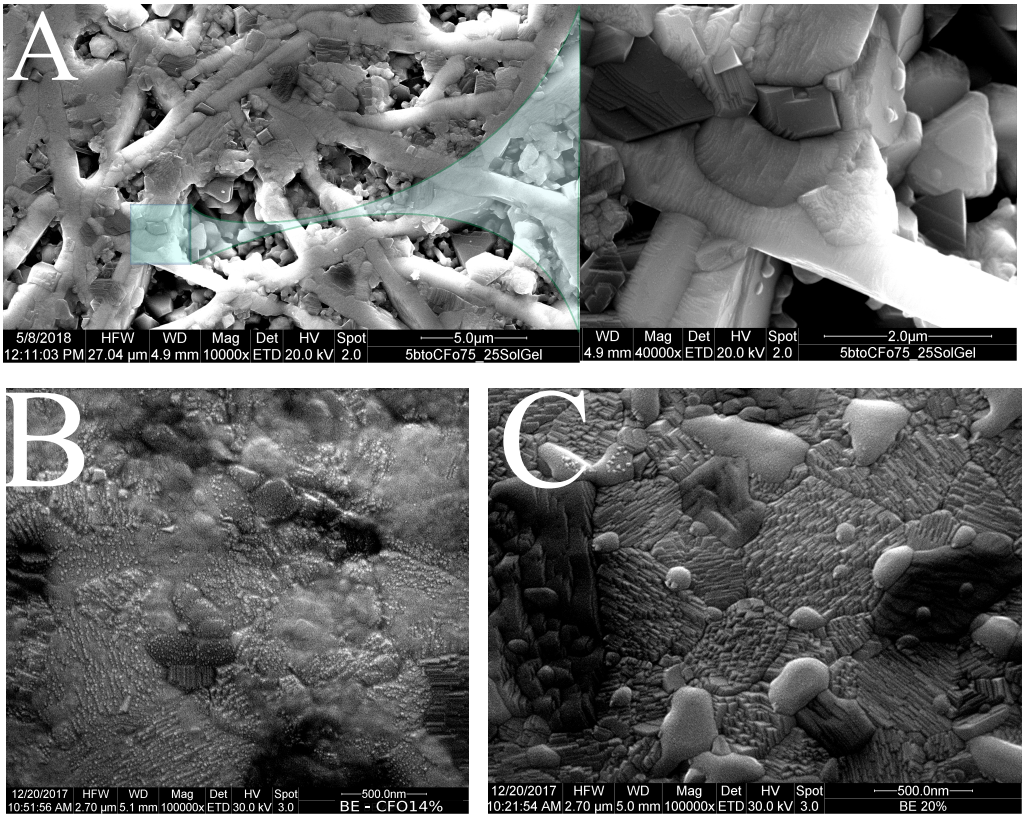

FIGURE A.3: SEM comparison between sol-gel and solid-state approach to synthesis ME-composites. A) The sol-gel route, with the nano-particles as starting powder of both constituents can lead to the formation of pores and stripes. B) and C) are displaying a solid-state synthesized sample with 14% and 20% CFO portion, respectively. The solid-state sintered samples show homogenous distribution of particle size and dense structure.

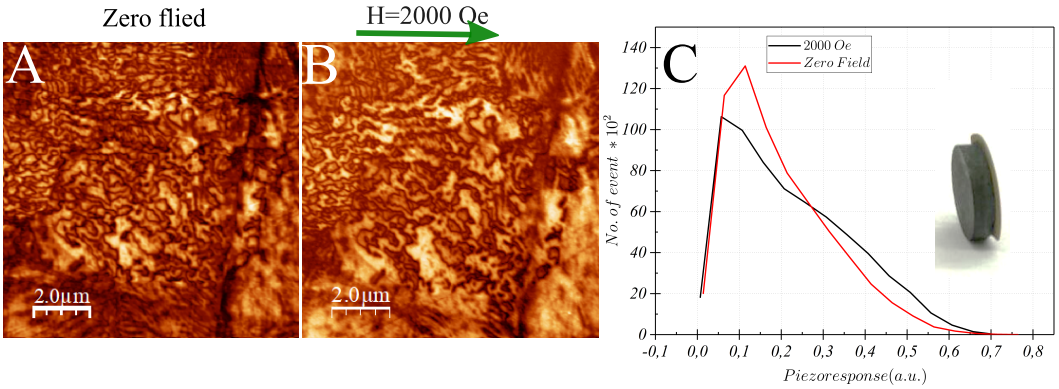

FIGURE A.4: MFM measurement performed on a bi-layer consisting of $PZT_{0.1mm}$ CFO_{1mm}. A) and B) show the so-called mixed piezoresponse signal (= *Color*: vertical and lateral signal, A cosθ). It is measured in the single frequency mode (f_{ac} = 50 kHz, V_{ac} = 5 V) [142]. Both samples were ground with a flat grinder and were polished with a 15μm grit size. Subsequently, they were fired in an oven at 1100°C under uniaxial pressure (10Pa) by weight. A) The ferroelectric domain at zero magnetic field. B) Domain switching due to the presence of a magnetic field with an in-plane field direction. C) The average amplitude response in a piezoreponse histogram. Inset: photograph of the structure. Measurement courtesy of H. Trivedi.

Appendix B

Device characterization

B.1 FEA and FEM

The finite element method (FEM) is a numerical approach that divides a continuous physical problem into a network of finite discrete elements to perform Finite Element Analysis (FEA). It is used in the case of complicated geometries by approximating them into solvable elements to comprehensively understand and quantify any physical phenomena. Furthermore, one of its advantages lies in calculating the influence of stimuli (e.g. stress) and mediums (fluid, gas, or solid-state) as a continuum response of each element by using simple formulas, then forwards on to the adjacent solvable elements. In this approach, each local problem is solved by using partial differential equations, or the solution is modelled by the functional minimization approach (the principle of minimization of energy). Due to a large number of equations, a computer-based simulation is needed to analyze and visualize the effect of the interactions between the force and medium. Consequently, the physical response to a given condition of the object is predicted, from which a better understanding of the material can be derived. In other words, if a particular boundary condition is applied to a body, this can lead to several configurations. However, only one particular configuration is realistically possible. In the context of the mechanical interpretation of the solution data, three terms related to the mechanical performance of the objects, as they are used for stress analysis in this work, are explained in the following paragraphs.

In the context of this work, a commercial program (Autodesk©Inventor Simulation) was used. All components of the setup were considered to work in linear response. No nonlinear FEM was used as its complexity goes behind the purpose of this work, even though it would be necessary for a conclusive description of the ferroics. Here it only serves to evaluate the performance of the setups.

The Von Mises stress is a crucial parameter for predicting the onset of yielding in anisotropic and ductile materials. It indicates when yielding begins by assessing the critical value of elastic energy distortion. This critical value is reached when the maximum distortion energy per unit volume in the material is surpassed.

Despite its significance, the Von Mises stress has limitations. It simplifies the complex nature of 3-dimensional combined stresses into a single scalar value. Additionally, it does not account for negative stress values, making it impossible to differentiate between tension and compression states.

The 1^{st} principal represents the normal stress acting on a plane where the shear stress is zero. It provides insight into the maximum tensile stress experienced by a part under the given loading conditions.

The 3^{rd} principal stress correlates with the *maximum compressive stress* endured by the part due to the loading conditions.

TABLE B.1: The material parameters used for FEA stress analysis simulation, Source: https://www.matweb.com/

Paramters	Al_2O_3	CFO	BTO	CuBe
General				
- mass density g/cm^3	3.75	8.92	5.519	8.25
- Yield strength MPa	9	130	400	130
- Tensile strength MPa	9	350	400	350
Stress				
- Young's Modulus GPa	300	240	116	125
- Poisson's number	0.2	0.33	0.35	0.33
- Shear modulus GPa	125	88.8	42.9	46.9

Parameters used for FEA stress analysis simulation

The program used for simulation is:
Autodesk© Inventor-Version: 2017 (Build 210142000, 142)

Following mesh settings was chosen for the simulation of Fig. 4.8, and Fig. 4.23 with $5kN$ applied from top to bottom (fixed):

Average element size (diameter):	0.03	0.1
Min. element size (average):	0.1	0.2
Pitch factor:	1.5	1.5

B.2 Alternative aspects

During the design phase of the setup, many alternative approaches with regard to all aspects of the setup were considered but discarded. This appendix section presents the collection of discarded ideas on various parts of the measurement setup, where some of them proved to be useful steps in the design process. This section gathers all the aspects of alternative approaches on each part of the setup, which would yield a new setup design, Fig. B.1.

B.2.1 Alternative strain measurement approach.

Generally, studying material with small absolute effects requires very high-resolution instrumentation. In this case, for the composites, this requires a design that includes a susceptible instrument for strain measurements, which should provide a resolution of less than 5-10 nm. This requires that the ambient vibrations affecting both measuring points can be neglected. Here, the conceptual consideration is that the strain measurement between the two points is kept in the same reference system.

AFM has a high resolution as it uses optical beam deflection from a cantilever, amplifying the displacement as the laser spot is shifted towards the cantilever free end [231]. This reflection is leveraged and detected with a quadrant PSD (Position sensitive device), which measures the intensity distribution of the reflected beam on the detection areas. As a result, a shift of the laser spot from the centre of the PSD sensor, caused by displacement of the sample, will be measured. By using this setup, sub-nanometer resolutions can be achieved. However, the idea is to avoid different reference systems as relative measuring points, like it is the case for AFM. The designed approach was purposed to use a piezo stack to shift the

point of reflection to the centre after the measurement. This is used in a feedback configuration to maintain the original intensity distribution for the subsequent size. The following points must be considered to achieve these results:

- Absolute noise-free environment, with a concrete base to decouple the ambient noise, as it requires an absolute fixed point for the cantilever
- Linear guide rail for the laser or lens to focus the spot, and
- Electronic to supply the laser and PSD with current

Also, the concept that the two measurement points of optical sensing (source and reflection point) are kept in the same reference frame was used in this work.

Due to this concept, the noise of the ambient vibrations affecting both points can be neglected. Also, here, it was required that a customized universal testing machine need to fulfil the requirement for the non-magnetic traverse.

B.3 Sensor head verification

The lens-hulls made by Attocube AG are crafted from titanium, known for its durability and resistance to harsh conditions(due to its low expansion coefficient $(8,6 \cdot 10^6 K^1)$,). However, during the manufacturing process, the titanium can absorb magnetic elements from the CNC cutter, potentially affecting its performance [1]. In order to ensure that the titanium-made sensor head of the manufacturer is not disturbed by the magnetic field, a similar sensor head was produced using plastic material for the lens housing (sensor head), see Fig. B.4A.

The design features a fixed focal length for precise alignment between the lens hull and the ferrule connector, enhancing stability. Additionally, the sensor head is seamlessly integrated with Attocube's interferometer control unit.

With these improvements, the sensor head can effectively detect electric field oscillations up to 100 Hz and accurately measure strains below 10 nm, ensuring reliable performance in various conditions.

In light of these considerations, it has been proven that this constellation can follow an electric field driven oscillation in the range of 100 Hz and resolve strains under pressure of below 10 nm.

[1] During the mechanical manufacturing process, crystal defects may occur, and the CNC cutter head can transfer material into the titanium, leading to magnetic properties. Consequently, the titanium lens housing may experience magnetic forces or strain when exposed to a magnetic field, altering the distance between the lens and the fiber entrance.

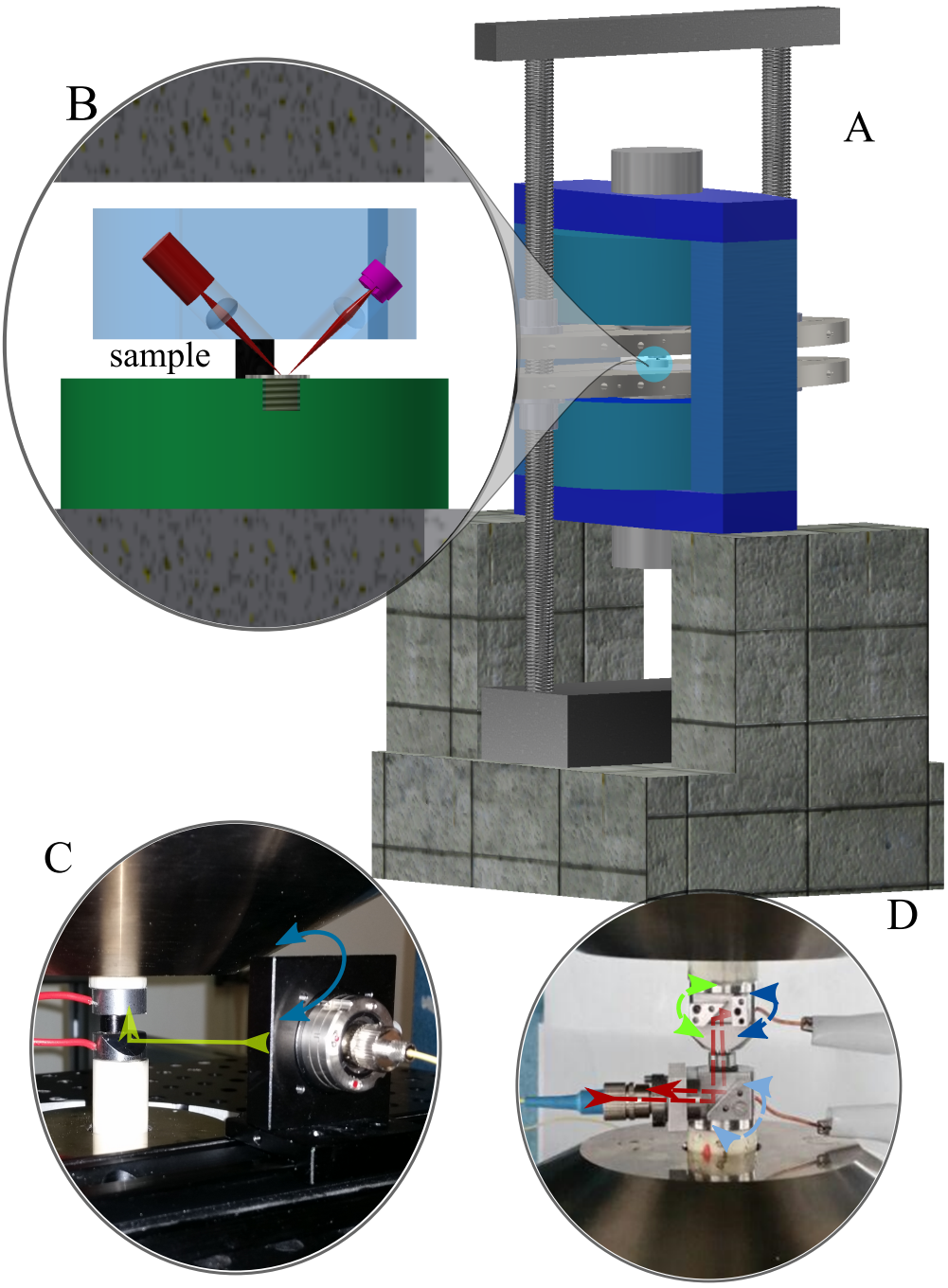

FIGURE B.1: Illustration of ideas and approaches that have been discarded during the optimization and evolution of the setup. A) Shows the sum of all the alternative ideas, yielding an entirely different concept for the setup. These two traverses would be located between the pole shoes with a titanium disk in the middle of both upper and lower traverses. In this case, there will be no need to drill the pole shoe of the electromagnet. The electromagnet and the universal testing machine are on a concrete base. B) Shows an AFM-like strain measurement as an example of primary consideration, and C) and D) show the failed approaches for integrating the Fabry-Pérot Interferometer.

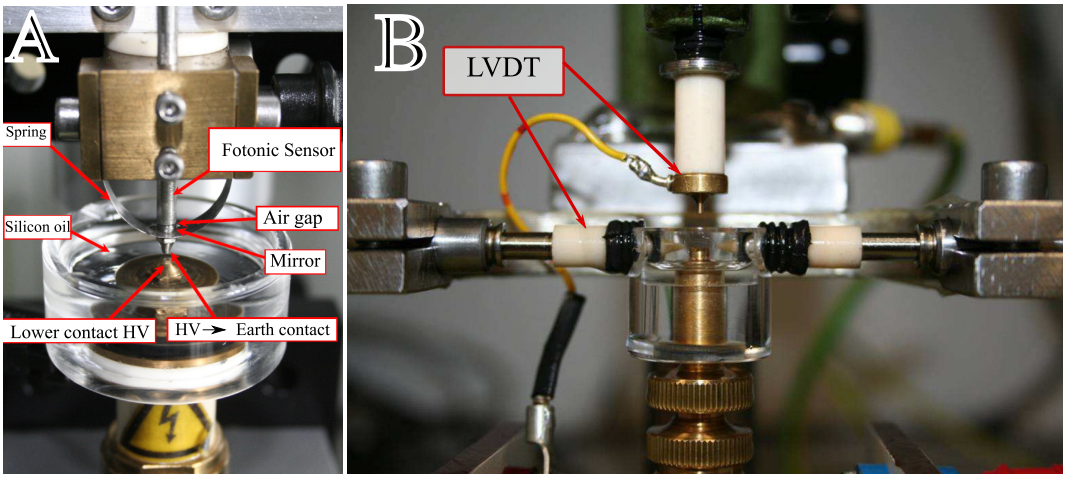

FIGURE B.2: Setups constructed by Emil Aulbach in the group of Prof. Rödel in Darmstadt for P-S-E-loop measurement. A) Uses a Photnic Fiberoptic Sensor (RC Model)[154] devised by PHILTEC, Inc, ©https://philtec.com/. Given the dimensions and the metallic components of the setups, they cannot be used in a magnetic environment.

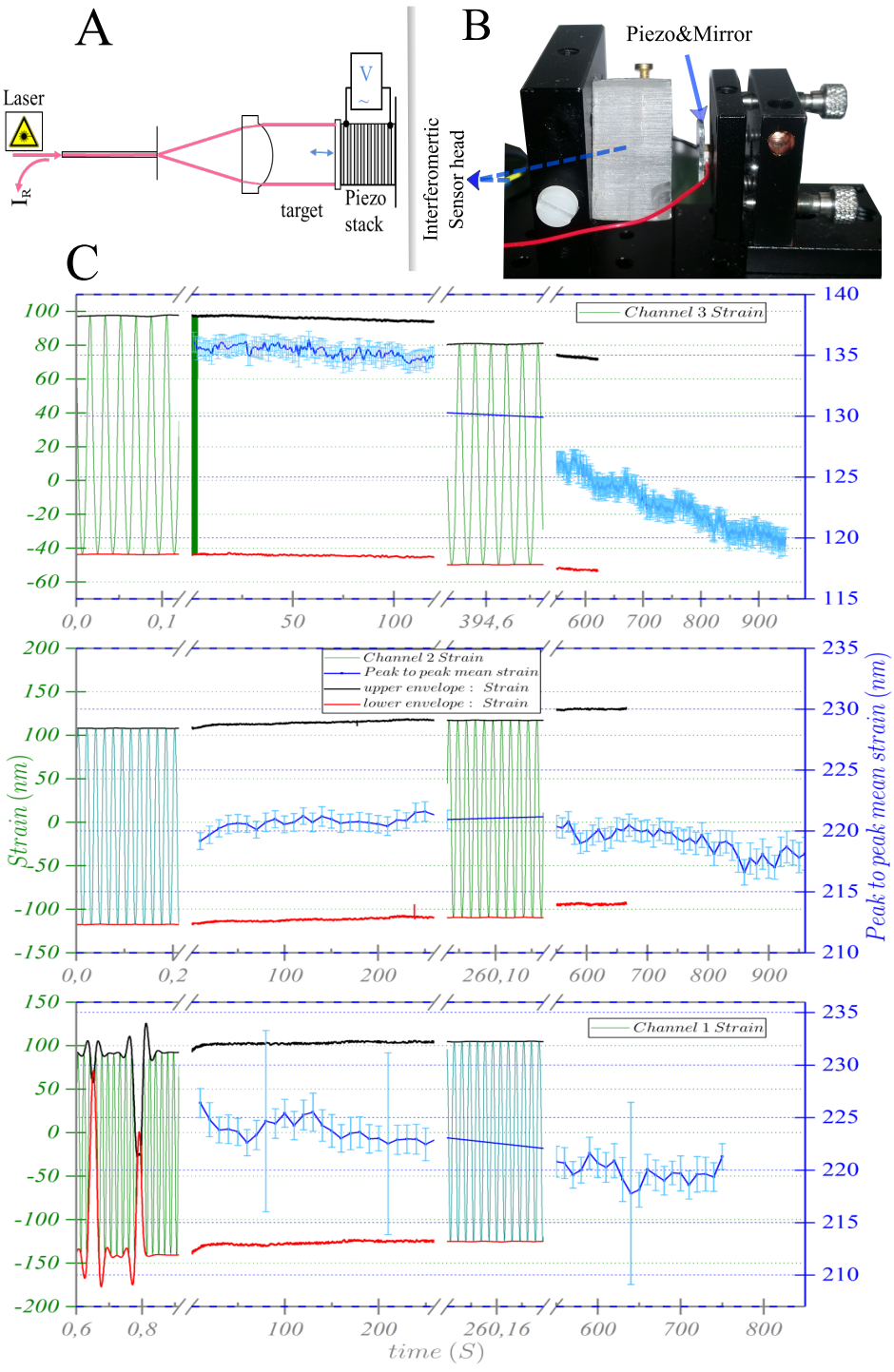

FIGURE B.3: This graph shows some characterization measurement of the Attocube Fabery-Pérot interferometer. Here, the displacement is measurement with a Piezostack from Thorlab. A) and B) display the experiment design. C) show all 3 channels of Attocube's FPS3010 interferometric sensor, (Haar Germany). The piezoactuator driving voltage 5 V.

B.3.1 Compatible measurement geometry for the initial setup design

For the magnetostriction measurement, a first approach was undertaken using the same geometry as the device performance test. Here a mirror was attached to a piezo actuator facing the senor head, see Fig. B.3. In the setup, all metallic elements of the construction were replaced by Perspex. This needed the development of an optical track line made of Perspex and a custom-made beam alignment insert installation, see Sec., with the details for alignment inserts 4.4, with the details for alignment inserts, Fig. 4.14 and B.4.

Further, the sensor heads[2] are also replaced by a custom-designed lens hull (sensor heads). Besides all the measures in the geometry, as displayed in Fig. B.3, the magnetostriction resulted in erroneous measurement. In general, however, the measurement indicates a hysteretic behaviour, see Fig. 4.22B. In the magnetostriction measurements, the values and shape of the graph weren't consistent with the literature values [46, 68, 163]. As a result of this, it is assumed that the hysteretic behaviour (Fig. 4.22) is related to some unknown nature of the distortion in polycrystalline materials due to a magnetic field, see Sec. 2.4.2. Moreover, the influence of magnetic shielding effects in each grain inside the polycrystalline CFO is unknown. Such an effect is inherent to noncrystalline grains of ferromagnetic materials [232]. Additionally, the direction of magnetization is not necessary for the direction of magnetostriction of the system, given the various anisotropies (shape, magnetocrystalline), Sec. 2.3.4, Fig. 2.5.

Following *Cullity* [49, p. 258], a *form effect* merges as the sample is magnetized, which has a different origin from that of magnetostriction. This is attributed to the tendency of a body to minimize its magnetostriction energy.

Signal alignment and calibration for Fabry-P'erot Interferometer

The experimental procedure for applying interferometric measurement requires self-calibration. The Attocube interferometer is equipped with an automated signal evaluation system, which processes the intensity of the reflected signal. It's necessary to perform this step each time after a new stress is applied (see Sec. B.4).

First, manual alignment of the mirror for the best signal is necessary. Afterward, the setup needs to be swung out, which requires a relaxation time of several minutes until the signal stabilizes. Once stabilized, the signal can be calibrated by Attocube (see Fig. B.4D).

In the outlook section (Sec. 6.1), we discuss the possibility of further miniaturizing the interferometric magnetostriction device (Fig. B.6B) to mount it on a rotating holder. Placing this device between the AC coils would enable measuring the strain derivative, strain sensitivity, and piezomagnetic coefficient (Fig. 2.11). This approach eliminates the need to synthesize a composite with a less optimal magnetic phase, as strain sensitivity is crucial for magnetoelectric coupling. The device can be positioned between the AC coils, as shown in Fig. B.6D, and mounted on the optical table (Fig. B.6B). This setup allows measuring the angular dependency of strain, aiding in identifying anisotropy from angle-dependent strain. It enables measuring the elements in the property tensor that couple to strain.

[2] A lens-hull with a fixed focal length, see Sec. B.4.

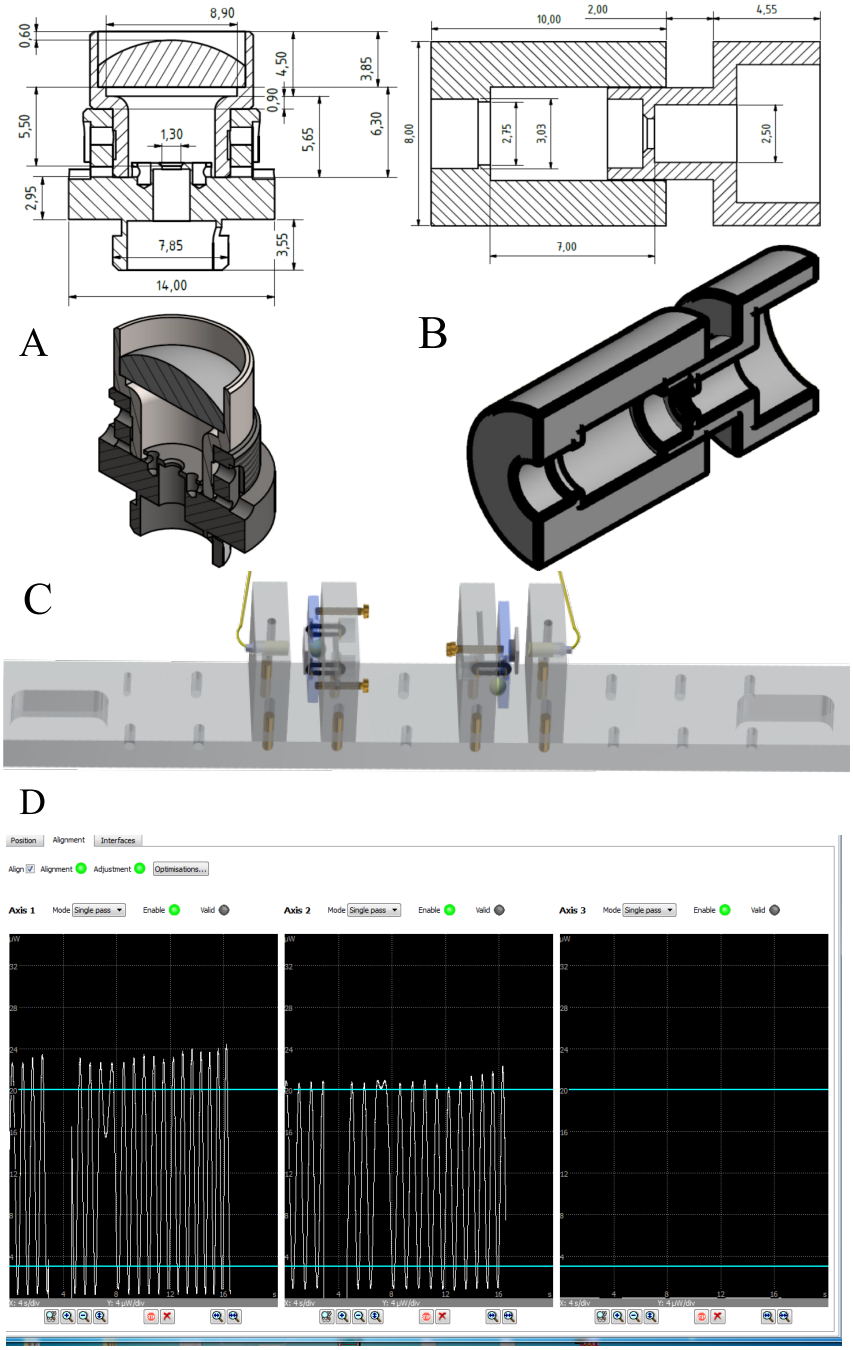

FIGURE B.4: Design and evaluation of a custom-made sensor head tailored to the requirements of a Fabry-P'erot Interferometer (see Fig. 4.13). A) Illustration of the technical realization of Attocube's sensor head from manufacturer. It was intended to replace the Ti-holder with a plastic one. Once a copy of the original (from manufacturer) made from plastic material was successfully tested, another customized sensor head B) was produced to fit the dimensions of the space available. The related lenses were ordered. C) The optical rail was custom-designed for the testing and evolution purposes of the Perspex sensor head, with a fixed distance between the sensors and sample. D) The signal alignment results for both sensor head were obtained using the developed alignment inserts, (see Fig. 4.14).

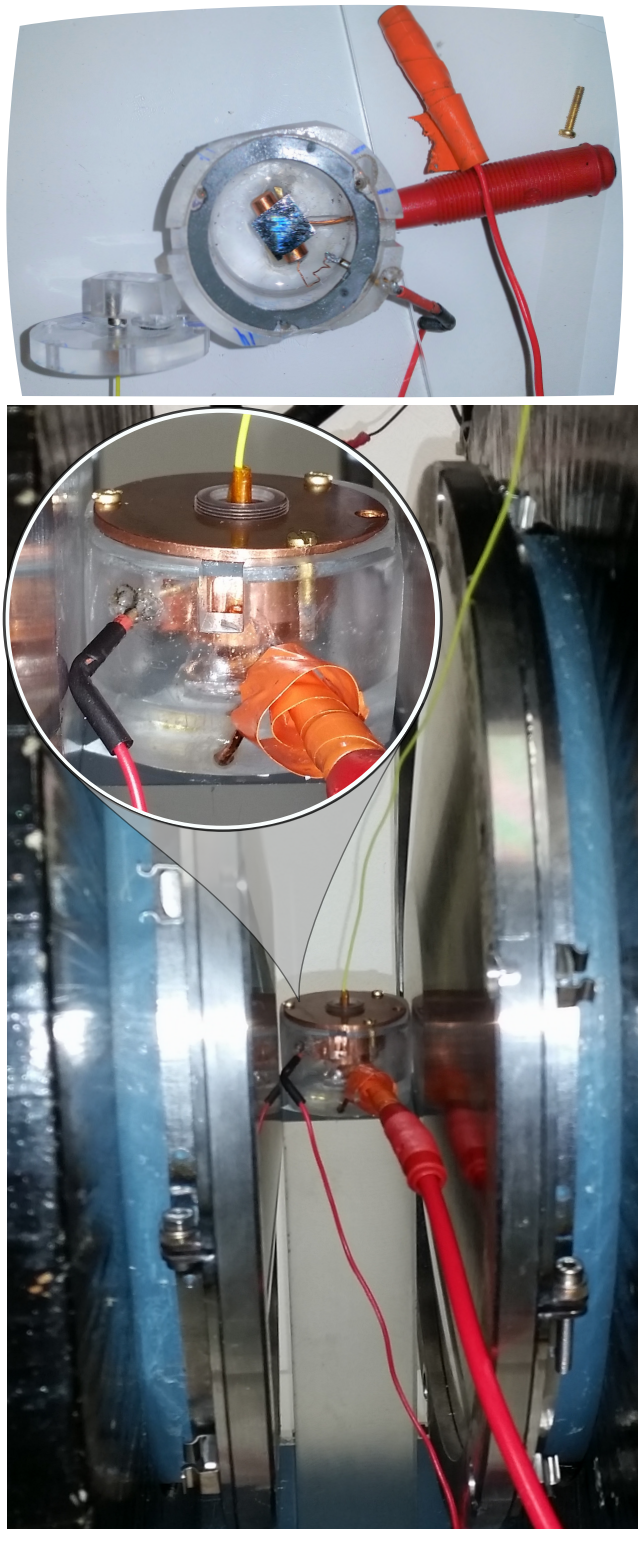

FIGURE B.5: This setup, located between pole shoes, allows for a perpendicular arrangement of the magnetic and electric fields. It is the 2nd electromagnet system available in the Institute of Material Science (UNI-DUE), capable of generating magnetic fields up to 0.4 T.

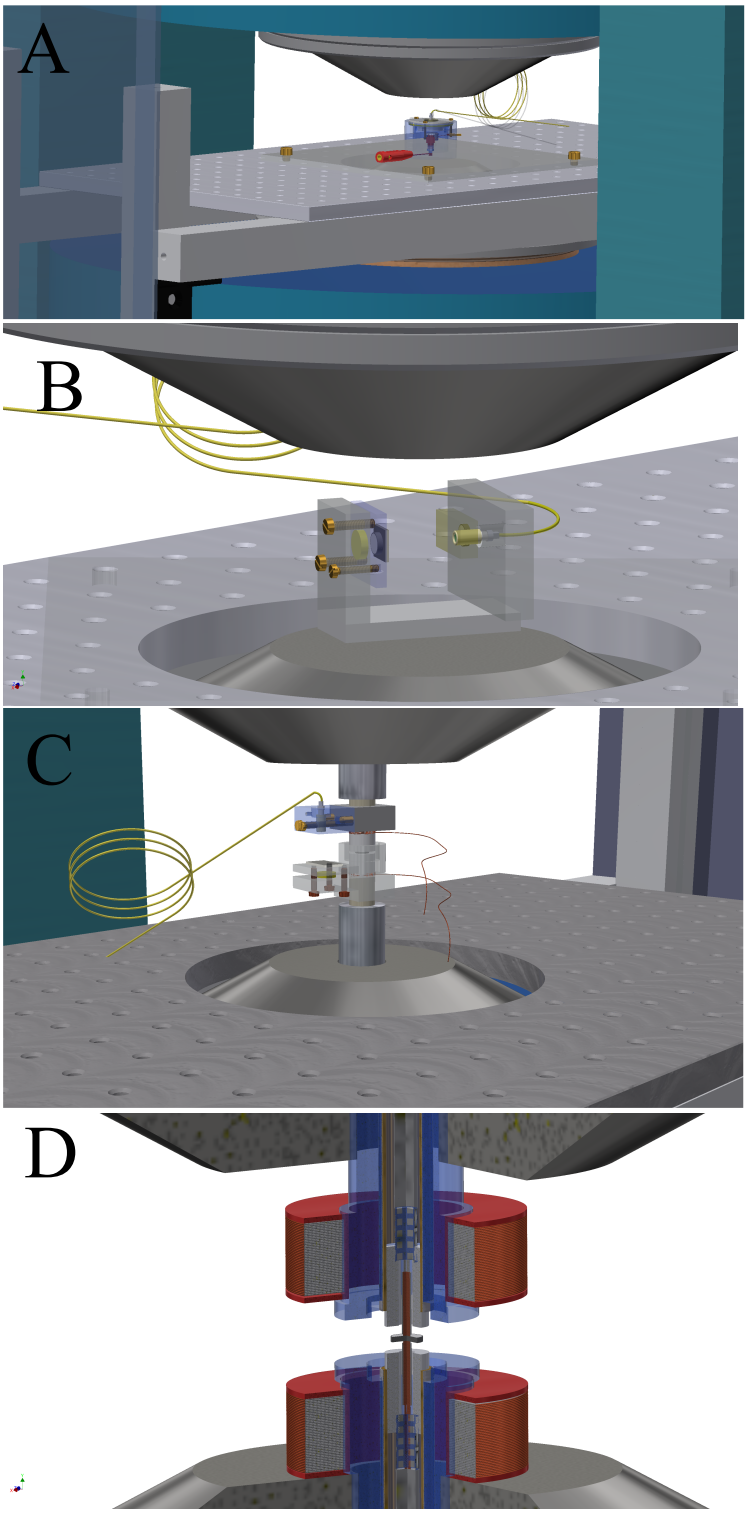

FIGURE B.6: This zooms in on the main setup (see Fig. 4.2), illustrating the capability to exchange between four different measurement modules between the pole shoes. A) This module measures the P-E hysteresis loops in parallel to the magnetic field (as described in Sec. 4.4.1). B) A miniaturized magnetostriction module (B) can also be placed between the AC-coils as shown in D. C) Depicts the P-E-S hysteresis loops module in parallel to the magnetic field and uniaxial stress. D) Shows the ME-measurement module in parallel to the magnetic field for direct ME-coefficient measurement, extendable with uniaxial stress.

B.4 Supplementary figures related to setups

B.4.1 PSELoop-Device

ModulesOptions

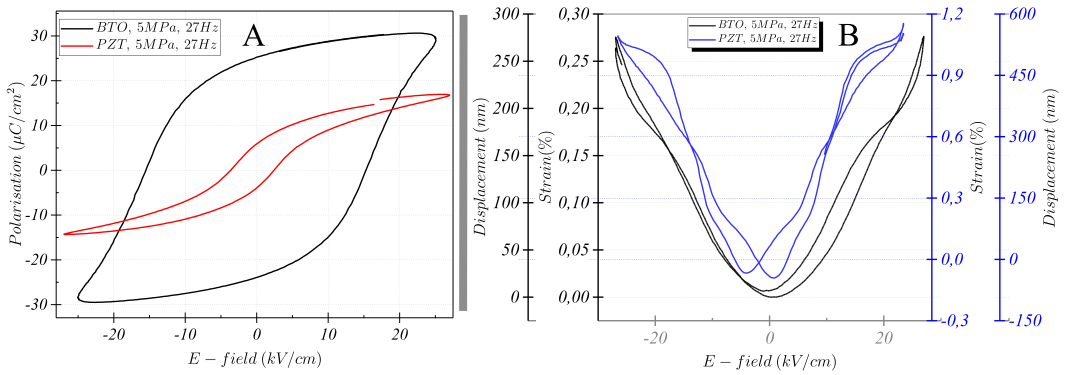

FIGURE B.7: A) Shows the polarization hysteresis for BTO and PZT in a clamped state. B) displays the strain hysteresis (butterfly loop) for both BTO and PZT at 27Hz in a clamped state. The shape of the strain curve remains distorted at 27 Hz due to the low frequency.

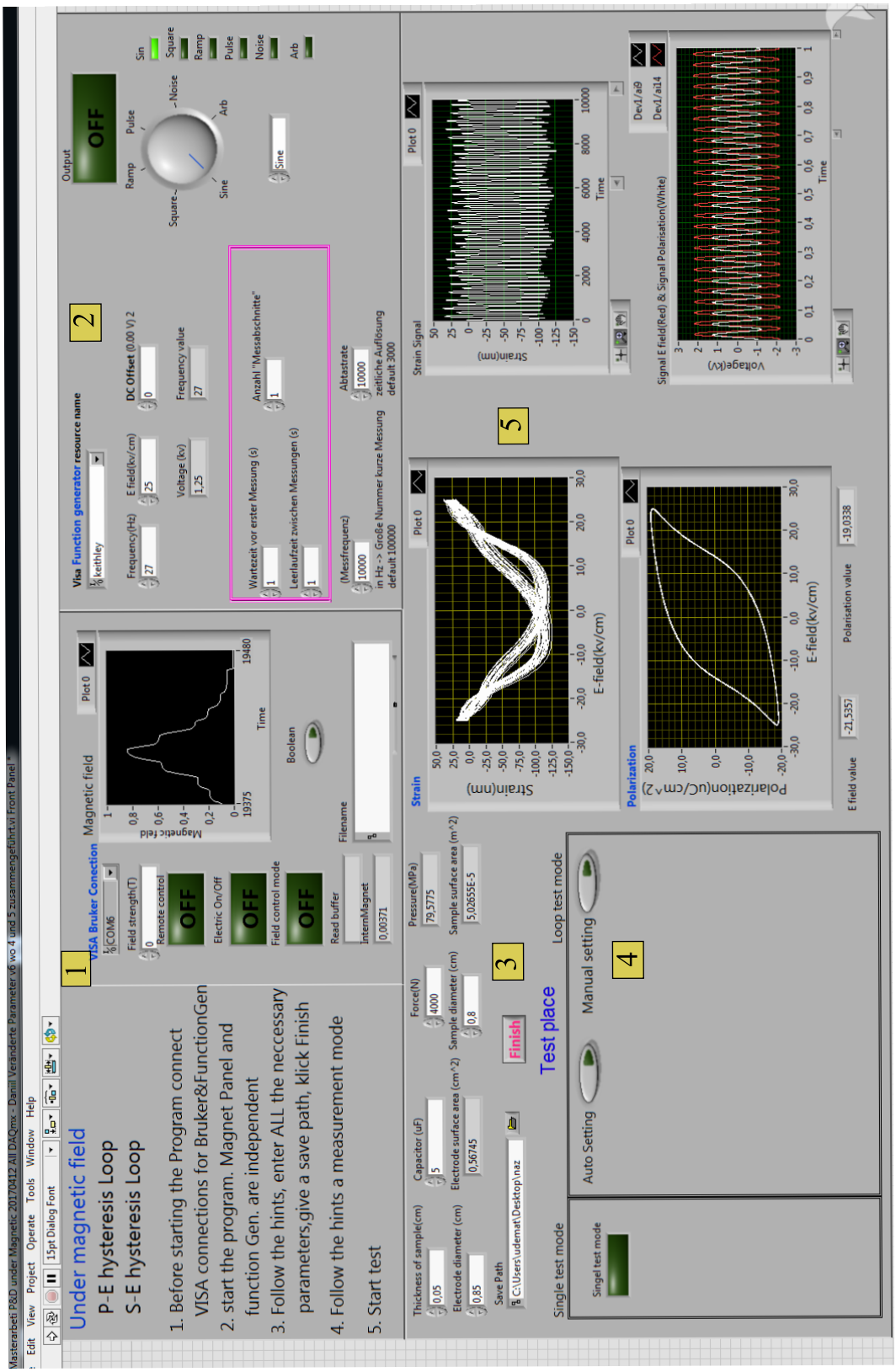

FIGURE B.8: Labview instruments modules for P-E, S-E- hysteresis loops. Block 1 : Operating instructions for the user are given in . Block 2 is the control panel for the magnetic field. In block 3 the function generator can be controlled. In block 4 the program offers two test modes available, namely the signal test mode and the loop test mode. Also an Idlye time option is given here, Fig. 3.9, For detailed description consult detailed [151]

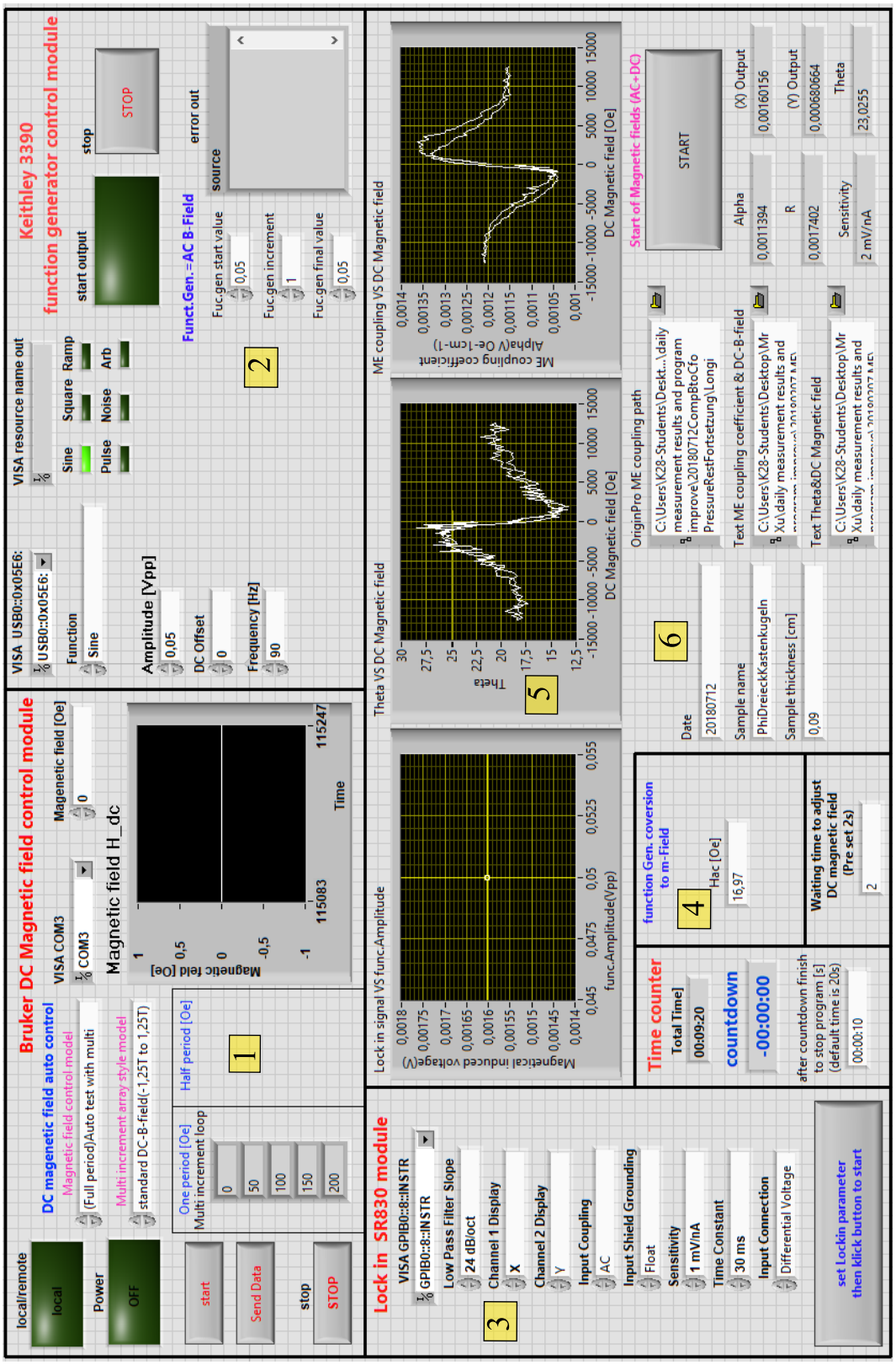

FIGURE B.9: LabVIEW front panel of for direct magnetoelectric measurement Fig. B.10. Block 1 is BRUKER DC magnetic field control module, block 2 is Keithley 3390 function generator control module, Block 3 is the lock-in amplifier SR830 control module, Block 4 is time counter module, and Block 5 is data acquisition and storage module. For detailed description consult [152]

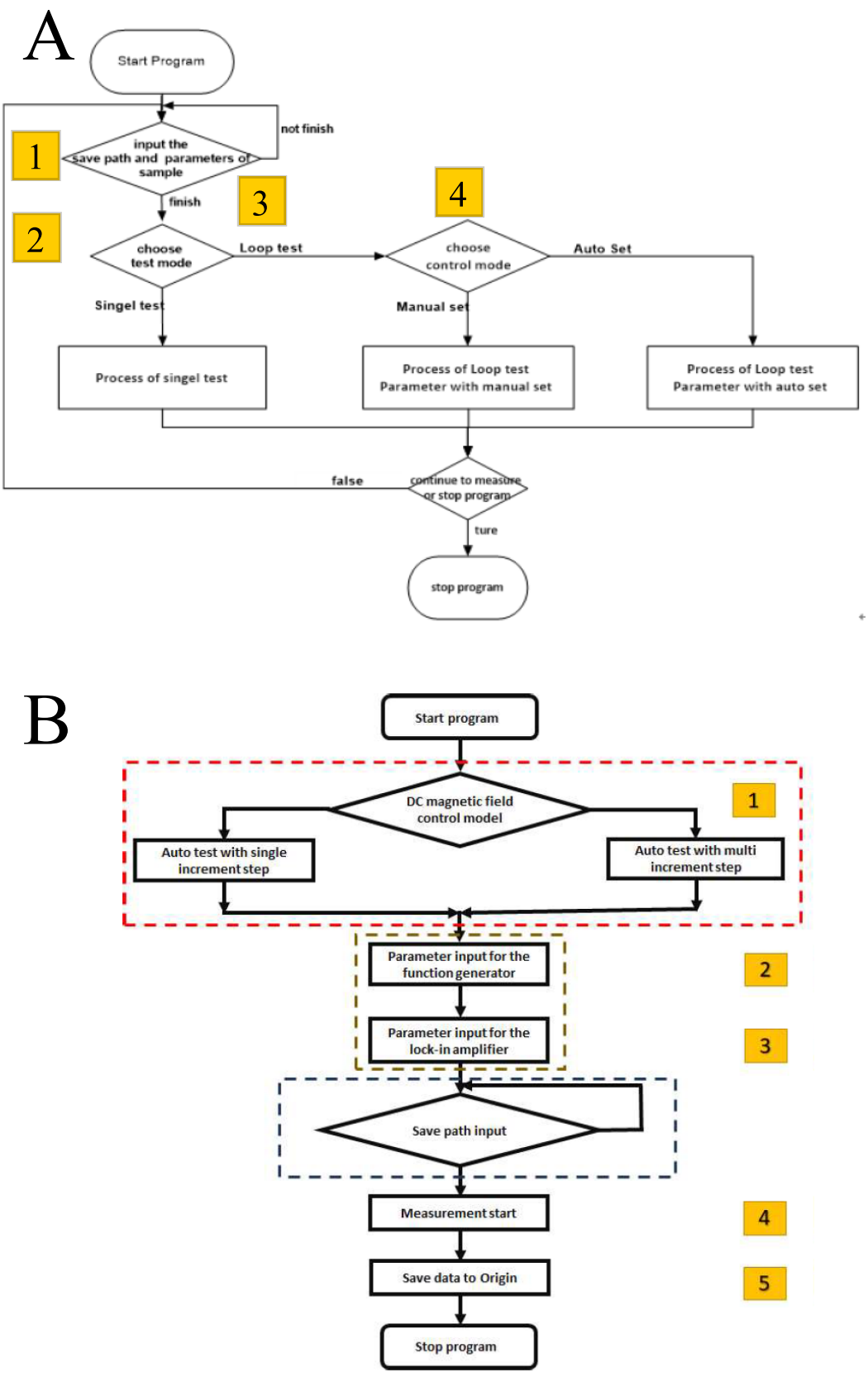

FIGURE B.10: A) shows the Flow chart for execution process of main program in Fig. B.8 B) show the algorithm flow chart of LabVIEW program for Fig. B.9

Bibliography

[1] A. Ferdowsi, D. Davis, and A. Nafisi. *Shahnameh: The Persian Book of Kings*. Penguin classics deluxe edition. Penguin Books, 2007.

[2] Yang Lu. "Industry 4.0: A survey on technologies, applications and open research issues". In: *Journal of Industrial Information Integration* 6 (2017), pp. 1 –10.

[3] Li Da Xu, Eric L. Xu, and Ling Li. "Industry 4.0: state of the art and future trends". In: *International Journal of Production Research* 56.8 (2018), pp. 2941–2962. eprint: https://doi.org/10.1080/00207543.2018.1444806.

[4] V K Varadan and V V Varadan. "Microsensors, microelectromechanical systems (MEMS), and electronics for smart structures and systems". In: *Smart Materials and Structures* 9.6 (2000), pp. 953–972.

[5] A.L. Herrera-May et al. "Mechanical design and characterization of a resonant magnetic field microsensor with linear response and high resolution". In: *Sensors and Actuators A: Physical* 165.2 (2011), pp. 399 –409.

[6] Joshua C. Agar et al. "Frontiers in strain-engineered multifunctional ferroic materials". In: *MRS Communications* 6.3 (2016), 151?166.

[7] Lisa Jogschies et al. "Recent Developments of Magnetoresistive Sensors for Industrial Applications." In: *Sensors (Basel, Switzerland)* 15 (2015), pp. 28665–89.

[8] Haluk E. Karaca et al. "Magnetic Field-Induced Phase Transformation in NiMnCoIn Magnetic Shape-Memory Alloys?A New Actuation Mechanism with Large Work Output". In: *Advanced Functional Materials* 19.7 (2009), pp. 983–998. eprint: https://onlinelibrary.wiley.com/doi/pdf/10.1002/adfm.200801322.

[9] Srinivasa Reddy Yeduru. "Development of Microactuators Based on the Magnetic Shape Memory Effect". PhD thesis. Faculty of Mechanical Engineering Karlsruhe Institute of Technology, 2013.

[10] S. Marauska et al. "Highly sensitive wafer-level packaged MEMS magnetic field sensor based on magnetoelectric composites". In: *Sensors and Actuators A: Physical* 189 (2013), pp. 321 –327.

[11] N. A. Spaldin and R. Ramesh. "Advances in magnetoelectric multiferroics". In: *Nature Materials* 18.3 (2019), pp. 203–212.

[12] Gopalan Srinivasan et al. "Special issue on magnetoelectrics and their applications". In: *Journal of Physics D: Applied Physics* 52.10 (2019), p. 100301.

[13] Melvin M. Vopson. "Fundamentals of Multiferroic Materials and Their Possible Applications". In: *Critical Reviews in Solid State and Materials Sciences* 40.4 (2015), pp. 223–250. eprint: https://doi.org/10.1080/10408436.2014.992584.

[14] Haribabu Palneedi et al. "Status and perspectives of multiferroic magnetoelectric composite materials and applications". English (US). In: *Actuators* 5.1 (Mar. 2016).

[15] Neil D. Mathur and James F. Scott. “Magnetoelectric phenomena and devices”. In: *Phil. Trans. R. Soc. A.* 372, 20120453 (2014), p. 20120453.

[16] W. Eerenstein, N. D. Mathur, and J. F. Scott. “Multiferroic and magnetoelectric materials”. In: *Nature* 442.7104 (2006), pp. 759–765.

[17] M. Fiebig. “Revival of the magnetoelectric effect”. In: *J. Phys. D: Appl. Phys.* 38 (2005), R123?–R152.

[18] Changyi Liu et al. “Novel instrument for characterizing comprehensive physical properties under multi-mechanical loads and multi-physical field coupling conditions”. In: *Review of Scientific Instruments* 89.2 (2018), p. 025112. eprint: https://doi.org/10.1063/1.5009152.

[19] Nickolaus M. Bruno et al. “High-field magneto-thermo-mechanical testing system for characterizing multiferroic bulk alloys”. In: *Review of Scientific Instruments* 86.11 (2015), p. 113902. eprint: https://doi.org/10.1063/1.4934571.

[20] Y. Ganor et al. “Testing system for ferromagnetic shape memory microactuators”. In: *Review of Scientific Instruments* 78.7 (2007), p. 073907. eprint: https://doi.org/10.1063/1.2753672.

[21] M. Labusch, J. Schr?der, and D.C. Lupascu. “Multiscale homogenization of magnetoelectric porous two-phase composites”. In: *Insights and Innovations in Structural Engineering, Mechanics and Computation, SEMC 2016*. Springer, 2017.

[22] Nicola A. Spaldin. “A beginner’s guide to the modern theory of polarization”. In: *Journal of Solid State Chemistry* 195 (2012). Polar Inorganic Materials: Design Strategies and Functional Properties, pp. 2 –10.

[23] W. Nolting. *Grundkurs Theoretische Physik. 3. Elektrodynamik*. Grundkurs: Theoretische Physik. Springer, 2003.

[24] S. Blundell. *Magnetism in Condensed Matter*. Oxford Master Series in Condensed Matter Physics. OUP Oxford, 2001.

[25] R.E. Newnham. *Properties of Materials; Anisotropy, Symmetry, Structure*. OUP Oxford, 2004.

[26] N.S. Ottosen and M. Ristinmaa. *The Mechanics of Constitutive Modeling*. The Mechanics of Constitutive Modeling. Elsevier Science, 2005.

[27] G. Srinivasan, S. Priya, and N. Sun. *Composite Magnetoelectrics: Materials, Structures, and Applications*. Woodhead Publishing Series in Electronic and Optical Materials. Elsevier Science, 2015.

[28] “IEEE Standard on Magnetostrictive Materials: Piezomagnetic Nomenclature”. In: *IEEE Std 319-1990* (1991), pp. 1–.

[29] M. I. Bichurin, V. M. Petrov, and G. Srinivasan. “Theory of low-frequency magnetoelectric coupling in magnetostrictive-piezoelectric bilayers”. In: *Phys. Rev. B* 68 (5 2003), p. 054402.

[30] G. Harshé, J. O. Dougherty, and R. E. Newnham. “Theoretical modelling of multilayer magnetoelectric composites”. In: *Int. J. Appl. Electromagn. Mater.* 4 (1993), pp. 145–159.

[31] E. Kiral and A.C. Eringen. *Constitutive Equations of Nonlinear Electromagnetic-Elastic Crystals*. Springer New York, 2012.

[32] K. Linnemann, S. Klinkel, and W. Wagner. “A constitutive model for magnetostrictive and piezoelectric materials”. In: *International Journal of Solids and Structures* 46.5 (2009), pp. 1149 –1166.

[33] Hans Schmid. “Multi-ferroic magnetoelectrics”. In: *Ferroelectrics* 162.1 (1994), pp. 317–338. eprint: https://doi.org/10.1080/00150199408245120.

[34] Robert E Newnham. “Domains in minerals”. In: *American Mineralogist* 59.9-10 (1974), p. 906. eprint: /gsw/content_public/journal/ammin/59/9-10/am-1974-906/1/am-1974-906.pdf.

[35] Carlos A. F. Vaz et al. “Magnetoelectric Coupling Effects in Multiferroic Complex Oxide Composite Structures”. In: *Advanced Materials* 22 (2010), pp. 2900–2918.

[36] Hans Schmid. “Some symmetry aspects of ferroics and single phase multiferroics∗”. In: *Journal of Physics: Condensed Matter* 20.43 (2008), p. 434201.

[37] Dragan Damjanovic. “Ferroelectric, dielectric and piezoelectric properties of ferroelectric thin films and ceramics”. In: *Reports on Progress in Physics* 61.9 (1998), p. 1267.

[38] R. Waser. *Nanoelectronics and Information Technology*. Wiley, 2003.

[39] R.E. Cohen. “Theory of ferroelectrics: a vision for the next decade and beyond”. In: *Journal of Physics and Chemistry of Solids* 61.2 (2000), pp. 139 –146.

[40] Nicola A. Spaldin. “Analogies and Differences between Ferroelectricsand Ferromagnets”. In: *Physics of Ferroelectrics: A Modern Perspective*. Berlin, Heidelberg: Springer Berlin Heidelberg, 2007, pp. 175–218.

[41] J.F. Nye. *Physical Properties of Crystals*. Oxford Science Publications, Clarendon Press, 1985.

[42] A.F. Devonshire. “Theory of ferroelectrics”. In: *Advances in Physics* 3.10 (1954), pp. 85–130. eprint: https://doi.org/10.1080/00018735400101173.

[43] R. W?sche, W. Denner, and Heinz Schulz. “Influence of high hydrostatic pressure on the crystal structure of barium titanate (Ba Ti O3)”. In: *Materials Research Bulletin* 16.5 (1981), pp. 497 –500.

[44] H. D. Megaw. “Origin of ferroelectricity in barium titanate and other perovskite-type crystals”. In: *Acta Crystallographica* 5.6 (1952), pp. 739–749.

[45] Ronald E. Cohen. “Origin of ferroelectricity in perovskite oxides”. In: *Nature* 358.6382 (1992), pp. 136–138.

[46] R. M. Bozorth, Elizabeth F. Tilden, and Albert J. Williams. “Anisotropy and Magnetostriction of Some Ferrites”. In: *Phys. Rev.* 99 (6 1955), pp. 1788–1798.

[47] J.M.D Coey. *Magnetism and Magnetic Materials*. Magnetism and Magnetic Materials. Cambridge University Press, 2010.

[48] R. Cardias et al. “The Bethe-Slater curve revisited; new insights from electronic structure theory”. In: *Scientific Reports* 7.1 (2017), pp. 4058–.

[49] B. D. Cullity and C. D. Graham. *Introduction to Magnetic Materials*. 2nd ed. Wiley-IEEE Press, 2009.

[50] A. Aubert et al. “Uniaxial anisotropy and enhanced magnetostriction of $CoFe_2O_4$ induced by reaction under uniaxial pressure with SPS”. In: *Journal of the European Ceramic Society* 37.9 (2017), pp. 3101 –3105.

[51] C B. Sawyer and C H. Tower. “Rochelle Salt as a Dielectric”. In: 35 (Jan. 1930), pp. 269–273.

[52] A. Chtchelkanova, S.A. Wolf, and Y. Idzerda. *Magnetic Interactions and Spin Transport*. Springer US, 2003.

[53] D.C. Jiles and D.L. Atherton. “Theory of ferromagnetic hysteresis”. In: *Journal of Magnetism and Magnetic Materials* 61.1 (1986), pp. 48 –60.

[54] C. Kittel and J.K. Galt. “Ferromagnetic Domain Theory”. In: ed. by Frederick Seitz and David Turnbull. Vol. 3. Solid State Physics. Academic Press, 1956, pp. 437 – 564.

[55] M. E. Lines and A. M. Glass. *Principles and Applications of Ferroelectrics and Related Materials*. Oxford: Oxford University Press, 2001, pp. 694–.

[56] D.C. Lupascu, E. Aulbach, and J. Rödel. “Mixed electromechanical fatigue of lead zirconate titanate”. In: *J. Appl. Phys.* 93.9 (2003), pp. 5551–5556.

[57] C.S. Lynch. “The effect of uniaxial stress on the electro-mechanical response of 8/65/35 PLZT”. In: *Acta Materialia* 44.10 (1996), pp. 4137 –4148.

[58] Ekhard K.H. Salje. “Ferroelastic Materials”. In: *Annual Review of Materials Research* 42.1 (2012), pp. 265–283. eprint: https://doi.org/10.1146/annurev-matsci-070511-155022.

[59] M. Kamlah. “Ferroelectric and ferroelastic piezoceramics - modelling of electromechanical hysteresis phenomena”. In: *Continuum mechanics and thermodynamics* 13.4 (2001). 41.03; LK 01, pp. 219–268.

[60] Ansgar B. Schaeufele and Karl Heinz Haerdtl. “Ferroelastic Properties of Lead Zirconate Titanate Ceramics”. In: *Journal of the American Ceramic Society* 79.10 (1996), pp. 2637–2640. eprint: https://ceramics.onlinelibrary.wiley.com/doi/pdf/10.1111/j.1151-2916.1996.tb09027.x.

[61] D J Craik and M J Wood. “Magnetization changes induced by stress in a constant applied field”. In: *Journal of Physics D* 3.7 (1970), p. 1009.

[62] Frederick T. Calkins, Alison B. Flatau, and Marcelo J. Dapino. “Overview of Magnetostrictive Sensor Technology”. In: 2007.

[63] M.R.J. Gibbs. *Modern Trends in Magnetostriction Study and Application*. Nato Science Series II: Springer Netherlands, 2000.

[64] Shekhar D. Bhame and Pattayil A. Joy. “Effect of Sintering Conditions and Microstructure on the Magnetostrictive Properties of Cobalt Ferrite”. In: *Journal of the American Ceramic Society* 91.6 (2008), pp. 1976–1980. eprint: https://ceramics.onlinelibrary.wiley.com/doi/pdf/10.1111/j.1551-2916.2008.02367.x.

[65] B. E. Lorenz and C. D. Graham. “Magnetostriction Versus Magnetization of Hiperco 50 From 20 ^{c}ircC to 700 ^{c}ircC”. In: *IEEE Transactions on Magnetics* 42.12 (2006), pp. 3886–3888.

[66] S. Chikazumi. *Physics of Ferromagnetism 2e*. International Series of Monographs on Physics. OUP Oxford, 2009.

[67] Daniel, Laurent. “An analytical model for the magnetostriction strain of ferromagnetic materials subjected to multiaxial stress”. In: *Eur. Phys. J. Appl. Phys.* 83.3 (2018), p. 30904.

[68] M. J. Sablik and D. C. Jiles. “Coupled magnetoelastic theory of magnetic and magnetostrictive hysteresis”. In: *IEEE Transactions on Magnetics* 29.4 (1993), pp. 2113–2123.

[69] G. Srinivasan, E. T. Rasmussen, and R. Hayes. “Magnetoelectric effects in ferrite-lead zirconate titanate layered composites: The influence of zinc substitution in ferrites”. In: *Phys. Rev. B* 67 (1 2003), p. 014418.

[70] Shekhar D. Bhame and P. A. Joy. "Tuning of the magnetostrictive properties of CoFe2O4 by Mn substitution for Co". In: *Journal of Applied Physics* 100.11 (2006), p. 113911. eprint: https://aip.scitation.org/doi/pdf/10.1063/1.2401648.

[71] Nalla Somaiah et al. "Magnetic and magnetoelastic properties of Zn-doped cobalt-ferrites???CoFe2???xZnxO4 (x=0, 0.1, 0.2, and 0.3)". In: *Journal of Magnetism and Magnetic Materials* 324.14 (2012), pp. 2286 –2291.

[72] D.P Bulte and R.A Langman. "Origins of the magnetomechanical effect". In: *Journal of Magnetism and Magnetic Materials* 251.2 (2002), pp. 229 –243.

[73] É. du Trémolet de Lacheisserie, D. Gignoux, and M. Schlenker. "Magnetoelastic EffectsMagnetoelastic Effects". In: *Magnetism*. Ed. by É. du Trémolet de Lacheisserie, D. Gignoux, and M. Schlenker. New York, NY: Springer New York, 2002, pp. 351–398.

[74] D C Jiles. "Theory of the magnetomechanical effect". In: *Journal of Physics D: Applied Physics* 28.8 (1995), p. 1537.

[75] C.G. Stefanita. *From Bulk to Nano: The Many Sides of Magnetism*. Vol. Band 117. Springer Series in Materials Science. Springer Berlin Heidelberg, 2008.

[76] D.C. Jiles. "Recent advances and future directions in magnetic materials". In: *Acta Materialia* 51.19 (2003). The Golden Jubilee Issue. Selected topics in Materials Science and Engineering: Past, Present and Future, pp. 5907 –5939.

[77] B. S. Berry and W. C. Pritchet. "Magnetic Annealing and Directional Ordering of an Amorphous Ferromagnetic Alloy". In: *Phys. Rev. Lett.* 34 (16 1975), pp. 1022–1025.

[78] R. E. Newnham and L. E. Cross. "Secondary ferroics and domain-divided piezoelectrics". In: *Ferroelectrics* 10.1 (1976), pp. 269–276. eprint: https://www.tandfonline.com/doi/pdf/10.1080/00150197608241994.

[79] Ulrich Boettger. "Dielectric Properties of Polar Oxides". In: *Polar Oxides*. John Wiley & Sons, Ltd, 2005. Chap. 1, pp. 11–38. eprint: https://onlinelibrary.wiley.com/doi/pdf/10.1002/3527604650.ch1.

[80] G A Smolenskii? And I E Chupis. "Ferroelectromagnets". In: *Soviet Physics Uspekhi* 25.7 (1982), p. 475.

[81] I.E. Dzyaloshinskii. "On the Magneto-Electrical Effect in Antiferromagnets". In: *Soviet Phys. JETP* 10.3 (1960), p. 628.

[82] D. N. Astrov. "Magnetoelectric Effect in Chromium Oxide". In: *Sov. Phys. JETP* 13.4 (1961), pp. 729–733.

[83] V. J. Folen, G. T. Rado, and E. W. Stalder. "Anisotropy of the Magnetoelectric Effect in Cr_2O_3". In: *Phys. Rev. Lett.* 6 (11 1961), pp. 607–608.

[84] T.H. O'Dell. *The Electrodynamics of Magneto-electric Media*. Series of monographs on selected topics in solid state physics. North-Holland Publishing Company, 1970.

[85] J. van SUCHTELEN. "PRODUCT PROPERTIES: A NEW APPLICATION OF COMPOSITE MATERIALS". In: *Philips Res. Repts* 27 (1972), pp. 27,28–37.

[86] J. van den Boomgaard and R. A. J. Born. "A sintered magnetoelectric composite material BaTiO3-Ni(Co, Mn) Fe2O4". In: *Journal of Materials Science* 13.7 (1978), pp. 1538–1548.

[87] A. M. J. G. Van Run, D. R. Terrell, and J. H. Scholing. "An in situ grown eutectic magnetoelectric composite material". In: *Journal of Materials Science* 9.10 (1974), pp. 1710–1714.

[88] C. Blaauw and F. van der Woude. "Magnetic and structural properties of BiFeO 3". In: *Journal of Physics C: Solid State Physics* 6.8 (1973), p. 1422.

[89] G. Srinivasan et al. "Magnetoelectric bilayer and multilayer structures of magnetostrictive and piezoelectric oxides". In: *Phys. Rev. B* 64 (21 2001), p. 214408.

[90] F. Zavaliche et al. "Electric Field-Induced Magnetization Switching in Epitaxial Columnar Nanostructures". In: *Nano Letters* 5.9 (2005). PMID: 16159226, pp. 1793–1796. eprint: https://doi.org/10.1021/nl051406i.

[91] H. Zheng et al. "Self-Assembled Growth of BiFeO3???CoFe2O4 Nanostructures". In: *Advanced Materials* 18.20 (), pp. 2747–2752. eprint: https://onlinelibrary.wiley.com/doi/pdf/10.1002/adma.200601215.

[92] Junyi Zhai et al. "Giant magnetoelectric effect in Metglas/polyvinylidene-fluoride laminates". In: *Applied Physics Letters* 89.8 (2006), p. 083507. eprint: https://doi.org/10.1063/1.2337996.

[93] M. Fiebig, V.V. Eremenko, and I.E. Chupis. *Magnetoelectric Interaction Phenomena in Crystals*. Nato Science Series II: Springer Netherlands, 2004.

[94] Nicola A. Hill. "Why Are There so Few Magnetic Ferroelectrics?" In: *The Journal of Physical Chemistry B* 104.29 (2000), pp. 6694–6709.

[95] T. Kimura et al. "Magnetic control of ferroelectric polarization". In: *Nature* 426 (2003), pp. 55–58.

[96] W. H. Meiklejohn and C. P. Bean. "New Magnetic Anisotropy". In: *Phys. Rev.* 102 (5 1956), pp. 1413–1414.

[97] Ce-Wen Nan. "Magnetoelectric effect in composites of piezoelectric and piezomagnetic phases". In: *Phys. Rev. B* 50 (9 1994), pp. 6082–6088.

[98] Norifumi Fujimura et al. "Epitaxially grown YMnO3 film: New candidate for nonvolatile memory devices". In: *Applied Physics Letters* 69.7 (1996), pp. 1011–1013. eprint: https://doi.org/10.1063/1.117969.

[99] Ce Wen Nan et al. "Possible giant magnetoelectric effect of ferromagnetic rare-earth???iron-alloys-filled ferroelectric polymers". In: *Applied Physics Letters* 78.17 (2001), pp. 2527–2529. eprint: https://doi.org/10.1063/1.1367293.

[100] M. I. Bichurin et al. "Resonance magnetoelectric effects in layered magnetostrictive-piezoelectric composites". In: *Phys. Rev. B* 68 (13 2003), p. 132408.

[101] Ce-Wen Nan. "Physics of inhomogeneous inorganic materials". In: *Progress in Materials Science* 37.1 (1993), pp. 1 –116.

[102] Shashidhar Srinivas and Jiang Yu Li. "The effective magnetoelectric coefficients of polycrystalline multiferroic composites". In: *Acta Materialia* 53.15 (2005), pp. 4135 –4142.

[103] R.E. Newnham, D.P. Skinner, and L.E. Cross. "Connectivity and piezoelectric-pyroelectric composites". In: *Materials Research Bulletin* 13.5 (1978), pp. 525 – 536.

[104] G. Arlt, D. Hennings, and G. de With. "Dielectric properties of fine?grained barium titanate ceramics". In: *Journal of Applied Physics* 58.4 (1985), pp. 1619–1625. eprint: https://doi.org/10.1063/1.336051.

[105] Rainer Waser. "Dielectric analysis of intergrated ceramic thin film capacitors". In: *Integrated Ferroelectrics* 15.1-4 (1997), pp. 39–51. eprint: https://doi.org/10.1080/10584589708015695.

[106] N. Cai et al. "Dielectric, ferroelectric, magnetic, and magnetoelectric properties of multiferroic laminated composites". In: *Phys. Rev. B* 68 (22 2003), p. 224103.

[107] Robert Jahns et al. "Giant Magnetoelectric Effect in Thin-Film Composites". In: *Journal of the American Ceramic Society* 96.6 (2013), pp. 1673–1681. eprint: https://ceramics.onlinelibrary.wiley.com/doi/pdf/10.1111/jace.12400.

[108] Carolin Schmitz-Antoniak et al. "Electric in-plane polarization in multiferroic $CoFe_2O_4$/$BaTiO_3$ nanocomposite tuned by magnetic fields". In: *Nature Comm.* 4, DOI: 10.1038/ncomms3051 (2013), p. 2051.

[109] G. Srinivasan et al. "Magnetoelectric interactions in hot-pressed nickel zinc ferrite and lead zirconate titanate composites". In: *Appl. Phys. Lett.* 85.13 (2004), pp. 2550–2552.

[110] S. Q. Ren et al. "$BaTiO_3$/$CoFe_2O_4$ particulate composites with large high frequency magnetoelectric response". In: *J. Mater. Sci.* 40 (2005), pp. 4375–4378.

[111] Jungho Ryu et al. "Piezoelectric and Magnetoelectric Properties of Lead Zirconate Titanate/Ni-Ferrite Particulate Composites". In: *Journal of Electroceramics* 7.1 (2001), pp. 17–24.

[112] XiaoYan Lu and Hui Li. "Size effect on magnetoelectric coupling in multiferroic heterostructures". In: *Journal of Applied Physics* 109.7 (2011), p. 074112. eprint: https://doi.org/10.1063/1.3569748.

[113] Marco Avellaneda and Girish Harsh? "Magnetoelectric Effect in Piezoelectric/Magnetostrictive Multilayer (2-2) Composites". In: *Journal of Intelligent Material Systems and Structures* 5.4 (1994), pp. 501–513. eprint: https://doi.org/10.1177/1045389X9400500406.

[114] M. Frey and D. Payne. "Grain-size effect on structure and phase transformations for barium titanate". In: *Physical Review B - Condensed Matter and Materials Physics* 54.5 (1996). cited By 764, pp. 3158–3168.

[115] Mark P. McNeal, Sei-Joo Jang, and Robert E. Newnham. "The effect of grain and particle size on the microwave properties of barium titanate (BaTiO3)". In: *Journal of Applied Physics* 83.6 (1998), pp. 3288–3297. eprint: https://doi.org/10.1063/1.367097.

[116] Zhigang Suo. "Stress and strain in ferroelectrics". In: *Current Opinion in Solid State and Materials Science* 3.5 (1998), pp. 486 –489.

[117] D. Lupascu and J. R??del. "Fatigue In Bulk Lead Zirconate Titanate Actuator Materials". In: *Advanced Engineering Materials* 7.10 (2005), pp. 882–898. eprint: https://onlinelibrary.wiley.com/doi/pdf/10.1002/adem.200500117.

[118] B. WUL. "Barium Titanate: a New Ferro-Electric". In: *Nature* 157.3998 (1946), pp. 808–808.

[119] E. Kaxiras. *Atomic and Electronic Structure of Solids*. Cambridge University Press, 2003.

[120] F. J. Pedrosa et al. "Tunable nanocrystalline CoFe2O4 isotropic powders obtained by co-precipitation and ultrafast ball milling for permanent magnet applications". In: *RSC Adv.* 6 (90 2016), pp. 87282–87287.

[121] Min Yi, Bai-Xiang Xu, and Dietmar Gross. “Mechanically induced deterministic 180?? switching in nanomagnets”. In: *Mechanics of Materials* 87 (2015), pp. 40 –49.

[122] Ce-Wen Nan et al. “Multiferroic magnetoelectric composites: Historical perspective, status, and future directions”. In: *Journal of Applied Physics* 103.3, 031101 (2008), p. 031101.

[123] Zhe Zhao et al. “Grain-size effects on the ferroelectric behavior of dense nanocrystalline $BaTiO_3$ ceramics”. In: *Phys. Rev. B* 70 (2 2004), p. 024107.

[124] Yongqiang Tan et al. “Enhancement of electric field-induced strain in BaTiO3 ceramics through grain size optimization”. In: *physica status solidi (a)* 212.2 (2015), pp. 433–438. eprint: https://onlinelibrary.wiley.com/doi/pdf/10.1002/pssa.201431233.

[125] Fumihiro Wakai. “Modeling and Simulation of Elementary Processes in Ideal Sintering”. In: *Journal of the American Ceramic Society* 89.5 (2006), pp. 1471–1484.

[126] Mohamed N. Rahaman. *Ceramic processing and sintering*. Marcel Dekker, New York, 2003.

[127] Hans Lueth. *Solid Surfaces, Interfaces and Thin Films* -. Berlin Heidelberg: Springer Science & Business Media, 2010.

[128] Jodi Liu, Robert E. Saw, and Y.-H. Kiang. “Calculation of Effective Penetration Depth in X-Ray Diffraction for Pharmaceutical Solids”. In: *Journal of Pharmaceutical Sciences* 99.9 (Sept. 2010), pp. 3807–3814.

[129] Ding-Yeong Wang and Chun-Yen Chang. “Switching Current Study: Hysteresis Measurement of Ferroelectric Capacitors using Current–Voltage Measurement Method”. In: *Japanese Journal of Applied Physics* 44.4A (2005), pp. 1857–1861.

[130] Jos? A. Giacometti et al. “Constant current: A method for obtaining hysteresis loops in ferroelectric materials”. In: *Review of Scientific Instruments* 70.6 (1999), pp. 2699–2702. eprint: https://doi.org/10.1063/1.1149830.

[131] H. Diamant, K. Drenck, and R. Pepinsky. “Bridge for Accurate Measurement of Ferroelectric Hysteresis”. In: *Review of Scientific Instruments* 28.1 (1957), pp. 30–33. eprint: https://doi.org/10.1063/1.1715701.

[132] Anatoli Deleniv and Spartak Gevorgian. “Measurements of the Dielectric Properties”. In: *Ferroelectrics in Microwave Devices, Circuits and Systems: Physics, Modeling, Fabrication and Measurements*. Ed. by Spartak Gevorgian. London: Springer London, 2009, pp. 287–349.

[133] Nasir Mahmood et al. *Handbook of Carbon Nanotubes-Polymer Nanocomposites*. Dec. 2014.

[134] David Serrate et al. “Imaging and manipulating the spin direction of individual atoms”. In: *Nature Nanotechnology* 5 (Apr. 2010), pp. 350–.

[135] J. Stoehr et al. “Principles of X-Ray Magnetic Dichroism Spectromicroscopy”. In: *Surface Review and Letters* 05.06 (1998), pp. 1297–1308. eprint: https://doi.org/10.1142/S0218625X98001638.

[136] Peter Fischer and Hendrik Ohldag. “X-rays and magnetism”. In: *Reports on Progress in Physics* 78.9 (2015), p. 094501.

[137] P. Borisov et al. “Superconducting quantum interference device setup for magnetoelectric measurements”. In: *Review of Scientific Instruments* 78.10, 106105 (2007), p. 106105.

[138] S. Foner. "The vibrating sample magnetometer: Experiences of a volunteer (invited)". In: *Journal of Applied Physics* 79.8 (1996), pp. 4740–4745. eprint: https://aip.scitation.org/doi/pdf/10.1063/1.361657.

[139] Julie Bowles. "SQUID Attack!" In: *IRM Quarterly* 19 (Apr. 2009), pp. 1, 8–11.

[140] John Clarke (ed.) *The SQUID handbook (3 vol.)* Wiley-VCH, Weinheim, 2004-2006.

[141] M. M. Vopson et al. "Measurement Techniques of the Magneto-Electric Coupling in Multiferroics". In: *Materials* 10.8 (2017).

[142] Harsh Trivedi et al. "Local manifestations of a static magnetoelectric effect in nanostructured BaTiO3???BaFe12O9 composite multiferroics". In: *Nanoscale* 7 (10 2015), pp. 4489–4496.

[143] Eiji Kita. "DC magnetoelectric effect measurements by a squid magnetometer". In: *Ferroelectrics* 162.1 (1994), pp. 397–400. eprint: https://doi.org/10.1080/00150199408245129.

[144] Soma Salamon. "Magnetic measurements on single-phase and composite multiferroics". PhD thesis. Faculty of Physics, University of Duisburg-Essen, 2018.

[145] G. Srinivasan. "Magnetoelectric Composites". In: *Annu. Rev. Mater. Res.* 40.1 (2010), pp. 153–178.

[146] Wolfgang Kleemann. "Multiferroic and magnetoelectric nanocomposites for data processing". In: *Journal of Physics D: Applied Physics* 50.22 (2017), p. 223001.

[147] W. Eerenstein et al. "Giant sharp and persistent converse magnetoelectric effects in multiferroic epitaxial heterostructures". In: *Nature Materials* 6.5 (2007), pp. 348–351.

[148] K.G. Webber et al. "Temperature-dependent ferroelastic switching of soft lead zirconate titanate". In: *Acta Materialia* 57.15 (2009), pp. 4614 –4623.

[149] Dayu Zhou, Marc Kamlah, and Dietrich Munz. "Effects of uniaxial prestress on the ferroelectric hysteretic response of soft PZT". In: *Journal of the European Ceramic Society* 25.4 (2005), pp. 425 –432.

[150] Jan Karthaus et al. "Influence of the mechanical fatigue progress on the magnetic properties of electrical steel sheets". In: *Archives of Electrical Engineering* 66 (Jan. 2017).

[151] Yang Lai. "Automation of a Set-up for mechanical characterization magneto-electric composite". MA thesis. Faculty of Engineering, University of Duisburg-Essen, Department of Civil Engineering, Institute of Materials Science., 2016.

[152] Zhouchen Xu. "Automation of a setup for the determination of magnetoelectric coefficients". MA thesis. Faculty of Engineering, University of Duisburg-Essen, Department of Civil Engineering, Institute of Materials Science., 2017.

[153] Doru C. Lupascu et al. "Measuring the magnetoelectric effect across scales". In: *GAMM-Mitteilungen* 38.1 (2015), pp. 25–74. eprint: https://onlinelibrary.wiley.com/doi/pdf/10.1002/gamm.201510003.

[154] Garry Berkovic and Ehud Shafir. "Optical methods for distance and displacement measurements". In: *Adv. Opt. Photon.* 4.4 (2012), pp. 441–471.

[155] A. L. Kholkin et al. "Interferometric measurements of electric field?induced displacements in piezoelectric thin films". In: *Review of Scientific Instruments* 67.5 (1996), pp. 1935–1941. eprint: https://doi.org/10.1063/1.1147000.

[156] V.L. Mathe and A.D. Sheikh. “Magnetostrictive properties of nanocrystalline Co?Ni ferrites”. In: *Physica B: Condensed Matter* 405.17 (2010), pp. 3594 –3598.

[157] Wei Chen and Christopher S. Lynch. “Multiaxial Constitutive Behavior of Ferroelectric Materials ”. In: *Journal of Engineering Materials and Technology* 123.2 (Sept. 2000), pp. 169–175. eprint: https://asmedigitalcollection.asme.org/materialstechnology/article-pdf/123/2/169/4880156/169_1.pdf.

[158] C. C. Perry. “The resistance strain gage revisited”. In: *Experimental Mechanics* 24.4 (1984), pp. 286–299.

[159] M Vaughan. *The Fabry-Perot Interferometer History, theory, practice and applications*. CRC Press, 1989.

[160] B. K. Nowakowski, D. T. Smith, and S. T. Smith. “Highly compact fiber Fabry-Perot interferometer: A new instrument design”. In: *Review of Scientific Instruments* 87.11 (2016), p. 115102. eprint: https://doi.org/10.1063/1.4964622.

[161] Klaus Thurner, Pierre-Fran?ois Braun, and Khaled Karrai. “Fabry-Perot interferometry for long range displacement sensing”. In: *Review of Scientific Instruments* 84.9 (2013), p. 095005. eprint: https://doi.org/10.1063/1.4821623.

[162] Byeong Ha Lee et al. “Interferometric Fiber Optic Sensors”. In: *Sensors (Basel, Switzerland)* 12.3 (Feb. 2012), pp. 2467–2486.

[163] E W Lee. “Magnetostriction and Magnetomechanical Effects”. In: *Reports on Progress in Physics* 18.1 (1955), p. 207.

[164] F. Claeyssen et al. “Actuators, transducers and motors based on giant magnetostrictive materials”. In: *Journal of Alloys and Compounds* 258.1 (1997), pp. 61 –73.

[165] O. Heczko. “Magnetic shape memory effect and highly mobile twin boundaries”. In: *Materials Science and Technology* 30.13 (2014), pp. 1559–1578. eprint: https://doi.org/10.1179/1743284714Y.0000000599.

[166] P. YANG et al. “MAGNETOELECTRIC STUDY IN TERFENOL-D/PFNT LAMINATE COMPOSITE”. In: *Integrated Ferroelectrics* 99.1 (2008), pp. 86–92. eprint: https://doi.org/10.1080/10584580802107742.

[167] A. M. Leary et al. “Stress induced anisotropy in CoFeMn soft magnetic nanocomposites”. In: *Journal of Applied Physics* 117.17 (2015), 17A338. eprint: https://doi.org/10.1063/1.4919230.

[168] Yongke Yan et al. “Correlation between tunability and anisotropy in magnetoelectric voltage tunable inductor (VTI)”. In: *Scientific Reports* 7.1 (2017), pp. 16008–.

[169] M. Lohndorf et al. “Strain sensors based on magnetostrictive GMR/TMR structures”. In: *IEEE Transactions on Magnetics* 38.5 (2002), pp. 2826–2828.

[170] K. Mydeen et al. “Pressure-Induced Ferromagnetism due to an Anisotropic Electronic Topological Transition in $Fe_{1.08}Te$”. In: *Phys. Rev. Lett.* 119 (22 2017), p. 227003.

[171] C. Salazar Mej?a et al. “Uniaxial-stress tuned large magnetic-shape-memory effect in Ni-Co-Mn-Sb Heusler alloys”. In: *Applied Physics Letters* 110.7 (2017), p. 071901.

[172] S Reich and T Godin. “A miniature pressure cell for a SQUID magnetometer”. In: *Measurement Science and Technology* 7.7 (1996), pp. 1079–1082.

[173] J. Kamarad et al. “Miniature uniaxial pressure cells for magnetic measurements”. In: *High Pressure Research* 28.4 (2008), pp. 633–636. eprint: https://doi.org/10.1080/08957950802338634.

[174] Yoshiya Uwatoko et al. “Material properties of $Ni - Cr - Al$ alloy and design of a 4 GPa class non-magnetic high-pressure cell”. In: *Journal of Physics: Condensed Matter* 14.44 (2002), p. 11291.

[175] T. C. Kobayashi et al. “Nonmagnetic indenter-type high-pressure cell for magnetic measurements”. In: *Review of Scientific Instruments* 78.2 (2007), p. 023909. eprint: https://doi.org/10.1063/1.2459512.

[176] Patricia Lebre Alireza and Gilbert George Lonzarich. “Miniature anvil cell for high-pressure measurements in a commercial superconducting quantum interference device magnetometer”. In: *Review of Scientific Instruments* 80.2 (2009), p. 023906. eprint: https://doi.org/10.1063/1.3077303.

[177] Naoyuki Tateiwa et al. “Miniature ceramic-anvil high-pressure cell for magnetic measurements in a commercial superconducting quantum interference device magnetometer”. In: *Review of Scientific Instruments* 82.5 (2011), p. 053906. eprint: https://doi.org/10.1063/1.3590745.

[178] V K Sharma, M K Chattopadhyay, and S B Roy. “The effect of external pressure on the magnetocaloric effect of Ni?Mn?In alloy”. In: *Journal of Physics: Condensed Matter* 23.36 (2011), p. 366001.

[179] Hiroshi Fujiwara, Hideoki Kadomatsu, and Kiyokazu Tohma. “Simple clamp pressure cell up to 30 kbar”. In: *Review of Scientific Instruments* 51.10 (1980), pp. 1345–1348. eprint: https://doi.org/10.1063/1.1136061.

[180] Jr. Matthew J. Donachie. *Titanium: A Technical Guide*. Tech. rep. AMS: the materials Information society, 2000.

[181] K. Koyama et al. “Instrument for high resolution magnetization measurements at high pressures, high magnetic fields and low temperatures”. In: *Review of Scientific Instruments* 69.8 (1998), pp. 3009–3014. eprint: https://doi.org/10.1063/1.1149048.

[182] F. D. Saccone et al. “Cobalt ferrite nanoparticles under high pressure”. In: *Journal of Applied Physics* 118.7 (2015), p. 075903. eprint: http://dx.doi.org/10.1063/1.4928856.

[183] L. M. Hrib and O. F. Caltun. “Effects of the chemical composition of the magnetostrictive phase on the dielectric and magnetoelectric properties of cobalt ferrite–barium titanate composites”. In: *Journal of Alloys and Compounds* 509.23 (2011), pp. 6644–6648.

[184] Giap V. Duong, R. Sato Turtelli, and R. Groessinger. “Magnetoelectric properties of $CoFe_2O_4$-$BaTiO_3$ core-shell structure composite studied by a magnetic pulse method”. In: *Journal of Magnetism and Magnetic Materials* 322.9(12) (2010). Proceedings of the Joint European Magnetic Symposia, pp. 1581–1584.

[185] Morad Etier et al. “$CoFe_2O_4$/$BaTiO_3$ core/shell nanoparticles”. In: *Ferroelectrics* 438 (2012), pp. 115–122.

[186] Y. S. Koo et al. “Strain-induced magnetoelectric coupling in BaTiO3/Fe3O4 core/shell nanoparticles”. In: *Applied Physics Letters* 94.3, 032903 (2009), p. 032903.

[187] V. V. Shvartsman et al. “Converse magnetoelectric effect in $CoFe_2O_4$-$BaTiO_3$ composites with a core-shell structure”. In: *Smart Materials and Structures* 20.7 (2011), p. 075006.

[188] V. Lemke et al. “FEM-analysis of a multiferroic nanocomposite, comparison of experiment and numerical simulation”. In: 17 (2017), pp. 521–522.

[189] J. Schröder et al. “Computation of Magneto-electric Product Properties for 0–3 composites”. In: *GAMM-Mitteilungen* 38 (1 2015), pp. 1–20.

[190] H. Balke and G. Suchaneck. “Commentary: On the linear coupling of mechanical and magnetic fields in magnetoelectrical composites”. In: *AIP Advances* 7.6 (2017), p. 060901. eprint: https://doi.org/10.1063/1.4986212.

[191] Morad Etier. “Preparation and Magnetoelctric Effect of Multiferroic Cobalt Ferrite-Barium Titanate Composites”. PhD thesis. University of Duisburg-Essen, Institut of Material Science, 2015.

[192] Muhammad Naveed Ul-Haq. “Magnetoelectric Effect in Lead-Free Multiferroic Composites and Thin Films”. PhD thesis. University of Duisburg-Essen, Institut of Material Science, 2017.

[193] R. Groessinger, Giap V. Duong, and R. Sato-Turtelli. “The physics of magnetoelectric composites”. In: *Journal of Magnetism and Magnetic Materials* 320.14 (2008), pp. 1972 –1977.

[194] Vincenzo Buscaglia and Maria Teresa Buscaglia. “Core-Shell Heterostructures: From Particle Synthesis to Bulk Dielectric, Ferroelectric, and Multiferroic Composite Materials”. In: *Nanoscale Ferroelectrics and Multiferroics*. John Wiley & Sons, Ltd, 2016. Chap. 3, pp. 72–99. eprint: https://onlinelibrary.wiley.com/doi/pdf/10.1002/9781118935743.ch3.

[195] Giorgio Schileo. “Recent developments in ceramic multiferroic composites based on core/shell and other heterostructures obtained by sol???gel routes”. In: *Progress in Solid State Chemistry* 41.4 (2013), pp. 87 –98.

[196] Morad Etier et al. “Magnetoelectric coupling on multiferroic cobalt ferrite and barium titanate ceramic composites with different connectivity schemes”. In: *Acta Materialia* 90 (2015), pp. 1 –9.

[197] Harsh Trivedi. “Mapping Local Manifestations of the Strain Mediated Magnetoelectric Effect in Composites”. PhD thesis. University of Duisburg-Essen, Institut of Material Science, 2015.

[198] Gabriel Caruntu et al. “Probing the local strain-mediated magnetoelectric coupling in multiferroic nanocomposites by magnetic field-assisted piezoresponse force microscopy”. In: *Nanoscale* 4 (2012), pp. 3218–3227.

[199] A. Rafferty, T. Prescott, and D. Brabazon. “Sintering behaviour of cobalt ferrite ceramic”. In: *Ceramics International* 34.1 (2008), pp. 15 –21.

[200] J.-H.; Kwon S.-J. Shin H.-S.; Lee. “A Study on the S-block Structure in Hexagonal Ferrites”. In: *J. Korean Ceram. Soc* 31.1 (1994), pp. 62–0. eprint: http://www.jkcs.or.kr/journal/view.php?number=3891.

[201] Morad Etier et al. “The Direct and the Converse Magnetoelectric Effect in Multiferroic Cobalt Ferrite?Barium Titanate Ceramic Composites”. In: *Journal of the American Ceramic Society* 99.11 (2016), pp. 3623–3631. eprint: https://ceramics.onlinelibrary.wiley.com/doi/pdf/10.1111/jace.14362.

[202] Andrey A. Kuznetsov. “Zero-Field and Field-Induced Interactions between Multicore Magnetic Nanoparticles”. In: *Nanomaterials* 9.5 (2019).

[203] D. A. Filippov et al. “Giant magnetoelectric effect in composite materials in the region of electromechanical resonance”. In: *Technical Physics Letters* 30.1 (2004), pp. 6–8.

[204] D. Bonnenberg and H.P.J. Wijn. “6.3.1.4 V spinels with V{3+} and V{4+}”. In: *Part B*. Ed. by K.-H. Hellwege and A. M. Hellwege. Berlin, Heidelberg: Springer Berlin Heidelberg, 1970, pp. 430–435.

[205] A C E Dent et al. “Effective elastic properties for unpoled barium titanate”. In: *Journal of the European Ceramic Society* 27.13-15 (2007), pp. 3739–3743.

[206] Zhang Rongjing. “Mechanical characterization of thin films with application to ferroelectrics. Dissertation”. PhD thesis. California Institute of Technology, 2006.

[207] “1994 5th International Symposium on Micro Machine and Human Science Proceedings”. In: *1994 5th International Symposium on Micro Machine and Human Science Proceedings*. 1994, 0_3˘.

[208] Tetsuro Tanaka. “Barium titanate ceramics and their applications”. In: *Bull. Inst. Chem. Res., Kyoto Univ* (1954), pp. 43–53.

[209] D. M. Evans et al. “Magnetic switching of ferroelectric domains at room temperature in multiferroic PZTFT”. In: *Nature Communications* 4 (2013), p. 1534.

[210] Florian H. Schader et al. “Influence of uniaxial stress on the ferroelectric-to-paraelectric phase change in barium titanate”. In: *Journal of Applied Physics* 113.17 (2013), p. 174103. eprint: https://doi.org/10.1063/1.4799581.

[211] X. Tan et al. “Effect of uniaxial stress on ferroelectric behavior of (Bi1/2Na1/2)TiO3-based lead-free piezoelectric ceramics”. In: *Journal of Applied Physics* 106.4 (2009), p. 044107.

[212] C A F Vaz. “Electric field control of magnetism in multiferroic heterostructures”. In: *Journal of Physics: Condensed Matter* 24.33 (2012), p. 333201.

[213] J. Wang. *Multiferroic Materials: Properties, Techniques, and Applications*. Series in Materials Science and Engineering. CRC Press, 2016.

[214] Hao-Miao Zhou et al. “An analytical nonlinear magnetoelectric coupling model of laminated composites under combined pre-stress and magnetic bias loadings”. In: *Smart Materials and Structures* 22.3 (2013), p. 035018.

[215] A. Clark, M. Spano, and H. Savage. “Effect of stress on the magnetostriction and magnetization of rare earth-Re1.95alloys”. In: *IEEE Transactions on Magnetics* 19.5 (1983), pp. 1964–1966.

[216] Yongping Wan, Daining Fang, and Keh-Chih Hwang. “Nonlinear constitutive relations for magnetostrictive materials”. In: *International Journal of Non-Linear Mechanics* 38.7 (2003), pp. 1053 –1065.

[217] Y. W. Li et al. “Large and electric field tunable superelasticity in BaTiO3 crystals predicted by an incremental domain switching criterion”. In: *Applied Physics Letters* 102.9 (2013), p. 092905. eprint: https://doi.org/10.1063/1.4795330.

[218] Tomohiro Yamasaki, Shinji Yamamoto, and Masahiko Hirao. “Effect of applied stresses on magnetostriction of low carbon steel”. In: *NDT & E International* 29.5 (1996). Asia-Pacific Conference on NDT, pp. 263 –268.

[219] H. Chiriac, M. Neagu, and C. Hison. “Magnetoelastic behavior in Co-based glass-covered amorphous wires”. In: *IEEE Transactions on Magnetics* 38.5 (2002), pp. 2823–2825.

[220] Zhengxin Chen and Yu Su. “The influence of low-level pre-stressing on resonant magnetoelectric coupling in Terfenol-D/PZT/Terfenol-D laminated composite structure”. In: *Journal of Applied Physics* 115.19 (2014), p. 193906. eprint: https://doi.org/10.1063/1.4876721.

[221] American National Standards Institute. et al. *IEEE standard on piezoelectricity : an American national standard*. New York, N.Y.: Institute of Electrical and Electronics Engineers, 1988, pp. –.

[222] X. J. Zheng and X. E. Liu. "A nonlinear constitutive model for Terfenol-D rods". In: *Journal of Applied Physics* 97.5 (2005), p. 053901. eprint: https://doi.org/10.1063/1.1850618.

[223] Mirza Bichurin et al. "Magnetoelectric Interactions in Lead-Based and Lead-Free Composites". In: *Materials* 4.4 (2011), pp. 651–702.

[224] Jungho Ryu et al. "Magnetoelectric Effect in Composites of Magnetostrictive and Piezoelectric Materials". English. In: *Journal of Electroceramics* 8.2 (2002), pp. 107–119.

[225] Dayu Zhou. "Experimental Investigation of Non-linear Constitutive Behavior of PZT Piezoceramics". PhD thesis. Faculty of Mechanical Engineering at the University of Karlsruhe, 2003.

[226] A. Aubert et al. "Dynamic Magnetostriction of $CoFe_2O_4$ and Its Role in Magnetoelectric Composites". In: *Phys. Rev. Applied* 9 (4 2018), p. 044035.

[227] Tingting Jia et al. "Domain switching in single-phase multiferroics". In: *Applied Physics Reviews* 5.2 (2018), p. 021102. eprint: https://doi.org/10.1063/1.5018872.

[228] M. Sajjia et al. "Magnetostrictive Cobalt Ferrite, Nanoparticles Preparation and Magnetic Characterization". In: *Reference Module in Materials Science and Materials Engineering*. Elsevier, 2016.

[229] Yongqiang Tan et al. "Unfolding grain size effects in barium titanate ferroelectric ceramics". In: *Scientific Reports* 5 (May 2015), pp. 9953–.

[230] R.D. Roseman and Niloy Mukherjee. "PTCR Effect in BaTiO3: Structural Aspects and Grain Boundary Potentials". In: *Journal of Electroceramics* 10.2 (2003), pp. 117–135.

[231] Maja Dukic, Jonathan D. Adams, and Georg E. Fantner. "Piezoresistive AFM cantilevers surpassing standard optical beam deflection in low noise topography imaging". In: *Scientific Reports* 5.1 (2015), pp. 16393–.

[232] Qiang Zhang. "Magnetic Field Shielding". In: *Advanced Materials for Electromagnetic Shielding*. John Wiley & Sons, Ltd, 2018. Chap. 6, pp. 109–146. eprint: https://onlinelibrary.wiley.com/doi/pdf/10.1002/9781119128625.ch6.